mgr inż. Łukasz Haryński

Scalable modifications of optical and electronic properties of TiO₂ nanotubes for solar electrochemistry

A doctoral dissertation
submitted to the Scientific Council
of the Institute of Fluid-Flow Machinery
Polish Academy of Sciences

Supervisor: dr hab. inż. Katarzyna Siuzdak, prof. IMP PAN

Gdańsk, *December* 2022

NATIONAL SCIENCE CENTRE
POLAND

I dedicate this work to my wife,

who has stood by my side from the very beginning.

Abstract

TiO_2 is one of the most studied compound in the world. Owing to its unique properties, it is used in photoelectrochemical systems, for instance, in photocatalysis and dye-synthesized solar cells. It can be obtained using chemical and physical methods, including sol-gel, hydrothermal, electrochemical, or chemical vapor deposition. However, many of them result in a product in the form of slurry, and further separation of the titanium dioxide from by-products and purification are required. Optimized electrochemical anodization of titanium allows the growth of highly ordered arrays of TiO_2 nanotubes already on the stable and conducting substrate. The geometric features of the nanotubes can be precisely tailored by the processing parameters such as electrolyte composition, voltage, or time. Moreover, anodization as a galvanic process can be realized on a technological scale in a cost and energy-efficient way. However, the wide band gap and indirect nature of dominating transition limit the commercial application of titania nanotubes in photoelectrochemical devices. One promising way of improving the electronic properties of TiO_2 nanotubes is defect introduction which can provide additional carriers for photon absorption. Another way is the formation of heterojunction. The resulting potential bias at the interface can facilitate the separation of excitons. The deposited species can also incorporate into titania, provide additional states deep within the band gap and contribute to the absorption of visible light. Nevertheless, to take an advantage of anodization as a fabrication process, any further modifications should be designed to make the technological scale easy to achieve. Taking into account the limitations of titanium dioxide and the challenges that it has to face to be widely applied in photoelectrochemical systems, the aim of this work is the elaboration and optimization of easily scalable methods improving the optical and electronic properties of TiO_2 nanotubes.

The basis of this doctoral dissertation is a series of four articles published in journals indexed in the Journal Citation Reports list in the field of mechanical engineering.

The first part of the thesis presents a scalable method for pulsed laser-induced structure modulation of TiO_2 nanotubes towards superior photoresponse. Controlled degradation of the crystal structure along with beam energy fluence leading up to a 1.45-fold increase in photoresponse was found. The novel approach concerns the optimization of the laser processing parameters in the system equipped with a beam homogenizer and motorized table which allows for modification of both precisely selected as well as any large area without the need for liquid media. These advances will hopefully enrich a state-of-the-art in the field of production engineering and bridge the gap between research and

successful industrial application of laser technology for the modifications of functional materials.

The second part of the thesis reports a study of the optical and electronic properties of TiO_2 nanotubes combined with thin films of chromium, molybdenum, and tungsten oxides using magnetron sputtering technology followed by thermal annealing. Because of the contradiction in the literature reports regarding the transition types occurring in the investigated metal oxides, a precise systematized method allowing for the determination of the Tauc exponent and corresponding transition types was elaborated. In particular, Taylor series expansion was applied to the logarithmic version of the Tauc equation, which after solving, allowed for determining the Tauc exponent directly from the experimental absorption data without any assumptions regarding the investigated material, such as band gap width. A further study showed an unambiguous correlation between the estimated transition types and sample photoresponse. The obtained results demonstrate that the transition type estimated based on the Tauc exponent is a crucial predictor for sample photoresponse, even better than the optical band gap width. This framework may help for a more precise determination of the optical band gap. The above considerations were supported by a theoretical study.

According to the gathered results, it was shown that optimized laser modification of titania nanotubes in a system equipped with a beam homogenizer and motorized table, as well as the formation of heterojunction with chromium oxides using magnetron sputtering technology, allow for the fabrication of materials exhibiting superior photoresponse compared to bare TiO_2 nanotubes. Moreover, the elaborated method for determining the Tauc exponent and corresponding transition type (or transition types) can be widely used in the detailed analysis of optical and photoelectrochemical properties of functional materials.

Streszczenie

TiO$_2$ jest jednym z najszerzej przebadanych związków na świecie. Dzięki unikalnym właściwościom znajduje zastosowanie w układach fotoelektrochemicznych, na przykład w fotokatalizie oraz barwnikowych ogniwach słonecznych. Ditlenek tytanu można otrzymać metodami chemicznymi oraz fizycznymi, w tym zol-żel, hydrotermalną, elektrochemiczną, lub osadzania z fazy gazowej. Jednakże, wiele z nich daje produkt w postaci zawiesiny, który wymaga oczyszczenia oraz oddzielenia ditlenku tytanu od produktów ubocznych. Zoptymalizowana elektrochemiczna anodyzacja tytanu pozwala wytworzyć wysoce uporządkowane nanorurki TiO$_2$ od razu na stabilnym i przewodzącym podłożu. Cechy geometryczne nanorurek można precyzyjnie dostosować za pomocą parametrów procesowych takich jak: skład elektrolitu, napięcie, czy czas. Ponadto, anodyzacja, jako proces galwaniczny może być realizowana na skalę technologiczną w sposób efektywny kosztowo i energetycznie. Jednakże, szeroka przerwa energetyczna oraz skośne przejście ditlenku tytanu limitują komercyjne wykorzystanie nanorurek w układach fotoelektrochemicznych. Jedną z metod mogącą przyczynić się do poprawy właściwości elektronowych jest wprowadzenie defektów strukturalnych. Mogą one stanowić źródło dodatkowych nośników ładunku, które będą brały udział w procesie absorpcji światła. Inną metodą jest utworzenie heterozłącza. Powstały potencjał na granicy faz może poprawić separację ekscytonów. Ponadto, osadzone związki mogą wbudować się w strukturę ditlenku tytanu oraz przyczynić do powstania dodatkowych stanów głębiej wewnątrz przerwy wzbronionej, które umożliwią absorpcję światła w zakresie długości fal odpowiadającym światłu widzialnemu. Niemniej, aby w pełni wykorzystać potencjał anodyzacji jako proces produkcji, późniejsze modyfikacje powinny być prowadzone w taki sposób, aby skala technologiczna była łatwa do osiągnięcia. Biorąc pod uwagę ograniczenia ditlenku tytanu oraz wyzwania jakie są mu postawione, by został powszechnie wykorzystany w układach fotoelektrochemicznych, celem tej rozprawy jest opracowanie i optymalizacja łatwo skalowalnych metod poprawiających właściwości optycznych i elektronowych nanorurek TiO$_2$.

Podstawą niniejszej rozprawy doktorskiej jest cykl czterech artykułów opublikowanych w czasopismach z listy filadelfijskiej w dyscyplinie inżynierii mechanicznej.

Pierwsza część rozprawy doktorskiej prezentuje skalowalną metodę modyfikacji struktury krystalicznej nanorurek TiO$_2$ prowadzącą do wzrostu fotoaktywności przy użyciu impulsowej wiązki promieniowania laserowego. Wyniki badań wykazały kontrolowaną degradację struktury wraz ze wzrostem fluencji wiązki, prowadzącą do wzrostu fotoaktywności nanorurek o 45 %. Nowe podejście dotyczy optymalizacji obróbki

laserowej w układzie z homogenizatorem oraz zmotoryzowanym stolikiem przesuwnym umożliwiającym modyfikację zarówno ściśle określonej, jak i dowolniej dużej powierzchni bez konieczności stosowania ciekłych mediów. Uważa się, że zaproponowane rozwiązania wzbogacą stan wiedzy w dziedzinie inżynierii produkcji i wypełnią lukę między badaniami podstawowymi oraz przemysłowym zastosowaniem technologii laserowej do modyfikacji materiałów funkcjonalnych.

W drugiej części rozprawy przedstawiano wyniki badań właściwości optyczne i elektronowe nanorurek TiO_2 wraz z osadzonymi cienkimi warstwami tlenków chromu, molibdenu oraz wolframu, z wykorzystaniem technologii rozpylania magnetronowego, poddanych następnie obróbce termicznej. Ze względu na sprzeczne doniesienia literaturowe dotyczące rodzaju przejść elektronowych w rozważanych tlenkach metali, opracowano usystematyzowaną, precyzyjną metodę, pozwalającą wyznaczyć wykładnik w równaniu Tauca oraz odpowiadające mu przejścia elektronowe. W szczególności, zlogarytmowane równanie Tauca rozwinięto w szereg Taylora, co po rozwiązaniu pozwoliło wyznaczyć wykładnik w oparciu o eksperymentalne dane absorpcyjne bez konieczności stosowania dodatkowych założeń odnośnie badanego materiału takich jak szerokość pasma wzbronionego. Dalsze badania wykazały jednoznaczną korelację pomiędzy generacją fotoprądu badanych elektrod, a wyznaczonymi rodzajami przejść elektronowych. Uzyskane wyniki wykazały, że rodzaj przejścia elektronowego wyznaczony w oparciu o równanie Tauca stanowi istotny parametr diagnostyczny w ocenie fotoaktywności materiałów, lepszy niż szerokość optycznej przerwy wzbronionej. Ponadto, opracowana metoda może pozwolić na bardziej precyzyjne wyznaczenie optycznej przerwy wzbronionej. Powyższe rozważania zostały uzupełnione badaniami teoretycznymi.

Zgodnie z uzyskanymi wynikami wykazano, że zoptymalizowana obróbka laserowa nanorurek TiO_2 w układzie z homogenizatorem wiązki oraz zmotoryzowanym stolikiem przesuwnym, a także utworzenie heterozłącza z tlenkami chromu wykorzystując technologię rozpylania magnetronowego, pozwalają na otrzymanie materiału charakteryzującego się wyższą fotoaktywnością w porównaniu do niemodyfikowanych nanorurek TiO_2. Ponadto, opracowana metoda wyznaczania wykładnika Tauca oraz odpowiadającego mu przejścia elektronowego (lub przejść elektronowych) może znaleźć szerokie zastosowanie w szczegółowej analizie właściwości optycznych i fotoelektro-chemicznych materiałów funkcjonalnych.

Table of Contents

Abbreviations

1D	—	one-dimensional
3D	—	three-dimensional
$\lvert a \rangle$	—	a discrete state
A	depending on the context:	
	—	Tauc slope
	—	surface area
AM	—	air mass
$\lvert b \rangle$	—	a discrete state
C	—	capacitance
CA	—	chronoamperometry
CE	—	counter electrode
CV	—	cyclic voltammetry
DFT	—	density functional theory
$\vec{d}$	—	dipole operator
e	—	elementary charge
E	—	potential
E_a	—	energy of a state $\lvert a \rangle$
E_b	—	energy of a state $\lvert b \rangle$
E_{bin}	—	binding energy
E_C	—	energy of a conduction band
ΔE_C	—	energy difference between conduction bands of two different semiconductors
E_F	—	energy of a Fermi level
E_{fb}	—	energy of a flat-band potential
E_G	—	energy of a band gap
$E_{g(1)}$	—	anatase Raman active mode
E_k	—	kinetic energy
E_V	—	energy of a valence band
ΔE_V	—	energy difference between valence bands of two different semiconductors
EIS	—	electrochemical impedance spectroscopy
$f(R)$	—	Kubelka-Munk function
G	—	global

h	—	Planck constant
$\hbar$	—	reduced Planck constant
I_o	depending on the context:	
	—	intensity of the incident light
	—	amplitude of the current response
I	depending on the context:	
	—	current
	—	intensity of the light which passed through the sample
IF	—	Impact Factor
j	—	spin-orbit splitting value
k	—	wave vector
k_B	—	Boltzmann constant
K	—	Kubelka-Munk absorption coefficient
l	—	azimuthal quantum number
LSV	—	linear sweep voltammetry
M	—	a high-symmetry point in the First Brillouin Zone
$\vec{n}$	—	unit vector of an electric field
n	depending on the context:	
	—	semiconducting properties with electrons as majority charge carriers
	—	Tauc exponent
	—	principal quantum number
N	—	a high-symmetry point in the First Brillouin Zone
N_D	—	donor density
Nd:YAG	—	neodymium-doped yttrium aluminum garnet
p	depending on context:	
	—	semiconducting properties with holes as majority charge carriers
	—	momentum
P	—	a high-symmetry point in the First Brillouin Zone
$P_{a \leftarrow b}(t)$	—	probability for transition from $|b\rangle$ to $|a\rangle$ as a function of time
$P(v)$	—	probability amplitude as a function of frequency
q	—	charge
R	—	reflectance
RE	—	reference electrode
s	depending on context:	
	—	scattering coefficient
	—	spin quantum number

|		
	—	orbital
S	—	Kubelka-Munk scattering coefficient
SEM	—	scanning electron microscopy
T	—	temperature
UV	—	ultraviolet
v	—	frequency
v_{ba}	—	frequency associated with a transition from $|a\rangle$ and $|b\rangle$
V_0	—	amplitude of the voltage signal
V	—	voltage
V_D	—	diffusion voltage
vis	—	visible
WE	—	working electrode
XPS	—	X-ray photoluminescence spectroscopy
XRD	—	X-ray diffraction
Z_0	—	magnitude of the impedance
Z	—	impedance
α	—	absorption coefficient
λ	—	wavelength
ε	—	dielectric constant
ε_0	—	vacuum permittivity
ϕ	depending on the context:	
	—	work function
	—	phase shift
χ	—	electron affinity
ψ	—	electric potential
ω	—	laser harmonic

Chapter 1. Outline

1.1 Renewable energy resources

Nowadays, decreasing number of fossil fuels forces demands for the use of renewable resources. The mainstream technologies for green energy production involve bioenergy, hydropower, as well as geothermal, ocean, solar, and wind energies. The development of each of these technologies is relevant for sustainable energy production due to the different environmental conditions in different parts of the world. Their contribution to total electricity generation is visualized in Figure 1 a.

Among various renewable resources, the use of solar energy for the generation of electricity increases exponentially (see Figure 1 b). It is used worldwide and can be harnessed directly from the Sun, even during cloudy weather. Semiconductors, due to their unique electronic properties, such as band gap, have been tremendously studied for the conversion of solar energy to electricity. In general, the electrons excited from the valence band to the conduction band through the band gap can be collected in an external circuit and generate current. Efficient conversion of solar energy to electricity demands, however, specific properties of materials including a proper optical band gap width or direct transition for photon absorption. Nevertheless, not only the performance but also a feedstock availability and fabrication technology are crucial for sustainable development. Therefore, a certain interest should be paid both to the properties of the material and the technology of its fabrication.
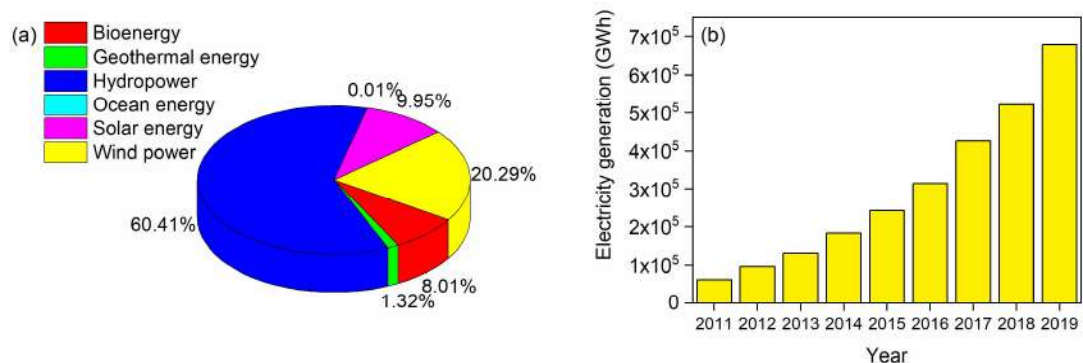

Figure 1. Electricity generation from (a) renewable energy resources in 2019, (b) from solar photovoltaics during the last decade [1].

1.2. Anodic TiO$_2$ nanotubes

Among various candidates for materials for photoelectrochemical devices, TiO$_2$ nanotubes, as a 1D structure exhibit high surface area [2], unique electronic properties [3], and very high mechanical strength [4]. There are various methods allowing for the fabrication of TiO$_2$ nanotubes, such as sol-gel [5], hydrothermal [6], template-assisted methods [7], or anodization [8]. In contrast to other methods, the anodization results in the formation of the highly ordered arrays of the nanotubes with direct contact with the metal support (see Figure 2). The principle of anodization is to apply an anodic bias voltage to the titanium substrate immersed in a fluorine ion-containing electrolyte, and maintain it for a certain time [8]. It allows for precise control of the nanotubes' geometric features including length, spacing, or wall-thickness through manipulation of processing parameters such as voltage, electrolyte composition, or time [8]. Taking that into account, and that the electrochemical processes are, in general, widely used in the industry (e.g. electroplating plants), the anodic TiO$_2$ nanotubes can be also distinguished by low-cost production and scalability. As proof for large-scale production one can find an example provided by Xiang et al. [9] who produced uniform titania nanotube arrays at the inner surface of a 1 m long and 1 cm in diameter titanium tube.

The as-obtained nanotubes are amorphous and exhibit poor photon-to-electron conversion efficiency [8], and due to that, usually, they are annealed at elevated temperatures to reach crystal structure and enhance photoresponse [10]. However, the limitations of TiO$_2$ nanotubes are related to the large band gap of TiO$_2$ (e.g. anatase, E_G = 3.2 eV; rutile, E_G = 3.0 eV) and the indirect nature of dominating transition, which are described in the following two subsections.
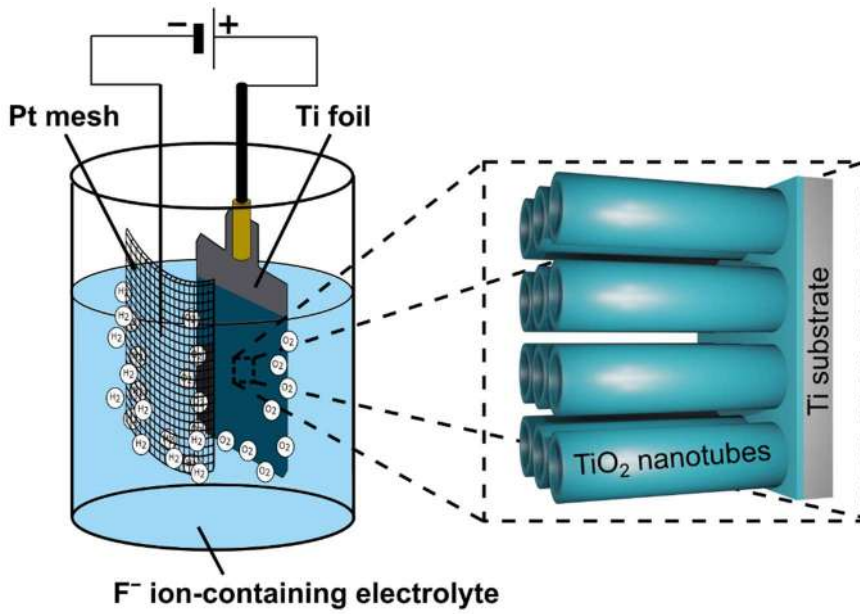
Figure 2. The electrochemical anodization process
and the self-organized TiO$_2$ nanotubes.

1.2.1. Optical band gap

A band gap is a minimum energy between the valence band maximum and the conduction band minimum. The transition between these two states is possible, however, it must be triggered by something to take a place. In fact, the electron occupying an eigenstate (such as a valence band) without any perturbation stays there forever [11]. Essentially, photons carrying the energy corresponding to the band gap can excite electrons from the valence to the conduction band. This interaction can be explained by the time-dependent perturbation theory. Probability amplitude as a function of time for the transition between two discrete states triggered by an interaction between atoms and light through a dipole interaction is given by [11]:

$$P_{a \leftarrow b}(t) = \frac{4 \left| \left(\vec{d} \cdot \vec{n} \right)_{ab} \right|^2}{\hbar^2} \frac{\sin^2 \left(\frac{v_{ba} - v}{2} t \right)}{(v_{ba} - v)^2} \tag{1}$$

where $\vec{d}$ is a dipole operator, and $\vec{n}$ is a unit vector of an electric field, $\hbar$ is a reduced Planck constant, v is a frequency of the external light, and v_{ab} is a frequency associated with a transition from $|b\rangle$ to $|a\rangle$: $v_{ab} = (E_b - E_a)/\hbar$. Based on Equation 1, one can relate the probability amplitude for the transition to the frequency of the incident light (see Figure 3 a). Here, it can be seen that only a photon with a frequency corresponding to the energy

difference between these two states (v_{ab}) contributes to the highest probability amplitude, and triggers the transition the most. Therefore, the ideal semiconductor should exhibit a band gap equal to the energy corresponding to the maximum intensity of the solar spectrum for the efficient photon-to-electron conversion. Based on the data presented in Figure 3 b, one can see that the maximum intensity is at about 500 nm. Hence the ideal band gap falls at about 2.48 eV. The optical band gap is therefore crucial not only for material characterization but also for its further modifications with light, for example, for crystallization [12] or defect introduction induced by laser radiation [13].

Determination of the band gap concerns both experimental and theoretical considerations. Experimentalists, usually determine band gap based on the Tauc equation:

$$(\alpha h v)^{1/n} = A(h v - E_G) \qquad (2)$$

where α is the absorption coefficient being a function of wavelength $\alpha(\lambda)$, h is a Planck constant, v is a frequency, n is a Tauc exponent, A is the proportionality constant, and E_G is an optical band gap. The method is to plot $(\alpha h v)^{1/n}$ vs. $h v$ and extrapolate the linear range beyond the absorption edge yielding the value of the band gap on the abscissa axis. However, to do so, the value of the Tauc exponent, hence the nature of the transition must be known. Typically, the Tauc exponent is chosen as one of four values: 1/2, 3/2, 2, and 3 corresponding to the direct (allowed), direct (forbidden), indirect (allowed), and indirect (forbidden) transitions, respectively [14]. In the case of TiO_2 nanotubes, the experimentalists consistently choose $n = 2$ corresponding to indirect (allowed) transition [15] which is in line with theoretical predictions that pure anatase TiO_2 exhibits indirect nature of the transition between the valence band maximum and conduction band minimum [16]. It is worth noticing that, for the construction of the Tauc plot, both absorption and photocurrent data can be taken [17].

According to Tauc plots [8], bare TiO_2 nanotubes fabricated in ethylene glycol exhibit a 2.85 eV wide band gap. In turn, the calculated band gap for anatase using a relatively accurate method involving density of functional theory with Hubbard U and Hund's J corrections is 3.5 eV. The calculated values are higher compared to experimental ones because they concern non-defected materials, and therefore, sub-band levels are not seen and the values are higher. Efficient utilization of solar energy for electricity production using TiO_2 nanotubes would therefore require further modifications resulting in considerable band gap narrowing, ideally to 2.48 eV which corresponds to the maximum intensity of solar light.
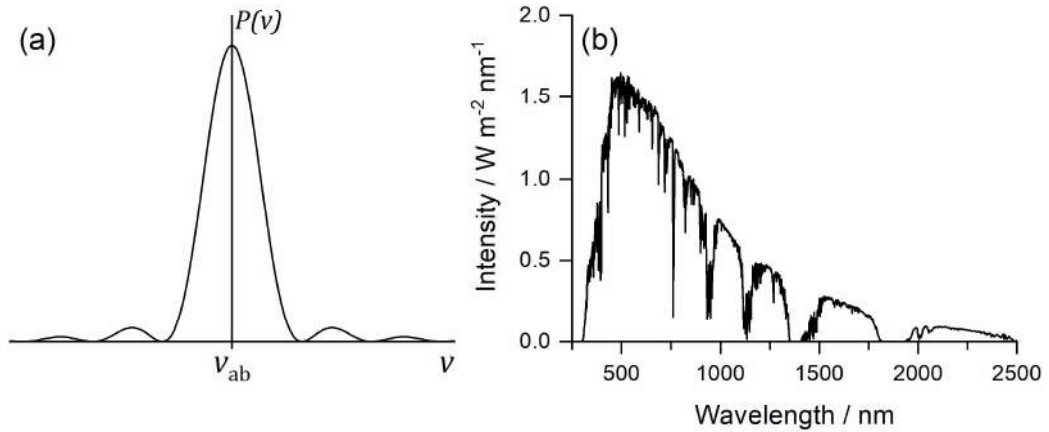
Figure 3. (a) Probability amplitude for a photon absorption through an electric dipole interaction with an electromagnetic wave as a function of the frequency [11].
(b) The spectrum of AM 1.5 Global [18].

1.2.2. Transition type

In general, there are two types of transition related to the direction in crystal, namely direct and indirect, and each of them can be allowed or forbidden. The difference between direct and indirect transition can be understood by studying band structure diagrams (see Figure 4). In the case of indirect transition, the valence band maximum and the conduction band minimum have different wave vectors (see arrow I). From de Broglie's relation, one can relate wave vector to momentum as $p = \hbar k$, and see that the creation of hole-electron pair through such as indirect transition is not allowed by momentum-conservation considerations. It can only take place if a phonon of a corresponding wave vector is created or destroyed. Hence, the probability of such a transition is very low compared to the direct transition (see arrow II) for which the wave vector of the electron remains essentially constant [19].

Both direct and indirect transitions can be forbidden or allowed by the selection rules depending on the probability amplitude for the transition is zero or not (see Equation 1). Forbidden transitions exhibit zero probability amplitude and zero transition rate due to the zero dipole matrix elements [20]. In other words, such transitions do not take place because no dipole moment is being induced, and there is no trigger for the transitions. In fact, in quantum mechanics, an electron occupying an eigenstate without any perturbation stays there forever [20]. Nevertheless, in real systems, such transitions will eventually take place either by collisions, or multiphoton absorption, however, the rates of these processes are orders of magnitude lower compared to the allowed electric dipole

transitions [20]. Therefore, another crucial, however, often underestimated aspect regarding optical absorption is the nature of the transition.

The literature in most cases assumes an indirect band gap of TiO_2 with allowed transition, for instance [21]. Since the rate of an indirect transition is many orders of magnitude lower compared to a direct transition [19], it is undesirable for electricity production from solar energy. Because of that, TiO_2 nanotubes were first sensitized by dyes to develop visible-light response, and then, intensively utilized in dye-sensitized solar cells [22]. However, dyes suffer from degradation [23] whereas a photovoltaic cell with TiO_2 nanotubes in their pristine form exhibits an efficiency of only about 5 % [24]. To enable their practical applications in the pristine form, one must elaborate strategies for band gap engineering. Since the biggest advantage of the TiO_2 nanotubes lies in the potential for low-cost large-scale production, any further modification should also involve techniques that can be easily commercialized.
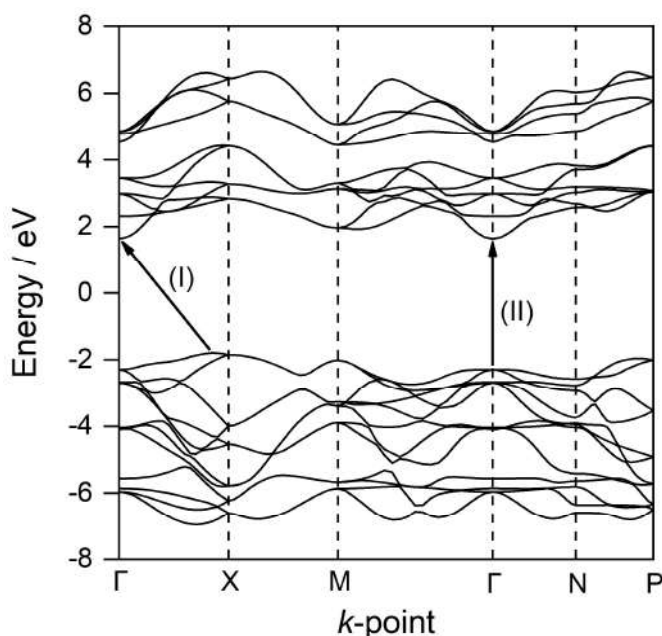
Figure 4. The band structure of anatase TiO_2 calculated using density functional theory with Hubbard U correction [25]. Arrows I and II indicate indirect and direct transitions, respectively.

1.3 Strategies toward improved electronic properties of anodic TiO₂ nanotubes

1.3.1 Defect introduction by laser treatment

Crystal structures of TiO_2 exhibit rather large band gaps (3.2 eV anatase and 3.0 eV rutile) limiting their absorption mainly to the UV which covers a minority of the solar spectrum (see Figure 3 b). However, significant visible activity can be enabled in TiO_2 by the formation of defects [26]. Extensive studies on black TiO_2 have shown that not solely the presence of defects, but rather the interplay of different factors like defect concentration, defect location, and anatase-to-rutile ratio play a key role in the photoactivity of defective TiO_2 [27]. Various methods have been studied for the defect introduction in TiO_2 including hydrogenation, metal reduction, plasma-assisted process, microwave radiation, laser ablation, electrochemical reduction, etc. [27]. In general, hydrogenation remains the most studied route, however, recently fast and more eco-friendly methods such as laser modification are getting more and more attention [27].

During the last decade, laser modification has been utilized for the introduction of defects in TiO_2 in different forms including thin films [28], and nanoparticles [29], however, pioneering work on the laser modification of TiO_2 nanotubes was reported in 2017 by Xu et al. [13]. The authors demonstrated that pulsed UV laser treatment of anatase TiO_2 nanotubes can significantly modify their electronic properties improving their photoresponse under solar illumination. XRD patterns of the laser-treated samples confirmed the degradation of the crystal structure. SEM images revealed increasing melting of the top of the nanotubes along with applied energy fluence of the laser beam. The analysis of Mott-Schottky plots for the sample under optimized processing parameters regarding photoresponse showed both a shift of flat band potential and an increase in donor density. It is not clear, however, if the authors calculated capacitance data using geometric or active surface area. Therefore, an increase in donor density could be related to a change in sample surface area. Nevertheless, the shift of the flat band potential (hence the Fermi level) strongly evidences the different electronic properties of the modified layer. In turn, the capacitance measurements suggested that the additional laser-induced states are rather shallow. Therefore, the authors assigned improved photoresponse to the additional intraband shallow states originating from disordered crystal structure within the melted layer. Nevertheless, during the irradiation, the samples were placed in a Petri dish filled with 15 ml of deionized water. Such a system can be successfully used for modifications in laboratory scale but can be problematic on a large scale. Owing to the low-cost and scalable production potential of anodic TiO_2 nanotubes,

it is convenient to design further modifications with the same potential. In the present dissertation, a scalable method utilizing a beam homogenizer and motorized table for laser modification of TiO₂ nanotubes was elaborated and developed and is described in Paper 1. Detailed literature revision regarding the interaction between titania and laser radiation is in turn presented in Paper 2.

1.3.2 Heterojunction

Combination with other metal oxides is a prominent strategy for alleviating issues related to the band gap of TiO$_2$ nanotubes. Their incorporation into titania can narrow the band gap through the formation of mid-gap states [30] and contribute to better efficiencies. Also, at the heterojunction, a space charge region with a high electric potential gradient can facilitate electron-hole separation and charge transport. Nevertheless, the band bending at the heterojunction depends on the work functions of the separated semiconductors [31], and not always facilitate electron transfer in the conduction band. Exemplar energy diagrams for two uncharged n-type semiconductors before and after heterojunction formation are displayed in Figure 5 a and b, respectively. Once they are brought into contact, an electron flow from semiconductor 1 into semiconductor 2 occurs until the equilibrium (constant Fermi level) is reached (Figure 5 b) [31]. The driving force for this process is the difference in work functions [31]. In the equilibrium, the conduction and valence bands are bent and a diffusion voltage is created [31]. Note that a potential barrier is different from left to right and right to left but it is always present in the n-n heterojunction regardless of the direction. A facile charge transfer without a potential barrier in the conduction band is possible for a p-n heterojunction, however, only when a work function of a p-type semiconductor is greater than the n-type (see Figure 5 c) [32]. It is also worth noting that work function depends on the size of the material, especially in the case of a nanoscale [33]. Therefore, the estimation of a potential bias at the heterojunction based on the literature values, even if similar compounds are joined, should be done carefully.
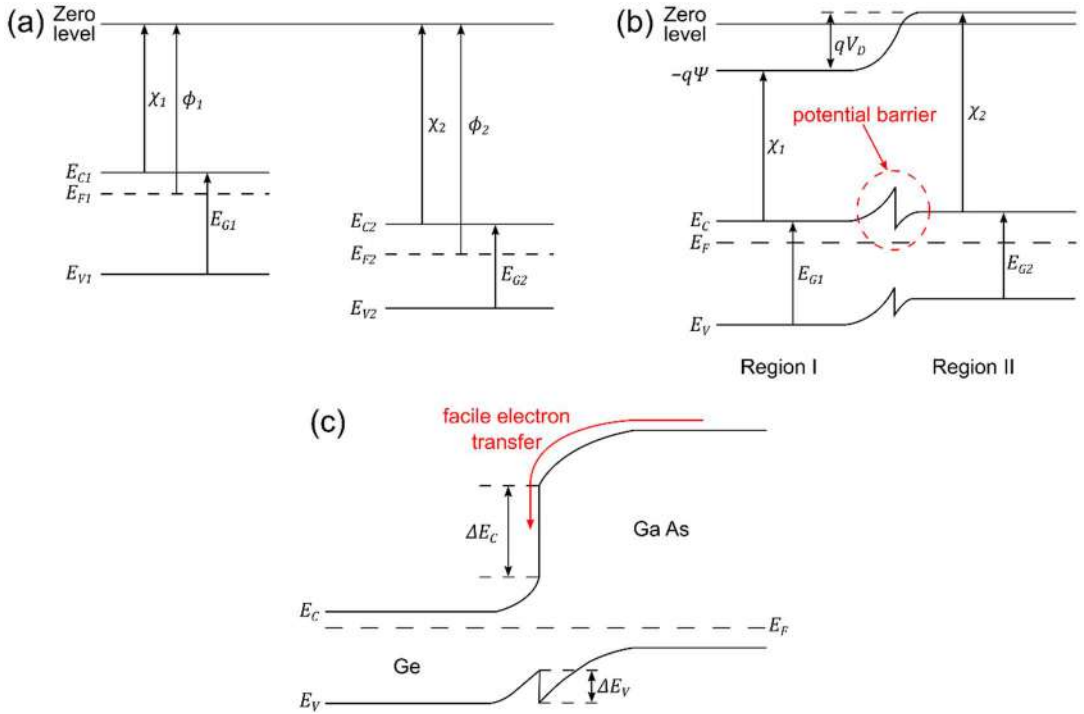
Figure 5. (a-b) Energy diagrams for two uncharged *n*-type semiconductors
(a) separated, (b) brought into contact (adapted from [31]).
(c) Energy diagram for Ge-GaAs *n-p* heterojunction (adapted from [32]).

Metal oxides of the 6th main group of the periodic table are in general considered as wide, about 3 eV band gap semiconductors [34–36]. Based on the literature [35,37], tungsten and molybdenum oxides are *n*-type semiconductors. In turn, the semiconducting properties of chromium oxides depend on the oxidation state – Cr_2O_3 is a *p*-type whereas CrO_2 is an *n*-type [38]. Therefore, a heterojunction between TiO_2 nanotubes and Cr_2O_3 would be particularly interesting because of the possibility of a facile electron transfer. In the case of the transition type, the literature is not consistent. For instance, for the Tauc plot construction for Cr_2O_3, one authors choose $n = 1/2$ [39] whereas others $n = 2$ [40] corresponding to direct and indirect (allowed) transitions, respectively. Furthermore, it has been observed that in many cases the authors choose the Tauc exponent from other articles in which the transition type is not justified, e.g. [41] and [42]. As it was mentioned, transition types can be anticipated from theoretical considerations, however, they are usually calculated for non-defected materials, hence are not valid for modified structures. It is also unclear which transition type should be assumed in a multi-component material in which each component exhibits a different transition. Therefore, a systematic procedure for determining the transition type, for instance, directly from measured data would be crucial not only for the precise determination of optical band gap

but also for predicting the transition rate (note that different transition types exhibit different transition rates). Such a method was first proposed by Sangiorgi et al. [43]. The principle of the method is to estimate the Tauc exponent from the Tauc equation (see Equation 2) using experimentally measured UV-vis spectroscopy data. To do so, the authors proposed to take both sides logarithm of the Tauc equation, which multiplied by n yields:

$$\ln(\alpha h v) = n \ln(h v - E_G) + const. \tag{3}$$

and estimated n from the linear dependence of $\ln(\alpha h v)$ on $\ln(h v - E_G)$:

$$n = \frac{\partial \ln(\alpha h v)}{\partial \ln(h v - E_G)} \tag{4}$$

To estimate the Tauc exponent using this method, one must assume the E_G value. Because the result depends on the assumed band gap value, the method cannot be recognized as precise.

In general, optical properties and photoresponse of the heterojunctions based on the TiO_2 and chromium, molybdenum, and tungsten oxides have already been reported in the literature [44–46]. Nevertheless, they have not been thoroughly investigated. Especially, the nature of optical transitions and their contribution to photoresponse. Therefore, in the present dissertation (Paper 3), an improved method allowing for the determination of the Tauc exponent without any assumption regarding the investigated material such as band gap was elaborated. It is particularly essential not only for precise optical band gap determination, but also for determining the transition type occurring in the investigated material. In the subsequent work (Paper 4), a correlation between the estimated transition types and the photoresponse was presented.

Chapter 2. Objective and scope of the thesis

Fabrication of TiO_2 nanotubes via anodization of titanium has a high production potential on an industrial scale. However, anodic TiO_2 nanotubes in the bare form exhibit undesirable optical and electronic properties for efficient solar energy to electricity conversion. Therefore, the main objective of this dissertation was the elaboration of methods for large-scale modification of TiO_2 nanotubes towards improved photoresponse as well as the characterization of the obtained materials using solid-state physics and photoelectrochemical methods. It was realized by the introduction of defects via laser annealing in a system equipped with a beam homogenizer and motorized table as well as by the formation of heterojunction with chromium, molybdenum, and tungsten oxides using magnetron sputtering technology.

The scope of the dissertation covered:

➢ Selection of optimum parameters of the laser beam towards a scalable modification of TiO_2 nanotubes surface,

➢ Examination of the impact of the laser modification on the morphology, crystal structure, optical and electronic properties, and photoresponse of the TiO_2 nanotubes,

➢ Literature revision regarding laser-induced modifications of TiO_2,

➢ Elaboration of a method allowing for the determination of Tauc exponent and corresponding transition types in TiO_2 nanotubes combined with chromium, molybdenum, and tungsten oxides,

➢ Investigation of the optical properties, band structure, and photoresponse of the TiO_2 nanotubes combined with chromium, molybdenum, and tungsten oxides,

➢ Design and construction of the experimental setup for photoelectrochemical tests.

The results of the conducted research have been published in articles indexed in the JCR list which are presented later on in Chapter 5.

Chapter 3. Experimental

3.1. Substrates

Titanium foil (Strem, 99.7 %) was used as a substrate for anodization. Prior to the process, it was cleaned in three solvents in a sequence in acetone, ethanol, and water for 10 minutes in each in an ultrasonic bath. To reduce waste and ensure solvent access to both sides of the foil, a container for substrates was designed and 3D printed in fused filament fabrication technology (see Figure 6). The inside was designed to separate the adjacent foils and allow for bilateral solvent access. Polyamide filament was chosen due to its resistance to acetone. The geometric features and application of the litter box are proprietary by a utility model [47].
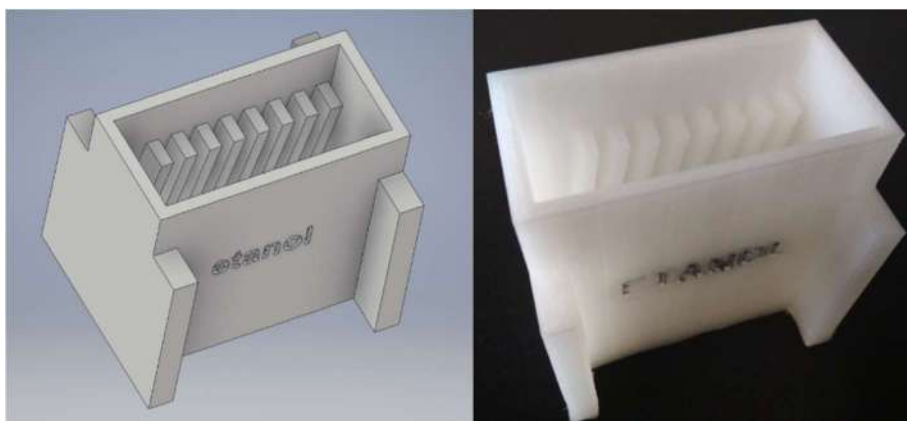

Figure 6. Titanium foil cleaning litter box 3D model (left) and a photo of the 3D printed element (right).

3.2. Fabrication procedures

3.2.1. Anodization of titanium foil

Anodization was realized in a two-electrode system where titanium foil served as an anode and platinum mesh as a cathode in a glycol ethylene-based electrolyte with 10 g L^{-1} of NH_4F and 15 % of H_2O. The temperature was set to 23 °C and it was controlled by a thermostat. During the process, 40 V was maintained for 15 minutes with a voltage ramp-up and ramp-down times of 6.66 minutes. Because the as-obtained TiO_2 nanotubes are amorphous and exhibit poor photon-to-electron conversion efficiency [8], after the anodization they were thermally annealed at 450 °C for 2 hours to reach crystal structure. A representation of the fabrication route of TiO_2 nanotubes is given in Scheme 1.
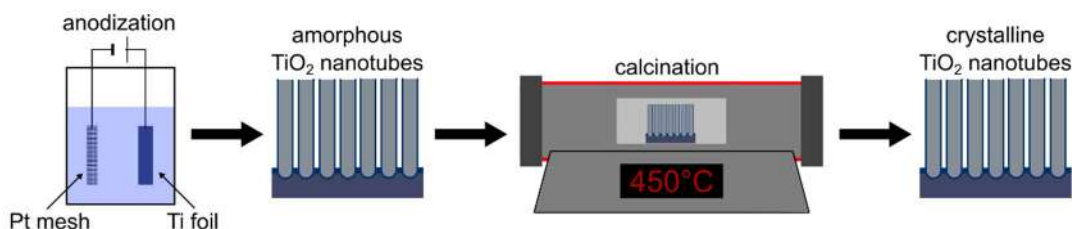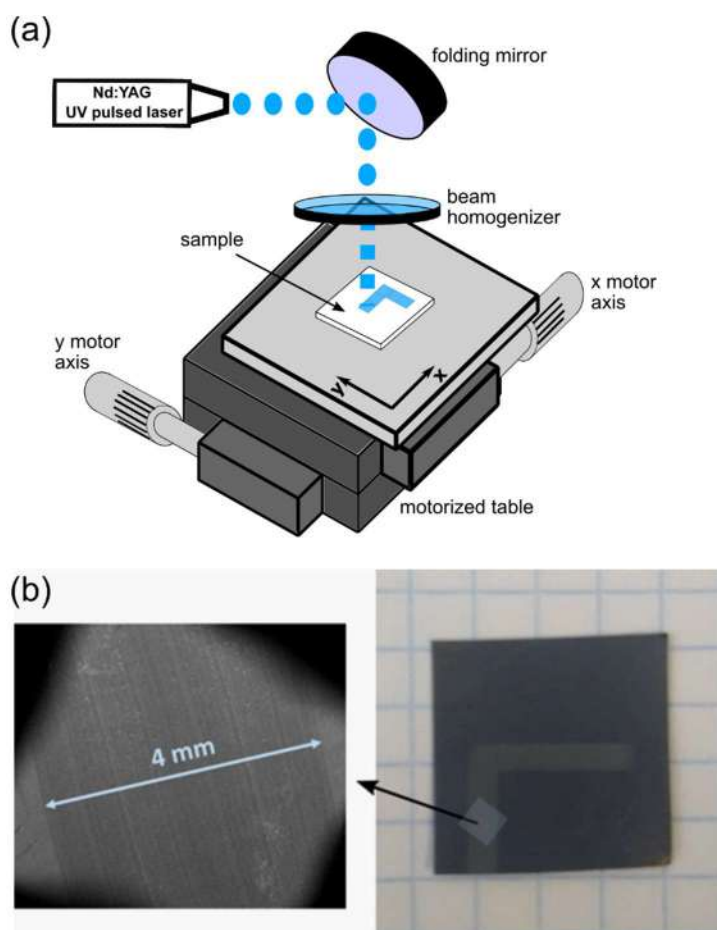
Scheme 1. Schematic diagram illustrating fabrication process of bare TiO$_2$ nanotubes.
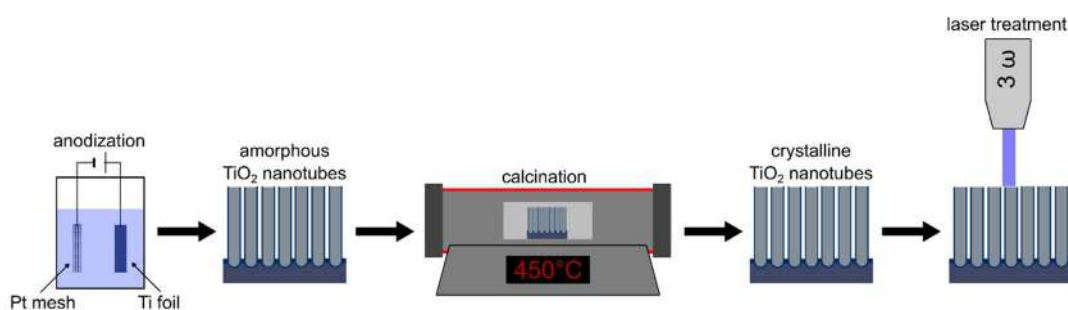
3.2.2. Laser treatment of TiO$_2$ nanotubes

Typically, laser modification is realized in a static conditions [48]. However, to take advantage of the industrial potential of anodic TiO$_2$ nanotubes any further modifications should account for a large scale. Therefore, in the present dissertation, a new scalable system equipped with a beam homogenizer ensuring a square beam spot and a motorized table was developed and elaborated. Such a system allows to modify precisely selected as well as any large area. A schematic diagram displaying the experimental setup for laser modification along with a photo showing an exemplar laser trace is presented in Figure 7.

In particular, laser treatment was realized using Nd:YAG laser with 6 ns pulse duration. Due to the large band gap of TiO$_2$ nanotubes, the 3rd harmonics (355 nm) was chosen. It is worth noticing that, the wavelength corresponding to the band gap of a semiconductor contributes to the highest absorption probability (see Figure 3 a). The samples were placed in a vacuum chamber and under 5×10^{-5} mbar pressure during the illumination was maintained. Nevertheless, in the preliminary tests, different wavelengths and atmospheres (air and vacuum) were also applied to verify how they affect the structure and surface morphology of nanotubes. The repetition rate was set to 2 Hz whereas the speed of the motorized table to 4 mm min^{-1}. Essentially, these two parameters can be easily scaled up without influencing other processing parameters, namely, the modification should remain the same if the speed of the motorized table and repetition rate were increased by the same factor. Beam energy fluence was set up to 50 mJ cm^{-2}. A representation of the fabrication route of UV-laser-treated TiO$_2$ nanotubes is shown in Scheme 2.

Figure 7. (a) Schematic diagram showing the experimental setup for laser modification.
(b) A photo of a sample after laser irradiation with a corresponding image.

Scheme 2. Schematic diagram illustrating the fabrication process of
UV-laser-treated TiO$_2$ nanotubes.

3.2.3. Deposition of Cr, Mo, and W oxides onto TiO_2 nanotubes

A combination of TiO_2 nanotubes with metal oxides from the 6th main group of the periodic table – chromium, molybdenum, and tungsten oxides was realized using magnetron sputtering technology. The method is to apply a high negative potential to the target and to knock the atoms out of it by the bombardment of positive ions from an electrical discharge in a gas. Specifically, the electrons are released from the target and are suspended in the magnetic field. Collisions between the electrons and gas atoms result in ionization. Then, the ionized gas atoms are accelerated toward the negatively charged target by the electric field. Finally, collisions between ionized gas atoms and the target lead to the detachment of the target material and allows for the deposition. In such a system, low pressure is required to maintain high ion energies and to prevent too many atom-gas collisions after the ejection of the target [49]. Compared to other methods such as atomic layer deposition [50], it allows coating of the nanotubes with a low sputtering depth (only about 200 nm from the top of the nanotubes [51,52]). Nevertheless, it is a process widely used by industry, for instance, for the fabrication of ITO coatings [53]. Therefore, it is a suitable coating method to follow the simplicity and low-cost production of anodic TiO_2 nanotubes.

The deposition was realized using metallic disks under a 5×10^{-3} mbar argon atmosphere. During the process, a sputtering current of 120 mA was maintained whereas termination thickness was set to 15 nm, and it was controlled by a quartz microbalance. A schematic diagram showing an experimental setup for magnetron sputtering is presented in Figure 8. The preliminary tests [54], however, revealed that the deposition of metal results in deteriorated photoresponse. Therefore, after the sputtering, the samples were thermally annealed both to crystallize and oxidize the deposited materials (see Scheme 3).
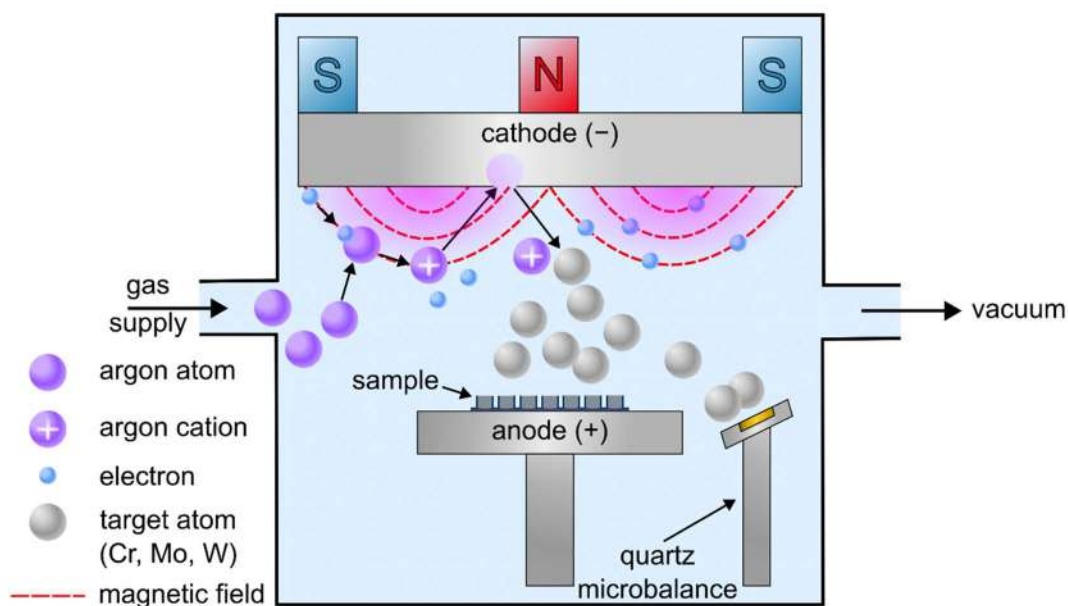
Figure 8. A schematic diagram showing the experimental setup for magnetron-sputtering.
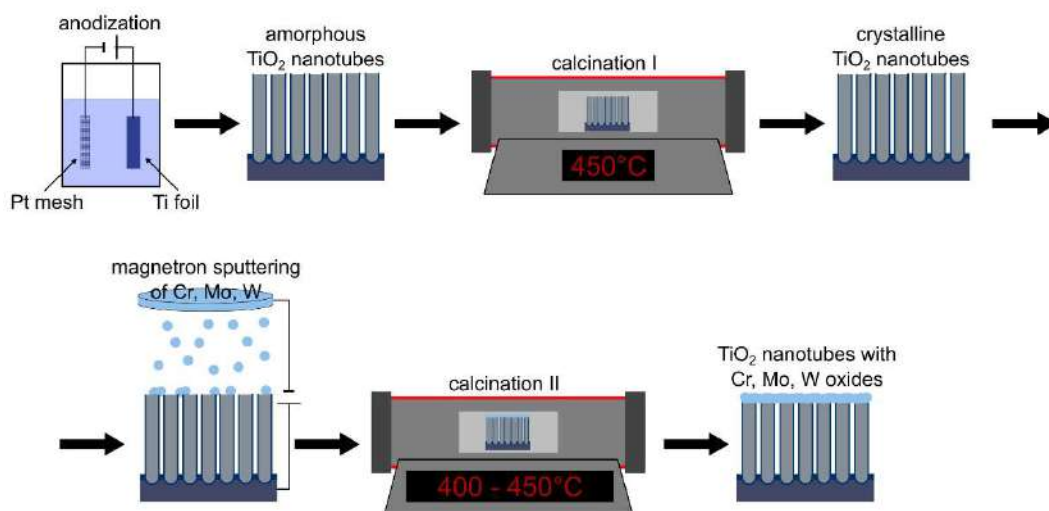
Scheme 3. Schematic diagram illustrating the fabrication process of TiO$_2$ nanotubes combined with Cr, Mo, and W oxides using magnetron-sputtering technology.

3.3. Characterization methods

3.3.1. Scanning electron microscopy

Scanning electron microscopy (SEM) is a technique allowing for surface imagining with a high resolution. During the measurement, a beam of electrons is bombarding the sample, scanning it line by line. A small part of electrons penetrate to a small depth and are backscattered; the majority of them are, however, preserved within the sample and give a contribution to the emission of secondary electrons, Auger electrons, X-radiation, and light.

SEM was performed to study the resultant morphology, distribution, and length of the TiO_2 nanotubes, the impact of the laser treatment on the melting of the nanotubes as well as morphology and distribution of the metal oxides onto the TiO_2 nanotubes after magnetron sputtering and subsequent calcination. SEM was performed by dr hab. inż. Jakub Karczewski, at Gdańsk University of Technology. The author of the present dissertation was responsible for the analysis of the obtained images.

3.3.2. Raman spectroscopy

During Raman spectroscopy measurement, the sample is illuminated with a laser beam and the scattered beam is registered. The principle of the method is that most of the scattered light is at the same wavelength as the source (Rayleigh component), however, a small amount is scattered at different wavelengths (Stokes and anti-Stokes components) which depend on the chemical structure of the sample. The scattered radiation can be therefore divided into three components:

— Rayleigh – when a molecule initially occupying the ground states returns to the ground state and the scattered photon exhibits the same energy.
— Stokes – when a molecule initially occupying the ground state returns to a higher vibrational energy state and the scattered photon exhibits lower energy.
— anti-Stokes – when a molecule is initially at an excited vibrational state returns to the ground state and the scattered photon exhibits higher energy.

Raman spectroscopy was performed to investigate the crystal structure of the TiO_2 nanotubes. In particular, based on the position of the main signal corresponding to the anatase active mode ($E_{g(1)}$), the degradation of the crystal structure after laser treatment was estimated. Raman spectroscopy measurements were performed using inVia™ confocal Raman microscope at the Institute of Fluid-Flow Machinery Polish Academy of Sciences. The author of the present dissertation was solely responsible for performing the measurements and the analysis of the obtained spectra.

3.3.3. X-ray diffraction measurements

X-ray diffraction (XRD) works on the principle of Bragg's equation:

$$n\lambda = 2d \sin \theta \qquad (5)$$

where n is any integer, λ is the wavelength of the beam, d is the distance between successive layers of atoms, and θ is the incident angle. During the measurement, the sample is illuminated with the monochromatic beam at different incident angles. Reflected waves from different atomic planes will add constructively only in directions where path-the length difference ($2d \sin \theta$) is equal to the integer multiple of the wavelength. Based on the peak positions and their intensity one can determine the structure and phase composition of the sample, respectively.

XRD measurements were performed to investigate the crystal structure of the TiO_2 nanotubes combined with Cr, Mo, and W oxides. However, it was not possible to detect peaks from the metal oxides due to the high propagation depth of the incident X-rays and the low signal-to-noise ratio. XRD measurements were performed by dr hab. inż. Jakub Karczewski at Gdańsk University of Technology. The author of the present dissertation was responsible for the analysis of the obtained diffractograms.

3.3.4. X-ray photoluminescence spectroscopy

X-ray photoluminescence spectroscopy (XPS) is a surface-sensitive quantitative technique that allows the identification of the elements existing in the surface of the sample as well as their chemical state. During the measurement, the sample is illuminated with electromagnetic radiation with energy from 100 eV to 500 keV (X-rays), and due to the photoelectric effect, core electrons are ejected. The detectors count the electrons and measure their kinetic energy (E_k). Knowing the energy of the incident radiation (usually Al Kα with 1486.6 eV or Mg Kα with 1253.6 eV sources are utilized) and the kinetic energy one can calculate binding energy (E_{bin}):

$$h v = E_{bin} + E_k \qquad (6)$$

Core levels in XPS use the nomenclature nl_j where n is a principal quantum number, l is an azimuthal quantum number, and $j = l + s$ where s is a spin quantum number and can be $\pm \frac{1}{2}$. Therefore, all orbital levels except the s levels give a rise to a doublet with two possible states having different binding energies which are known as spin-orbit coupling [55] (see Table 1).

Table 1. Spin-orbit splitting j values.

Subshell	j value
s	$^1/_2$
p	$^1/_2$ and $^3/_2$
d	$^3/_2$ and $^5/_2$
f	$^5/_2$ and $^7/_2$

High-resolution XPS measurements were carried out to study the resultant chemical composition. In particular, to verify the presence of oxygen vacancy in TiO_2 nanotubes after laser treatment and to reveal the chemical composition of the Cr, Mo, and W onto the TiO_2 nanotubes after magnetron sputtering followed by the calcination. XPS measurements along with fitting of the obtained spectra were performed by dr hab. inż. Jacek Ryl at Gdańsk University of Technology. The author of the present dissertation was responsible for the interpretation of the obtained results.

3.3.5. UV-visible spectroscopy

UV-vis spectroscopy is a quantitative technique used to study the optical properties of materials. The method is based on the phenomena of transmission, absorption, and scattering of light by matter. Absorption spectroscopy is used for diluted solutions and semitransparent thin films. During the absorption measurement, the intensities of the beams that have passed through the sample (I_0) and the incident (I) are measured yielding the formula for absorbance:

$$A = \log\left(\frac{I_0}{I}\right) \tag{7}$$

In turn, for opaque materials, diffuse reflectance spectroscopy is used. During the reflectance measurement, the reflectance with respect to the standard is directly registered.

The investigated materials were studied in reflectance due to the opacity of the substrate (titanium foil). The registered data was then used to extract a quantity proportional to the absorption coefficient using a Kubelka-Munk model:

$$f(R) = \frac{K}{S} = \frac{(1-R)^2}{R^2} \tag{8}$$

where R stays for reflectance, whereas K and S for the Kubelka-Munk coefficients.

The Kubelka-Munk coefficients are, in turn, proportional to the absorption (α) and reflection (s) coefficients:

$$\frac{K}{S} \propto \frac{\alpha}{s} \tag{9}$$

This particular model was used due to its frequent use in other literature reports. The obtained data allowed to estimate the absorption range and optical band gap of the investigated materials which are essential regarding further analysis of the photocurrent generation from the electrodes exposed to the light. The measurements were performed using PerkinElmer Lambda 35 spectrometer at Institute of Fluid-Flow Machinery Polish Academy of Sciences. The author of the present dissertation was solely responsible for performing the measurements and took a part in the analysis of the obtained results.

3.3.6. Density functional theory calculation

Density functional theory (DFT) is nowadays one of the most commonly used approaches to studying electronic structures of solids. It is based on the concept that the energy of electrons in atoms or molecules is a functional of density.

In the present work, the DFT was used to calculate band structures and absorption spectra of the TiO_2 after combination with Cr_2O_3, MoO_3, and WO_3. The calculations and analysis of the obtained results were solely realized by mgr. inż. Adrian Olejnik at the Institute of Fluid-Flow Machinery Polish Academy of Sciences.

3.3.7. Electrochemical tests

All the electrochemical tests were performed in a well-estimated three-electrode system with an Ag|AgCl|3 M KCl reference electrode and a Pt mesh as a counter electrode in a 0.5 M Na_2SO_4 solution. The pH of the electrolytes was chosen based on the Atlas of Electrochemical Equilibria in Aqueous Solutions by Marcel Pourbaix [56]. Before the measurements, each electrolyte was deaerated with argon 5.0, and during the testing, a continuous flow of Ar above the solution was kept. All the tests were performed using Autolab (PGSTAT302N) at Institute of Fluid-Flow Machinery Polish Academy of Sciences. The author of the present dissertation was responsible for performing the measurements and the analysis of the registered data.

3.3.7.1. Polarization methods

Polarization methods are in general, used to the study kinetics and mechanisms of the electrode processes. In the present thesis, three different polarization methods were

used, namely cyclic voltammetry (CV), linear sweep voltammetry (LSV), and chronoamperometry (CA).

— In a CV, the working electrode potential is changed linearly vs. time, and the resultant current is recorded. Once the set potential is being reached, the working electrode potential is ramped in the opposite direction to return to the initial potential.

— In a LSV, the potential of working electrode is changed linearly with time, and the current is registered. Unlike in the CV, the electrode is polarized only towards the anodic or cathodic direction, and is not reversed.

— In a CA, the potential of the working electrode is held at a given value and the current is recorded as a function of time.

CV was carried out prior to other electrochemical tests to verify the stability of electrodes in a contact with an aqueous electrolyte and determine the working potential range. Additionally, the registered data allowed the identification of oxidation and reduction reactions taking place at the electrode's surface. In turn, LSV and CA were carried out under light-chopped illumination to study sample photoresponse (for the description, please see 3.3.8. section)

3.3.7.2. Electrochemical Impedance Spectroscopy

Electrochemical impedance spectroscopy (EIS) is an alternating current method. During the measurement, a small sinusoidal voltage signal is applied to the working electrode and a current response is measured. The principle of the impedance (Z) is linearity so the current response is shifted in phase and exhibits different amplitude, hence it can be defined as:

$$Z = \frac{V_0 \sin(\omega t)}{I_0 \sin(\omega t + \phi)} = Z_0 \exp(i\phi) = Z_0[\cos(\phi) + i \sin(\phi)] \qquad (10)$$

where V_0 and I_0 are amplitudes of the voltage signal and current response, respectively, ω is frequency, t is time, ϕ is phase shift, and Z_0 is the magnitude of impedance. The impedance can be, therefore, expressed as a vector with real and imaginary parts. The obtained data were used for the analysis with an electric circuit (equivalent circuit) with resistors, capacitors, etc. to reveal electrical properties such as resistance of solution, double-layer capacitance, or charge transfer resistance.

In this work, EIS tests were performed to estimate the capacitance of the electrodes which was further used to determine a flat-band potential (E_{fb}) and effective donor density (N_D) based on the Mott-Schottky relationship [57]:

$$C^{-2} = \left(\frac{2}{\varepsilon\varepsilon_0 e N_D A^2}\right)\left(E - E_{fb} - \frac{k_B T}{e}\right) \tag{11}$$

where: ε is the dielectric constant of the semiconductor, and A is the surface area. On the basis of this relationship, E_{fb} was determined from the point of intersection of a C^{-2} vs E plot with the abscissa axis while N_D was calculated from the slope using a geometric surface area and assuming $\varepsilon = 38$ for anatase TiO$_2$ [58].

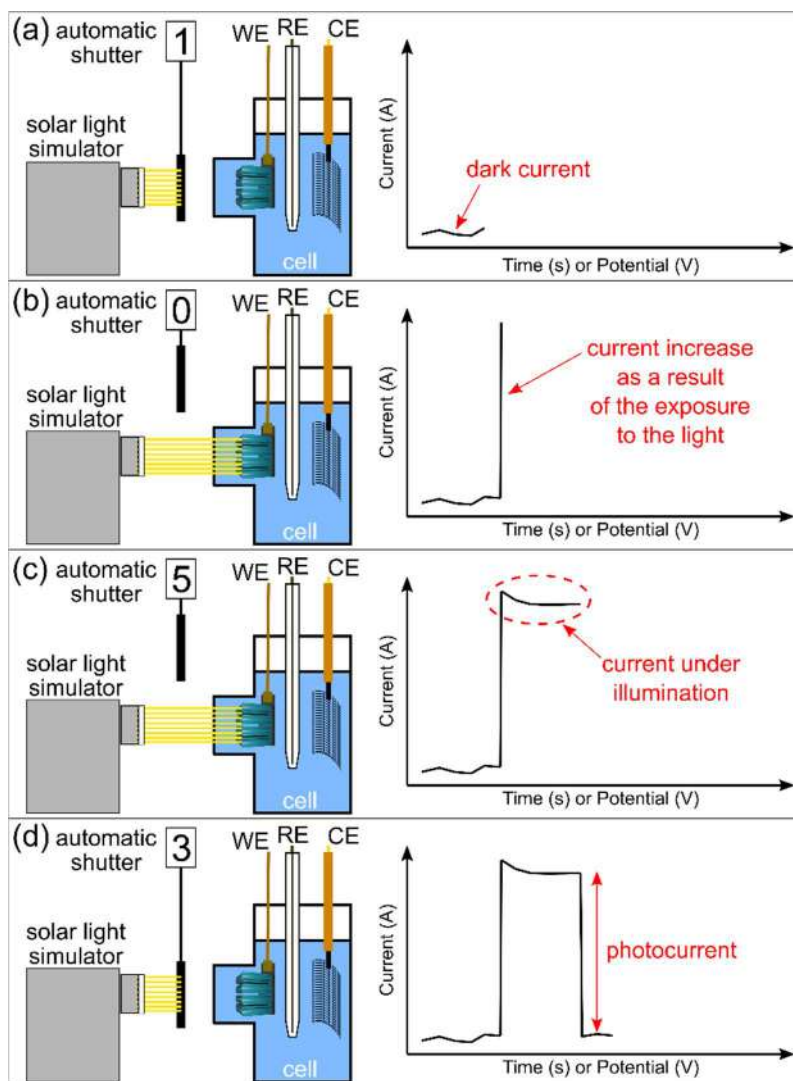### 3.3.8. Photoelectrochemical tests

To study sample photoresponse, LSV and CA tests were performed under the light-chopped illumination from the solar light simulator (LOT Quantum Design, Series LS0500 equipped with an automatic light shutter). LSV allowed studying charge recombination processes upon light on and off cycles as well as photocurrent saturation which is a crucial factor affecting the photoresponse of 1D materials. CA tests revealed the stability of electrodes upon illumination. A principle of current evolution during the LSV and CA tests under light-chopped illumination is visualized in Figure 9.

Nevertheless, to study photoelectrochemical performances of the investigated materials, the author of the present dissertation had to design and assemble an experimental setup for the tests. There were several requirements regarding the construction of the cell and its location with respect to the light source:

- ✓ cell must contain pins for three electrodes and scrubber, gas outlet, and opening for quartz glass window;
- ✓ front of the cell must be equipped with a quartz glass window allowing for sample illumination. The joint must allow for disassembly for cleaning purposes; it must be opposite to the light source at the fixed height and distance.
- ✓ sample must be placed in the axis of the cell facing the light source; the assembly of the sample must be relatively simple and repetitive.

To meet the requirements, the author of the present dissertation designed and completed the experimental setup which is shown in Figure 10. It consists of an electrochemical cell, clamp, quartz glass window, stand, and port for the sample holder. The top of the electrochemical cell contains three side grinding holes for the reference electrode, counter electrode, and scrubber, one middle grinding hole for a port for sample holder, and a u-tube for the gas outlet. Precise and repetitive sample replacement is achieved by a port for a sample holder with a side screw locking the sample holder in the axis of the cell. The cell is locked in a proper position by a stand which contained a hole in the front part blocking the position of the cell in front of the light source. The quartz glass window

joint is a three-element clamp that was designed and 3D printed in fused filament fabrication technology from the polylactic acid filament. The clamp contains recesses for 1 mm thick gaskets. The front and rear elements of the clamp are connected by screw joints.

Figure 9. A schematic diagram showing a time-dependent (a-d) evolution of current during electrochemical tests under light-chopped illumination programmed for 5 seconds.
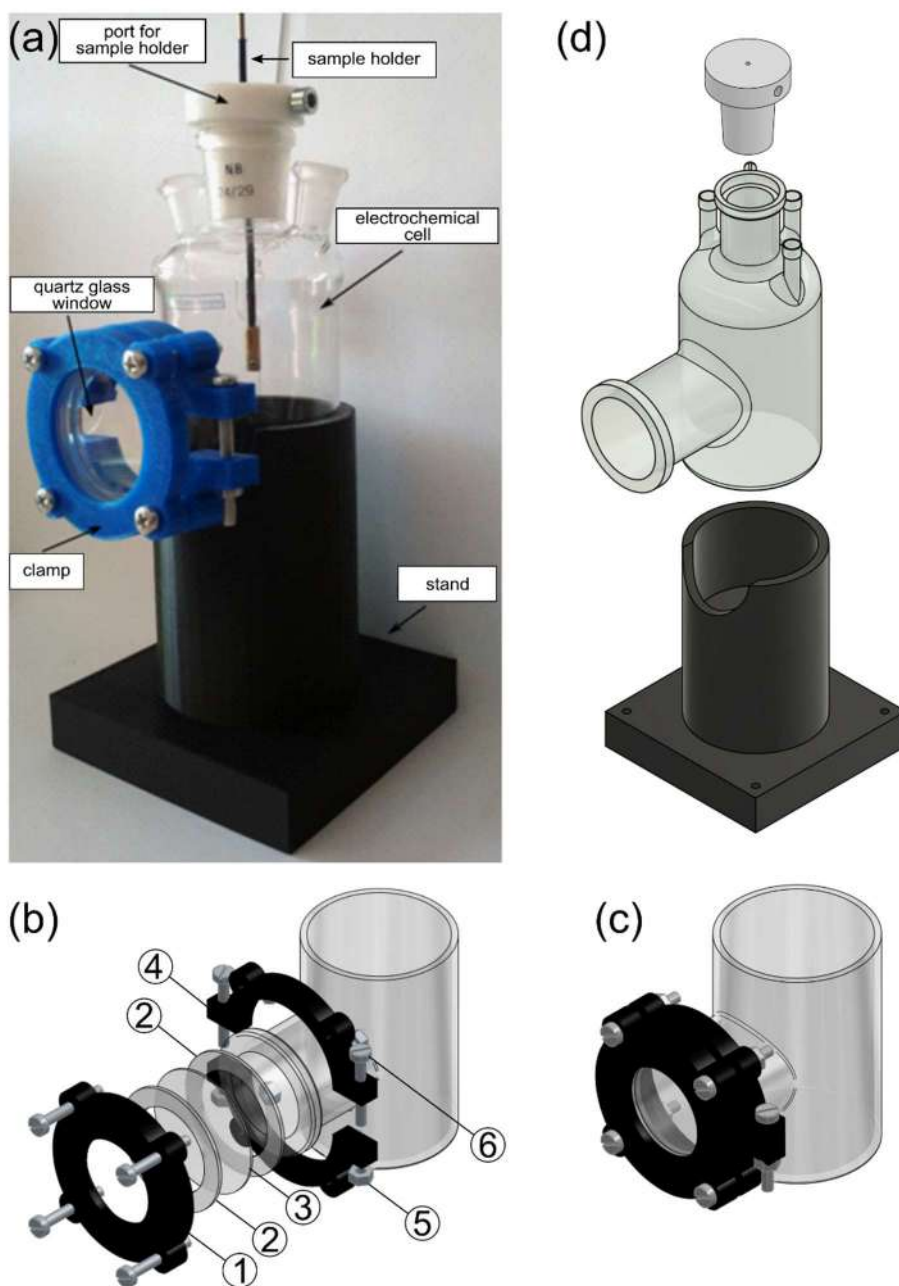
Figure 10. (a) A photo of the experimental setup. (b-c) 3D models of the clamp connecting a quartz glass window and electrochemical cell (b) before and (c) after the assembly: 1 – the front part of the clamp, 2 – gasket, 3 – round quartz glass, 4 – the back part of the clamp, 5 – screw, 6 – nut. (d) 3D models showing the electrochemical cell, stand, and port for the sample holder.

Chapter 4. Guide to papers

The basis of this work is a series of the four publications listed below. The first two papers study laser modification of TiO_2 nanotubes, in particular, the scalable setup equipped with a beam homogenizer and motorized table presented in Paper 1. The next two papers investigate the optical, electronic, and photoelectrochemical properties of TiO_2 after combination with other metal oxides using magnetron sputtering technology followed by calcination.

Paper 1   **Łukasz Haryński**, Katarzyna Grochowska, Jakub Karczewski, Jacek Ryl, Katarzyna Siuzdak, Scalable route toward superior photoresponse of UV-laser-treated TiO_2 nanotubes, *ACS Applied Materials & Interfaces* 2020, *12*, 3225-3235, doi:10.1021/acsami.9b19206.
(IF$_{2020}$ = 9.229; MEiN = 200 pts)

Paper 2   Katarzyna Siuzdak, **Łukasz Haryński**, Jakub Wawrzyniak, Katarzyna Grochowska, Review on robust laser light interaction with titania – Patterning, crystallization and ablation processes, *Progress in Solid State Chemistry* 2021, *62*, 100297, doi:10.1016/j.progsolidstchem.2020.100297.
(IF$_{2021}$ = 8.389; MEiN = 200 pts)

Paper 3   **Łukasz Haryński**, Adrian Olejnik, Katarzyna Grochowska, Katarzyna Siuzdak, A facile method for Tauc exponent and corresponding electronic transitions determination in semiconductors directly from UV–vis spectroscopy data, *Optical Materials* 2022, 127, 112205, doi:10.1016/j.optmat.2022.112205.
(IF$_{2021}$ = 3.754; MEiN = 70 pts)

Paper 4   **Łukasz Haryński**, Adrian Olejnik, Katarzyna Grochowska, Katarzyna Siuzdak, Linking optical and electronic properties to photoresponse of heterojunctions based on titania nanotubes and chromium, molybdenum, and tungsten oxides, *Optical Materials* 2022, 134, 113183, doi: 10.1016/j.optmat.2022.113183.
(IF$_{2021}$ = 3.754; MEiN = 70 pts)

Chapter 5. Papers

5.1. Paper 1: Scalable Route toward Superior Photoresponse of UV-Laser-Treated TiO$_2$ Nanotubes

In 2017, Xu et al. [13] demonstrated that pulsed UV laser treatment of TiO$_2$ nanotube arrays can increase the disorder of the crystal structure and enhance photocurrent generation by increasing the number of states (called shallow donors) and reducing the density of deep trap states. However, during the irradiation, the samples were immersed in deionized water in a Petri dish. Such an approach could be problematic regarding the modification of larger surfaces. Motivated by this and many other works in the literature (detailed literature revision regarding laser modifications of titania nanotubes is presented in Paper 2), in the present work, a scalable method for laser modification resulting in superior photoresponse is presented. For this purpose, a pulsed UV laser (6 ns) equipped with 3rd harmonics (355 nm) was utilized. The harmonic was chosen taking into account the optical band gap of the aligned TiO$_2$ nanotubes fabricated in the glycol-based electrolyte (2.85 eV – 432 nm) [8]. The optical system was equipped with a beam homogenizer ensuring a square beam spot. During the irradiation, the samples were mounted onto a moving motorized table. The repetition rate and speed of the table were set to 2 Hz and 4 mm min^{-1}, respectively. It is worth noticing that, by increasing both of these parameters proportionally, the modification should essentially remain the same. Therefore, the entire elaborated method can be easily scaled up. The variable processing parameter was beam energy fluence. Based on the preliminary investigations [59], 10, 20, 30, 40, and 50 mJ cm^{-2} were chosen.

SEM images in the top view and cross-section (see Figure 2 in the paper) revealed melting of the top of the nanotubes along with the increasing beam energy fluence. The melted layer was estimated to be about 200 nm in height. Raman spectra (see Figure 3 in the paper) showed a red shift of the signal corresponding to the main active anatase mode from 144.6 to 147.5 cm^{-1} for 10 and 50 mJ cm^{-2} which suggests degradation of crystal structure. High-resolution XPS spectra (see Figure 4 in the paper) revealed that titanium is solely in the +4 oxidation state while oxygen in the form of lattice oxygen and adsorbed surface hydroxyl species. No oxygen vacancy has been found. In turn, UV-vis spectra and Tauc plots (see Figure 5 in the paper) indicated a decrease in UV absorption and band gap narrowing from 3.10 to 2.24 eV along with the increasing beam energy fluence. Reconsidering these results, it is anticipated that they could be affected by an increase in surface reflection which decreases the signal-to-noise ratio in diffuse reflectance spectroscopy [14,17]. Cyclic voltammograms (see Figure 6 in the paper)

confirmed the stability of the electrodes both in neutral and alkaline solutions. Linear sweep voltammograms measured under AM 1.5 G, 100 mW cm^{-2} illumination (see Figures 7 a and 8 a in the paper) demonstrated superior up to 1.45-fold photoresponse of the laser-treated samples compared to bare TiO_2 nanotubes. The optimum beam energy fluence of 40 mJ cm^{-2} regarding the photoresponse has been identified. The registered chronoamperograms (see Figures 7 c and 8 c in the paper) suggest the stability and photocorrosion resistance of the obtained samples. Linear voltammograms registered under the visible part of the solar spectrum (see Figures 7 b and 8 b) revealed no significant increase in photoresponse compared to the bare TiO_2 nanotubes, hence the states are rather shallow than deep in the band gap which is in line with Xu et al. [13].

The analysis of Mott-Schottky plots (see Figure 9 in the paper) revealed a significant over an order of magnitude increase in donor density from 2.2 $\times 10^{19}$ to 14.1 $\times 10^{20}$ and +0.74 V shift of flat band potential compared to the bare TiO_2 nanotubes. For n-type semiconductors, the position of flat band potential is equal to the position of the Fermi level [60]. The modification resulted, therefore, in the occupation of additional states. An increase in donor density in turn can contribute to better absorption since the process is governed by the probability (the higher number of carriers the higher probability for absorption – see Equation 1).

In conclusion, processing parameters regarding the photoresponse of TiO_2 nanotubes in the scalable system equipped with a beam homogenizer and motorized table have been established. Comparable performances with the pioneering work [13] using the static system for the laser modification of TiO_2 nanotubes have been achieved. Thus, the elaborated method can be successfully used for large-scale modification of TiO_2 nanotubes.

Scalable Route toward Superior Photoresponse of UV-Laser-Treated TiO$_2$ Nanotubes

Łukasz Haryński,*,[†] Katarzyna Grochowska,[†] Jakub Karczewski,[‡] Jacek Ryl,[§] and Katarzyna Siuzdak[†]

[†]Centre for Plasma and Laser Engineering, The Szewalski Institute of Fluid-Flow Machinery Polish Academy of Sciences, Fiszera 14 Street, 80-231 Gdańsk, Poland

[‡]Faculty of Applied Physics and Mathematics and [§]Faculty of Chemistry, Gdańsk University of Technology, Narutowicza 11/12 Street, 80-233 Gdańsk, Poland

Ⓢ *Supporting Information*

ABSTRACT: Titanium dioxide nanotubes gain considerable attention as a photoactive material due to chemical stability, photocorrosion resistance, or low-cost manufacturing method. This work presents scalable pulsed laser modification of TiO$_2$ nanotubes resulting in enhanced photoactivity in a system equipped with a motorized table, which allows for modifications of both precisely selected and any-large sample area. Images obtained from scanning electron microscopy along with Raman and UV−vis spectra of laser-treated samples in a good agreement indicate the presence of additional laser-induced shallow states within band gap via degradation of crystalline structure. However, X-ray photoelectron spectroscopy spectra revealed no change of chemical nature of the modified sample surface. Photoelectrochemical measurements demonstrate superior photoresponse of laser-treated samples up to 1.45-fold for an energy beam fluence of 40 mJ/cm^2 compared to that of calcined one. According to the obtained results, optimal processing parameters were captured. Mott−Schottky analysis obtained from impedance measurements indicates an enormous (over an order of magnitude) increase of donor density along with a +0.74 V positive shift of flat band potential. Such changes in electronic structure are most likely responsible for enhanced photoactivity. Thus, the elaborated method of laser nanostructuring can be successfully employed to the large-scale modification of titania nanotubes resulting in their superior photoactivity. According to that, the results of our work provide a contribution to wider applications of materials based on titania nanotubes.

KEYWORDS: *titanium dioxide, nanotubes, laser modification, Mott−Schottky analysis*
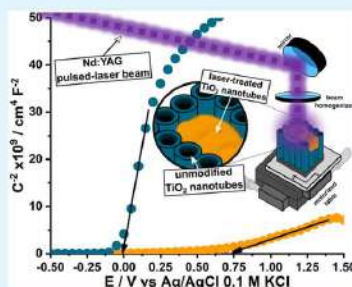
1. INTRODUCTION

Due to the drastic devastation of environment, especially because of greenhouse gas emittance, as well as the decreasing reserves of fossil fuels combined with rapidly growing energy demand, a global movement toward the generation of clean energy from renewable sources can be observed in the last decades. Renewable resources can be divided, in general, into solar energy, wind energy, water energy, and biomass. Nevertheless, as Sun is an unlimited source of energy, most of the works are focused onto the conversion of sun energy into electrical or chemical ones. It is well known that solar energy can be directly utilized not only to power production by solar panels[1] or hydrogen generation through water electrolysis[2] but also to environmental purification via photocatalytic degradation of organic pollutants.[3] The only limitation is the ability to energy conversion in a cost-effective and efficient way.

In the search for material that ensures effective energy conversion and characterized by an adjustable band gap, flexibility, good stability, and long lifetime, semiconductors

have gained considerable attention mainly due to electron−hole pair generation following exposure to the suitable electromagnetic radiation. Among many different semiconductors, titanium dioxide (TiO$_2$) has gained particular interest as a photoactive material due to its chemical stability[4] and photocorrosion resistance.[5] TiO$_2$ can form structures of different and very sophisticated geometry including nanospheres, nanofibers, or nanosheets. However, particularly well-ordered hollow-like titanium dioxide nanotubes (TiO$_2$NTs) are distinguished by a high surface area, directional charge transfer, and the possibility of a precise control of the geometric features of the tubular structure during electrochemical synthesis.[6] During electrochemical anodization, the morphology of NTs can be directly manipulated by a proper selection of processing parameters such as the applied voltage between both electrodes, electrolyte composition, time, or

3225

temperature[8]. The alternative method for anodization that also results in the growth of a quasi-one-dimensional TiO_2 porous material was proposed by Matarrese et al. and takes advantage from the pulsed laser deposition (PLD).[7,8] The fabrication of different architectures including dense non-porous films or vertically oriented and connected porous structures can be achieved by manipulating processing parameters such as O_2 pressure, deposited mass, and annealing temperature, as well as laser working parameters. The material obtained under the optimized conditions exhibits photoactivity comparable to the one for nanotubes of similar length fabricated via anodic oxidation. Despite the length of nanotubes and the thickness of the porous layer being similar, the maximum photocurrent efficiency recorded for anodized nanotubes occurred at higher potential values regarding the structure obtained using PLD method. Additionally, since the morphology influences semiconducting properties of TiO_2NTs, anodization as a simple, undemanding expensive experimental setup method seems to be the most suitable technique to obtain nanotubes compared to others, namely, hydrothermal[9] or template syntheses.[10] However, as-anodized TiO_2NTs exhibit an amorphous phase, while it is well known that the crystalline phase is essential for application purposes. The process of phase conversion is traditionally performed in a furnace at elevated temperatures, and the whole surface of the material undergoes thermal treatment. Furthermore, additional modifications of TiO_2NTs for individual applications are usually required to overcome issues related to the two major disadvantages hampering their photoconversion efficiency: (i) a large band gap (ca. 3.2 eV) limiting absorption to the UV part of the solar spectrum (approximately 5% of the spectrum) and (ii) a high recombination rate of photogenerated electron–hole pairs.[11] Many strategies, including metal[12,13] and nonmetal dopings,[14,15] sensitization,[16] or introducing defects,[17] have been employed to extend the absorption range to the visible part of the solar spectrum, as well as reduce the recombination rate of the photogenerated electron–hole pairs. Nevertheless, besides the structural or optical modifications, the electronic properties of the TiO_2NTs/solution interfacial junction should be taken into account as it has a significant impact on the photoresponse process.[18]

To improve conductivity, even to reach the semimetallic behavior, hydrogenation has been proposed. It could be realized via the electrochemical way,[19] exposition to hydrogen plasma,[20] or calcination in hydrogen-rich atmosphere.[21] The method enables enormous changes in the structure[22–24] and improves optical,[2,4,25] photocatalytic,[3,4] and electronic[4] properties of TiO_2 without the introduction of any dopant atoms. Su et al.[26] remarked on the essence of investigating the electronic properties influenced by furnace hydrogenation of TiO_2 nanocrystals. According to the Mott–Schottky analysis of the recorded impedance spectra, they estimated an increment of carrier density and a positive shift of flat band potential, which is responsible for an increased driving force for electrons injected into the conductive band and improved charge separation at the interface between the electrolyte and surface of hydrogenated TiO_2. The modification of these electronic parameters resulted in facilitated charge transfer and increased overall performance of modified samples compared to those of calcined ones. The same aim could be reached, utilizing an electrochemical approach instead of a furnace as was reported by Liu et al.[27] In this case, anodization was followed by potentiostatic polarization in a two-electrode arrangement,

where TiO_2NTs served as a cathode and 4 V was maintained for 20 min at an ambient temperature, which resulted in superior photoactivity of the obtained material. Nevertheless, in those cases, modification is conducted over the whole sample, requires work with the high cost and dangerous hydrogen gas, or needs electrochemical cell with dimensions appropriate for a particular substrate size and shape. Moreover, concerning the electrochemical approach, the sample has to be mounted onto some conductive holder and the preparation for experiment extends the whole modification process. Analyzing particular techniques, it is worth taking into account not only the conditions that can be achieved in the laboratory scale but also facile upscaling of the elaborated procedure toward the technological scale production. Calcination in a H_2 atmosphere needs hydrogen supply and a special valve system containing an oven. Therefore, when the sample size increases, the dimensions of the oven should be increased, which leads to the enormous consumption of expensive hydrogen. Regarding the electrochemical procedure, this approach also needs the preparation of the electrolyte and its further disposal. Moreover, adaptation of the electrochemical process for larger substrates requires sequential procedure optimization to reach the same result as was for electrodes of less than 1 cm^2 area typically used in a laboratory routine.

Therefore, pulsed laser nanostructuring is proposed here, which could be regarded as a promising alternative for the above-discussed titania modification that does not require any inert gasses or substrate handling. This method also offers a wide range of processing parameters including the type of laser, pulse duration, wavelength, frequency, exposure time, or type of atmosphere. Moreover, on the contrary to hydrogenation where the whole sample is modified, laser modification can be realized only within a selected part by the use of shadow masks, different optical systems, or a motorized table.[28,29] Xu et al.[30] utilized pulsed KrF laser for surface modification of anatase TiO_2NTs. During laser irradiation, samples were immersed in deionized water inside a Petri dish, which was mounted on a rotating actuator (samples were rotating). An optimized laser fluence of 0.3 J/cm^2 with 30 pulses along with the selected length of nanotubes about 1 μm allowed for up to 1.6-fold increment in photocurrent. However, the following approach does not provide the possibility of the entire surface modification. Moreover, expanding round laser spot by the use of a motorized table does not allow for a uniform modification due to the incomplete overlapping at the top and bottom of the spot. Another problem concerns a liquid medium utilized as a beam homogenizer. Each subsequent modification would require installing the same amount and quality of water. Thus, the development of a novel modification method should be accompanied by its practical application.

In this work, we report optimized pulsed UV laser processing of TiO_2NTs in vacuum, resulting in a photo-response enhancement. The effect of laser treatment was studied by scanning electron microscopy (SEM), UV–vis, and Raman and X-ray spectroscopies to reveal the impact of laser radiation on morphology, absorbance, crystallinity, and chemical nature, respectively. Photoactivity along with the photocorrosion resistance of TiO_2NTs was evaluated according to linear voltammetry and chronoamperometry. Photoelectrochemical measurement data were collected for two different electrolytes, namely, neutral and alkaline. Electrochemical impedance spectroscopy (EIS) was employed for a further Mott–Schottky analysis and revealed an increase of

charge carrier density for an order of magnitude and a positive ca. +0.75 V shift of flat band potential. The obtained results indicate that the laser nanostructuring can be successfully adopted for the modification of TiO_2NT electronic structure resulting in a superior photoresponse of these materials. In our approach, during laser irradiation, samples were mounted onto a moving motorized table in a system equipped with a beam homogenizer ensuring a square laser spot. Owing to the substrate displacement along with the laser treatment, the results of our work can be scaled up to any sample dimensions and shapes. Therefore, taking into account the spectacular impact of laser treatment on the improved electronic properties of TiO_2NTs, including flat band potential and donor density, one can take advantage of the presented method, seeking for a rapid scalable, however, precisely selective method.

2. METHOD

Prior to anodization, samples (Ti foil Strem, 99.7%) were ultrasonically cleaned in turns in three solvents: acetone, ethanol, and water for 10 min. Subsequently, they were rinsed with isopropanol and afterward allowed to dry in the air. The anodization process was realized in a two-electrode setup, where the titanium plate served as an anode and the platinum mesh as a cathode. TiO_2NTs were prepared in a one-step anodization at 40 V for 15 min in a glycol ethylene-based electrolyte containing 4 g NH_4F and 15 vol % H_2O. During the process, a fixed distance of 2 cm between the electrodes was kept. The temperature was set to 23 °C and maintained by a thermostat (Julabo F-12) working in the flow mode. After anodization, the samples were rinsed with ethanol and again allowed to dry in the air. The as-obtained TiO_2NTs were thermally heated to 450 °C using a heating ramp of 2 °C/min; subsequently, the applied temperature was maintained for 2 h. After that time, the samples were allowed to cool down freely to an ambient temperature. Laser treatment of the material was performed by means of a 355 nm Nd:YAG pulsed laser (Quantel) equipped with a beam homogenizer. A repetition rate of 2 Hz was set to minimize the accumulation of thermal energy in the sample. During laser modifications, the samples were mounted onto a motorized table with a constant speed of 4 mm/min in a vacuum chamber under a 5×10^{-5} mbar pressure. The energy fluencies were set to 10, 20, 30, 40, and 50 mJ/cm^2.

The surface morphology along with the cross sections of TiO_2NTs was revealed using the Schottky field emission scanning electron microscopy (SEM, FEI Quanta FEG 250) with an ET secondary electron detector. The voltage was kept at 10 kV.

The UV−vis reflectance spectra were recorder by means of a dual-beam UV−vis spectrophotometer (Lambda 35, PerkinElmer) equipped with a diffuse reflectance accessory. The spectra were recorded in the range of 300−1100 nm with a scanning speed of 120 nm/min.

The Raman spectra were measured by a confocal micro-Raman spectrometer (InVia Renishaw) with sample excitation by means of an argon ion laser emitting at 514 nm and operating at 10% of its total power (50 mW).

The sample after a laser treatment of 40 mJ/cm^2 fluence was analyzed by X-ray photoelectron spectroscopy (XPS), using a multispectrometer Escalab250Xi. The investigated sample was not subjected to any preliminary chemical treatment prior to the analysis. Next, the sample was introduced into the analytic chamber of the UHV system and subjected to a specific XPS analysis. X-ray radiation from the Al anode ($K\alpha$ = 1486.7 eV) was used. The sample was irradiated with a low-energetic electron source and low-energetic Ar^+ ion source EFG (Electron Flood Gun, E = 2.0 V, beam current = 200 mA) to eliminate electrostatic charging of specimens. The parameters of XPS spectra registration are as follows: (a) for the survey spectrum: pass energy 150 eV, range: −10−1350 eV, step size: 1 eV, time for the single step: 0.1 s; (b) for a high-resolution spectrum in the oxygen O 1s, titanium Ti 2p, and carbon C 1s binding energy (E_{bin}) range: pass energy 20 eV, step size: 0.1 eV.

The electrochemical measurements were carried out using an Autolab PGStat 302 N potentiostat−galvanostat system (Metrohm, Autolab) in a three-electrode system, where TiO_2NTs served as a working electrode, Pt-mesh as a counter electrode, and Ag/AgCl/0.1 M KCl as a reference electrode. Samples were examined in two electrolytes: Na_2SO_4 and NaOH with the same concentration equal to 0.5 M. Before measurements, each electrolyte was deaerated with argon 5.0, and during the testing, a continuous flow of Ar above the solution was kept. Electrochemical cell was equipped with a high transmittance quartz window allowing for sample irradiation. Solar light was simulated by a 150 W xenon lamp (Osram XBO 150) equipped with an AM 1.5 filter. For measurements carried out in the visible range, additional UV filter was utilized that allows for sample irradiation with wavelengths above 420 nm. During transient photocurrent tests, electrode irradiation was controlled by an automated light chopper programmed for a period of 5 s.

The linear voltammetry measurements were registered from −1.0 to +1.0 V with a scan rate of 50 mV/s in dark and under illumination. The chronoamperometry curves were registered at +0.5 V vs Ag/AgCl/0.1 M KCl under the chopped irradiation. The measurements were carried out for 200 s under both the UV−vis and vis illuminations using an optical filter (GG420, Schott) for the UV elimination. The cyclic voltammetry (CV) data was collected in the range of −1.0 to +1.5 V with a scan rate of 50 mV/s.

The electrochemical impedance spectroscopy (EIS) measurements were conducted in 0.5 M Na_2SO_4 for a frequency of 1000 Hz and with a 10 mV amplitude of the AC signal. For the Mott−Schottky analysis, EIS spectra were recorded at 25 °C in the range of −0.7 to +0.8 V and −0.4 to +1.5 V for calcined and laser-treated samples (fluence: 40 mJ/cm^2), respectively. Before each spectrum registration, the potential was held to achieve a steady-state condition. The capacitance of the space charge layer was further calculated from the imaginary part of the measured impedance according to the following equation[31]

$$C_{SC} = \frac{-1}{2\pi f Z_{im}}$$

where f is the frequency of the AC signal, and Z_{im} is the imaginary part of impedance. Each capacitance of the Mott−Schottky plot was calculated for a frequency of 1000 Hz and the corresponding Z_{im} value. The donor densities were calculated according to the Mott−Schottky space charge capacitance of the semiconductor theory given by the following equation[53]

$$N_d = \left(\frac{2}{\varepsilon_0 \varepsilon e}\right)[\frac{d\left(\frac{1}{C_{SC}^2}\right)}{dE}]^{-1}$$

where ε is the dielectric constant of TiO_2, ε_0 is the vacuum permittivity, e stays for the electron charge, and E is the applied potential; in calculations, $\varepsilon_0 = 8.85 \times 10^{-12}$ F/m, $\varepsilon = 38$ for anatase-TiO_2,[32] and $e = 1.602 \times 10^{-19}$ C were used.

3. RESULTS AND DISCUSSION

SEM images of well-ordered aligned TiO_2NTs after calcination process are shown in Figure 1. The internal diameter and the
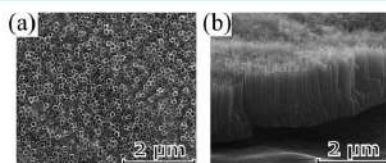

Figure 1. SEM images of calcined TiO_2NTs: (a) top view and (b) cross section.

wall thickness of obtained nanotubes are estimated to be 100 ± 10 and 10.5 ± 3.5 nm, respectively, whereas the length was estimated to be 1.4 ± 0.1 μm. SEM images of laser-modified TiO_2NTs are presented in Figure 2. It can be seen that laser beam with an energy fluence of 10 mJ/cm^2 did not modify the morphology in a significant way. However, higher energy fluences, namely, 20, 30, 40, and 50 mJ/cm^2, resulted in a partial surface melting. It is worth noting that beneath the melted layer that is covering the top of the nanotubes, a tubular structure was preserved and fixed to a titanium foil. The melted layer thickness did not change significantly with an increasing energy fluence in the range from 20 to 50 mJ/cm^2, and it is estimated to be ca. 200 nm. Nevertheless, along with an increasing energy fluence, the destruction of nanotube morphology within the melted layer increases. The top view of the laser-modified area showing a laser trace formed from the square spot expansion by means of a motorized table is presented in Figure 2f. From this perspective, the selectively modified surface area with sharp edges indicating a high

precision of the optical system and a motorized table can be seen.

Structural changes of modified titanium dioxide nanotubes were investigated by means of Raman spectroscopy. Raman spectra recorded for laser-modified TiO_2NTs along with the calcined one are presented in Figure 3. The curves were
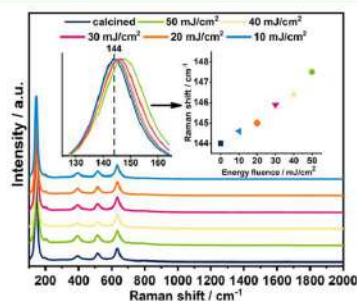

Figure 3. Raman spectra recorded for laser-treated and calcined TiO_2NTs. The inset represents the dependence of the $E_{g(1)}$ positions on the utilized laser energy fluences.

normalized for a better presentation of the results. Signals recorded for the calcined sample at 144, 197, 395, 515, and 636 cm^{-1} are corresponding to the $E_{g(1)}$, $E_{g(2)}$, B_{1g}, A_{1g}, and $E_{g(3)}$ active anatase modes, respectively.[33] Signal positions corresponding to main $E_{g(1)}$ active anatase mode of laser-treated samples depend on the utilized energy fluences during laser modifications; $E_{g(1)}$ is located at 144.6, 145.0, 145.9, 146.4, and 147.5 cm^{-1} for 10, 20, 30, 40, and 50 mJ/cm^2 energy fluences, respectively (see Figure 3 inset). In the literature, such a blue shift is usually referred to the presence of oxygen vacancies originating from crystal structure degradation in defected TiO_2.[34] It is worth noting that signal positions of laser-modified samples related to $E_{g(2)}$, B_{1g}, A_{1g}, and $E_{g(3)}$ remained unchanged compared to the reference one. For all obtained samples, no signals originating from rutile or brookite modes are observed. Moreover, laser treatment did not lead to band broadening. Results of Raman spectroscopy indicate an increasing distortion of anatase structure along with an
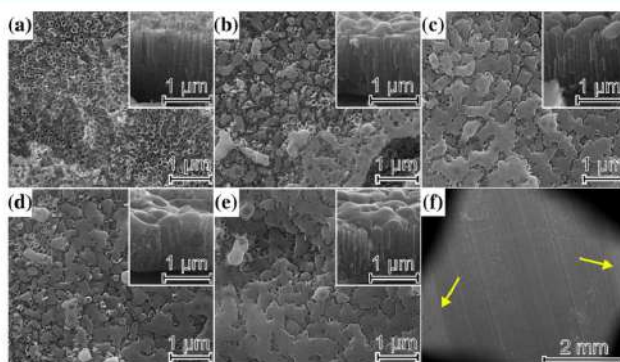
Figure 2. SEM images with cross sections (insets) of laser-treated TiO_2NTs with different energy fluences: (a) 10 mJ/cm^2, (b) 20 mJ/cm^2, (c) 30 mJ/cm^2, (d) 40 mJ/cm^2, and (e) 50 mJ/cm^2. (f) Laser trace obtained for a 40 mJ/cm^2 energy fluence.
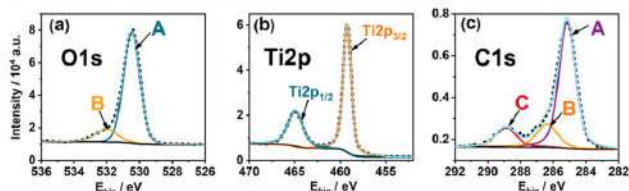
Figure 4. XPS spectra of (a) O 1s, (b) Ti 2p, and (c) C 1s core levels recorded for TiO$_2$NTs treated with a laser beam of 40 mJ/cm^2 fluence.

increasing energy fluence, and this dependence is approximately linear (see Figure 3 inset).

Due to the highest photoelectrochemical performance, described later on, XPS survey spectra (see Figure S1) was recorded for TiO$_2$NT substrate treated with a laser beam of 40 mJ/cm^2 fluence. Signals registered in the binding energies typical for oxygen O 1s, titanium Ti 2p, and carbon C 1s peaks are presented in Figure 4.

The maxima found for O 1s are located at 530.5 and 532.0 eV (see Figure 4a). The A peak corresponds to Ti−O arrangement known as lattice oxygen,[35] whereas signal B could be attributed to the surface hydroxyl species.[36] The Ti 2p region, shown in Figure 4b, was deconvoluted into one doublet: Ti 2p$_{1/2}$ and Ti 2p$_{3/2}$, assigned to the +4 oxidation state. The Ti 2p$_{3/2}$ peak maximum was found at 459.2 eV, and the doublet split value was 5.8 eV, which is typical for the stoichiometric anatase (101) phase.[37] The detailed quantification of the XPS spectra, including the share of each component, the peak binding energy (E_{bin}), as well as the full width at half-maximum (FWHM) of each decomposed peak, is summarized in Table 1. The Ti/O ratio of atoms

and no Ti^{3+} has been identified. Lack of oxygen vacancies on the sample surface may result from its oxidation after exposure to air. No changes on XPS spectra between modified and calcined samples were also observed for hydrogenated TiO$_2$.[43]

To study the optical properties of the obtained material, UV−vis spectroscopy was employed, and the absorbance spectra calculated from reflectance data for all samples are shown in Figure 5. According to the spectrum recorded for
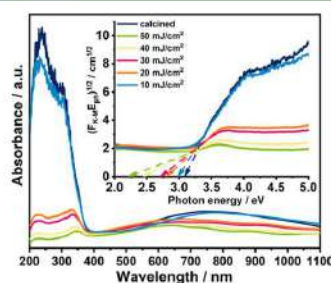
Figure 5. Absorbance spectra for calcined and laser-treated TiO$_2$NTs. The inset presents Tauc plots for all samples.

calcined TiO$_2$NTs, it can be seen that absorption is primarily limited to the UV part of the spectrum, which is related to the anatase wide band gap. Within this range, the maximum absorption corresponds to ca. 235 nm with an additional hill at ca. 305 nm. Beyond this range, a broad absorption band extends from 400 to 1100 nm with a maximum at ca. 800 nm. The spectrum shape of the laser-treated sample with an energy fluence of 10 mJ/cm^2 remains unchanged with a small decrement of absorbance. In the case of higher energy fluences, a significant drop of absorbance in the UV region is observed compared to that of the reference sample. This phenomenon is in good correlation with the SEM analysis, where significant surface layer remelting occurred for beam energy fluences starting from 20 mJ/cm^2. It can be also seen that the higher utilized energy fluence results in the material exhibiting lower absorbance comparing to the pristine titania. Such a decrement is most likely related to the decreasing active surface area[44] observed on SEM images along with an increasing laser beam energy fluence. Moreover, absorption maxima for laser-treated samples are located at ca. 330 nm, whereas the calcined one is at ca. 235 nm.

The shape of band edges was studied according to Tauc plots presented in Figure 5 inset. Herein, for the higher energy fluences, band edges are less sharp, which indicates band-gap narrowing. Band-gap (E_{bg}) values are summarized in Table 2. The E_{bg} value estimated for the calcined sample equals 3.10 eV and is slightly lower compared to bulk anatase (3.20 eV).[45]

Table 1. High-Resolution XPS Spectra Deconvolution Results in Ti 2p$_{3/2}$ and O 1s Regions, for TiO$_2$NTs Treated with Laser Beam of the Fluence of 40 mJ/cm^2

	Ti 2p$_{3/2}$	O 1s	
	TiO$_2$	Ti−O	Ti−OH
E_{bin} (eV)	459.2	530.5	532.0
FWHM (eV)	1.1	1.2	1.5
atomic content (%)	28.7	60.7	10.6

within the lattice of the nanotubes is 0.47:1, revealing a nearly perfect TiO$_2$ stoichiometry. Thus, despite laser modification, oxygen atoms are not removed from the titania surface as in the case of, e.g., Ar$^+$ ion bombardment[38] or strong hydrogenation.[39] This finding is in agreement with the preservation of the Ti/O ratio after laser treatment was carried out for the sample immersed in water.[30] The spectrum recorded in the binding energy region of C 1s (see Figure 4c) was fitted by three singlets: A (285.1 eV), B (288.9 eV), and C (286.4 eV). The first one corresponds to C−C bonds originating from graphitic carbon,[40] which has been used for calibration of the XPS spectra and is typically regarded as a contaminant adsorbed onto the substrate.[41] The maxima labeled as B and C are attributed to the oxidized carbon species.[42] The carbon species are typically present in anodized titania nanotubes since the electrolyte contains an organic precursor that cannot be completely removed via calcination. It is also possible that some small amount of carbon atoms may be introduced into the titania lattice as a dopant. Following XPS results, laser modification does not change the chemical nature of titania

Table 2. Band-Gap Energy Values Determined for the Laser-Modified Materials and Calcined Sample as Reference

| laser beam energy fluence (mJ/cm^2)	band gap (eV)
0	3.10
10	3.00
20	2.80
30	2.70
40	2.45
50	2.24

This small difference results from the particular geometric features of titania NTs that influence the optical properties.[46] In the literature, such a phenomenon is usually attributed to the presence of shallow impurities, particularly the presence of Ti^{3+} states originating from oxygen vacancies, below the conduction band.[27,44]

Summarizing, the SEM analysis along with Raman and UV–vis spectroscopies suggests the presence of additional laser-induced shallow states within the band gap originating from degradation of the crystalline structure, which might give a contribution to superior photoactivity of TiO$_2$NTs. Excitation of electrons from the valence band into the shallow states can be induced by lower energy electromagnetic radiation compared to the charge transfer toward the conduction band. This might give a contribution to band-gap narrowing. On the other hand, since photogenerated electrons from the conduction band can be trapped within these states instead of recombining with holes, the additional states may improve charge separation.[26]

Cyclic voltammograms registered for laser-treated and calcined TiO$_2$NTs in 0.5 M Na$_2$SO$_4$ and 0.5 M NaOH are shown in Figure 6a,b, respectively. In general, all curves exhibit typical run for TiO$_2$NTs—very low capacitive current in the anodic potential ranges from 0 to +0.6 V, and a significant electrochemical activity in the cathodic ranges from −0.6 to −1.0 V vs Ag/AgCl/0.1 M KCl.[47] Current density increment recorded from a potential of ca. +0.65 V in the alkaline electrolyte is related to oxygen evolution reaction (OER). Herein, electrochemical water decomposition occurred at lower potentials regarding neutral solution. This could be explained by the potential pH dependence for water splitting reaction. According to that, the higher the pH of a water solution, the lower the potential forces of oxygen evolution on an anode. In addition, at ca. +0.7 V vs Ag/AgCl/0.1 M KCl, the current density increases gradually and reaches a plateau at +1.0 V vs Ag/AgCl/0.1 M KCl for the materials immersed in

the NaOH solution. This could be attributed to the oxidation of surface species or some local defects.[48] The highest current density corresponding to OER was recorded for the laser-treated sample with an energy fluence of 50 mJ/cm^2 in both neutral and alkaline solutions. Regarding the cathodic range, the peak at −0.32 V vs Ag/AgCl/0.1 M KCl in neutral and −0.5 V in alkaline electrolyte could be ascribed to Ti^{4+} reduction to Ti^{3+} combined with H$^+$ intercalation, while the accompanying anodic peak could be assigned to H$^+$ release.[43] Considering peak positions in Na$_2$SO$_4$ and NaOH, according to Yu et al.,[49] such a negative shift is observed when the number of H$^+$ decreases in electrolyte. Moreover, the current density increment at lower potentials, starting from −0.55 to −0.7 V for neutral and alkaline electrolytes, respectively, is related to H$_2$ evolution reaction. Significant cathodic current densities were recorded for all TiO$_2$NTs. According to Kavan et al.[50] such a run is related to charging of localized surface acceptors, namely, to redox reactions: Ti^{4+} + e$^-$ → Ti^{3+}. Laser modification, particularly with an energy fluence of 50 mJ/cm^2, resulted in a higher current density of TiO$_2$NTs in the cathodic range regarding the calcined sample in alkaline solution. This suggests the presence of additional laser-induced Ti^{4+} states on the electrode surface. This is in good agreement with the conclusions from Raman spectra and Tauc plots.

The photoelectrochemical behavior of laser-treated as well as calcined TiO$_2$NTs in neutral solution exposed to illumination from a solar simulator without and with a UV filter is presented in Figure 7. Along with increasing potential applied to the working electrode, photocurrent densities increased for all examined samples. Considering the results without an installed UV filter that allows for UV–vis irradiation of the electrode during measurements (Figure 7a), it can be clearly seen that laser modifications with energy fluences in the range of 10–40 mJ/cm^2 increased the TiO$_2$NT photoresponse, whereas those with 50 mJ/cm^2 decreased. Thus, optimal processing parameters could be established. The highest photoresponse was recorded for 40 mJ/cm^2—it increased about 45% compared to the response of the calcined sample. Considering the shape of recorded voltammograms, it can be seen that the current densities of calcined TiO$_2$NTs along with laser-modified with energy fluences of 10 and 20 mJ/cm^2 ones reach a plateau starting from ca. +0.2 V On the contrary, when the fluence of 30, 40, and 50 mJ/cm^2 was applied during modification, the recorded current for the laser treated titania increases along with the applied potential in the whole measured range. Beranek et al.[51] observed saturation of the photoresponse for TiO$_2$ nanotubes and an increasing
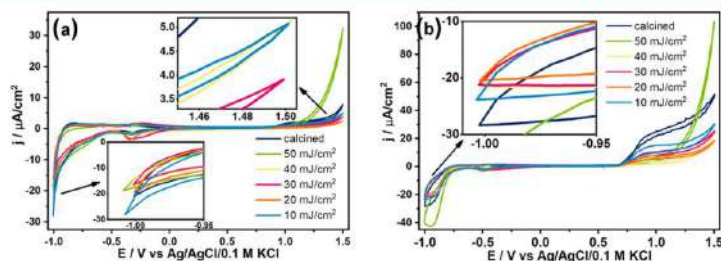
Figure 6. Cyclic voltammograms recorded for laser-modified and calcined TiO$_2$NTs in different electrolytes: (a) 0.5 M Na$_2$SO$_4$ and (b) 0.5 M NaOH.
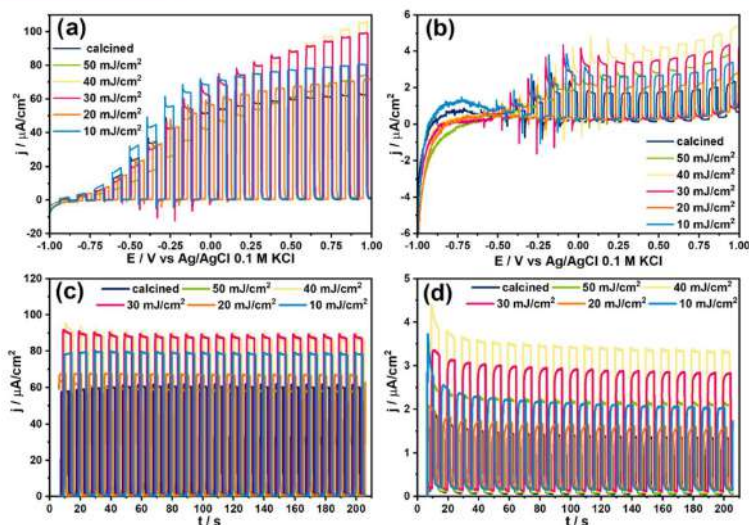
Figure 7. Linear voltamperograms of laser-modified and calcined TiO$_2$ nanotubes recorded (a) without and (b) with a UV filter and transient photocurrent response registered at +0.5 V vs Ag/AgCl/0.1 M KCl without (c) and with (d) a UV filter. All measurements were carried out in 0.5 M Na$_2$SO$_4$.
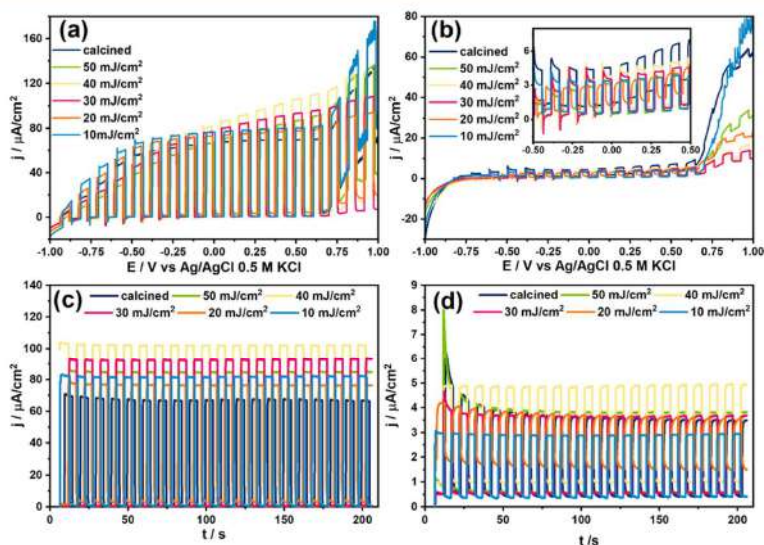
Figure 8. Linear voltamperograms of laser-treated and calcined TiO$_2$ nanotubes carried out in a 0.5 M NaOH electrolyte (a) without and (b) with a UV filter and transient photocurrent response registered at +0.5 V vs Ag/AgCl/0.1 M KCl without (c) and with (d) a UV filter.

behavior for the compact layer. This phenomenon is related to the increasing depletion layer along with the applied voltage in n-type semiconductors. In the case of TiO$_2$NT ordered architecture, there is a potential value corresponding to the depletion layer higher than the tube wall thickness. From that particular value, further polarization does not increase the current and a plateau is observed. Since our modification resulted in the melted layer that is covering the top of the

nanotube, the surface resembles the compact layer, and this is in good accordance with our findings. Considering materials illuminated only with $\lambda > 420$ nm (see Figure 7b), several dozen times lower photocurrent densities were registered compared to the results obtained with the full solar spectrum. For example, the photoresponse of the laser-treated sample with a 40 mJ/cm^2 energy fluence decreased from ca. 88 to ca. 3.4 μA/cm^2. It is most likely related to the large band gap of

TiO$_2$, which is hampering absorption in the visible part of the solar spectrum. Moreover, starting from the potential corresponding to the photocurrent onset, namely, −0.5 V vs Ag/AgCl/0.1 M KCl, spikes were registered in the current voltammograms when the light was turned on and off. Once the potential reached +0.3 V, the spikes were no longer observed. The presence of such rapid current changes results from the electron recombination with the surface-trapped holes and the back-reaction of electrons from the conduction band with accumulated holes. On the other hand, Poornajar et al.[52] pointed out that such spikes are related to electron−hole recombination rate at low external bias. By increasing the applied potential, recombination rate is inhibited by an electric field forced charge separation (electrons are collected on the counter electrode faster along with an increasing potential, reducing the probability of their recombination with holes). Spikes in dark conditions were described to originate from electron back-injection. To investigate the stability of photoelectrode response, the current was measured at + 0.5 V vs Ag/AgCl/0.1 M KCl bias voltage. Chronoamperograms for calcined and laser-treated TiO$_2$NTs registered for on−off cycles without and with a UV filter are shown in Figure 7c,d, respectively. The running of transient photocurrents exhibited a rapid increase and decrease when the irradiations were switched on and off, respectively, except those registered for laser-modified TiO$_2$NTs with energy fluences of 20 and 30 mJ/cm^2 in the vis range (see Figure 7d). Herein, a continuous photocurrent density increment upon a light that is switched on can be seen. According to Tsuchiya et al.,[53] this is attributed to a trap filling. The difference between the current responses when the light is switched on/off is related to the generation of current under illumination, namely, photocurrent. The dark current densities were negligible for all tested samples. The results indicate that all examined electrodes were resistant to photocorrosion. Some initial current decrement observed for several titania samples can be explained as an initial hole accumulation, and it is typical for the photoanode behavior. The stability of these materials under illumination from solar light simulator enables their applications for long-term processes induced by light.

Photoelectrochemical performance of all TiO$_2$NTs in a 0.5 M NaOH electrolyte is shown in Figure 8. Herein, all registered linear voltammograms (see Figure 8a,b) preserved increasing photocurrent densities along with the applied potential, as well as improved photocurrent densities of all laser-treated samples compared to the calcined one. Higher photocurrent densities of laser-treated samples were registered regarding the neutral solution. This is related to the presence of hydroxyl groups in an alkaline electrolyte, which react with photogenerated holes hampering recombination rate.[54] The highest photocurrent density was measured for the laser-modified sample with an energy fluence of 40 mJ/cm^2, which is in good agreement with the results obtained for neutral solution. It is worth noting that photocurrent densities significantly increase in an alkaline electrolyte due to oxygen evolution starting from a potential of ca. +0.65 V. Such an increment was observed also for CV curves and was described earlier. Chronoamperograms recorded in an alkaline solution are presented in Figure 8c,d. Photocurrent transients exhibit similar run compared to those obtained for neutral solution— rapid increase and decrease along with some initial decrement and negligible dark currents. It can be concluded that all

electrodes are stable under prolonged illumination in both pH regimes.

The Mott−Schottky analysis was employed to reveal the impact of laser treatment on the electronic properties of TiO$_2$NTs, namely, the position of the flat band. The impedance spectra were registered within the potential range from +1.5 to −0.5 V, where no faradic activity was recorded, as observed on the cyclic voltammetry curves. According to the Mott−Schottky plot presented in Figure 9, flat band potential
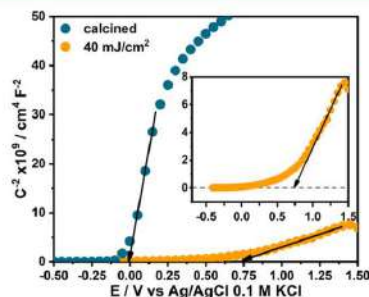

Figure 9. Mott−Schottky plots for calcined and laser-modified TiO$_2$NTs with an energy fluence of 40 mJ/cm^2.

(E_{fb}) for calcined TiO$_2$NTs was estimated to be ca. 0.00 V, while the literature value of E_{fb} for thermally annealed TiO$_2$NTs is reported to be ca. −0.10 V.[53] The difference could be related to the different geometry of titania samples or system nonstationarity. For the laser-treated sample, a significant anodic shift of E_{fb} of about + 0.74 V can be seen. It is worth noting that herein, the slope of the linear range (C^{-2}) decreases regarding calcined TiO$_2$NTs, which means that C increases. Such a C increment is often observed for specific surface area enlargement in porous semiconductors.[55] However, this is contradictory with SEM images obtained for laser-modified samples, which indicate surface area decrement. On the other hand, the impact of the flat band potential position on the electronic structure of laser-treated and calcined TiO$_2$NTs at the electrode/electrolyte interface is schematically presented in Figure 10. In general, for n-type semiconductors, a positive shift of flat band potential means a shift of its Fermi level toward the conduction band.[56] According to that, the Fermi level value of the laser-treated sample is higher compared to that of the calcined one. After immersion of the electrode in an electrolyte, it is starting to reach equilibrium with the Fermi level of redox pair. During that, the electrons are flowing from the conduction band toward the electrolyte, and the electrode's Fermi level is going down giving contribution to band bending.[57] The higher the drop of the Fermi level, the higher is the band bending, which facilitates transfer of electrons and holes toward the back-titanium contact and electrolyte, respectively, and as a result, efficient charge separation.[38] On the other hand, taking into account the inversely proportional relation between the slope and donor density, it can be clearly seen from Figure 9 that laser modification with an energy beam fluence of 40 mJ/cm^2 resulted in a significantly increased donor density value. Calculated N_d values are estimated to be 2.2 × 10^{19} and 14.1 × 10^{20} cm^{-3} for calcined and laser-modified samples, respectively. Thus, the results obtained from the Mott−Schottky analysis
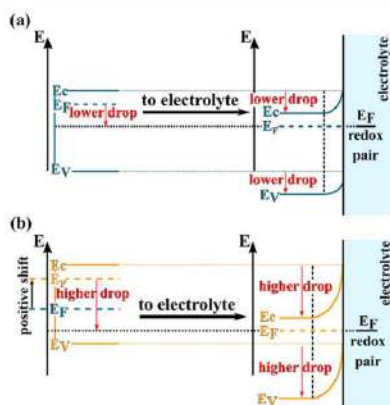
Figure 10. Schematic diagram illustrating the influence of a positive shift of flat band potential on band bending at the electrode/electrolyte interface of laser-treated and calcined TiO$_2$NTs.

prove the validity of the conclusions that laser irradiation induces additional shallow states within the band gap, originating from degradation of the crystalline structure within the melted layer.

4. CONCLUSIONS

This work showed that pulsed laser modification can be successfully employed as a large-scale method to enhance the electronic properties of TiO$_2$ nanotubes. Thanks to the utilization of a motorized table along with a beam homogenizer, the results of our work can be scaled up to any large sample area, and no sample immersion in water is required. Optimum laser processing parameters have been identified, leading to the enhanced photoactivity. According to the linear voltammograms, the highest photocurrent density response was recorded for laser-treated TiO$_2$NTs with an energy fluence of 40 mJ/cm^2. An increment was estimated to be about 45% in comparison to that of the calcined sample. Chronoamperograms indicate that electrodes were stable during simulated solar light irradiation in both neutral and alkaline environments. SEM images showed that laser treatment resulted in a melted layer that is covering the top of the nanotubes, leaving a tubular structure beneath intact. The preserved nanotubes act here as a straight percolation path provided to the electrons[58] photogenerated at the melted titania layer/electrolyte interface where the exciton dissociation takes part. The charge is then easily transported along the tube to the back-contact—titanium foil. Raman spectra along with Tauc plots obtained from UV−vis spectroscopy suggest that the laser-induced distortion of the crystalline structure resulted in the presence of additional shallow states observed as a band-gap narrowing, which could be responsible for an enhanced photoelectrochemical activity. Further, the Mott−Schottky analysis revealed an enormous positive shift of flat band potential of about +0.74 V along with an increased donor density over an order of magnitude, most likely originating from additional shallow states suggested by Raman and UV−vis spectroscopies. Thus, the laser-enhanced electronic structure of TiO$_2$ nanotubes presented in this work may give a contribution to improved photocatalytic or photovoltaic performance of these materials.

■ ASSOCIATED CONTENT

ⓢ Supporting Information

The Supporting Information is available free of charge at https://pubs.acs.org/doi/10.1021/acsami.9b19206.

Survey XPS spectrum recorded for the TiO$_2$NTs sample treated with laser fluence of 40 mJ/cm^2 (Figure S1) (PDF)

■ AUTHOR INFORMATION

Corresponding Author
*E-mail: lharynski@imp.gda.pl. Tel.: +48 58 522-52-55.

ORCID ⓘ
Łukasz Haryński: 0000-0001-9615-9996
Katarzyna Grochowska: 0000-0001-7577-3399
Jacek Ryl: 0000-0002-0247-3851
Katarzyna Siuzdak: 0000-0001-7434-6408

Notes
The authors declare no competing financial interest.

■ REFERENCES

(1) Husain, A. A. F.; Zuha, W.; Hasan, W.; Shafie, S.; Hamidon, M. N.; Pandey, S. S. A Review of Transparent Solar Photovoltaic Technologies. *Renewable Sustainable Energy Rev.* **2018**, *94*, 779−791.
(2) Ni, M.; Leung, M. K. H.; Leung, D. Y. C.; Sumathy, K. A Review and Recent Developments in Photocatalytic Water-Splitting Using TiO$_2$ for Hydrogen Production. *Renewable Sustainable Energy Rev.* **2007**, *11*, 401−425.
(3) Nagpal, M.; Kakkar, R. Use of Metal Oxides for the Adsorptive Removal of Toxic Organic Pollutants. *Sep. Purif. Technol.* **2019**, *221*, 522−539.
(4) Mahajan, V. K.; Mohapatra, S. K.; Misra, M. Stability of TiO$_2$ Nanotube Arrays in Photoelectrochemical Studies. *Int. J. Hydrogen Energy* **2008**, *33*, 5369−5374.
(5) Nischk, M.; Mazierski, P.; Wei, Z.; Siuzdak, K.; Konuame, N. A.; Kowalska, E.; Remita, H.; Zaleska-Medynska, A. Enhanced Photocatalytic, Electrochemical and Photoelectrochemical Properties of TiO$_2$ Nanotubes Arrays Modified with Cu, AgCu and Bi Nanoparticles Obtained via Radiolytic Reduction. *Appl. Surf. Sci.* **2016**, *387*, 89−102.
(6) Kulkarni, M.; Mazare, A.; Schmuki, P.; Iglic, A. Influence Of Anodization Parameters On Morphology Of TiO$_2$ Nanostructured Surfaces. *Adv. Mater. Lett.* **2016**, *7*, 23−28.
(7) Matarrese, R.; Nova, I.; Bassi, A. L.; Casari, C. S. Preparation and Optimization of TiO$_2$ Photoanodes Fabricated by Pulsed Laser Deposition for Photoelectrochemical Water Splitting. *J. Solid State Electrochem.* **2017**, *21*, 3139−3154.
(8) Casari, C. S.; Bassi, A. L. *Oxide Nanostructures: Growth, Microstructures, and Properties: Pulsed Laser Deposition of Nanostructured Oxides for Emerging Applications*; Srivastav, A. K., Ed.; Pan Stanford Publishing: Singapore, 2012; pp 99−114.
(9) Ranjitha, A.; Muthukumarasamy, N.; Thambidurai, M.; Velauthapillai, D.; Agilan, S.; Balasundaraprabhu, R. Effect of Reaction Time on the Formation of TiO$_2$ Nanotubes Prepared by Hydrothermal Method. *Optik* **2017**, *126*, 2491−2494.
(10) He, G.; Zhang, J.; Hu, Y.; Bai, Z.; Wei, C. Dual-Template Synthesis of Mesoporous TiO$_2$ Nanotubes with Structure-Enhanced Functional Photocatalytic Performance. *Appl. Catal., B* **2019**, *250*, 301−312.
(11) Roy, P.; Berger, S.; Schmuki, P. TiO$_2$ Nanotubes: Synthesis and Applications. *Nanoscience* **2011**, *50*, 2904−2939.

(12) Deng, J.; Zhuo, Q.; Lv, X. Hierarchical TiO$_2$/Fe$_2$O$_3$ Heterojunction Photoanode for Improved Photoelectrochemical Water Oxidation. *J. Electroanal. Chem.* **2019**, *292*, 287−292.

(13) Ma, X.; Sun, Z.; Hu, X. Synthesis of Tin and Molybdenum co-doped TiO$_2$ Nanotube Arrays for the Photoelectrocatalytic Oxidation of Phenol in Aqueous Solution. *Mater. Sci. Semicond. Process.* **2018**, *85*, 150−159.

(14) Huang, R.; Zhang, S.; Ding, J.; Meng, Y.; Zhong, Q.; Kong, D.; Gu, C. Effect of Adsorption Properties of Phosphorus-Doped TiO$_2$ Nanotubes on Photocatalytic NO Removal. *J. Colloid Interface Sci.* **2019**, *553*, 647−654.

(15) Lu, N.; Zhao, H.; Li, J.; Quan, X.; Chen, S. Characterization of Boron-Doped TiO$_2$ Nanotube Arrays Prepared by Electrochemical Method and its Visible Light Activity. *Sep. Purif. Technol.* **2008**, *62*, 668−673.

(16) Singh, L. K.; Koiry, B. P. Natural Dyes and their Effect on Efficiency of TiO$_2$ Based DSSCs: a Comparative Study. *Mater. Today* **2008**, *5*, 21112−2122.

(17) Zuñiga-Ibarra, V. A.; Shaji, S.; Krishnan, B.; Johny, J.; Kanakkillam, S. S.; Avellanda, D. A.; Martinez, J. A. A.; Roy, T. K. D.; Ramos-Delgado, N. A. Synthesis and Characterization of Black TiO$_2$ Nanoparticles by Pulsed Laser Irradiation in Liquid. *Appl. Surf. Sci.* **2019**, *483*, 156−164.

(18) Radecka, M.; Rekas, M.; Trenczek-Zajac, A.; Zakrzewska, K. Importance of the Band Gap Energy and Flat Band Potential for Application of Modified TiO$_2$ Photoanodes in Water Photolysis. *J. Power Sources* **2008**, *181*, 46−55.

(19) Lačnjevac, U.; Vasilic, R.; Tokarski, T.; Cios, G.; Zabinski, P.; Elezovic, N.; Krstajic, N. Deposition of Pd Nanoparticles on the Walls of Cathodically Hydrogenated TiO$_2$ Nanotube Arrays via Galvanic Displacement: A Novel Route to Produce Exceptionally Active and Durable Composite Electrocatalysts for Cost-Effective Hydrogen Evolution. *Nano Energy* **2018**, *47*, 527−538.

(20) Singh, A. P.; Kodan, N.; Mehta, B. R.; Dey, A.; Krishnamurthy, S. In-Situ Plasma Hydrogenated TiO$_2$ Thin Films for Enhanced Photoelectrochemical Properties. *Mater. Res. Bull.* **2016**, *76*, 284−291.

(21) Cui, L. H.; Wang, Y.; Shu, X.; Zhang, J. F.; Yu, C. P.; Cui, J. W.; Zheng, H. M.; Zhang, Y.; Wu, Y. C. Supercapacitive Performance of Hydrogenated TiO$_2$ Nanotube Arrays Decorated with Nickel Oxides Nanoparticle. *RSC Adv.* **2016**, *6*, 12185−12192.

(22) Zheng, Z.; Huang, B.; Lu, J.; Wang, Z.; Qin, X.; Zhang, X.; Daib, Y.; Whangboc, M. Hydrogenated Titania: Synergy of Surface Modification and Morphology Improvement for Enhanced Photocatalytic Activity. *J. Chem. Soc.* **2012**, *48*, 5733−5735.

(23) Yan, Yong.; Han, M.; Konkin, A.; Koppe, T.; Wang, D.; Andreu, T.; Chen, G.; Vetter, U.; Morantee, J. R.; Schafa, P. Slightly Hydrogenated TiO$_2$ with Enhanced Photocatalytic Performance. *J. Mater. Chem. A* **2014**, *2*, 12708−12716.

(24) Samsudin, E. M.; Hamida, S. B. A.; Juana, J. C.; Basiruna, W. J.; Kandjani, A. E. Surface Modification of Mixed-Phase Hydrogenated TiO$_2$ and Corresponding Photocatalytic Response. *Appl. Surf. Sci.* **2015**, *359*, 883−896.

(25) Wang, Z.; Yang, C.; Lin, T.; Yin, H.; Chen, P.; Wan, D.; Xu, F.; Huang, F.; Xie, X.; Jiang, M.; et al. H-Doped Black Titania with Very High Solar Absorption and Excellent Photocatalysis Enhanced by Localized Surface Plasmon Resonance. *Adv. Funct. Mater.* **2013**, *23*, 5444−5450.

(26) Su, T.; Yang, Y.; Na, Y.; Fan, R.; Li, L.; Wei, L.; Yang, B.; Cao, W. An Insight Into the Role of Oxygen Vacancy in Hydrogenated TiO$_2$ Nanocrystals in the Performance of Dye Sensitized Solar Cells. *ACS Appl. Mater. Interfaces* **2015**, *7*, 3754−3761.

(27) Liu, J.; Dai, M.; Wu, J.; Hu, Y.; Zhang, Q.; Cui, J.; Wang, Y.; Tan, H. H.; Wu, Y. Electrochemical Hydrogenation of Mixed-Phase TiO$_2$ nanotube arrays enables remarkably enhanced photoelectrochemical water splitting performance. *Sci. Bull.* **2018**, *63*, 194−202.

(28) Siuzdak, K.; Szkoda, M.; Sawczak, M.; Karczewski, J.; Ryl, J.; Cenian, A. Ordered Titania Nanotubes Layer Selectively Annealed by Laser Beam for High Contrast Electrochromic Switching. *Thin Solid Films* **2018**, *659*, 48−56.

(29) Vásquez, G. C.; Peche-Herrero, M. A.; Maestre, D.; Gianoncelli, A.; Ramirez-Castellanos, J.; Cremades, A.; Gonzalez-Calbet, J. M.; Piqueras, J. Laser-Induced Anatase-to-Rutile Transition in TiO$_2$ Nanoparticles: Promotion and Inhibition Effects by Fe and Al Doping and Achievement of Micropatterning. *J. Phys. Chem. C* **2015**, *119*, 11965−11974.

(30) Xu, Y.; Melia, A.; Tsui, L.; Fitz-Gerald, J. M.; Zangari, G. Laser-Induced Surface Modification at Anatase TiO$_2$ Nanotube Array Photoanodes for Photoelectrochemical Water Oxidation. *J. Phys. Chem. C* **2017**, *32*, 17121−17128.

(31) Beranek, R. Photoelectrochemical Methods for the Determination of the Band Edge Positions of TiO$_2$-Based Nanomaterials. *Adv. Chem. Phys.* **2011**, *2011*, 1−14.

(32) Park, B. H.; Li, L. S.; Gibbson, B. J.; Huang, J. Y.; Jia, Q. X. Photovoltaic Response and Dielectric Properties of Epitaxial Anatase-TiO$_2$ Films Grown on Conductive La$_{0.5}$Sr$_{0.5}$CoO$_3$ Electrodes. *Appl. Phys. Lett.* **2001**, *79*, 2797−2799.

(33) Chen, X.; Mao, S. S. Titanium Dioxide Nanomaterials: Synthesis, Properties, Modifications, and Applications. *Chem. Rev.* **2007**, *107*, 2891−1959.

(34) Wang, B.; Shen, S.; Mao, S. S. Black TiO$_2$ for Solar Hydrogen Conversion. *J. Materiomics* **2017**, *3*, 96−111.

(35) Syres, K. L.; Thomas, A. G.; Flavell, W. R.; Spencer, B. F.; Bondino, F.; Malvenstuto, M.; Preobrajenski, A.; Gratzel, M. Adsorbate-Induced Modification of Surface Electronic Structure: Pyrocatechol Adsorption on the Anatase TiO$_2$ (101) and Rutile TiO$_2$ (110) Surfaces. *J. Phys. Chem. C* **2012**, *116*, 23515−23525.

(36) Yuan, B.; Wang, Y.; Bian, H.; Shen, T.; Wu, Y.; Chen, Z. Nitrogen Doped TiO$_2$ Nanotube Arrays with High Photoelectrochemical Activity for Photocatalytic Applications. *Appl. Surf. Sci.* **2013**, *280*, 523−529.

(37) Siuzdak, K.; Szkoda, M.; Lisowska-Oleksiak, A.; Karczewski, J.; Ryl, J. Highly stable organic-inorganic junction composed of hydrogenated titania nanotubes infiltrated by a conducting polymer. *RSC Adv.* **2016**, *6*, 33101−33110.

(38) Jackman, M. J.; Thomas, A. G.; Muryn, C. Photoelectron Spectroscopy Study of Stoichiometric and Reduced Anatase TiO$_2$ (101) Surfaces: the Effect of Subsurface Defects on Water Absorption at Near −Ambient Pressures. *J. Phys. Chem. C* **2015**, *119*, 16382−13690.

(39) Zhang, Z.; Haedhili, M. N.; Zhu, H.; Wang, P. Electrochemical Reduction Induced Self-Doping of Ti^{3+} for Efficient Water Splitting Performance on TiO$_2$ Based Photoelectrodes. *Phys. Chem. Chem. Phys.* **2013**, *15*, 15637−15644.

(40) Srinivasu, P.; Islam, A.; Singh, S. P.; Han, L.; Kantam, M. L.; Bhargava, K. Highly Efficient Nanoporous Graphitic Carbon with Tunable Textural Properties for Dye-Sensitized Solar Cells. *J. Mater. Chem.* **2012**, *22*, 20866−20869.

(41) Isimjan, T. T.; Ruby, A. E.; Rohani, S.; Ray, A. K. The Fabrication of Highly Ordered and Visible-Light-Responsive Fe-C-N-Codoped TiO$_2$ Nanotubes. *Nanotechnology* **2010**, *21*, No. 055706.

(42) Tsai, C.; Pan, Y.; Tseng, Y.; Liu, C.; Kuo, T.; His, H. Influence of Carbon-Functional Groups with Less Hydrophilicity on a TiO$_2$ Photocatalyst for Removing Low-Level Elemental Mercury. *Sustainable Environ. Res.* **2017**, *27*, 70−76.

(43) Leshuk, T.; Parviz, R.; Everett, P.; Krishnakumar, H.; Varin, R. A.; Gu, F. Photocatalytic Activity of Hydrogenated TiO$_2$. *ACS Appl. Mater. Interfaces* **2013**, *5*, 1892−1895.

(44) Ly, N. T.; Nguyen, V. C.; Dao, T. H.; To, L. H. H.; Pham, D. L.; Do, H. M.; Vu, D. L.; Le, V. H. Optical Properties of TiO$_2$ Nanotube Arrays Fabricated by the Electrochemical Anodization Method. *Adv. Nat. Sci.: Nanosci. Nanotechnol.* **2014**, *5*, No. 015004.

(45) Dette, C.; Perez-Osorio, M. A.; Kley, C. S.; Punke, P.; Patrick, C. E.; Jacobson, P.; Giustino, F.; Jung, J. S.; Kern, K. TiO$_2$ Anatase with a Bandgap in the Visible Region. *Nano Lett.* **2014**, *14*, 6533−6538.

(46) Freitas, R. G.; Santanna, M. A.; Pereira, E. C. Dependence of TiO$_2$ Nanotube Microstructural and Electronic Properties on Water Splitting. *J. Power Sources* **2014**, *251*, 178−186.

— 54 —

(47) Macak, J. M.; Tsuchiya, H.; Ghicov, A.; Yasuda, K.; Hahn, R.; Bauer, S.; Schmuki, P. TiO$_2$ Nanotubes: Self-Organized Electrochemical Formation, Properties and Applications. *Curr. Opin. Solid State Mater. Sci.* **2007**, *11*, 3–18.

(48) Mazare, A.; Dilea, M.; Ionita, D.; Demetrescu, I. Eletrochemical Behaviour in Simulated Body Fluid of TiO$_2$ Nanotubes on TiAlNb Alloy Elaborated in Various Anodizing Electrolyte. *Surf. Interface Anal.* **2014**, *45*, 186–192.

(49) Yu, H.; Ma, J.; Zhang, Y.; Zhang, X.; Shi, W. Cyclic Voltammetry Studies of TiO$_2$ Nanotube Arrays Electrode: Conductivity and Reactivity in the Presence of H$^+$ and Aqueous Redox Systems. *Electrochim. Acta* **2011**, *56*, 6498–6502.

(50) Kavan, L.; Gratzel, M.; Rathousky, J.; Zukal, A. Nanocrystalline TiO$_2$ (Anatase) Electrodes: Surface Morphology, Adsorption, and Electrochemical Properties. *J. Electrochem. Soc.* **1996**, *143*, 394–400.

(51) Beranek, R.; Tsuchiya, H.; Sugishima, T.; Macak, J. M.; Taveira, L.; Fujimoto, S.; Kisch, H.; Schmuki, P. Enhancement and Limits of the Photoelectrochemical Response from Anodic TiO$_2$ Nanotubes. *Appl. Phys. Lett.* **2005**, *87*, No. 243114.

(52) Poornajar, M.; Nguyen, N. T.; Ahn, H.; Buchler, M.; Liu, N.; Kment, S.; Zboril, R.; Yoo, J. E.; Schmuki, P. Blocking Layer Produced by Cyclic Voltammetry Leads to Improved Photoelectrochemical Performance of Hematite Nanorods. *Surfaces* **2019**, *2*, 131–144.

(53) Tsuchiya, H.; Macak, J. M.; Ghicov, A.; Rader, A. S.; Taveira, L.; Schmuki, P. Characterization of Electronic Properties of TiO$_2$ Nanotube Flms. *Corros. Sci.* **2007**, *49*, 203–210.

(54) Crawford, S.; Thimsen, E.; Biswas, P. Impact of Different Electrolytes on Photocatalytic Water Splitting. *J. Electrochem. Soc.* **2009**, *156*, H346–H351.

(55) Muñoz, A. G.; Chen, Q.; Schmuki, P. Interfacial Properties of Self-Organized TiO$_2$ Nanotubes Studies by Impedance Spectroscopy. *J. Solid State Electrochem.* **2006**, *11*, 1077–1084.

(56) Rambabu, Y.; Jaiswal, M.; Roy, S. C. Probing the Charge Recombination in rGO Decorated Mixed Phase (Anatase-Rutile) TiO$_2$ Multi-Leg Nanotubes. *AIP Adv.* **2016**, *6*, No. 115010.

(57) Cheng, X.; Kong, D.; Wang, Z.; Feng, Y.; Li, W. Inhibiting Effect of Carbonate on the Photoinduced Flatband Potential Shifts During Water Photooxidation at TiO$_2$/Solution Interface. *J. Solid State Electrochem.* **2017**, *21*, 1467–1475.

(58) Mohamed, A. E. R.; Rohani, S. Modified TiO$_2$ Nanotube Arrays (TNTAs): Progressive Strategies Towards Visible Light Responsive Photoanode, a Review. *Energy Environ. Sci.* **2011**, *4*, 1065–1086.

— 55 —

Scalable route towards superior photoresponse of UV laser-treated TiO$_2$ nanotubes

Łukasz Haryński[*][1], Katarzyna Grochowska[1], Jakub Karczewski[2], Jacek Ryl[3] and Katarzyna Siuzdak[1]

[1]Centre for Plasma and Laser Engineering, The Szewalski Institute of Fluid-Flow Machinery Polish Academy of Sciences, Fiszera 14 St., 80-231 Gdańsk, Poland
[2]Faculty of Applied Physics and Mathematics, Gdańsk University of Technology, Narutowicza 11/12 St., 80-233 Gdańsk, Poland
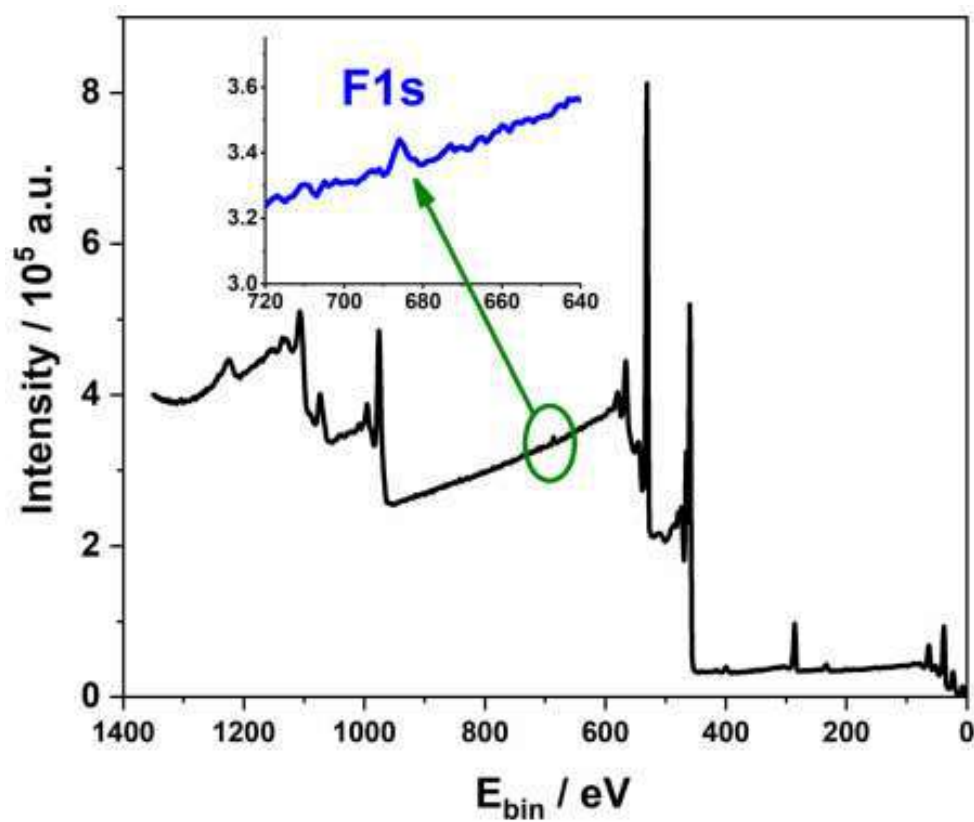[3]Faculty of Chemistry, Gdańsk University of Technology, Narutowicza 11/12 St., 80-233 Gdańsk, Poland

*Corresponding author: e-mail: lharynski@imp.gda.pl (Łukasz Haryński);
Tel.: +48 58 522-52-55

TABLE OF CONTENTS

S-1

Figure S1. The survey XPS spectrum recorded for the TiO₂NTs sample treated with laser fluence of 40 mJ/cm².

S-2

5.2. Paper 2: Review on robust laser light interaction with titania – Patterning, crystallization and ablation processes

TiO_2 can be found in the amorphous phase as well as in different polymorphs. The amorphous phase exhibits poor incident photon-to-current conversion efficiency (IPCE). This is because of the disordered structure exhibiting a high number of recombination centers for photogenerated carriers. Practical applications of TiO_2 in photoelectrochemical systems require therefore phase transformation from amorphous to crystalline. The most common crystal forms in this regard are rutile and anatase. Among them, rutile is more a thermodynamically stable phase with a band gap of about 3.0 eV while anatase is metastable and exhibits a 3.2 eV band gap. Among them, anatase, despite a larger band gap, exhibits superior IPCE compared to rutile. Nevertheless, the highest performances are reached for a mixed phase, which, as demonstrated by Li et al. [61], is clearly related to the improved charge separation at the anatase-rutile junction.

Traditionally, the phase transformation from amorphous to crystalline is realized in furnaces at elevated temperatures (450°C and 750-850°C for anatase and rutile, respectively). Taking into account heating and cooling down periods, the whole process can take over 10 hours. Moreover, most furnaces utilize resistive heating, hence it is associated with high energy losses. Different alternative methods have been proposed including water immersion or flame annealing, however, they are also limited to the whole volume of the sample. In this regard, laser technology can not only shorten the process and reduce energy consumption but can also allow for modification of selected area instead of the whole volume. This can be particularly advantageous in the case of multi-component materials in which one of the components is not resistant to high temperatures, for example for flexible solar cells made on plastic substrates.

The presented work describes the literature revision of patterning, ablation, and change in the crystal structure of TiO_2. The author of the present thesis was solely responsible for the preparation of section 5 entitled *Laser-induced phase transformation* where the literature regarding the phase transformation of TiO_2 was reviewed. The chapter was divided into two sections dedicated to continuous and pulsed lasers, which in turn, was additionally split into three subdivisions according to the different pulse durations: nano-, pico-, and femtosecond. Detailed revision showed that despite the use of various lasers including continuous and pulsed in nano and picosecond regimes, it was not possible to crystalline TiO_2 nanotubes over the entire volume. This is because the radiation is absorbed only within the laser spot by the top of the nanotubes while the crystallization outside the spot and alongside the nanotubes is a result of the heat transport (see Fig. 15 b-c and 16 a-b in the paper, respectively). Promising results have

been obtained for laser-induced defect in crystalline forms of TiO_2 including anodic nanotubes and powder. In the case of nanotubes, optimum beam energy fluence allowed the introduction of shallow defects providing additional charge carriers for photon absorption which was revealed by the analysis of Mott-Schottky plots both in static and scalable systems (see Fig. 16 f and g). In the case of the powder, far more higher beam energy fluence could be applied resulting in significant degradation of crystal structure giving a rise to highly defective, so-called black TiO_2 (see Fig. 16 h), which allowed to overcome limitations of pristine TiO_2 through enhanced visible light absorption. In addition to that, different features affecting laser-induced phase transformation including laser mode, wavelength, optical path, sample holding system, environment, beam intensity, and irradiation period were indicated. In particular, aspects during the modification with a motorized table including beam profile and adjacent lines overlap during modification were discussed.

Based on the literature revision, it is concluded that the application potential of laser technology is limited in the matter of crystallization from the amorphous phase, however, it is a promising tool for the introduction of defects in titania substrates.

Review on robust laser light interaction with titania – Patterning, crystallisation and ablation processes

Katarzyna Siuzdak [*], Łukasz Haryński, Jakub Wawrzyniak, Katarzyna Grochowska

Centre for Plasma and Laser Engineering, The Szewalski Institute of Fluid-Flow Machinery, Polish Academy of Sciences, Fiszera 14 St., 80-231, Gdańsk, Poland

ARTICLE INFO

ABSTRACT

Titanium dioxide is regarded as a very promising semiconducting material that is widely applied in many everyday-use products, devices, and processes. In general, those applications can be divided into energy or environmental categories, where a high conversion rate, and energy and power density are of particular interest. Therefore, many efforts are being put towards the elaboration of novel production routes, and improving the material's properties such as light absorption, and charge concentration, as well as development of the surface area to improve the efficiency of particular process. Typically, bulk doping and surface modifications can be distinguished, applying some sol-gel, chemical vapour deposition, and hydrothermal processes in the presence of dopant precursors. However, development of waste disposal and many up-scaling optimisation routes have to be performed to consider the proposed path worthy of wide scale, commercial use. In contrast to the wet-chemistry methods, laser technology offers unique material treatment by light of a particular wavelength, fluence, and pulse repetition rate. In consequence, the changes can affect the bulk structure or only its surface. Such an approach provides a wide range of possible modifications without the use of any chemical products, and therefore avoids the formation of any by-products. Moreover, knowing the facile scaling up of laser treatment towards a higher technology readiness level, we believe such an approach stands out from synthesis and/or modification carried out first in small flasks and using small amounts of substrates. In this review, we would like to emphasize the results of selected studies presenting possible laser beam and titania interactions ensuring changes in the surface zone or deeply in the internal structure. The works evoked here indicate that this powerful technique can, among other things, provide slight surface melting of titania nanotubes, their phase transition from an amorphous solid to anatase or, when the fluence exceeds a certain threshold, the ablation of material out of the titania target.

Paper 2

to ensure the phase transition from the amorphous to the crystalline, providing the appropriate electric properties. In such a process, the material is placed in a furnace and high temperature annealing is carried out. According to the standard protocols, in the majority of cases, this process is performed at 450 °C for 1–2 h, resulting in complete phase conversion [21,22]. Therefore, including the heating up period and the final cooling, the whole procedure can last even over a dozen hours. Nevertheless, a single or a mixture of the most common crystalline phases can be obtained: anatase, rutile, and brookite [23] since, in some particular applications, a synergistic effect arises when the rutile and anatase become neighbouring phases. Regarding the other important features exhibited by semiconducting materials, namely the optical properties and the bandgap energy value, for anatase TiO_2, the latter equals 3.2 eV [24]. Therefore, the light absorption of titania is limited to the UV range, which is favourable for light protective creams, but on the other hand, significantly hampers usability in processes driven by solar light, e.g. photocatalytic decomposition of organic pollution present in the air and water, or water photo-splitting when hydrogen or/and oxygen generation is enhanced by electrode irradiation. Nevertheless, this aspect stands as a point of intense research towards bandgap widening, resulting in shifting the absorbance to the visible range. To lower the energy band gap, many strategies have been undertaken, and include covering titania with non-metals [25,26] (e.g. B, I, N) and noble (Au, Ag, Pd) [27,28], as well as non-noble (Ni, Co, Cu) [29,30] metal doping, decoration by nanoparticles (PbS, CdS, CdSe, Fe_2O_3) [31], deposition of dye molecules, and the formation of heterojunctions with other materials active under visible light (conducting polymer [32], quantum dots [33], some narrow bandgap semiconductors [34]). Apart from changes in the structure related to the introduction of foreign atoms or the formation of oxygen vacancies, many attempts related to manipulation of the morphology have been proposed. Both the selection of the synthesis route, and post-reaction surface modification can also lead to changes in the optical properties. Summarising, titania can be regarded as a very attractive platform for further modifications, while those modifications can tune its optical features, structure and morphology towards particular material applications.

Until now, many works have focused on titania, its modification and application [35–37]. As can be seen in Fig. 1, in the last year, the number of documents where titanium dioxide was evoked reached almost 12, 000, and since 2000, the trend can be described as dynamic growth. In general, those reports can be classified as being within many disciplines, however more than 10% can be ascribed to the following subjects: material science, chemistry, environmental science, engineering, and chemical engineering.

Analysing the trend depicted in Fig. 1, it seems that the limit has still not been reached, and titania will continue to attract significant interest for a long time, despite the simplicity of the compound built using only two elements: oxygen and titanium. However, we can observe that recently undertaken efforts which also exhibit high commercialisation potential are strategies that could easily be transferred to the production line, and can be remotely controlled. Among other routes, the application of laser technology, already well mastered on the technological scale [38], is a promising and powerful tool used in titania deposition [39], surface modification (patterning [40], welding [41]), and phase transitioning [42]. Laser light, as compared to other light sources, is characterised by high intensity, coherence, and monochromaticity [43]. We can frequently find various lasers in many applications on the market (from simple pointers to lasers responsible for cutting [44] and drilling [45], and aesthetic medicine) as well as in research [46]. Among others, we can distinguish devices generating pulsed and continues radiation, at different wavelengths, operating at very low fluence, and with significant power reaching several kW [47,48]. Depending on the purpose, the intense light beam can almost destroy the structure of the materials [49], change the crystalline phase [50], or just lead to some slight changes in the morphology, but resulting in completely different surface properties, like, e.g. hydrophilicity [51]. Therefore, titania can be regarded as a starting material for modification and on the other hand, as laser technology is a tool that provides a wide spectrum of possibilities while enabling a relatively fast path through technology to readiness levels, allowing the real advantages of the interaction between
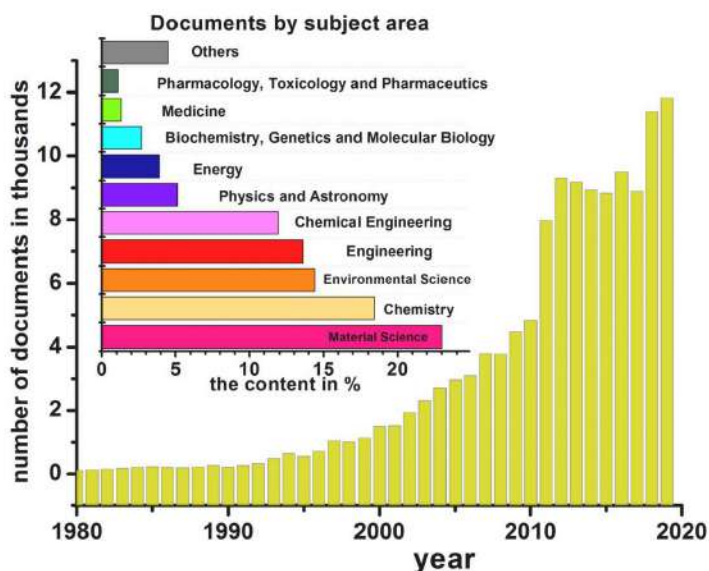

Fig. 1. The dynamic increase in the number of documents dedicated to titanium dioxide, inset: the content of the documents by subject area (source: Scopus, 14-04-2020).

laser technology and TiO$_2$ to be reached.

Herein, we report on the usage of laser radiation on titania of different morphologies, including compact and porous, as well as ordered tubular layers, and thin films composed of nanoparticles. Moreover we look at the issue of the impact of the laser on the crystalline phase when an amorphous or already crystalline substrate is used as a staring material. In the second paragraph, we focus on the phenomena arising when laser radiation contacts with the material surface. We point out the possible mechanisms depending on the type of laser irradiation. The proper choice of the values of the laser parameters can only slightly change the surface, induce phase transition, or lead to partial melting, fragmentation, or ablation. In the third part, we describe surface modification affected by laser radiation that as a consequence can alter not only the morphology, but also the wettability, structure defects, or introduction of active sites. The fourth part is dedicated to titania ablation and its further deposition onto a substrate, since laser technology can also be used for the fabrication of thin layers out of a metal oxide target. Therefore, in this section, we will focus on titania evaporation via a laser beam followed by the vapour contacting the substrate and becoming immobilised on the material. The last section is mainly about phase transitions affected by laser radiation used as a rapid alternative to the traditional calcination process implemented in a furnace. Moreover, in this section, we underline the differences in the heat distribution responsible for the change from the amorphous to the crystalline phase. In each section, when reporting different aspects of laser-titania interactions, we will evoke the properties and further applications of the laser-treated materials in comparison to the unmodified ones, or to those where a traditional, non-laser-assisted method was applied. Finally, we will try to indicate some recently discovered areas where the use of laser illumination onto titania was introduced while the commonly known chemical and physical approaches do not work efficiently.

2. Laser-material interaction

In contrast to material processing in a furnace where the heating

occurs in the entire volume, a laser interacts with the material only locally. In effect of laser annealing, both inside and in the outer part of the material, many optical, electromagnetic, and thermodynamic phenomena occur [52]. The most important are: refraction of the laser beam from the material surface, and transmission and absorption of the beam within the material. The numerous variety of processes are shown in Fig. 2.

Nevertheless, the processing of the material with a laser is mainly based on absorption of the radiation. The absorbed energy induces thermodynamic effects such as melting and vaporisation, as well as chemical reactions, e.g. breaking of the chemical bonds.

It is well-known that the intensity of the laser radiation penetrating the material can be described by the Beer-Lambert law:

$$I(z) = I_0 e^{-\alpha z} \tag{1}$$

where I_0 is the intensity of the incident radiation (the loss due to reflected irradiation is taken into account), α is the absorption coefficient, and z is the depth of the laser propagation as measured from the affected surface of the material. However, it should be remembered that the absorption coefficient is not constant, and depends on, among other things, the laser wavelength, pulse duration, and temperature of the material [53]. The reciprocal of α is recognised as a penetration depth, and, e.g. in the case of metals that are characterised by a large α, the penetration depth is very low, even below 10 nm [54]. This means that practically all of the laser beam energy is absorbed in the surface zone. As it comes to dielectrics, they possess smaller absorption coefficients, and therefore the penetration depth is much larger than in the case of pure metals.

Basically, absorption is related to the excitation of electrons by the electric component of the laser beam. During irradiation, first the laser energy is transformed into electronic excitation energy, and next, through collisions between electrons and lattices, is transferred to the lattices of the material. Nevertheless, the exact mechanism of the absorption depends on the kind of material, i.e. metal, semiconductor, or dielectric. For metals, the dominant mechanism is due to intraband transition related to free electrons in the conduction band. Free electrons
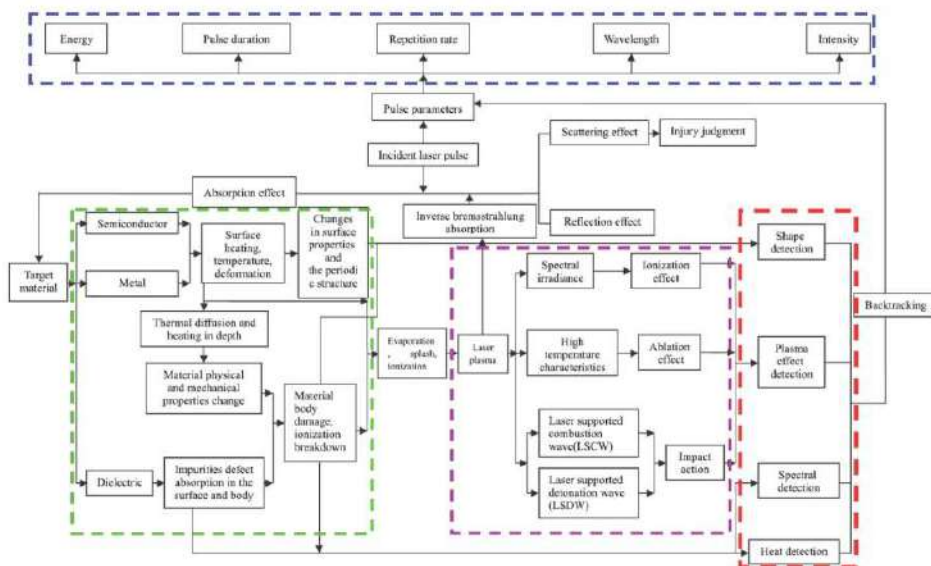

Fig. 2. The effects of laser interaction with materials [52].

3

can move from a low energy level to a higher energy level inside the conduction band. This mechanism can be easily described by the classical Drude model which can be used to estimate the behaviour of an electron gas influenced by an alternating electric field [55]. For dielectrics, the main absorption mechanism is interband transition, meaning that the electrons go from the valence band to conduction one. In such a case, the absorbed energy quanta has an energy at least equal to the value of the energy bandgap. Lastly, for semiconductors, such as, e.g. titania, both mechanisms can occur at the same time [56].

Of course, the absorbed energy can cause a thermodynamic effect in the material structure, as was briefly mentioned above. These changes strongly depend not only on the laser processing parameters, but also on the physical and chemical properties of the material itself. The most important parameters of laser radiation that influence the thermodynamic effect are: intensity, wavelength, temporal and spatial coherence, polarisation, incident angle, and time of interaction. Whereas the absorption coefficient, heat diffusion coefficient, heat capacity, density, and latent heat are regarded as the most important ones in terms of the material properties. Most of these parameters are gathered and shown in Table 1.

The changes that arise in the material due to the absorbed energy can be divided into reactive and nonreactive. Reactive changes, also known as photochemical or photolytic, are associated with chemical reactions [58]. Breaking the chemical bond of a molecule in the material can be considered here as an example. In that case, if the valence electron absorbs a photon of high enough energy, ionisation of the molecule occurs - in other words: the bond is then broken. Nevertheless, this phenomena occurs mainly for materials for which the covalent bond energy is relatively low - e.g. polymers [59], which are not the studied case in this work. Almost all materials undergo reactive changes - the absorbed energy induces thermal effects. In consequence, the final effect strongly depends on the method of energy transfer inside the material. The typically observable visual effects of such changes are melting and vaporisation of the processed material.

The energy transfer due to laser interaction begins with carrier excitation. The energy is absorbed by the electrons of the material and

Table 1
Parameters influencing laser interaction with material based on ref. [57].

Parameters	Variables
Laser radiation parameters	Wavelength
	Working mode (continuous, pulsed)
	Intensity
	Angle of incidence
	Polarisation state
	Beam profile
	Pulse duration
	Energy and peak power
	Repetition rate
	Type of transverse mode
Laser beam focusing parameters	Focal length
	Focal position
	Focus laser beam divergence
	Temporal and spacial coherence
Processing parameters	Processing speed
	Repetition rate of processing
	Spot overlap
	Physical properties (e.g. phase structure, structure, density, thickness, type of material)
	Optical properties (e.g. absorption coefficient, surface reflectivity, bandgap, transmittance)
	Thermal properties (e.g. thermal conductivity, heat capacity, heat of vaporisation)
	Chemical properties (e.g. composition, stoichiometry)
Environmental parameters	Temperature
	Humidity
	Type of gas
	Gas pressure
	Velocity/flow rate

the whole process lasts only about 1 fs. Afterwards, thermalisation occurs, which is the local equalisation of the electrons' energy, and takes place as a result of electron collisions. This part lasts ca. 100 fs [60]. It should be kept in mind that the temperature of the electrons can be then described by the Maxwell-Boltzmann distribution. Next, relaxation of the electron energy is observed as the energy is transferred to ions - here, we are dealing with lattice ion excitation, and as a consequence, phonons arise, playing a role in the energy transfer between the ions [61]. The duration of this process depends on the material type, and, e.g. for nonmetals, is in the range of 1 ps to 1 μs [62]. Following that, equilibrium between the energy of the electrons and ions is established. In the next step, diffusion of energy through the material occurs, mainly via electron and phonon heat transfer [63]. For metals, both electrons and phonons can transfer heat, whereas for nonmetals, transport is dominated by phonons [64]. The timescales of particular processes, and representations of various mechanisms that can take place for semiconductors exposed to a laser beam are shown in Figs. 3 and 4, respectively.

In general, Fourier's law of heat conduction can be used to describe the interaction of a laser with a material; in the case where phase changes are omitted. Although, it should be remembered that this is a simplified approach. The empirical Fourier's law assumes that the cause of heat transfer in a material is the presence of a temperature gradient, and the transfer occurs immediately after the temperature gradient arises. Such reasoning allows us to introduce the concept of the thermal diffusion length, L_d, defined by Ref. [65]:

$$L_d = \sqrt{2Dt} \qquad (2)$$

where D stands for the thermal diffusivity, and t for the pulse duration. The correlation between the thermal diffusion length and the above-mentioned inverse of the absorption coefficient, d, is shown in Fig. 5. The values for semiconductors are highlighted. Moreover, typical processes that take place during laser irradiation are shown as they relate to the pulse duration.

Nevertheless, for the detailed analysis of lasers' interactions with materials, three different time regimes of laser pulse durations are considered, namely: (i) continuous and long pulses, (ii) short pulses, and (iii) ultrashort pulses. The most common way to divide the regimes is as follows: (i) is represented by pulses longer than 1 μs, (ii) by nanosecond and long picosecond pulses, and (iii) by short picosecond and femtosecond pulses [66].

In the first regime, the time of laser interaction with the material is usually much longer than the duration of most processes that occur during this interaction. Therefore, the classical Fourier's law can be applied to describe the heat transfer [67]:

$$\rho c_s \frac{\delta T}{\delta t} = \nabla(\kappa \nabla T) + S(x, y, z, t) \qquad (3)$$

where ρ is material density, c_s – heat capacity, T – temperature, κ – thermal conductivity coefficient, and $S(x, y, z, t)$ – source heat: the laser. In short, the temperature of the material at the point where the interaction occurs depends on the energy fluence and the pulse duration. For constant fluence, the shorter the pulse, the higher the temperature increase. This means that for shorter pulses, the heat "has less time" to diffuse into the material in comparison to longer pulses of the same energy. In this regime of pulse duration, the majority of the absorbed energy is used to heat the material, providing a large heat-affected zone. In consequence, application of this type of irradiation is limited to bulk modification - see Fig. 5.

When it comes to shorter laser pulses, the energy transport into the material is described by a two-temperature model [68]:

$$C_e \frac{\delta T}{\delta t} = -\frac{\delta Q(z)}{\delta z} - \gamma(T_e - T_i) + S \qquad (4)$$
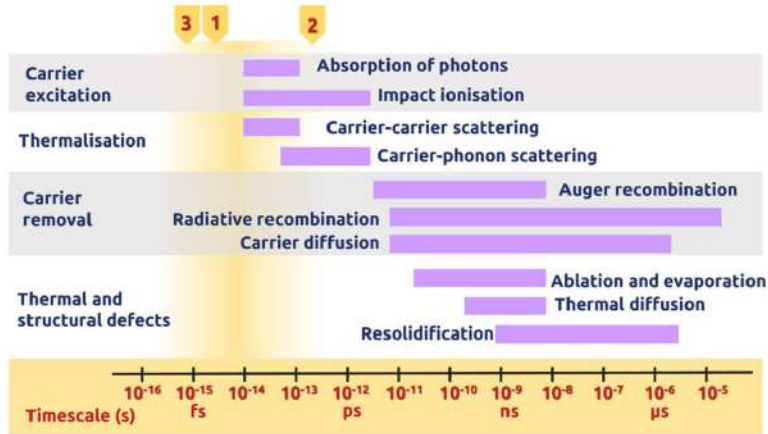
4

Fig. 3. Timescales of laser-material interaction with corresponding processes.
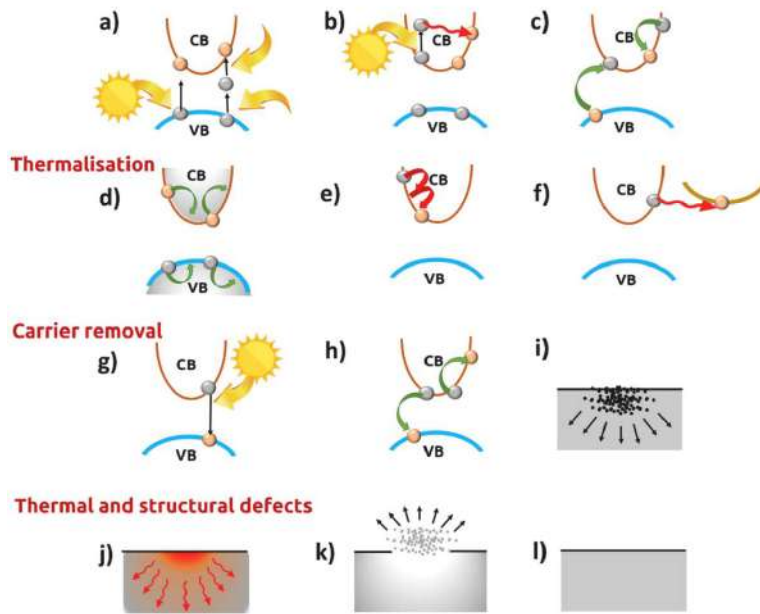

Fig. 4. Various mechanisms of the electron and lattice dynamic for a semiconductor excited with laser irradiation. CB and VB correspond to the conduction and valence bands, respectively. a) represents multi-photon absorption, b) free carrier absorption, c) impact ionisation, d) carrier distribution before scattering, e) carrier-carrier scattering, f) carrier-phonon scattering, g) radiative recombination, h) Auger recombination, i) diffusion of excited carriers, j) thermal diffusion, k) ablation, and l) resolidification or condensation.

$$C_i \frac{\delta T_i}{\delta t} = \gamma (T_e - T_i) \qquad (5)$$

$$Q(z) = -k_e \frac{\delta T_e}{\delta z} \qquad (6)$$

$$S = I(t) A \alpha e^{-\alpha z} \qquad (7)$$

where $Q(z)$ is heat flux, A – surface transmissivity, $I(t)$ – laser intensity, z – direction perpendicular to the material surface, C_e and C_i – heat capacities of the electron and lattice subsystems, respectively, γ – parameter that characterises the electron-lattice coupling, T_e – electron temperature, T_i – lattice temperature, and k_e – electron thermal conductivity. Moreover, femto-, pico- and nanosecond time regimes are related to the following parameters: electron cooling time ($\tau_e = C_e/\gamma$), lattice heating time ($\tau_i = C_i/\gamma$, $\tau_e \ll \tau_i$), and duration of a single laser pulse.

In the case of nanosecond lasers, when $t \gg \tau_i$, the electron and lattice temperatures are equal. Also, the pulse duration is much longer than most of the phenomena happening during the light-matter interaction-like for continuous and long pulses. This means that a relatively large amount of energy is used to heat the material, and the affected-heat zone is still quite large. Nevertheless, such lasers can be used for surface
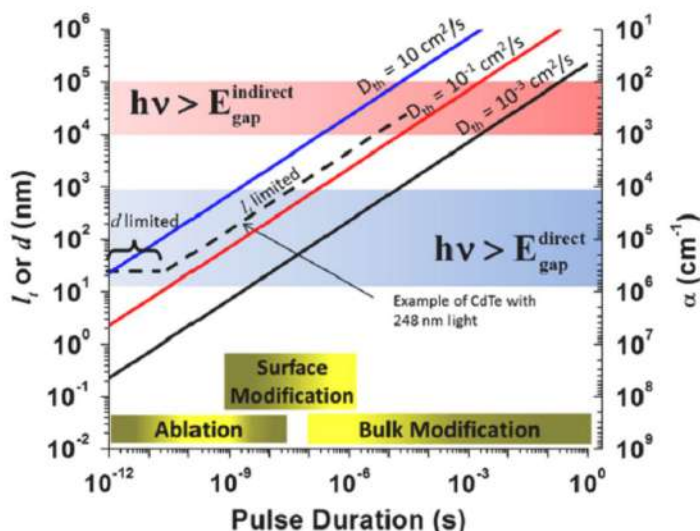
5

Fig. 5. Correlation between thermal diffusivity, penetration depth, absorption coefficient, and laser pulse duration. Reprinted with permission from Ref. [65].

modification, and with a high enough energy, ablation of the material. For $\tau_e \ll t \ll \tau_i$ and $t \ll \tau_e$, picosecond and femtosecond regimes, respectively, are distinguished. For a picosecond pulse duration, the electron-phonon energy-transfer time is longer than t, meaning that the electrons and lattice have different temperatures, and as a consequence, they will be in a state of non-thermal equilibrium [69]. Finally, the ablation of the irradiated material is the process induced by the laser beam. In the case of the interaction of an ultrashort laser pulse with the material, the electron energy, defined by T_e, increases very quickly, while the energy of the ions, given by T_i, increases much slower. Therefore, like for short pulses, there is no thermodynamic equilibrium of the electron-lattice system in the material. Overall, the diffusion heat depth is much smaller in comparison to that of longer pulses, meaning that this kind of irradiation can be used particularly for the ablation of material, like in the case of picosecond lasers.

Of course, as was listed in Table 1, parameters like the optical, and thermal properties, as well as, e.g. the processing environment, should also be taken into account when considering the selection of the appropriate laser parameters, as they highly influence the laser-material interaction and the final effect. Nevertheless, in this part of the work, we gave only the brief state-of-art as it is not the focus of this work. A thorough background on this matter can be found in many publications [70–72]. However, to show the variety of possibilities, we listed the commonly used lasers with their most important working parameters in Table 2.

Table 2
Examples of most frequently used lasers.

Laser type	Gain medium	Wavelength	Pulse duration regime
solid state	Nd-YAG	266–1064 nm	nanosecond
	Nd:YVO$_4$	266–1064 nm	nanosecond
	Ti:sapphire	800 nm	femtosecond
fibre	Yb doped fibre	1030 nm	femtosecond
excimer	ArF	193 nm	nanosecond
	KrF	248 nm	nanosecond
gas	CuBr	511 nm	nanosecond
	CO$_2$	10.64 um	continuous
disc	Yb:YAG	1030 nm	nanosecond

3. Surface modification and patterning via laser irradiation

Using pulsed or continuous laser radiation as a means to modify surface features of titania is by itself a very interesting topic. On the one hand, it is an incredibly fast process which can be scaled up almost indefinitely and applied towards any kind of surface. On the other side, the feature size created by the focused laser beam is heavily restricted by the heat distribution (influenced by the pulse duration) as well as the diffraction-limited spot size. The minimum diameter to which the laser beam can be focused is $d = 1.22\lambda/NA$, where d is the minimal diameter of the beam, λ is the wavelength used, and NA is the numerical aperture of the lens.

Considering that TiO$_2$ is the most often used as a photoactive material in the solar spectrum, the feature size of the patterned surface should be at a sub-wavelength scale, in the order of nanometres. This, however, rules out the feasibility of using a focused laser beam as a patterning method due to the large, diffraction-limited spot size of the focused beam. Therefore, more often, E-beam lithography [73,74], photolitography [75–80], direct imprint [81–83], templating [84], or chemical methods [85–89] are used to obtain nanostructured titania. There are, however, a few works devoted to the microstructuring of titania using both continuous and pulsed lasers, see Table 3.

3.1. Continuous laser

Continuous lasers provide an uninterrupted stream of energy to the modified surface. With the incorporation of XY movement during irradiation, they can be used to seamlessly modify any shape on the surface. Because of the heat dissipation in the material, the effective modification size can be much larger than the laser spot size. Therefore, continuous lasers can provide a very homogeneously modified material, but at the cost of the bigger minimal feature size.

Crespo-Monteiro et al. [90] investigated 250 nm thick, amorphous, and mesoporous TiO$_2$ films before and after irradiation with visible (488 nm) and UV (244 nm) continuous radiation. The group reports that the processing threshold is located at as low as 3 ± 1 kW/cm^2, and the overall layer thickness decreases with the increased laser energy. At 97 kW/cm^2, the layer is 150 nm thinner due to layer densification, and

6

Table 3
The set of lasers (depending on pulse length and wavelength) applied for titania processing.

Laser type regarding pulse length	Wavelength	Titania phase	Ref
Continuous	244 nm	Amorphous	[90]
	488 nm		
	10.6 µm	Degussa P25	[91]
Nanosecond	248 nm	Amorphous	[92–94]
	355 nm	Degussa P25, Ti-nanoxide T/SP, Ti-nanoxide R/SP	[95]
	532 nm	Degussa P25, Anatase powder, Rutile powder	[96]
	248 nm	TiO_2NTs - amorphous	[97]
	248 nm	TiO_2NTs - anatase	[98]
	355 nm	TiO_2NTs - anatase	[99]
Femtosecond	800 nm	Glass - $Ba_2TiSi_2O_8$	[100]
	780 nm	$Ti(OBu^n)_4$, with benzylacetone and methanol	[40]

colour-switching is observed, as the primarily transparent film becomes yellow. At 129 kW/cm^2, the homogenously yellow path becomes more heterogeneous with visible holes, indicating partial remelting of the titania layer. A further increase in lasing power, up to 242 kW/cm^2, results in complete ablation of the layer, and no trace of titania in either form can be detected (see Fig. 6). A visible-wavelength laser, however, did not induce any changes in the pure titania layer.

Wu et al. [91] investigated the densification of standard Degussa P25 titania powder in the field of photocatalytic reactions, containing anatase and rutile phases in a ratio of about 3:1. The process was performed using 10.6 µm continuous radiation within a power density of 3.57 and 4.08 W/mm^2. The findings show that the grain size of the nanoparticles is directly correlated with the lasing power, as their size increased along with higher investigated beam energies. Moreover, the laser-modified surface was reported to be denser than the respective furnace-calcined reference samples, indicating the feasibility of laser-densification of titania films.

3.2. Nanosecond laser

The pulse characteristics of nanosecond lasers mean that the effective power that reaches the modified surface is orders of magnitude higher than in the case of continuous lasers. The short pulse duration and relatively low pulse frequency, however, mean that the material's surface can often reach a steady-state between pulses. Therefore, nanosecond lasers are characterised by high precision, and the modification is often considered as a function of the number of pulses applied.

Van Overschelde et al. [92] investigated patterning thin TiO_2 films via selective, diffraction-induced ablation. By the very simple use of a razor blade, on which the diffraction occurs, a 1D pattern can be clearly seen on the irradiated surface. Although the modified shape begins to show only when a fluence of 1.25 J/cm^2 is used, an interesting phenomenon is observed at lower fluencies, as the thickness of the measured layer increases up to this point. At higher fluencies, ablation occurs. The amount of ablated material scales linearly with the applied fluence, up to a point (1.5 J/cm^2) where the irradiated layer detaches from the substrate, which aligns with their previous work [93]. Furthermore, findings of Overschelde et al. [94] show the effects of a single laser pulse on the surface grain structure. They describe the titania prior to the irradiation as a smooth, wavy surface, with grains of approximately 2 nm. Upon laser treatment with low fluence (1–1.2 J/cm^2), the grains become slightly textured, losing some of their initial height. As the fluence rises above 1.2 J/cm^2, the grains are effectively erased, and a flat, but rough surface is left.

The impact of nanosecond laser irradiation on nanoparticulate matter was studied by Kim et al. [95]. The investigators compared the performance of titania pastes (TiP – Ti-nanoxide T/SP and Ti-nanoxide R/SP from Solaronix, as well as a homemade paste made from Degussa P25) placed onto transparent conducting oxide (TCO), working as a mesoporous electrode in dye-sensitised solar cells (DSSCs) pre- and post-laser treatment. As a transparent conductive oxide fluorine tin oxide (FTO) is applied. A 355 nm laser beam was used, which is heavily absorbed by the titania but passes easily through the TCO. Therefore, the irradiation was directed through the TCO directly onto the TCO-TiP interface. In all investigated cases, laser-treatment of the interfacial region boosted the performance of the DSSCs considerably (35–65%), regardless of the used paste material. Although high-porosity of a material is usually associated with better photoactivity, it is not desirable at the electrode interface, where no charge-generation, but charge-transport at the material/current collector occurs. Laser-induced welding of the nanoparticles allows a selective melting only within the TCO-TiP interface, while preserving the porosity in the charge-generating layer on the other side of the TiP, as schematically presented in Fig. 7.

Filice el al. [96], on the other hand, investigated the effects of laser-processed TiO_2 on photocatalytic water splitting. Interestingly, the
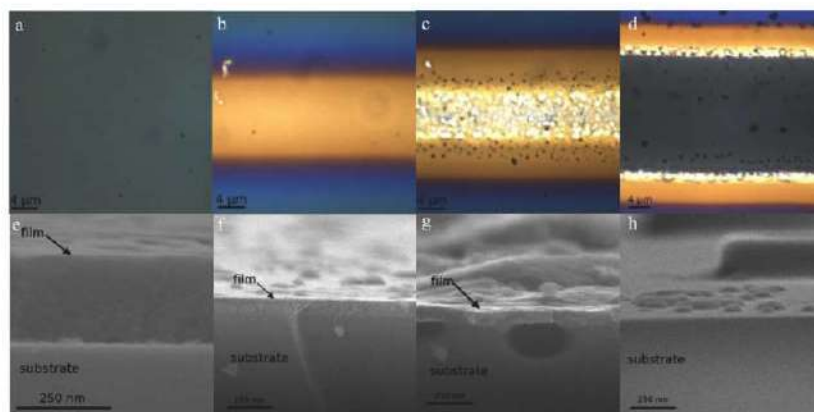
Fig. 6. Optical (ad) and SEM (eh) images of a mesoporous titania film before (a, e), and after irradiation with 244 nm laser at 97 (b, f), 129 (c, g), and 242 kW/cm^2 (d, h) [90].
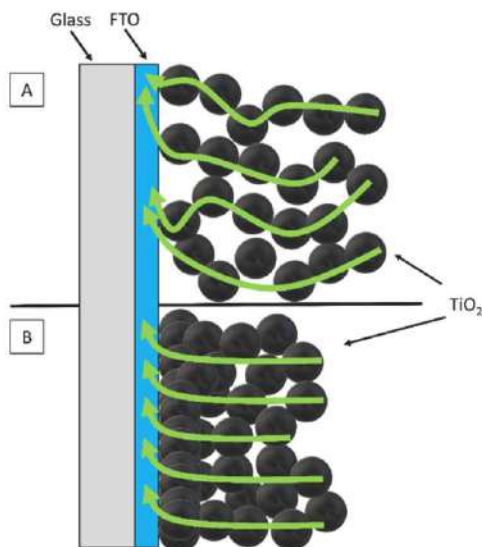
7

Fig. 7. Schematic representation of the adhesion of the TiP on the FTO (acting here as TCO) pre (a) and post (b) laser treatment.

authors chose a 532 nm laser with a photon energy well below the titania bandgap. Nonetheless, after 30 min of irradiation with 0.5 J/cm^2 at 10 Hz, the originally polyhedral nanoparticles became perfectly spherical, and increased the number of oxygen vacancies present. Most importantly, the hydrogen production tripled in comparison to non-irradiated reference samples (Fig. 8).

An interesting approach towards patterning titania was performed by Hsu et al. [97]. Instead of patterning thin layers or TiO$_2$ powders, the investigators focused on the patterning of the titania nanotube arrays. Because the approach relies on a pre-patterned surface (the nanotubes), the beam does not have to be focused in order to achieve a sub-wavelength feature size - it is controlled by the original morphology of the nanotubes. Hsu et al. found that irradiation of the amorphous nanotubes led to the partial remelting of the upper parts of the NTs into flower-like structures, leaving the tubular structures underneath intact.

Xu et al. [98] focused on the patterning of already crystalline, anatase TiO$_2$NTs. At 0.3 J/cm^2 and with only five laser impulses, the investigators managed to form a porous structure on top of the TiO$_2$NTs. Additionally, by increasing the number of pulses, the topography of the surface could be adjusted. With each additional pulse, the topmost layer was gradually aggregating into bumps, revealing pristine nanotubes

between them at 40 pulses (Fig. 9A–C).

A continued investigation by Wawrzyniak et al. [99] into laser-modified titania nanotubes revealed that via laser-modification of the NTs at an angle, the pores can be directionally-arranged, which could improve the light-harvesting capabilities for irradiation at a set angle. Moreover, irradiation at 30° resulted in the formation of necks just below the melted parts of the nanotubes (Fig. 9D–F).

3.3. Femtosecond laser

The ultra-short pulse duration of femtosecond lasers opens up a very interesting path towards materials modification. For example, it allows for a local heat accumulation and refractive index change, without causing destructive damages, such as microcracks [101].

For example, Liu et al. [100] used this to a great extent, forming 2D TiO$_2$ micropatterns within a titania-containing glassy material. Similarly, Passinger et al. [40] managed to pattern complex 3D structures of titania from TiO$_2$ resist (see Fig. 10). Owing to the controlled laser-induced bond-breaking within the focal point, the irradiated regions could not be dissolved by organic solvents. The authors demonstrated the feasibility of femtosecond laser patterning by creating complex three-dimensional meshes, but believe that any other computer-programmed shape could be made with this technique. Moreover, the authors presented a feature size well below the diffraction limit. They claim to have done this by controlling the pulse energy and the number of applied pulses per area. Although the presented feature size is still too great for the patterning for photoactive devices, it can be used as a scaffolding for a variety of other applications.

4. Ablation-induced TiO$_2$ deposition

4.1. Deposition of titania layers

In this section, we consider a laser beam interacting with a titania target when the ablation threshold is exceeded. Typically, this process is applied toward the formation of thin layers of titanium dioxide onto a substrate situated in the near vicinity of the target. The setup used for such a kind of experiment is depicted in Fig. 11.

Ardakani et al. [103] performed an investigation of the phase composition of ablated titanium oxide layers. In their experiment, as the partial oxygen pressure dropped in favour of hydrogen, the number of oxygen vacancies increased. While depositing on Si (100) heated to 400 °C, the predominant phase in the oxygen-deficient conditions was a Ti$_5$O$_9$, although some amorphous content was detected as well. On the other hand, when the deposition was performed on glass, only the amorphous phase could be found. In all cases, however, the elevated temperature of the substrate (550 °C) promoted the formation of crystalline Ti$_3$O$_5$. During the optical analysis of the ablated material, the authors noted a significantly increased extinction coefficient, which may be related to the increased surface roughness, volume imperfections,
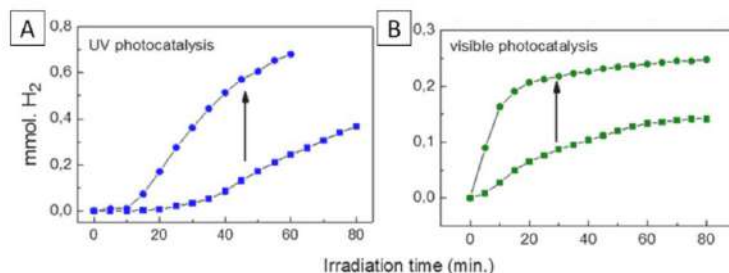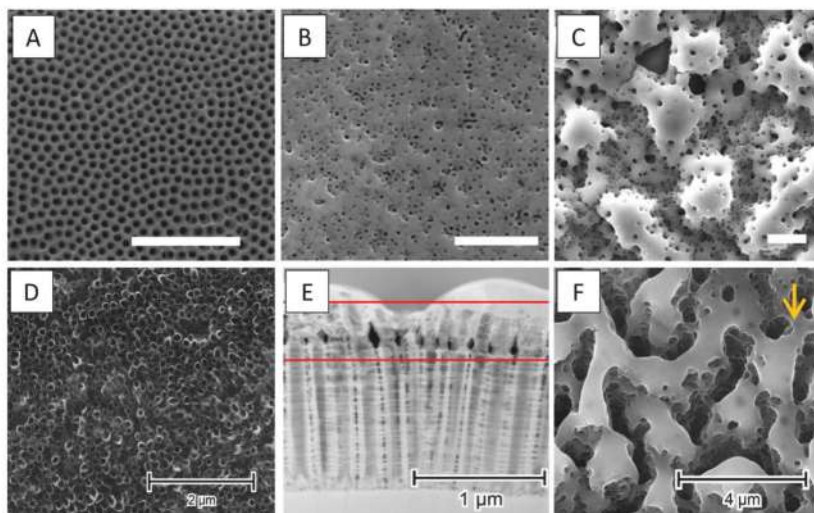

Fig. 8. Comparison of the hydrogen evolution reaction pre- and. post-laser treatment of titania nanocolloids, with permission [96].

Fig. 9. Images of the structures obtained by Xu [98] (a–c) and Wawrzyniak [99] (d–f).
The unmodified NTs (a, c), NTs modified with 300 mJ/cm^2 and 5 (B) and 40 (C) impulses per area, and TEM (E) and SEM (F) images obtained after irradiating nanotube arrays with 75 mJ/cm^2 at 30°.
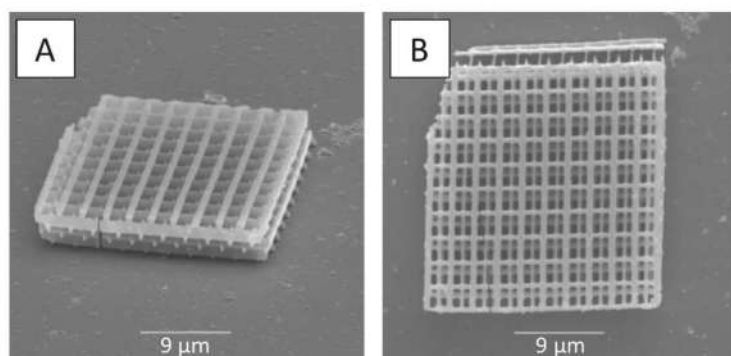
Fig. 10. Three-dimensional mesh created by femtosecond laser irradiation of TiO$_2$-based resist [40].

and deviations from stoichiometry. Additionally, 17 orders of magnitude higher conductivity of the ablated titania layer was reported, compared to bulk TiO$_2$.

Under very similar experimental conditions, Wang et al. [102] agrees that ablation of titania without access to an oxygen-rich atmosphere can only yield amorphous films. While at 1 mTorr of oxygen pressure, mostly the rutile phase is present, it gives in to anatase closer to 30 mTorr. Although only lower crystallinity is reported up to 60 mTorr due to the short mean-free path of oxygen, the decomposition rate of methylene blue accelerates throughout the whole investigated region. Moreover, the visible grain size and surface roughness decreased noticeably with more oxygen present during the process (see Fig. 12).

Several other investigators [104–107] report similar findings on the effects of temperature and oxygen partial pressure, and the growth of ablation-induced titania layers (see Table 4).

4.2. Nanoparticle synthesis through laser ablation

Synthesis of the titania nanoparticles through laser ablation can often be done using an experimental setup very similar to the one depicted in Fig. 11. Instead of a heated substrate, however, a particle collector is used, accompanied by a set gas flow, directing the movement of the NPs through a heated tube after ablation. Such a setup was utilised by Hirasawa et al. [108], who ablated a rutile target to obtain titania nanoparticles as small as 4 nm. The size of the NPs was also controlled by the temperature of the tube through which the particles were directed via the set gas flow.

TiO$_2$ nanoparticles can also be synthesised through a process called pulsed laser ablation in liquid (PLAL). In general, it has some significant advantages in comparison to producing NPs through chemical synthesis, such as speed, simplicity, and environmental friendliness. A model example of this technique was presented by Abdul-Hassan et al. [110],
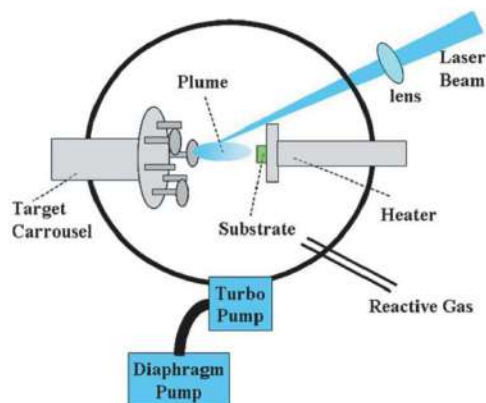
9

Fig. 11. Commonly used setup for depositing thin layers via ablation [102].

who ablated a clean TiO$_2$ plate immersed in distilled water, creating nanometre-sized nanoparticles, though a wide size distribution was observed.

Interestingly, laser radiation can also be used to modify particles in titania solutions. Zuñiga-Ibarra et al. [109] demonstrated how black-TiO$_2$ with increased visible-light absorption can be obtained via laser irradiation of white titania powder in water. After 45 min of irradiation, the white, polyhedral nanoparticles formed bigger micrometre-sized particles with rough surfaces and cracks. During prolonged modification, the agglomerates become bigger, and their surfaced exhibited less resemblance to the original morphology (Fig. 13).

5. Laser induced phase transformation

There are three crystalline phases of TiO$_2$: anatase, rutile, and brookite. The rutile phase is the most thermodynamically stable, while the anatase and brookite are metastable. They differ in their physical

properties, which are briefly summarised in Table 5 [111]. Among them, anatase is distinguished by the highest photocatalytic activity. According to Zhang et al. [112], this is related to the indirect band of anatase which extends the lifetime of photogenerated electron-hole pairs as compared to the other phases (rutile and brookite belong to the direct band gap). Additionally, anatase exhibits the lowest density, which means faster migration of the excitons from the bulk to the surface, thus reducing the recombination rate. It is also worth noting that the combination of anatase and rutile, which forms a hetero-phase junction, exhibits enhanced photoelectrochemical performance in comparison to pure anatase or rutile [113].

Traditionally, the phase transformation of TiO$_2$ from amorphous to crystalline is performed in a furnace via thermal annealing at elevated temperature. According to the literature, to ensure complete crystallisation to anatase, a temperature of 450 °C should be applied for ca. 2 h, whereas anatase to rutile transformation requires 750–800 °C [114]. However, there are several issues concerning this method. First, the process is associated with high energy loses, since widely utilised resistance furnaces work on the principle of electric resistance heating. Moreover, the sample dimensions are considerably smaller in comparison to the heating zone. Second, during the process, the whole volume of the sample is being heated. This could be a problem in the case of sandwich material synthesis. For instance, furnace crystallisation of a TiO$_2$ film deposited onto flexible material, usually made of plastic, would cause degradation of the thermally sensitive substrate. The high temperature can also cause mismatching between the subsequent layers through thermal expansion [70]. Third, taking into account the heating and cooling times, the whole process can take over 10 h. In the literature, one can find several alternative time- and energy-reducing methods, including water-vapour treatment [115], water immersion

Table 4
Set of reports where the laser-titania interaction ensures the ablation process.

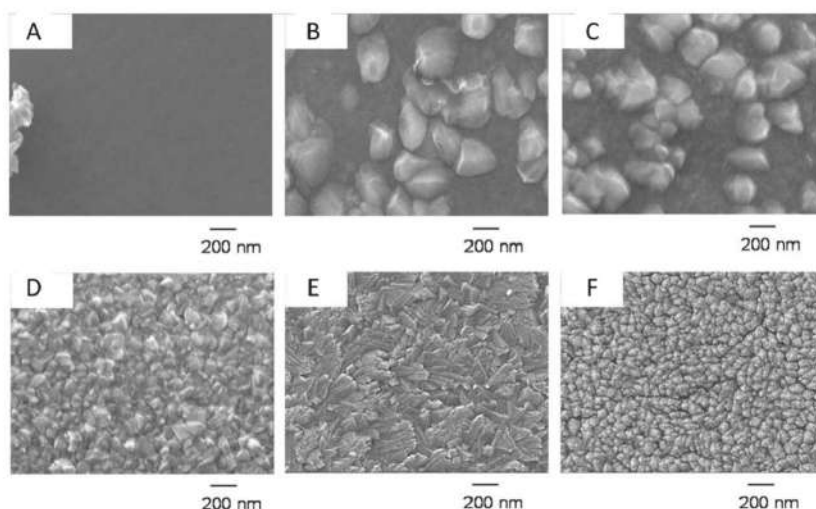| Laser type	Wavelength	Product	Reference
Nanosecond	248 nm	Film	[102–106]
	532 nm		[107]
	532 nm	Nanoparticles	[108,109]
	1064 nm		[110]

Fig. 12. Images of ablated TiO$_2$ film grown on Si (100) in no oxygen (a), and 1 (b), 5(c), 15 (d), 30 (e) and 60 (f) mTorr of oxygen partial pressure [102].

10

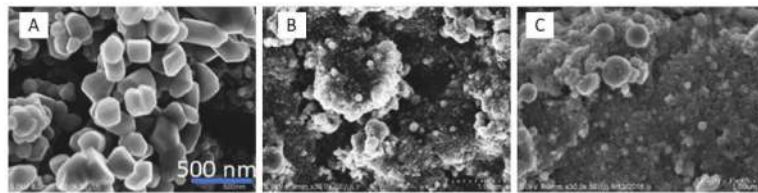**Fig. 13.** White, unmodified titania nanoparticles (A), particles after 45 (B), and 60 (C) minutes of irradiation [109].

Table 5

Typical physical properties of different TiO_2 polymorphs [111].

Crystal structure	Anatase	Rutile	Brookite
Crystal system	Tetragonal	Tetragonal	Orthorhombic
Lattice constant (Å)	a = 3.79	a = 4.59	a = 9.17
	b = 9.51	b = 2.96	b = 5.46
			c = 5.14
Density (g cm^{-3})	3.79	4.13	3.99
Mohr's hardness	5.5–6.0	6.0–6.5	5.5–6.0
Refractive index	2.561,	2.605–2.616,	2.583, 2.700
	2.488	2.890–2.903	
Band gap (eV)	3.2 ± 0.1	3.0 ± 0.1	3.4 ± 0.1
Light absorption (nm)	<390	<415	–
Bulk conductivity (S cm^{-1})	5×10^{-8}	10^{-2}-10^{-7}	3×10^{-7}

[116,117], and flame annealing [118]. However, the methods listed above are also limited to the whole sample, and not a particular area of the material. Therefore, one can see the advantages of laser annealing. An enormous number of the processing parameters can be manipulated during the process (see Table 6), which enables phase transformation not only within a selected surface area and depth, but in a time- and energy-saving way.

Depending on the irradiation time, different processes within the material occur (see Fig. 3) [119]. Thermal and structural effects take place at the nanosecond timescale. The literature review devoted to the laser-induced phase transformations of TiO_2 presented below has been divided into two groups: continuous and pulsed lasers - see Fig. 14. The section where the use of pulsed laser is characterised is split into nano-, pico- and femtosecond subdivisions since they should accordingly limit the thermal and structural effects. Limited heat exchange between the laser spot and their nearest neighbourhood allows modification of a precisely selected area, leaving the surface at a distance and/or some

Table 6

Processing parameters utilised for pulsed laser phase transformation of TiO_2.

| Pulse duration	Frequency	Laser type	λ [nm]	Fluence [mJ cm^{-2}]/ *Energy	Atmosphere	TiO$_2$ architecture	Phase transformation	Ref
25 ns	not specified	KrF	248	100	air	magnetron sputtered thin film	amorphous to anatase	[129]
13–20 ns	10 Hz	KrF	248	65–95	air	loaded sol-gel thin film	amorphous to anatase/rutile	[130]
5 ns	2 Hz	Nd:YAG	355	25	air/vac	anodised nanotubes	amorphous to anatase	[99, 131]
25 ns	10 Hz	KrF	248	≤400	air	anodised nanotubes	amorphous to anatase	[97]
10 ns	10 Hz	KrF	248	110–200	air	pulsed laser deposited TiO$_2$/WO$_3$/glass	amorphous to anatase	[145]
6 ns	2 Hz	Nd:YAG	266, 355	30–60	air	anodised nanotubes	amorphous to anatase	[133]
26 ns	10 Hz	KrF	248	20–80	air	spin-coated titanium organic precursor	amorphous to rutile	[134]
25 ns	50 kHz	diode-pumped	355	1113	air	spin-coated titanium organic precursor	amorphous to crystalline (not specified)	[135]
5 ns	10 Hz	Nd:YAG	532	500	air	aqueous TiO$_2$ nanopowder suspension	amorphisation	[96]
25	not specified	KrF	248	150–1000	DI water	anodised nanotubes	amorphisation	[98]
5 ns	2 Hz	Nd:YAG	355	25	vac	anodised nanotubes	amorphisation	[136]
26	50 Hz	KrF	248	50–170	air/low vac	spin coated titanium organic precursor	amorphisation	[137]
10 ns	10 Hz	Nd:YAG	532	65	DI water	aqueous TiO$_2$ nanopowder suspension	amorphisation	[109]
40 ns	85 kHz	diode-pumped	355	65	DI water	aqueous TiO$_2$ nanopowder suspension	amorphisation	[139]
10 ps	100 kHz	Nd:YAG	532	30	DI water	aqueous TiO$_2$ nanopowder suspension	amorphisation	[139]
6.2 ps	50–100 kHz	not specified	343	0.5–4	air	sol-gel TiO$_2$ dip coated onto microscopic glass	amorphous to anatase	[140]
2 ps	89 kHz	diode-pumped	257.5	1	not specified	TiO$_2$ NTs	amorphous to anatase	[141]
120 fs	250 kHz	Ti:sapphire	800	477	air	TiO$_2$ single crystal	rutile to anatase	[142, 143]
280 fs	2000 kHz	not specified	1030	100–200	air	TiO$_2$ thin film	amorphous to rutile	[144]
100 fs	5 kHz	not specified	800	400	air	TiO$_2$ thin film	amorphous to rutile	[144]
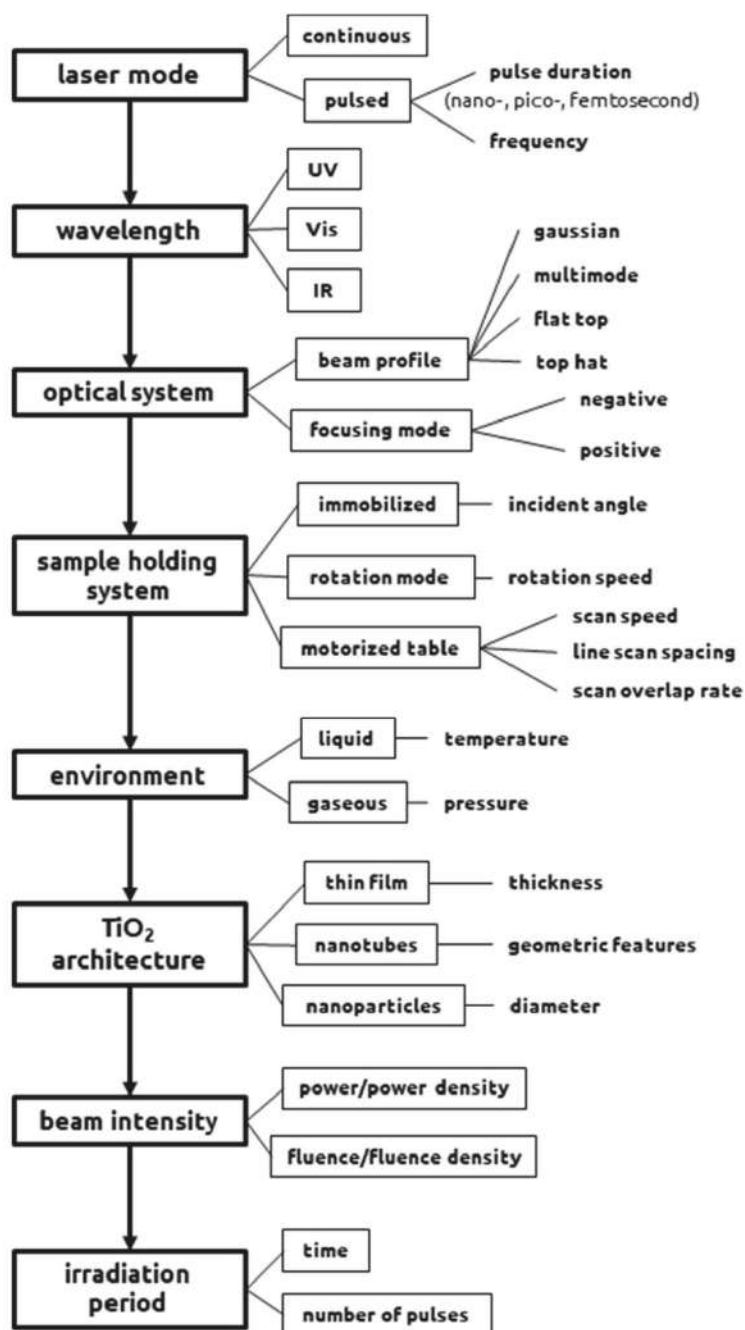
Fig. 14. Features affecting laser-material phase transformation.

12

— 71 —

deeply located layers intact. This is a key advantage of laser induced phase transformations over traditional furnace annealing.

5.1. Continuous lasers

In 2008, Likodimos et al. [120] reported for the very first time the local structural transformation of amorphous TiO_2 nanotubes to the anatase phase under laser radiation from a Raman spectrometer (Ar^+ ion laser, 514.5 nm). It was simply achieved by exposing the sample to a green laser beam with a power of 6 mW μm^{-2} for only 1 s. According to the Stokes and anti-Stokes Raman spectra, during the irradiation, the temperature of the nanotubes reached 650–700 °C. A Raman spectrum obtained from the same spot revealed well distinguished signals corresponding to the active anatase modes. However, contrary to a thermally annealed sample, a broad shoulder at ~1400 cm^{-1} and a graphitic G band at 1592 cm^{-1} were observed (see Fig. 15 a) as well. These were assigned to some organic residuals originating from the ethylene glycol-based electrolyte used during the manufacturing process. It was assumed that the carbon-containing matrix did not burn up completely during the laser annealing but rather evolved into hydrogenated carbonaceous species. Nevertheless, the above-discussed work proved the possibility of TiO_2 crystallisation by means of laser radiation in a shorter time comparing to furnace annealing. However, there are some additional aspects, including the organic residuals, that should be taken into account during laser treatment. Another widely used synthesis method of titania is sol-gel. Chung et al. [121] investigated the impact of sol-gel film composition and laser energy on the light-induced crystallisation process (CO_2 laser, 10.6 μm). They demonstrated that an increased concentration of the titania precursor along with a low laser power (0.5 W) favours transformation towards the anatase phase. In turn, both a higher laser power (established at 1.5 and 3.0 W) and an amount of distilled water along with a lower alcohol content in the mixture results in the rutile formation. According to the ANSYS calculations, the temperature in the illuminated material reaches locally 325 °C and 1839 °C for 0.5 W and 3.0 W, respectively.

During irradiation with a continuous beam, heat transfer from the irradiated area towards the surroundings plays a significant role. It is a key difference regarding pulsed laser treatment, in which the material is allowed to relax between the subsequent pulses (including cooling down in the case of a photothermal process). Enachi et al. [122] investigated the structural properties of TiO_2 nanotubes in the heat-affected zone around the laser spot (diode-pumped solid-state laser, 532 nm). A sample exposed to a 460 mW beam was melted and recrystallised in the central part of the spot, also causing degradation of the well-organised tubular structure. The Raman spectra collected from several points starting from the region (see Fig. 15 b and c) where the laser beam was focused towards the surroundings areas revealed rutile structure formation within the melted area (point 1). At some distance from that point, pure anatase (Fig. 15 b, point 4) was reached, while the morphology was preserved. It was concluded that the area affected by the treatment depends on the laser beam intensity, and the heat transport of the material. The same phenomenon was observed by Parussulo et al. [123].

In the cases discussed above, visible laser radiation was utilised. Taking into account the quite wide bandgap value of TiO_2, the material should be nearly transparent to this wavelength. To explain this phenomenon, Ricci et al. [124] proposed the mechanisms responsible for visible light absorption of a layer composed of anatase nanoparticles in the air and in a vacuum (see Fig. 15 d). Oxygen vacancies were proposed to be responsible for the absorption, since they provide an intra-band state located slightly above the valence band (VB) (black line in Fig. 15 e). Indeed, according to the work of Serpone [125], the loss of an O atom leaves behind an electron or electrons trapped in the cavity. Depending on the number of electrons in the vacancy, different F colour centres (F, F^+ or F^{++}) are formed in the TiO_2 giving rise to the additional states located above the VB. On the other hand, there are also electrons
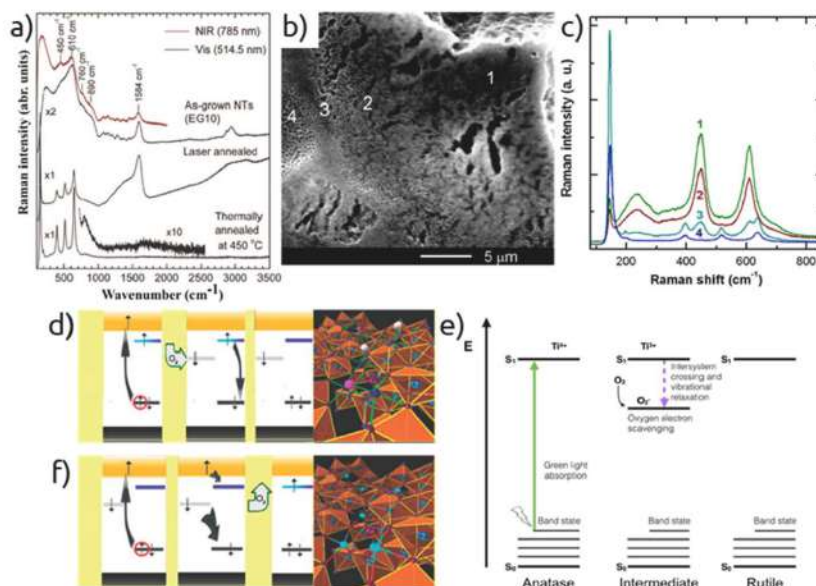

Fig. 15. a) Raman spectra of as-grown, thermally and laser annealed TiO_2 NTs [120], (b, c) SEM image and Raman spectra of the laser spot and the heat affected zone of the TiO_2 NTs after the laser irradiation; particular spectra correspond to the marked points on the SEM image [122], (d–f) schemes of energy levels illustrating electronic transitions in anatase TiO_2 under visible laser irradiation in different oxidising atmospheres: (d, f) in air by Ricci et al. and (e) Benavides et al. [126], respectively, (f) under vacuum conditions.

13

trapped in other defects localised in the surface region. They are described as Ti^{3+} states located below the CB (cyan line in Fig. 15 d). Starting from the scenario where an electron-hole pair is trapped in the F colour centre and one electron is in the Ti^{3+} surface defect, the visible beam radiation can already be absorbed since the radiation energy is equal or greater than the difference between those levels. From now, the absorption mechanism depends on the environment. In an oxygen-rich atmosphere, an O_2 molecule can be adsorbed on the surface, giving rise to an additional O_2 level located slightly below the CB (grey line in Fig. 15 d). Thus, photoexcited electrons that occupy the CB spontaneously pass to the O_2 level since the transition is energetically favourable. Subsequently, electrons from the Ti^{3+} surface defect level recombine with the hole left in the F centre. A similar mechanism was proposed by Benavides et al. [126] (see Fig. 15 e) for anatase films. The exception is that the electrons from the band states (F colour centres from previous description) are excited to the Ti^{4+} states instead of the CB. In a vacuum, the opposite mechanism is considered (see Fig. 15 f) [124]. Here, the initial electronic structure is as follows: O_2^- is adsorbed ($^-$ since the molecule accepted 1 electron) and a Ti^{4+} surface state is available. Visible illumination causes excitation from the F centre to the CB. Photoexcited electrons become trapped in the available Ti^{4+} level, resulting in its reduction to Ti^{3+} (cyan line changes colour to blue in Fig. 15 f). Subsequently, an electron from the O_2 level follows the path of lowest energy and recombines with the hole left in the F centre. The recombination process causes the desorption of the O_2 molecule.

It is worth noting that, in further work, Ricci et al. [127] ascribed the above-described electronic transitions to the increase of surface reactivity leading to the formation of stable chemical bonds between the surfaces (twin boundaries) of neighbouring anatase particles. Those regions were recognised as preferential sites for the nucleation of the rutile phase. Therefore, the process is not thermally driven. The estimated temperature, according to the Stokes and anti-Stokes signals, was about 370 °C, and proves the validity of a photochemical nature of the process.

Another approach describing the impact of oxygen vacancies on laser-induced phase transformation was proposed by Vásquez et al. [128]. They investigated the impact of dopant multivalence on anatase-to-rutile transition in Fe- and Al-doped TiO_2 nanoparticles. It was found that in an Fe-doped sample, Fe^{3+} is partially reduced to Fe^{2+}, providing oxygen vacancies, and hence promoting phase conversion, whereas monovalent Al inhibited the process. It is worth noting that the obtained TEM images indicate the presence of twin boundaries during the rutile formation, which is in good agreement with the observations of Ricci et al.

5.2. Pulsed lasers

5.2.1. Nanosecond lasers

Less than a decade ago, Overschelde et al. [129] reported pulsed laser-(KrF, 248 nm) induced crystallisation of a TiO_2 film deposited onto ITO via magnetron sputtering. They found that the phase transition propagates from the substrate-film towards the film-air interface. Taking that into account, the authors assumed that the mechanical stress is responsible for the changes of phase. A similar approach was reported by Joya and Liu [130] who laser-(KrF, 248 nm, 10 Hz) treated amorphous TiO_2 sol-gel film. TEM results revealed that the crystalline structure propagation depth was 100 nm out of 412 nm. In the work of Haryński et al. [131], grazing-incidence X-ray diffraction (gi-XRD) revealed that the laser irradiation (Nd:YAG, 355 nm, 2 Hz) of as-anodised TiO_2 nanotubes resulted in anatase formation, but this was only detected at 480 nm and below, whereas the surface remained amorphous (see Fig. 15 a). In the SEM images, one can observe that the surface was melted, however the tubular structure beneath was preserved. This is typical for the interaction of pulsed lasers with matter since there is a very short fluence window for heating the surface without melting it [132]. Therefore, it was assumed that the crystallisation in the middle

and bottom parts of the nanotubes was thermally induced as a result of the heat transport from the surface down to the titania NTs' bases. The initial 480 nm depth is the area which directly experiences the impact of the laser radiation. Here, the nanotubes received the radiation energy in a few nanoseconds. Most likely, fast heating and cooling occurred, which facilitated amorphous phase formation. Similar surface damage was observed by Hsu et al. [97] investigating the impact of the radiation angle on the crystallisation of as-anodised TiO_2 nanotubes. They assigned surface degradation to the pulse duration of 25 ns, and observed that the nanotubes' morphology are less damaged by a laser modification (KrF, 248 nm, 10 Hz) in a tilted mode regarding parallel. It is worth noting that the opposite crystallinity distribution along the nanotubes was observed in the results of Haryński et al. [131]. According to the HRTEM images (see Fig. 16 b), it was found that the tops of the nanotubes exhibited the anatase phase, the middle part were mixed anatase/amorphous, whereas the bottom zone was pure amorphous. A previous work of ours, which we refer to here [99], confirms less surface degradation along with the increasing angle between the laser beam (Nd:YAG, 266 nm, 2 Hz) and sample, and only partial crystallisation of the TiO_2 nanotubes being achieved. Moreover, the obtained photoluminescence spectra revealed an increased number of trapped holes in the laser-crystallised sample compared to the material thermally treated in a furnace.

Contrary to traditional calcination, laser annealing offers both superficial and spatial control of the modification. The former can be achieved by using specially designed masks which allow for the selection of a particular surface area. Such an approach was demonstrated by our group [133]. The experimental setup was equipped with a shadow mask with a patterned logo (see Fig. 16 c). Laser treatment (Nd:YAG, 266 and 355 nm, 2 Hz) of TiO_2 nanotubes in the described configuration resulted in the selective crystallisation only within the preferred area, which afterwards was covered by a conducting polymer via electrochemical deposition. The results clearly indicate that, owing to the application masks, laser annealing can be successfully utilised for crystallisation over the preferred sample surface area. In the case of spatial control during the crystallisation of TiO_2, we would like to distinguish two works. Nishigawa et al. [134] investigated the photocatalytic properties (hydrogen evolution) of a Cu_2O photoanode. The problem is that Cu_2O undergoes self-reduction to Cu^0 in water electrolytes, and therefore a stabilisation layer is essential. In this case, TiO_2 was chosen as the protective layer due to its high stability in water electrolytes. However, effective electron transport through the catalyst layer requires phase conversion from amorphous to crystalline. However, traditional furnace annealing, in addition to TiO_2 crystallisation, would reduce the bottom layer from Cu_2O to CuO which is inactive towards photocatalytic water reduction. Therefore, a photoanode consisting of conducting FTO with an electrodeposited Cu_2O layer covered by a spin-coated titania precursor solution was irradiated by laser (KrF, 248 nm, 10 Hz). Regardless of the energy fluence (20–80 mJ cm^2), laser annealing resulted in rutile formation. The underlying Cu_2O layer was reduced to CuO exclusively at higher energy fluences than 40 mJ cm^{-2} after a certain number of pulses (a few thousand). According to the performed temperature simulations after 1 pulse, at the interface between the TiO_2 and Cu_2O, the temperature reached 300, 600, 900, and 1200 °C for 20, 40, 60, and 80 mJ cm^{-2}, respectively. It is worth noting that Cu_2O is reduced to CuO at 300 °C in a furnace. Thus, according to the simulations, even a single pulse was adequate for the reduction. The lack of reduction was ascribed to the short-term temperature stimulation during pulsed laser treatment which was insufficient for CuO formation. Because of this, fabrication of a crystalline $TiO_2/Cu_2O/FTO$ photoanode was achieved.

Similarly, Wilkes et al. [135] employed pulsed laser (solid-state, 355 nm, 50 kHz) annealing to crystallise a TiO_2 layer spin-coated onto indium tin oxide/poly(ethylene naphthalate) (ITO/PEN) since high temperature annealing causes degradation of the polymer substrate. Comparing the current-voltage performance of the thermally and laser
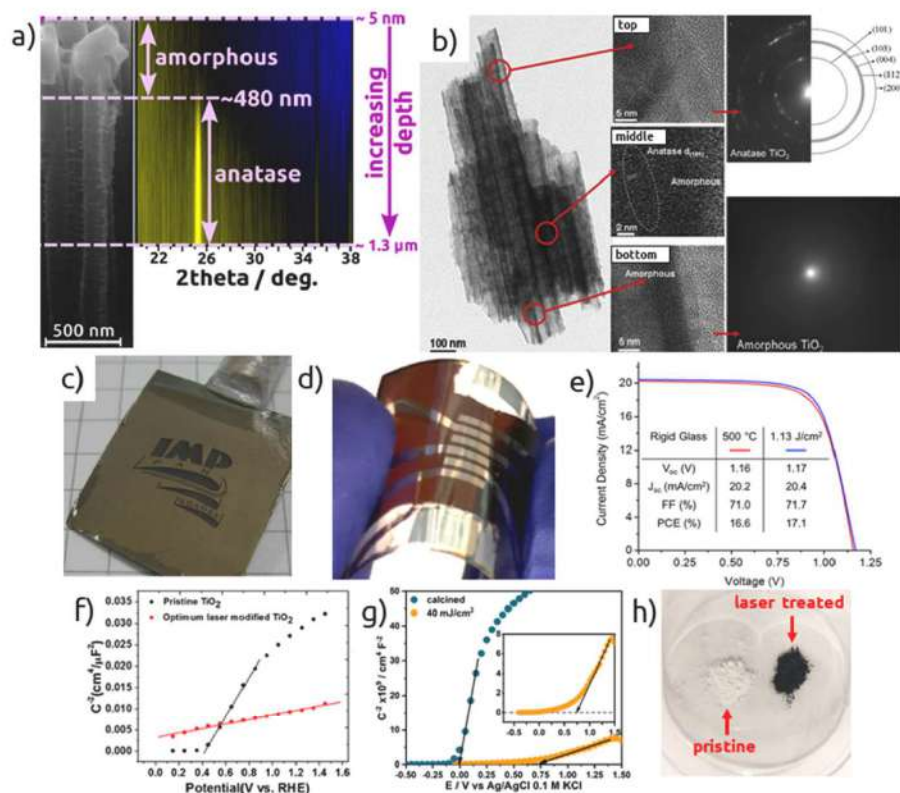
Fig. 16. a) Crystalline structure propagation depth of laser-treated as-anodised TiO$_2$NTs; gi-XRD results are shown with respect to a cross-sectional SEM image [131], (b) TEM images of the particular parts of the amorphous TiO$_2$NTs laser annealed in 85° tilted mode [97], (c) a photo of as-grown TiO$_2$NTs selectively annealed with an IMP PAN logo pattern by 355 nm laser beam and afterwards modified with conducting polymer [133], (d) photo of a flexible perovskite solar cell obtained thanks to laser-induced crystallisation of spin-coated TiO$_2$ onto ITO/PEN, and (e) the corresponding current-voltage curve including reference - thermally annealed device at 500 °C [135], (f, g) Comparison of Mott-Schottky plots for the laser-treated crystalline TiO$_2$ NTs: (f) placed on a Petri dish and filled with 15 mL of DI water [98], and (g) mounted on a motorised table in a vacuum chamber [136], (h) photo of the white and black TiO$_2$ powder [109].

annealed samples, one can observe an increased IPCE by 0.5% reaching a total of 17.1% for the laser-processed device (see Fig. 16 e). Moreover, with the help of the laser treatment, the device was fabricated on a flexible substrate (see Fig. 16 d) which is not possible via elevated temperature annealing.

The above-discussed approaches are particularly focused on the phase transformation from the amorphous to crystalline. However, we would also like to distinguish the opposite phase transition - amorphisation. Filice et al. [96] treated an aqueous suspension of TiO$_2$ nanopowder (20% rutile, 80% anatase) by Nd:YAG laser (532 nm, 10 Hz). The recorded Raman spectra revealed a blue shift of the main phonon band E$_{g(1)}$ corresponding to the anatase mode of the irradiated sample, indicating crystalline structure distortion. The modification allowed for the enhanced hydrogen evolution performance of the laser-treated sample in comparison to an unmodified one. Xu et al. [98] investigated the impact of laser modification (KrF, 248 nm) on anatase TiO$_2$ NTs' photoactivity, defined as the difference between the recorded current density during sample illumination and that exhibited in the dark. For laser modifications, samples were placed in a Petri dish filled with 15 mL of deionised (DI) water. Under optimised processing parameters, the TiO$_2$ NTs showed a 1.6-fold photocurrent density

increment in comparison to unmodified ones. SEM inspection and XRD diffractograms indicated a melted surface and degradation of the crystalline structure, respectively. Analysis of the Mott-Schottky plot (see Fig. 16 f) revealed an increased number of charge carriers of over an order of magnitude while the flat band potential shift towards the cathodic direction compared to the unmodified material. The authors assigned the boosted photoactivity to the laser-induced shallow states located in the CB which give rise to the additional carriers (shallow donors). Based on this approach, Haryński et al. [136] performed laser modification of crystalline TiO$_2$ NTs in a vacuum. Similarly, they observed photocurrent enhancement (by 45%), surface melting, and some degradation of the crystalline structure. A Mott-Schottky analysis revealed an increased carried density (over an order of magnitude) as well as a significantly shifted flat band potential towards the anodic direction (see Fig. 16 g). It was explained that such a change in the energy bands' positions hampered the recombination of the photoexcited charge carriers at the electrode/electrolyte interface due to the favourable band bending (similar to in p-n junctions).

Nanosecond pulsed lasers were also successfully employed for the fabrication of black TiO$_2$. Nakajima et al. [137] observed darkening of a crystalline TiO$_2$ thin film after excimer laser irradiation (KrF, 248 nm,

15

50 Hz) in a low vacuum (500 Pa) followed by thermal annealing at 700 °C for 6 h in the air. The obtained materials exhibited significant absorption in the visible light. The Raman spectra revealed a slight blue shift of the signal at 144 cm^{-1}. Despite this, the XPS spectra revealed no oxygen vacancies, and the authors labelled the received modified material as black titania according to the Raman and absorbance spectra along with the visual changes. A distinct change in the colour of the TiO_2 from white to black (see Fig. 16 h) can be found in the work of Zuñiga-Ibarra et al. [109] where they laser treated (532 nm, 10 Hz) an aqueous suspension of commercial TiO_2 powder (60–80 nm). Herein, the Raman and reflectance spectra indicated significant anatase degradation along with increased visible light absorption. The formation of oxygen vacancies was also confirmed by XPS analysis.

We would like to emphasize the aspects that should be kept in mind during laser treatment in scanning mode which is usually realised with the use of a motorised table as a sample holder, or laser beam positioning systems. Several factors should be carefully considered in this case. Square beam profiles offer higher homogeneity distribution during forward scan compared to round ones, especially for low beam frequencies and high scan rates (see Fig. 17 a). In turn, subsequent line overlapping plays a significant role in the uniform temperature distribution during the modification (see Fig. 17 b). In the case of a Gaussian beam profile, the distance between the adjacent lines should be carefully selected. Mincuzii et al. [138] demonstrated the principle of Gaussian beam overlapping based on the surface temperature distribution within the laser spot. Proper overlap of the adjacent laser scanning lines allowed for a very uniform modification of TiO_2 film. Another important aspect is the correlation between the pulse frequency and scan rate. They should be adjusted in order to modify the entire line without excessive overlapping or unmodified areas. Finally, the pulse energy fluence should dose enough energy for phase transformation, but not enough to damage the material. Therefore, it can be clearly seen that scalable and rapid modifications include multiple processing parameters, which are dependent on one another.

5.2.2. Pico- and femtosecond lasers

At the beginning of this section, we would like to draw attention to the work presented by Lau et al. [139], in which the effect of nano- (diode-pumped solid-state, 355 nm, 85 kHz) and picosecond (Nd:YAG, 532 nm, 100 kHz) laser treatment on TiO_2 nanoparticle suspension is compared. The results indicate that, as the energy dose of a ns laser increased, the anatase-to-rutile ratio along with the formation of surface defects, whereas bulk defects decreased. In turn, ps laser irradiation resulted in the generation of new defects close to pre-existing ones. The number of already present surface and bulk defects increased, then decreased by the diffusion of bulk defects to the surface where laser-induced reactions with surrounding water resulted in defect healing. Belka et al. [140] investigated the impact of picosecond laser

treatment on the structural properties of an amorphous TiO_2 film deposited onto microscopic glass via dip coating. Depending on the processing parameters, they crystallised the film into anatase or rutile. A higher frequency (100 kHz) along with a fluence of 0.3–0.4 mJ cm^{-2} promoted rutile formation. Anatase was formed under milder conditions, namely 66 kHz and 0.1–0.2 mJ cm^{-2}.

Recently, Sopha et al. [141] laser modified amorphous TiO_2 NTs with a picosecond pulsed laser beam (diode pumped thin-disk laser, 257.5 nm, 89 kHz). The use of short pulses with a low fluence and a high repetition rate allowed for the phase transformation of the NTs without melting them, however, the NTs were not fully crystallised, according to HRTEM. The authors assigned the low degree of crystallinity to the 8–10% instability of the beam fluence. However, as previously discussed, the heat generated by absorption of UV radiation is limited to the top of the NTs (ca. 480 nm according to Haryński et al. [131]). Therefore, inhomogeneous crystallinity within the NTs originates from inhomogeneous spatial heat distribution rather than instability of the laser beam energy. Over a decade ago, Ma et al. [142] and Yang et al. [143] demonstrated phase transformation from rutile to anatase by femtosecond laser irradiation. In both works, the authors observed intensification of Raman signals corresponding to the anatase with the increasing number of pulses. The obtained microscope photographs of the laser spots are shown in Fig. 18 a and c. It can be clearly seen that the modification affected not only the spot, but also the outer area. In the work of Ma et al. [142], this was explained by thermal energy diffusion from the focal point (the spot), where the temperature would rise, towards the surroundings. In turn, in the work of Yang et al. [143], the area was recognised as a recrystallised TiO_2 formed during the plasma quenching formed above the spot during irradiation. More recently, Hoppius et al. [144] crystallised amorphous TiO_2 thin film via fs laser treatment. The obtained results suggest that pulse-to-pulse temperature accumulation during fs laser irradiation occurs, and can be manipulated
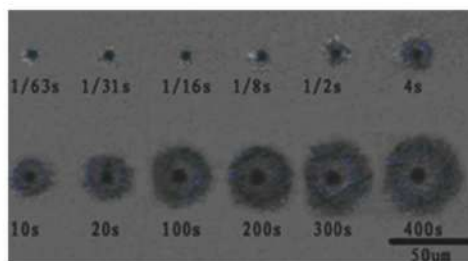

Fig. 18. A photographs of the laser spots obtained from. femtosecond laser treatment of a single TiO_2 crystal [142].
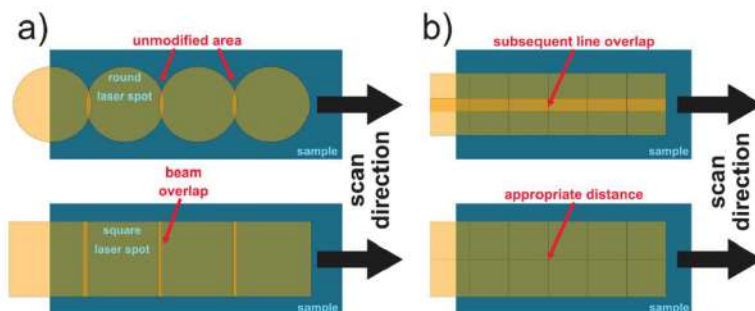

Fig. 17. Sample areas being modified during forward scan for (a) round and square spots, and (b) different line overlapping.

16

only by the laser repetition rate. Moreover, in case of the phase transformation, the temperature should not decrease to the initial value between subsequent pulses.

Taking into account the discussed works, one can conclude that regardless of the pulse duration (ns, ps, or fs), the laser-induced phase transformation is affected by heat accumulation between the subsequent pulses. As Hoppius et al. [144] pointed out, the heat accumulation can be controlled by the repetition rate, number of pulses, laser spot size, and thermal diffusion. The last one concerns different TiO$_2$ architectures, including nanotubes, nanoparticles, or a dense film of course exhibiting different thermal conductivity.

6. Conclusions and perspectives

A major societal challenge is sustainable energy conversion and its storage, which requires materials with a highly developed surface area, plenty of active sites, high activity towards effective water splitting, or a narrow band gap as well as high conductivity if solar power continues as an energy source. Among others, titanium dioxide is considered a promising candidate to play various roles: as a photocatalyst, electrode material, through to one of the main components of cosmetics and paints. Such a wide range of applications results not only from its nontoxicity, chemical inertness, photostability, and also the possibility to perform many different modifications including metal and non-meal doping, surface tailoring, and formation of a heterostructure via combination with other materials. In some cases, it leads only to a slight change in the material, e.g. introduction of some additional hydroxyl groups onto the surface, but is can also result in completely different matrix of properties targeted to a particular application.

These improvements can be achieved using both chemical and physical routes covering sol-gel, hydrothermal, chemical vapour deposition, but especially those requiring low cost substrates, generating a negligible amount of by-products, and exhibiting high application potential are gathering the greatest attention. Therefore, herein, we have focused on laser-assisted modification, which is regarded as a very powerful tool where light can play a crucial role in surface modification, controlling the crystalline phase, and even enabling the formation of thin layers. As has been underlined, an optimised approach covering the selection of the laser wavelength, fluence, repetition rate, and atmosphere affects the final properties of the material. It has been shown how significant changes in this well-known semiconductor can be achieved without any chemicals, further purification steps, or worry regarding waste management. The reports dedicated to the morphological changes and phase transitions induced by laser light have been discussed and compared to the results achieved via traditional thermal annealing in a furnace. Moreover, we have highlighted that laser treatment can be combined with other modification routes, eg. by integration with other metal/metal oxide nanoparticles. Despite laser techniques being well-known in materials engineering, their application towards titania modification is not fully utilised, unfortunately. We believe that the growing interest in interdisciplinary research works will result in positive, synergistic effects where laser treatment will be combined with other, most commonly applied chemical approaches.

Acknowledgements

References

[1] Dréno B, Alexis A, Chuberre B, Marinovich M. Safety of titanium dioxide nanoparticles in cosmetics. J Eur Acad Dermatol Venereol 2019;33:34–46. https://doi.org/10.1111/jdv.15943.

[2] Hassan MM, Dylla H, Mohammad LN, Rupnow T. Methods for the application of titanium dioxide coatings to concrete pavement, vol. 9; 2012.

[3] Akila Y, Muthukumarasamy N, Velauthapillai D. TiO$_2$-based dye-sensitized solar cells. Nanomater. Sol. Cell Appl. 2019:127–44. https://doi.org/10.1016/B978-0-12-813337-8.00005-9. Elsevier.

[4] Song T, Paik U. TiO$_2$ as an active or supplemental material for lithium batteries. J Mater Chem A 2016;4:14–31. https://doi.org/10.1039/C5TA06888F.

[5] Elmouwahidi A, Bailón-García E, Castelo-Quibén J, Pérez-Cadenas AF, Maldonado-Hódar FJ, Carrasco-Marín F. Carbon-TiO$_2$ composites as high-performance supercapacitor electrodes: synergistic effect between carbon and metal oxide phases. J Mater Chem A 2018;6:633–44. https://doi.org/10.1039/C7TA08023A.

[6] Binas V, Venieri D, Kotzias D, Kiriakidis G. Modified TiO$_2$ based photocatalysts for improved air and health quality. J Materiomics 2017;3:3–16. https://doi.org/10.1016/j.jmat.2016.11.002.

[7] Kozak M, Mazierski P, Żebrowska J, Kobylański M, Klimczuk T, Lisowski W, et al. Electrochemically obtained TiO$_2$/Cu$_x$O$_y$ nanotube Arrays presenting a photocatalytic response in processes of pollutants degradation and bacteria inactivation in aqueous phase. Catalysts 2018;8:237. https://doi.org/10.3390/catal8060237.

[8] Moma J, Baloyi J. Modified titanium dioxide for photocatalytic applications. In: Bahadar Khan S, Akhtar K, editors. Photocatal. - appl. Attrib. IntechOpen; 2019. https://doi.org/10.5772/intechopen.79374.

[9] Noman MT, Ashraf MA, Ali A. Synthesis and applications of nano-TiO$_2$: a review. Environ Sci Pollut Res 2019;26:3262–91. https://doi.org/10.1007/s11356-018-3884-z.

[10] Gupta S, Tripathi M. A review on the synthesis of TiO$_2$ nanoparticles by solution route. Open Chem 2012;10. https://doi.org/10.2478/s11532-011-0155-y.

[11] Macwan DP, Dave PN, Chaturvedi S. A review on nano-TiO$_2$ sol–gel type syntheses and its applications. J Mater Sci 2011;46:3669–86. https://doi.org/10.1007/s10853-011-5378-y.

[12] Wang WB, Yanguas-Gil A, Yang Y, Kim D-Y, Girolami GS, Abelson JR. Chemical vapor deposition of TiO$_2$ thin films from a new halogen-free precursor. J Vac Sci Technol Vac Surf Films 2014;32. https://doi.org/10.1116/1.4894454. 061502.

[13] Kim JH, Noh BH, Lee G-D, Hong S-S. Hydrothermal synthesis of titanium dioxide using acidic peptizing agents and their photocatalytic activity. Kor J Chem Eng 2005;22:370–4. https://doi.org/10.1007/BF02719413.

[14] Regonini D, Bowen CR, Jaroenworaluck A, Stevens R. A review of growth mechanism, structure and crystallinity of anodized TiO$_2$ nanotubes. Mater Sci Eng R Rep 2013;74:377–406. https://doi.org/10.1016/j.mser.2013.10.001.

[15] Wang X, Li Z, Shi J, Yu Y. One-dimensional titanium dioxide nanomaterials: nanowires, nanorods, and nanobelts. Chem Rev 2014;114:9346–84. https://doi.org/10.1021/cr400633s.

[16] Chae SY, Park MK, Lee SK, Kim TY, Kim SK, Lee WI. Preparation of size-controlled TiO$_2$ nanoparticles and derivation of optically transparent photocatalytic films. Chem Mater 2003;15:3326–31. https://doi.org/10.1021/cm030171d.

[17] Wang T-H, Navarrete-López AM, Li S, Dixon DA, Gole JL. Hydrolysis of TiCl$_4$: initial steps in the production of TiO$_2$. J Phys Chem A 2010;114:7561–70. https://doi.org/10.1021/jp102020h.

[18] Luan Y, Feng Y, Cui H, Cao Y, Jing L. Enhanced photocatalytic activity of P25 TiO$_2$ after modification with phosphate-treated porous SiO$_2$. ChemPlusChem 2014;79:1271–7. https://doi.org/10.1002/cplu.201402063.

[19] Matsubara M, Yamaki T, Itoh H, Abe H, Asai K. Preparation of TiO$_2$ nanoparticles by pulsed laser ablation: ambient pressure dependence of crystallization. Jpn J Appl Phys 2003;42:L479–81. https://doi.org/10.1143/JJAP.42.L479.

[20] Cui C, Liu H, Li Y, Sun J, Wang R, Liu S, et al. Fabrication and biocompatibility of nano-TiO$_2$/titanium alloys biomaterials. Mater Lett 2005;59:3144–8. https://doi.org/10.1016/j.matlet.2005.05.037.

[21] Xie Z, Shuang S, Ma L, Zhu F, Liu X, Zhang Z. Annealing effect on the photoelectrochemical and photocatalytic performance of TiO$_2$ nanorod arrays. RSC Adv 2017;7:51382–90. https://doi.org/10.1039/C7RA09801D.

[22] Sugapriya S, Sriram R, Lakshmi S. Effect of annealing on TiO$_2$ nanoparticles. Optik 2013;124:4971–5. https://doi.org/10.1016/j.ijleo.2013.03.040.

[23] Reyes-Coronado D, Rodríguez-Gattorno G, Espinosa-Pesqueira ME, Cab C, de Coss R, Oskam G. Phase-pure TiO$_2$ nanoparticles: anatase, brookite and rutile. Nanotechnology 2008;19:145605. https://doi.org/10.1088/0957-4484/19/14/145605.

[24] Madhusudan Reddy K, Manorama SV, Ramachandra Reddy A. Bandgap studies on anatase titanium dioxide nanoparticles. Mater Chem Phys 2003;78:239–45. https://doi.org/10.1016/S0254-0584(02)00343-7.

[25] Nasirian M, Lin YP, Bustillo-Lecompte CF, Mehrvar M. Enhancement of photocatalytic activity of titanium dioxide using non-metal doping methods under visible light: a review. Int J Environ Sci Technol 2018;15:2009–32. https://doi.org/10.1007/s13762-017-1618-2.

[26] Lisowska-Oleksiak A, Szybowska K, Jasulaitiené V. Preparation and characterisation of visible light responsive iodine doped TiO$_2$ electrodes. Electrochim Acta 2010;55:5881–5. https://doi.org/10.1016/j.electacta.2010.05.039.

[27] Panpranot J, Kontapakdee K, Praserthdam P. Effect of TiO$_2$ crystalline phase composition on the physicochemical and catalytic properties of Pd/TiO$_2$ in selective acetylene hydrogenation. J Phys Chem B 2006;110:8019–24. https://doi.org/10.1021/jp057395z.

[28] Ribao P, Rivero MJ, Ortiz I. TiO$_2$ structures doped with noble metals and/or graphene oxide to improve the photocatalytic degradation of dichloroacetic acid. Environ Sci Pollut Res 2017;24:12628–37. https://doi.org/10.1007/s11356-016-7714-x.

[29] Amorós-Pérez A, Cano-Casanova L, Castillo-Deltell A, Lillo-Ródenas M, Román-Martínez M. TiO$_2$ modification with transition metallic species (Cr, Co, Ni, and

Cu) for photocatalytic abatement of acetic acid in liquid phase and propene in gas phase. Materials 2018;12:40. https://doi.org/10.3390/ma12010040.

[30] Clarizia L, Spasiano D, Di Somma I, Marotta R, Andreozzi R, Dionysiou DD. Copper modified-TiO2 catalysts for hydrogen generation through photoreforming of organics. A short review. Int J Hydrogen Energy 2014;39:16812–31. https://doi.org/10.1016/j.ijhydene.2014.08.037.

[31] Trenczek-Zajac A, Kusior A, Lacz A, Radecka M, Zakrzewska K. TiO2 flower-like nanostructures decorated with CdS/PbS nanoparticles. Mater Res Bull 2014;60: 28–37. https://doi.org/10.1016/j.materresbull.2014.08.010.

[32] Siuzdak K, Szkoda M, Lisowska-Oleksiak A, Karczewski J, Ryl J. Highly stable organic-inorganic junction composed of hydrogenated titania nanotubes infiltrated by a conducting polymer. RSC Adv 2016;6:33101–10. https://doi.org/10.1039/C6RA01986B.

[33] Peng W, Yang C, Yu J. Bi2O3 and g-C3N4 quantum dot modified anatase TiO2 heterojunction system for degradation of dyes under sunlight irradiation. RSC Adv 2020;10:1181–90. https://doi.org/10.1039/C9RA07424D.

[34] Tada H, Jin Q, Iwaszuk A, Nolan M. Molecular-scale transition metal oxide nanocluster surface-modified titanium dioxide as solar-activated environmental catalysts. J Phys Chem C 2014;118:12077–86. https://doi.org/10.1021/jp412312m.

[35] Xu F. Review of analytical studies on TiO2 nanoparticles and particle aggregation, coagulation, flocculation, sedimentation, stabilization. Chemosphere 2018;212: 662–77. https://doi.org/10.1016/j.chemosphere.2018.08.108.

[36] Haider AJ, Jameel ZN, Al-Hussaini IHM. Review on: titanium dioxide applications. Energy Procedia 2019;157:17–29. https://doi.org/10.1016/j.egypro.2018.11.159.

[37] Cheng Y, Yang H, Yang Y, Huang J, Wu K, Chen Z, et al. Progress in TiO2 nanotube coatings for biomedical applications: a review. J Mater Chem B 2018;6: 1862–86. https://doi.org/10.1039/C8TB00149A.

[38] Schmidt B, Schaefer M. Advanced industrial laser systems and applications. In: Kaierle S, Heinemann SW, editors. High-power laser mater. Process. Appl. Diagn. Syst. VII. San Francisco, United States: SPIE; 2018. p. 203. https://doi.org/10.1117/12.2299534.

[39] Garapon C, Champeaux C, Mugnier J, Panczer G, Marchet P, Catherinot A, et al. Preparation of TiO2 thin films by pulsed laser deposition for waveguiding applications. Appl Surf Sci 1996;96–98:836–41. https://doi.org/10.1016/0169-4332(95)00593-5.

[40] Passinger S, Saifullah MSM, Reinhardt C, Subramanian KRV, Chichkov BN, Welland ME. Direct 3D patterning of TiO2 using femtosecond laser pulses. Adv Mater 2007;19:1218–21. https://doi.org/10.1002/adma.200602264.

[41] Mamuschkin V, Roesner A, Aden M. Laser transmission welding of white thermoplastics with adapted wavelengths. Phys Procedia 2013;41:172–9. https://doi.org/10.1016/j.phpro.2013.03.067.

[42] Gerlein LF, Benavides-Guerrero JA, Cloutier SG. Laser-assisted, large-area selective crystallization and patterning of titanium dioxide polymorphs. Adv Eng Mater 2020;22:1901014. https://doi.org/10.1002/adem.201901014.

[43] Träger F, editor. Springer handbook of lasers and optics. Berlin, Heidelberg: Springer Berlin Heidelberg; 2012. https://doi.org/10.1007/978-3-642-19409-2.

[44] Patidar D, Rana RS. The effect of CO2 laser cutting parameter on Mechanical & Microstructural characteristics of high strength steel-a review. Mater Today Proc 2018;5:17753–62. https://doi.org/10.1016/j.matpr.2018.06.099.

[45] Geng Y, Wang K, Dong X, Duan W, Mei X, Wang W. Laser drilling of micro-holes with small diameter beyond the limits of focused spot by using a sieve plate or a cover plate. Int J Adv Manuf Technol 2016;87:2471–84. https://doi.org/10.1007/s00170-016-8643-z.

[46] Preissig J, Hamilton K, Markus R. Current laser resurfacing technologies: a review that delves beneath the surface. Semin Plast Surg 2012;26:109–16. https://doi.org/10.1055/s-0032-1329413.

[47] Ruffino F, Grimaldi MG. Nanostructuration of thin metal films by pulsed laser irradiations: a review. Nanomaterials 2019;9:1133. https://doi.org/10.3390/nano9081133.

[48] Patil UA, Dhami LD. Overview of lasers. Indian J Plast Surg Off Publ Assoc Plast Surg India 2008;41:S101–13.

[49] Jian-Ke Y, Yun-Xia J, Yuan-An Z, Hong-Bo H, Jian-Da S, Zheng-Xiu F. Effect of process parameters on laser damage threshold of TiO2 coatings. Chin Phys Lett 2007;24:2606–8. https://doi.org/10.1088/0256-307X/24/9/040.

[50] Russo P, Liang R, He RX, Zhou YN. Phase transformation of TiO2 nanoparticles by femtosecond laser ablation in aqueous solutions and deposition on conductive substrates. Nanoscale 2017;9:6167–77. https://doi.org/10.1039/C7NR00201G.

[51] Takeuchi M, Sakamoto K, Martra G, Coluccia S, Anpo M. Mechanism of photoinduced superhydrophilicity on the TiO2 photocatalyst surface. J Phys Chem B 2005;109:15422–8. https://doi.org/10.1021/jp058075i.

[52] Han Jinghua. Interaction between pulsed laser and materials. In: Li ED1 Yaguo, Jakubczak Krzysztof, editors. Lasers. Rijeka: IntechOpen; 2011. https://doi.org/10.5772/25061. Ch. 6.

[53] Palik ED, editor. Handbook of optical constants of solids. San Diego, Calif: Acad. Press; 1998.

[54] Nath AK. High power lasers in material processing applications: an overview of recent developments. In: Majumdar JD, Manna I, editors. Laser-assist. Fabr. Mater., vol. 161. Berlin, Heidelberg: Springer Berlin Heidelberg; 2013. p. 69–111. https://doi.org/10.1007/978-3-642-28359-8_2.

[55] Kolwas K, Derkachova A, Shopa M. Size characteristics of surface plasmons and their manifestation in scattering properties of metal particles. J Quant Spectrosc Radiat Transf 2009;110:1490–501. https://doi.org/10.1016/j.jqsrt.2009.03.020.

[56] Dressel G Gruner. Electrodynamics of solids. Optical properties of electronics in matter. Cambridge: University Press; 2002. p. 119–48.

[57] Mathew J, Goswami GL, Ramakrishnan N, Naik NK. Parametric studies on pulsed Nd:YAG laser cutting of carbon fibre reinforced plastic composites. J Mater Process Technol 1999;89(90):198–203. https://doi.org/10.1016/S0924-0136(99)00011-4.

[58] Laser fabrication and machining of materials. Boston, MA: Springer US; 2008. https://doi.org/10.1007/978-0-387-72344-0.

[59] Kuhnke M, Cramer L, Dyer PE, Dickinson JT, Lippert T, Niino H, et al. F2 excimer laser (157 nm) ablation of polymers: relation of neutral and ionic fragment detection and absorption. J Phys Conf Ser 2007;59:625–31. https://doi.org/10.1088/1742-6596/59/1/132.

[60] Breitling D, Ruf A, Dausinger F. In: Herman PR, Fieret J, Pique A, Okada T, Bachmann FG, Hoving W, et al., editors. Fundamental aspects in machining of metals with short and ultrashort laser pulses; 2004. p. 49. https://doi.org/10.1117/12.541434. San Jose, Ca.

[61] Gamaly EG. The physics of ultra-short laser interaction with solids at non-relativistic intensities. Phys Rep 2011;508:91–243. https://doi.org/10.1016/j.physrep.2011.07.002.

[62] Bäuerle D. Laser processing and chemistry. Berlin, Heidelberg: Springer Berlin Heidelberg; 2011. https://doi.org/10.1007/978-3-642-17613-5.

[63] Tritt TM, editor. Thermal conductivity: theory, properties, and applications. New York: Kluwer Academic/Plenum Publishers; 2004.

[64] Wu X, Luo T. Effect of electron-phonon coupling on thermal transport across metal-nonmetal interface A second look. EPL Europhys Lett 2015;110:67004. https://doi.org/10.1209/0295-5075/110/67004.

[65] Simonds BJ, Meadows HJ, Misra S, Ferekides C, Dale PJ, Scarpulla MA. Laser processing for thin film chalcogenide photovoltaics: a review and prospectus. J Photon Energy 2015;5. https://doi.org/10.1117/1.JPE.5.050999. 050999.

[66] Bleiner D, Bogaerts A. Multiplicity and contiguity of ablation mechanisms in laser-assisted analytical micro-sampling. Spectrochim Acta Part B At Spectrosc 2006;61:421–32. https://doi.org/10.1016/j.sab.2006.02.007.

[67] Grigoropoulos CP. Transport in laser microfabrication: fundamentals and applications. Cambridge: Cambridge University Press; 2009. https://doi.org/10.1017/CBO9780511596674.

[68] Chichkov BN, Momma C, Nolte S, Alvensleben F, Tünnermann A. Femtosecond, picosecond and nanosecond laser ablation of solids. Appl Phys Mater Sci Process 1996;63:109–15. https://doi.org/10.1007/BF01567637.

[69] Hamad AH. Effects of different laser pulse regimes (nanosecond, picosecond and femtosecond) on the ablation of materials for production of nanoparticles in liquid solution. In: Viskup R, editor. High energy short pulse lasers. InTech; 2016. https://doi.org/10.5772/63892.

[70] Palneedi H, Park JH, Maurya D, Peddigari M, Hwang G-T, Annapureddy V, et al. Laser irradiation of metal oxide films and nanostructures: applications and advances. Adv Mater 2018;30:1705148. https://doi.org/10.1002/adma.201705148.

[71] Phillips KC, Gandhi HH, Mazur E, Sundaram SK. Ultrafast laser processing of materials: a review. Adv Optic Photon 2015;7:684. https://doi.org/10.1364/AOP.7.000684.

[72] Sands D. Pulsed laser heating and melting. In: Vikhrenko V, editor. Heat transf.-eng. Appl. InTech; 2011. https://doi.org/10.5772/28736.

[73] Hotový I, Kostič I, HAsčík Š, REháček V, Liday J, Sitter H. Development and fabrication of TiO2 tip arrays for gas sensing. J Electr Eng 2011;62:363–6. https://doi.org/10.2478/v10187-011-0058-3.

[74] Saifullah MSM, Subramanian KRV, Tapley E, Kang D-J, Welland ME, Butler M. Sub-10 nm electron beam nanolithography using spin-coatable TiO2 resists. Nano Lett 2003;3:1587–91. https://doi.org/10.1021/nl034584p.

[75] Ganesan R, Dumond J, Saifullah MSM, Lim SH, Hussain H, Low HY. Direct patterning of TiO2 using step-and-flash imprint lithography. ACS Nano 2012;6: 1494–502. https://doi.org/10.1021/nn204405k.

[76] Zanchetta E, Della Giustina G, Brusatin G. One-step patterning of double tone high contrast and high refractive index inorganic spin-on resist. J Appl Phys 2014; 116:103504. https://doi.org/10.1063/1.4893724.

[77] Perotto G, Antonello A, Ferraro D, Mattei G, Martucci A. Patterned TiO2 nanostructures fabricated with a novel inorganic resist. Mater Chem Phys 2013; 142:712–6. https://doi.org/10.1016/j.matchemphys.2013.08.029.

[78] Chen D, Gao Y, Wang G, Zhang H, Lu W, Li J. Surface tailoring for controlled photoelectrochemical properties: effect of patterned TiO2 microarrays. J Phys Chem C 2007;111:13163–9. https://doi.org/10.1021/jp074003a.

[79] Francioso L, Siciliano P. Top-down contact lithography fabrication of a TiO2 nanowire array over a SiO2 mesa. Nanotechnology 2006;17:3761–7. https://doi.org/10.1088/0957-4484/17/15/025.

[80] Vogel R, Meredith P, Kartini I, Harvey M, Riches JD, Bishop A, et al. Mesostructured dye-doped titanium dioxide for micro-optoelectronic applications. ChemPhysChem 2003;4:595–603. https://doi.org/10.1002/cphc.200200494.

[81] Lim SH, Saifullah MSM, Hussain H, Loh WW, Low HY. Direct imprinting of high resolution TiO2 nanostructures. Nanotechnology 2010;21:285303. https://doi.org/10.1088/0957-4484/21/28/285303.

[82] Zhong P, Que W, Hu X. Direct imprinting of ordered and dense TiO2 nanopore arrays by using a soft template for photovoltaic applications. Appl Surf Sci 2011; 257:9872–8. https://doi.org/10.1016/j.apsusc.2011.06.060.

[83] Lee J, Park J, Lee M. Nanostructured TiO2 diffraction grating fabricated via imprinting and TiCl4 treatment. J Mater Chem C 2014;2:981–5. https://doi.org/10.1039/C3TC32018A.

[84] Langner A, Knez M, Müller F, Gösele U. TiO2 microstructures by inversion of macroporous silicon using atomic layer deposition. Appl Phys A 2008;93: 399–403. https://doi.org/10.1007/s00339-008-4784-8.

18

[85] Yang P, Yang M, Zou S, Xie J, Yang W. Positive and negative TiO$_2$ micropatterns on organic polymer substrates. J Am Chem Soc 2007;129:1541–52. https://doi.org/10.1021/ja0637160.

[86] Duoss EB, Twardowski M, Lewis JA. Sol-gel inks for direct-write assembly of functional oxides. Adv Mater 2007;19:3485–9. https://doi.org/10.1002/adma.200701372.

[87] Ozkan S, Nguyen NT, Mazare A, Schmuki P. Optimized spacing between TiO$_2$ nanotubes for enhanced light harvesting and charge transfer. ChemElectroChem 2018;5:3183–90. https://doi.org/10.1002/celc.201801136.

[88] Ozkan S, Mazare A, Schmuki P. Critical parameters and factors in the formation of spaced TiO$_2$ nanotubes by self-organizing anodization. Electrochim Acta 2018; 268:435–47. https://doi.org/10.1016/j.electacta.2018.02.120.

[89] Nah Y-C, Paramasivam I, Schmuki P. Doped TiO$_2$ and TiO$_2$ nanotubes: synthesis and applications. ChemPhysChem 2010;11:2698–713. https://doi.org/10.1002/cphc.201000276.

[90] Crespo-Monteiro N, Destouches N, Saviot L, Reynaud S, Epicier T, Gamet E, et al. One-step microstructuring of TiO$_2$ and Ag-TiO$_2$ films by continuous wave laser processing in the UV and visible ranges. J Phys Chem C 2012;116:26857–64. https://doi.org/10.1021/jp3096264.

[91] Wu Y, Choy K-L, Hench LL. Laser densification of TiO$_2$ films prepared by aerosol assisted vapour deposition. Appl Surf Sci 2005;247:378–83. https://doi.org/10.1016/j.apsusc.2005.01.077.

[92] Van Overschelde O, Wautelet M. Diffraction-aided laser-induced microstructuring of thin TiO$_2$ films on glass. Appl Phys Lett 2006;89:161114. https://doi.org/10.1063/1.2364462.

[93] Van Overschelde O, Dinu S, Guisbiers G, Monteverde F, Nouvellon C, Wautelet M. Excimer laser ablation of thin titanium oxide films on glass. Appl Surf Sci 2006; 252:4722–7. https://doi.org/10.1016/j.apsusc.2005.07.147.

[94] Van Overschelde O, Boisdequin JM, Leclère Ph, Wautelet M. Excimer-laser induced structural transformations of TiO$_2$ thin films. Phys Status Solidi C 2008;5: 3255–8. https://doi.org/10.1002/pssc.200779518.

[95] Kim J, Kim J, Lee M. Laser welding of nanoparticulate TiO$_2$ and transparent conducting oxide electrodes for highly efficient dye-sensitized solar cell. Nanotechnology 2010;21:345203. https://doi.org/10.1088/0957-4484/21/34/345203.

[96] Filice S, Compagnini G, Fiorenza R, Scirè S, D'Urso L, Fragalà ME, et al. Laser processing of TiO$_2$ colloids for an enhanced photocatalytic water splitting activity. J Colloid Interface Sci 2017;489:131–7. https://doi.org/10.1016/j.jcis.2016.08.013.

[97] Hsu M-Y, Van Thang N, Wang C, Leu J. Structural and morphological transformations of TiO2 nanotube arrays induced by excimer laser treatment. Thin Solid Films 2012;520:3593–9. https://doi.org/10.1016/j.tsf.2011.12.036.

[98] Xu Y, Melia MA, Tsui L, Fitz-Gerald JM, Zangari G. Laser-induced surface modification at anatase TiO$_2$ nanotube Array photoanodes for photoelectrochemical water oxidation. J Phys Chem C 2017;121:17121–8. https://doi.org/10.1021/acs.jpcc.7b05368.

[99] Wawrzyniak J, Karczewski J, Kupracz P, Grochowska K, Załęski K, Pshyk O, et al. Laser-assisted modification of titanium dioxide nanotubes in a tilted mode as surface modification and patterning strategy. Appl Surf Sci 2020;508:145143. https://doi.org/10.1016/j.apsusc.2019.145143.

[100] Liu Y, Zhu B, Wang L, Dai Y, Ma H, Lakshminarayana G, et al. Femtosecond laser direct writing of TiO$_2$ crystalline patterns in glass. Appl Phys B 2008;93:613–7. https://doi.org/10.1007/s00340-008-3166-4.

[101] Eaton SM, Zhang H, Herman PR, Yoshino F, Shah L, Bovatsek J, et al. Heat accumulation effects in femtosecond laser-written waveguides with variable repetition rate. Optic Express 2005;13:4708. https://doi.org/10.1364/OPEX.13.004708.

[102] Wang SJ, Chang W-T, Ciou J-Y, Wei M-K, Wong MS. Preparation of TiO$_2$ thin films by laser ablation for photocatalytic applications. J Vac Sci Technol Vac Surf Films 2008;26:898–902. https://doi.org/10.1116/1.2870228.

[103] Ardakani HK. Electrical and optical properties of in situ "hydrogen-reduced" titanium dioxide thin films deposited by pulsed excimer laser ablation. Thin Solid Films 1994;248:234–9. https://doi.org/10.1016/0040-6090(94)90017-5.

[104] Murugesan S, Kuppusami P, Parvathavarthini N, Mohandas E. Pulsed laser deposition of anatase and rutile TiO$_2$ thin films. Surf Coating Technol 2007;201: 7713–9. https://doi.org/10.1016/j.surfcoat.2007.03.004.

[105] Long H, Yang G, Chen A, Li Y, Lu P. Growth and characteristics of laser deposited anatase and rutile TiO$_2$ films on Si substrates. Thin Solid Films 2008;517:745–9. https://doi.org/10.1016/j.tsf.2008.08.179.

[106] Stankova NE, Atanasov PA, Dikovska AO, Dimitrov IG, Socol G, Mihailescu IN. In: Atanasov PA, Gateva SV, Avramov LA, Serafetinides AA, editors. Growth of anatase TiO$_2$ thin films by laser ablation; 2005. p. 60. https://doi.org/10.1117/12.617327. Bourgas, Bulgaria.

[107] Escobar-Alarcón L, Haro-Poniatowski E, Camacho-López MA, Fernández-Guasti M, Jímenez-Jarquín J, Sánchez-Pineda A. Growth of rutile TiO$_2$ thin films by laser ablation. Surf Eng 1999;15:411–4. https://doi.org/10.1179/026708499101516803.

[108] Hirasawa M, Seto T, Orii T, Aya N, Shimura H. Synthesis of size-selected TiO$_x$ nanoparticles. Appl Surf Sci 2002;197–198:661–5. https://doi.org/10.1016/S0169-4332(02)00436-1.

[109] Zuñiga-Ibarra VA, Shaji S, Krishnan B, Johny J, Sharma Kanakkillam S, Avellaneda DA, et al. Synthesis and characterization of black TiO$_2$ nanoparticles by pulsed laser irradiation in liquid. Appl Surf Sci 2019;483:156–64. https://doi.org/10.1016/j.apsusc.2019.03.302.

[110] Abdul-Hassan IA, Abbas AK, Ibrahim IM, Shallal ZS. Characterization and antimicrobial effects of titanium dioxide nanoparticles produced by Laser Ablation 2018;8:8.

[111] Yan X, Chen X. Titanium dioxide nanomaterials. In: Scott RA, editor. Encycl. Inorg. Bioinorg. Chem. Chichester, UK: John Wiley & Sons, Ltd; 2015. p. 1–38. https://doi.org/10.1002/9781119951438.eibc2335.

[112] Zhang J, Zhou P, Liu J, Yu J. New understanding of the difference of photocatalytic activity among anatase, rutile and brookite TiO$_2$. Phys Chem Chem Phys 2014;16:20382–6. https://doi.org/10.1039/C4CP02201G.

[113] Ai C, Xie P, Zhang X, Zheng X, Li J, Kafizas A, et al. Explaining the enhanced photoelectrochemical behavior of highly ordered TiO$_2$ nanotube Arrays: anatase/rutile phase junction. ACS Sustainable Chem Eng 2019;7:5274–82. https://doi.org/10.1021/acssuschemeng.8b06219.

[114] Asiah MN, Mamat MH, Khusaimi Z, Achoi MF, Abdullah S, Rusop M. Thermal stability and phase transformation of TiO$_2$ nanowires at various temperatures. Microelectron Eng 2013;108:134–7. https://doi.org/10.1016/j.mee.2013.02.010.

[115] Lamberti A, Chiodoni A, Shahzad N, Bianco S, Quaglio M, Pirri CF. Ultrafast room-temperature crystallization of TiO$_2$ nanotubes exploiting water-vapor treatment. Sci Rep 2015;5:7808. https://doi.org/10.1038/srep07808.

[116] Liao Y, Que W, Zhong P, Zhang J, He Y. A facile method to crystallize amorphous anodized TiO$_2$ nanotubes at low temperature. ACS Appl Mater Interfaces 2011;3: 2800–4. https://doi.org/10.1021/am200685s.

[117] Wang D, Liu L, Zhang F, Tao K, Pippel E, Domen K. Spontaneous phase and morphology transformations of anodized titania nanotubes induced by water at room temperature. Nano Lett 2011;11:3649–55. https://doi.org/10.1021/nl2015262.

[118] Mazare A, Paramasivam I, Schmidt-Stein F, Lee K, Demetrescu I, Schmuki P. Flame annealing effects on self-organized TiO$_2$ nanotubes. Electrochim Acta 2012;66:12–21. https://doi.org/10.1016/j.electacta.2012.01.001.

[119] Sundaram SK, Mazur E. Inducing and probing non-thermal transitions in semiconductors using femtosecond laser pulses. Nat Mater 2002;1:217–24. https://doi.org/10.1038/nmat767.

[120] Likodimos V, Stergiopoulos T, Falaras P, Kunze J, Schmuki P. Phase composition, size, orientation, and antenna effects of self-assembled anodized titania nanotube Arrays: a polarized micro-Raman investigation. J Phys Chem C 2008;112: 12687–96. https://doi.org/10.1021/jp8027462.

[121] Chung CK, Lin SL, Cheng SY, Chuang KP, Wang HY. Effect of sol–gel composition ratio and laser power on phase transformation of crystalline titanium dioxide under CO$_2$ laser annealing. Micro & Nano Lett 2011;6:494. https://doi.org/10.1049/mnl.2011.0133.

[122] Enachi M, Stevens-Kalceff MA, Sarua A, Ursaki V, Tiginyanu I. Design of titania nanotube structures by focused laser beam direct writing. J Appl Phys 2013;114: 234302. https://doi.org/10.1063/1.4849836.

[123] Parussulo ALA, Huila MFG, Araki K, Toma HE. N3-Dye-Induced visible laser anatase-to-rutile phase transition on mesoporous TiO$_2$ films. Langmuir 2011;27: 9094–9. https://doi.org/10.1021/la201838z.

[124] Ricci PC, Casu A, Salis M, Corpino R, Anedda A. Optically controlled phase variation of TiO$_2$ nanoparticles. J Phys Chem C 2010;114:14441–5. https://doi.org/10.1021/jp105091d.

[125] Serpone N. Is the band gap of pristine TiO$_2$ narrowed by anion- and cation-doping of titanium dioxide in second-generation photocatalysts. J Phys Chem B 2006; 110:24287–93. https://doi.org/10.1021/jp065659r.

[126] Benavides JA, Trudeau CP, Gerlein LF, Cloutier SG. Laser selective photoactivation of amorphous TiO$_2$ films to anatase and/or rutile crystalline phases. ACS Appl Energy Mater 2018;1:3607–13. https://doi.org/10.1021/acsaem.8b00171.

[127] Ricci PC, Carbonaro CM, Stagi L, Salis M, Casu A, Enzo S, et al. Anatase-to-Rutile phase transition in TiO$_2$ nanoparticles irradiated by visible light. J Phys Chem C 2013;117:7850–7. https://doi.org/10.1021/jp312325h.

[128] Vásquez GC, Peche-Herrero MA, Maestre D, Gianoncelli A, Ramírez-Castellanos J, Cremades A, et al. Laser-induced anatase-to-rutile transition in TiO$_2$ nanoparticles: promotion and inhibition effects by Fe and Al doping and achievement of micropatterning. J Phys Chem C 2015;119:11965–74. https://doi.org/10.1021/acs.jpcc.5b01736.

[129] Overschelde OV, Guisbiers G, Wautelet M. Nanocrystallization of anatase or rutile TiO$_2$ by laser treatment. J Phys Chem C 2009;113:15343–5. https://doi.org/10.1021/jp905163j.

[130] Joya YF, Liu Z. Effect of the excimer laser irradiation on sol–gel derived tungsten–titanium dioxide thin films. Appl Phys A 2011;102:91–7. https://doi.org/10.1007/s00339-010-6151-9.

[131] Haryński Ł, Grochowska K, Kupracz P, Karczewski J, Coy E, Siuzdak K. The in-depth studies of pulsed UV laser-modified TiO$_2$ nanotubes: the influence of geometry, crystallinity, and processing parameters. Nanomaterials 2020;10:430. https://doi.org/10.3390/nano10030430.

[132] Van Overschelde O, Delsate T, Snyders R. Determination of the melting threshold of TiO$_2$ thin films processed by excimer laser irradiation. J Appl Phys 2012;111: 123108. https://doi.org/10.1063/1.4728159.

[133] Siuzdak K, Szkoda M, Sawczak M, Karczewski J, Ryl J, Cenian A. Ordered titania nanotubes layer selectively annealed by laser beam for high contrast electrochromic switching. Thin Solid Films 2018;659:48–56. https://doi.org/10.1016/j.tsf.2018.05.045.

[134] Nishikawa M, Fukuda M, Nakabayashi Y, Saito N, Ogawa N, Nakajima T, et al. A method to give chemically stabilities of photoelectrodes for water splitting: compositing of a highly crystalized TiO$_2$ layer on a chemically unstable Cu$_2$O

19

photocathode using laser-induced crystallization process. Appl Surf Sci 2016;363: 173–80. https://doi.org/10.1016/j.apsusc.2015.12.002.

[135] Wilkes GC, Deng X, Choi JJ, Gupta MC. Laser annealing of TiO_2 electron-transporting layer in perovskite solar cells. ACS Appl Mater Interfaces 2018;10: 41312–7. https://doi.org/10.1021/acsami.8b13740.

[136] Haryński Ł, Grochowska K, Karczewski J, Ryl J, Siuzdak K. Scalable route toward superior photoresponse of UV-Laser-Treated TiO_2 nanotubes. ACS Appl Mater Interfaces 2020;12:3225–35. https://doi.org/10.1021/acsami.9b19206.

[137] Nakajima T, Nakamura T, Shinoda K, Tsuchiya T. Rapid formation of black titania photoanodes: pulsed laser-induced oxygen release and enhanced solar water splitting efficiency. J Mater Chem A 2014;2:6762–71. https://doi.org/10.1039/C4TA00557K.

[138] Mincuzzi G, Schulz-Ruhtenberg M, Vesce L, Reale A, Di Carlo A, Gillner A, et al. Laser processing of TiO_2 films for dye solar cells: a thermal, sintering, throughput and embodied energy investigation: laser processing of TiO_2 films for dye solar cells. Prog Photovoltaics Res Appl 2014;22:308–17. https://doi.org/10.1002/pip.2261.

[139] Lau M, Reichenberger S, Haxhiaj I, Barcikowski S, Müller AM. Mechanism of laser-induced bulk and surface defect generation in ZnO and TiO_2 nanoparticles: effect on photoelectrochemical performance. ACS Appl Energy Mater 2018;10 (10):5366–85. https://doi.org/10.1021/acsaem.8b00977. acsaem.8b00977.

[140] Belka R, Kęczkowska J, Sęk P. In: Romaniuk RS, Kopczynski K, Jabczyński JK, Mierczyk Z, editors. Raman study of TiO_2 coatings modified by UV pulsed laser; 2016. 101590V. https://doi.org/10.1117/12.2261655. Jastarnia, Poland.

[141] Sopha H, Mirza I, Turčičova H, Pavlinak D, Michalicka J, Krbal M, et al. Laser-induced crystallization of anodic TiO_2 nanotube layers. RSC Adv 2020;10: 22137–45. https://doi.org/10.1039/D0RA02929G.

[142] Ma H, Guo G, Yang J, Guo Y, Ma N. Femtosecond laser irradiation-induced phase transformation on titanium dioxide crystal surface. Nucl Instrum Methods Phys Res Sect B Beam Interact Mater Atoms 2007;264:61–5. https://doi.org/10.1016/j.nimb.2007.08.006.

[143] Yang JY, Ma HL, Ma GH, Lu B, Ma H. Phase transformation at the surface of TiO_2 single crystal irradiated by femtosecond laser pulse. Appl Phys A 2007;88:801–4. https://doi.org/10.1007/s00339-007-4089-3.

[144] Hoppius JS, Bialuschewski D, Mathur S, Ostendorf A, Gurevich EL. Femtosecond laser crystallization of amorphous titanium oxide thin films. Appl Phys Lett 2018; 113. https://doi.org/10.1063/1.5027899. 071904.

[145] Zamharir SG, Ranjbar M, Salamati H. Excimer laser treatment of TiO_2/WO_3 thin films for self-cleaning gasochromic applications: preparation and characterization. Sol Energy Mater Sol Cells 2014;130:27–35. https://doi.org/10.1016/j.solmat.2014.06.029.

20

5.3. Paper 3: A Facile Method for Tauc Exponent and Corresponding Electronic Transitions Determination in Semiconductors directly from UV-Vis Spectroscopy Data

The Tauc equation is a widely used approach for the determination of the optical band gap of semiconducting materials. However, to do so, information regarding optical transition must be known. Studying the literature, it has been observed that in most cases the authors choose the transition type from other articles without any justification. For instance, in the literature dedicated to Cr_2O_3, one can find that different authors choose different Tauc exponents [36,40] (hence assuming different transition types). It is also unclear which transition should be considered for example for multicomponent materials, in which each one exhibits a different transition type. The nature of dominating transition can be explained through the analysis of electronic band structure. However, band structures result from theoretical considerations, and usually, do not concern many essential physical properties such as morphology or structural defects which are crucial. Therefore, a systematic procedure for the determination of the Tauc exponent directly from the experimentally measured data would be a key to the correct estimation of the optical band gap. A pioneering work of a spectroscopic method allowing for the determination of the Tauc exponent from the experimentally measured UV-vis spectroscopy data was reported by Sangiorgi et al. [43]. The principle of the method is to take both side logarithm of the Tauc equation (see Equation 2) which allows estimating the Tauc exponent from the linear slope on the $\ln(\alpha hv)$ vs. $\ln(hv - E_G)$ plot. However, this approach requires knowledge of the band gap, hence the method does not solve the problem.

This work presents an improved method allowing for the determination of the Tauc exponent directly from the measured UV-vis spectroscopy data. It was applied to the TiO_2 nanotubes combined with Cr, Mo, and W oxides, deposited using magnetron sputtering technology (see Scheme 3). On contrary to the work reported by Sangiorgi et al. [43], the Tauc exponent can be estimated without any assumptions regarding the investigated material such as band gap width. It is possible thanks to the Taylor expansion of the logarithmic version of the Tauc equation. Specifically, the Tauc exponent can be obtained from the linear range (or ranges) from the $\log(\alpha hv)$ vs. hv dependence. The procedure involves: the calculation of the registered data to the absorption coefficient and photon energy, plotting $\log(\alpha hv)$ vs. hv, fitting the obtained data beyond the absorption edge with linear or quadratic functions which allows for estimating the Tauc exponent from the slope factor (see Fig. 1 in the paper). Then, a corresponding transition type (or types) can be assigned based on the commonly used values: 1/2, 2, 3/2, and 3

corresponding to direct (allowed), indirect (allowed), direct (forbidden), and indirect (forbidden) transitions, respectively.

For the bare TiO$_2$ nanotubes (see Figure 3 in the paper) two linear ranges outside the absorption edge were found. The first ($n = 1.9$) corresponds to well estimated indirect (allowed) transition whereas the second ($n = 1.1$) to direct (allowed) and others. Indeed, more than one transition is possible as it is proven by calculated band diagrams (see Figure 6 in the paper). In the case of the TiO$_2$ nanotubes decorated with Cr oxides, a single linear range ($n = 1.0$) assigned to direct (allowed) and other transitions was found. The TiO$_2$ nanotubes decorated with Mo and W oxides also exhibit a single linear range ($n = 1.5$) which corresponds to the direct (forbidden) transition.

It is believed that the elaborated method will help to determine the transition types as well as for a more precise determination of optical band gap occurring in other nano-sized or multicomponent semiconducting materials. The obtained results are also the basis for further work which verifies a correlation between the estimated transition types and the photoresponse of the investigated sample.

A facile method for Tauc exponent and corresponding electronic transitions determination in semiconductors directly from UV–Vis spectroscopy data

Łukasz Haryński [a],[*],[1], Adrian Olejnik [a],[b],[1], Katarzyna Grochowska [a], Katarzyna Siuzdak [a]

[a] Centre for Plasma and Laser Engineering, The Szewalski Institute of Fluid–Flow Machinery, Polish Academy of Sciences, Fiszera 14 Street, 80-231, Gdańsk, Poland
[b] Faculty of Electronics, Telecommunications and Informatics, Gdańsk University of Technology, Narutowicza 11/12 Street, 80-233, Gdańsk, Poland

ABSTRACT

In this work, a facile method allowing for estimation of the exponent in the Tauc equation directly from the UV–vis spectra is presented. It is based on the Taylor expansion of the logarithmic version of the Tauc equation. The Tauc exponent is calculated from the tangent slope of the absorption data. Knowledge of this coefficient provides information about the optical transition types and is used as an input for the calculations of the band gap. As an exemplar material, TiO_2 in form of thin film and nanotubes as well as their nanocomposites with other metal oxides are chosen. For the transparent thin 15 nm film of TiO_2, two linear ranges with $n = 2.0$ and 1.2 are found. The first is assigned to the well-established indirect (allowed) transition. In the case of the second one, the n does not correspond to typically used values. Therefore, it is speculated that more than one transition is probable. This consideration is supported with *ab-initio* DFT calculations of the band structure of TiO_2 with Hubbard U correction. Similar results are found for TiO_2 nanotubes using diffuse reflectance spectroscopy indicating that the presented method applies both to transmission and reflection.

1. Introduction

Nowadays, a significant interest is paid to photoactive materials which are aimed to convert solar to electrical energy efficiently. Therefore, the synthesis and examination of novel semiconducting materials are essential for sustainable energy conversion.

Knowledge of the band structure of a semiconductor allows to predict its properties and often estimate which transitions occur under illumination [1]. There are several methods allowing to determine the band structure of a semiconductor. In the range of computational ones, GW approximation [2], density-functional theory (DFT) calculations especially with Hubbard U corrections [3] or semi-empirical Slater-Koster method [4] are proposed. On the other hand, Angle-Resolved Photoemission Spectroscopy can be used to probe the electronic structure and access the shape of the bands [5]. However, knowledge of the whole band structure is not always needed, and typically, a Tauc plot from the ultraviolet–visible (UV–vis) spectroscopy data is used to estimate only the optical band gap [6]. The procedure of estimating the optical band gap is *via* fitting the experimentally determined absorption coefficient to the Tauc equation, which is a power-law expression in the form of Equation (1):

$$(\alpha h\nu)^{1/n} = A(h\nu - E_g) \qquad (1)$$

where α is absorption coefficient being a function of wavelength $\alpha(\lambda)$, h is Planck constant, E_g is an optical band gap of a semiconductor, ν is frequency, A is proportionality constant, and n is Tauc exponent. Tauc coefficient is typically chosen as one of four values depending on the type of dominating transition in a studied semiconductor and according to the commonly used rules:

$n = 1/2$ for direct (allowed) transitions,
$n = 3/2$ for direct (forbidden) transitions,
$n = 2$ for indirect (allowed) transition,
$n = 3$ for indirect (forbidden) transitions.

Practically, the method includes plotting $(\alpha h\nu)^{1/n}$ vs. $h\nu$ and extrapolating the linear range beyond the absorption edge yielding the value of the band gap on the abscissa axis. However, the value of n, *i.e.* the nature of the transition needs to be known.

Originally, Tauc derived his formula for $n = 2$ in the case of optical transition in amorphous germanium by linking the imaginary part of dielectric function with transition probabilities described by the Fermi

golden rule [7]. However, in the case of semiconductors with a direct band gap, it can be also understood intuitively with the following argumentation. Assuming that the conduction band is empty and the valence band is completely filled, one can state that for an intrinsic semiconductor the absorption coefficient is proportional to the transition probability $|M^2|$ and the joint density of states ρ_{JDOS}. It is commonly known that for bulk semiconductors the density of states (DOS) is proportional to the square root of the difference between photon energy and band gap value [8]:

$$\alpha \propto |M^2|\rho_{JDOS} = |M^2|\sqrt{h\nu - E_g} \qquad (2)$$

Therefore, the square of the absorption coefficient is proportional to the light energy minus the band gap which corresponds to the Tauc formula with exponent $n = 1/2$.

$$\alpha \propto (h\nu - E_g)^{1/2} \qquad (3)$$

However, Feng et al. [9] has shown theoretically that for a crystalline spherical semiconductor with a radius R the n is equal to $1/2$ for a bulk limit (i.e. when R approaches infinity), whereas n equals 1 for a point limit (i.e. when R approaches 0). These implications stem from two different approximations of the transition rate integrals obtained via solving a proper time-independent Schrödinger equation and applying the Fermi golden rule to the obtained states. For real semiconducting materials though, the n value is then between the limits $1/2$ and 1, depending on the R size and could be estimated via error analysis of linear fits for many different trial n values. In this case, minimized error stands for the correct n value. According to Feng et al. [9] optical band gap values are estimated with less uncertainty using corrected n values and the overestimation of a band gap value due to quantum confinement is minimized. It is worth noting that, the discrepancy between the band gap values estimated by assuming $n = 1/2$ and corrected n (e.g. $n = 0.68$) depends on the size of the crystal, crystallographic defects and the chemical formula of a semiconductor [9–11].

It might be confusing that the n value is not equal to the one of the most commonly fitted values ($1/2$, $3/2$, 2 or 3), but physically it is not forbidden. In fact, even in one of the very first works devoted to the estimation of optical band gaps Mott and Davis derived a formula where n was equal to 1 for an amorphous semiconductor [12]. The lack of n quantization can be further justified with the following example. As it was mentioned, the Tauc exponent is equal to $1/2$ for direct transition because the joint density of states is dependent on the $(h\nu - Eg)^{1/2}$ for a bulk intrinsic semiconductor [8]. However, this relationship changes when withe th dimensions of a nanomaterial [13], and therefore, the Tauc exponent is also expected to change. Moreover, when a semiconductor is doped, both the density of states and transition probabilities (Equation (2)) are modified and the Tauc coefficient may undergo further adjustments.

Typically, an optical band gap value of a material is estimated by taking the Tauc exponent n from the literature and simply using this value for fitting a straight line to the Tauc plot. However, studying the literature (particularly dedicated to TiO$_2$ nanotubes), one can find that in most cases the authors choose n results from the articles, without justification [14–18]. Therefore, there is a chain of publications in which experimentalists choose the same value of n as others and it is very hard or even impossible to find how it was estimated.

Nevertheless, TiO$_2$ has a well-estimated transition type - indirect (allowed), however, the problem arises for other metal oxides. For instance, in the literature dedicated to chromium oxide, one can find that some authors choose $n = 1/2$ corresponding to direct transition [19] whereas other ones $n = 2$ corresponding to the indirect one [20]. The problem of choosing Tauc exponent n also concerns composite materials if one exhibits a different transition than another.

It is worth noting that, there is also a potential source of uncertainty in taking inappropriate fitting range. The deviations from the linearity in the energies close to E_g are identified as Urbach tail and can lead to

erroneous estimates during Tauc plot fitting [8,21]. In particular, the band gap value is underestimated when the Tauc exponent is taken too high, or when the Urbach tail is more pronounced.

Apart from choosing the Tauc exponent, taking one linear range might be an insufficient analysis in some cases and could lead to the loss of physical insight into the variety of transitions occurring in the semiconductor. Indeed, semiconductors [7] and semiconducting heterostructures [22] can have multiple transitions and even multiple band gaps [23]. Therefore, it is often necessary to fit a few lines to gain a few corresponding transitions with different energy level separations. In particular, one can extract information about both direct and indirect transitions occurring in a formally indirect semiconductor such as silicon [8,24].

In this work, we present a simplified method allowing the determination of Tauc exponent n and transition type (or types) from registered UV–vis absorbance spectra. Considering the experience of our group with titanium dioxide, the most emphasis is put on this particular semiconductor allowing us to study the Tauc method and the introduced improvements. The general principle of the method is shown by estimating n for transparent TiO$_2$ thin film, TiO$_2$ nanotubes and composite materials made of TiO$_2$ nanotubes decorated with selected transition metal oxides. The proposed method is a development of the approach already introduced by Sangiorgi et al. [25]. Through the application of Taylor expansion to the logarithmic Tauc equation our approach allows to estimate Tauc exponent n and the transition types directly from absorption data without prior knowledge of the band gap value. In principle, it could be very useful for studying unknown materials and structures with a complicated set of transitions, as well as nanocrystalline semiconductors where the n value changes with the crystal size. Moreover, our experimental investigations showed that the method gives similar results for both absorbance and reflectance spectroscopy data.

2. Mathematical methods

The idea of our method is to estimate Tauc coefficient n from UV–vis spectroscopy data which can be accomplished by a series of steps. We start from the original Tauc equation (Equation (1)) and take both sides logarithm obtaining Equation (4):

$$\frac{1}{n}\log(\alpha h\nu) = \log(A) + \log(h\nu - E_g) \qquad (4)$$

It is not possible to give a closed expression of the difference of logarithms and to exactly separate the α dependence on the band gap and photon energy. To do so, Taylor expansion will be used, but firstly the substitution described by Equation (5) is introduced:

$$h\nu - E_g = t \qquad (5)$$

and for further convenience in the Taylor expansion another substitution is used:

$$t = 1 - x \qquad (6)$$

Therefore, Equation (4) can be expressed in the form of Equation (7):

$$\frac{1}{n}\log(\alpha h\nu) = \log(A) + \log(1 - x) \qquad (7)$$

Then, two Tylor expansions of the $\log(1 - x)$ series exist depending on the value of x:

$$\log(1 - x) = -\sum_{k=1}^{\infty}\frac{x^k}{k} \quad for|x| < 1 \qquad (8)$$

$$\log(1 - x) = \log(-x) - \sum_{k=1}^{\infty}\frac{x^{-k}}{k} \quad for|x| > 1 \qquad (9)$$

In our previous studies, we have shown that the difference between

the photon energy and the band gap energy for titania nanotubes is below 1 eV [26]. In other words, the values of $(1 - x)$ lie in the interval $(0, 1)$ and x is between 0 and 1. Therefore, only the expansion given by Equation (8) is taken into account, because Equation (9) does not fulfil this condition. Then, the Taylor expansion is put into Equation (7), yielding:

$$\frac{1}{n}\log(\alpha h\nu) = \log(A) - \left(x + \frac{x^2}{2} + \frac{x^3}{3} + \dots\right) \quad (10)$$

Finally, the substitutions from Equations (4) and (5) are reversed, and the following series are obtained:

$$\frac{1}{n}\log(\alpha h\nu) = \log(A) - (1 + E_g - h\nu) - \frac{(1 + E_g - h\nu)^2}{2} - \frac{(1 + E_g - h\nu)^3}{3} - \dots \quad (11)$$

As a result, a set of equations reflecting first, second, third, and higher-order approximations can be written. This enables determining the Tauc coefficient n. In the first-order approximation, one gets Equation (12):

$$\log(\alpha h\nu) = n\log(A) - n(1 + E_g) + nh\nu \quad (12)$$

Experimental data is then used to plot the $\log(\alpha h\nu)$ vs. $h\nu$ where n is obtained as a slope within the linear range. Another option is a derivative plot to obtain n directly:

$$n = \frac{\partial \log(\alpha h\nu)}{\partial(h\nu)} \quad (13)$$

In some cases, the shape of the plot is composed of few linear ranges and first order approximation is valid. However, a second-order approximation is needed in other cases when the plot becomes parabolic. The second-order can be expressed by Equation (14):

$$\log(\alpha h\nu) = n\left[\log(A) - (1 + E_g) - \frac{(1 + E_g)^2}{2}\right] + n[2 + E_g]h\nu - \frac{n}{2}(h\nu)^2 \quad (14)$$

For a better precision of the fitting range of the parabola one can use the first and second derivative (Equation (15)) and identify constant ranges that correspond to the linear or parabolic areas on the experimental logarithmic plot.

$$-n = \frac{\partial^2 \log(\alpha h\nu)}{\partial(h\nu)^2} \quad (15)$$

3. Experimental

3.1. Cleaning of fluorine-doped tin oxide (FTO)

FTO glass (Xinyan, 10 Ω/sq) was cut into (2.5×2) cm^2 pieces. Then, it was cleaned in sequence in acetone (Chempur, czda), isopropanol (Chempur, 96%, czda) and deionized water (HYDROLAB, 0.05 µS) for 10 min in each solvent in an ultrasound bath (Ultrasonic Cleaner, YJ5120-1). Subsequently, it was dried in a stream of cold air (Air Liquide, ALPHAGAZ™ 1 Air).

3.2. Fabrication of the TiO$_2$ nanotubes (TNT) and the composites - TNT with sputtered transition metal oxides

TiO$_2$ nanotubes were fabricated via 1 step anodization of titanium foil (abcr, 99.7%). First, the foil was cut into (2×3) cm^2 pieces. Subsequently, it has been cleaned in sequence in three solvents: acetone (Chempur, czda), ethanol (Chempur, 96%, czda) and deionized water (HYDROLAB, 0.05 µS), for 10 min in each one in an ultrasonic bath (ULTRASONIC CLEANER, YJ5120-1). Afterwards, plates were dried in the stream of cold air (Air Liquide, ALPHAGAZ™ 1 Air). Each anodization was realized in a two-electrode system where titanium foil served as an anode and platinum mesh as a cathode in a cell filled with

50 ml electrolyte containing: 0.5 g NH$_4$F (Chempur, czda), 7.5 ml deionized H$_2$O and 42.5 ml glycol ethylene (Chempur, czda). A fixed distance of 2 cm was kept between the electrodes. The temperature was set to 23 °C and it was controlled by a thermostat (Julabo F-12) working in flow mode. During the process, 40 V was maintained for 15 min with a voltage ramp-up and ramp-down times of 6.66 min. After the process, the samples were rinsed with ethanol and allowed to dry in the air freely. The as-obtained TNT were thermally annealed in a tubular furnace (Nabertherm, P330) at 450 °C in the air for 2 h using a heating ramp-up of 2 °C min^{-1}. After that time, the samples were allowed to cool down freely to an ambient temperature. The physicochemical properties of the resulting TiO$_2$ nanotubes can be found in our previous works [27].

Transition metals were deposited using a magnetron sputtering machine (Quorum, Q150T S) and metallic disc targets of chromium (TK8845, Quorum Technologies, Ø57 × 0.3 mm), molybdenum (Micro to nano, Ø57 × 0.25 mm, 99.95% Mo) and tungsten (Ø57 × 0.25 mm, 99.95% W). Prior to the deposition, the chamber has been thoroughly cleaned with isopropanol and a dust-free handkerchief. Each target was cleaned just before the deposition by applying current with the shutter closed. During the process, the amount of the deposited material was controlled by quartz crystal microbalance and it was set to 15 nm. After the deposition, the samples were thermally annealed at 450 °C for 2 h in a tubular furnace both to crystallize and oxidize the deposited materials.

3.3. UV–vis spectroscopy

Ultraviolet–visible spectroscopy measurements were performed using Lambda 35 UV-Vis Spectrometer. The data was collected in transmittance and reflectance ordinate modes for transparent TiO$_2$ thin film on FTO and TiO$_2$ nanotubes, respectively. Scan speed was set to 120 nm min^{-1} and slide width to 2 nm. Prior to the measurements, the device has been calibrated using clean FTO glass (Xinyan, 10 Ω/sq) and certified reflectance standard (Labsphere) for measurements performed in transmittance and reflectance modes, respectively.

The collected data from transmittance measurements was firstly used to calculate absorbance:

$$A = -\log_{10}(T) \quad (16)$$

and then, the absorption coefficient α was calculated using the following expression:

$$\alpha = -\frac{\ln(T)}{L} \frac{1 - (T + R)}{1 - T} \quad (17)$$

where L is the thickness of the TiO$_2$ film, T is the transmittance, and R is the reflectance.

In the case of reflectance measurements, the Kubelka-Munk radiative transfer model was used to extract a value proportional to α, since reflectance R is not directly proportional to the absorption coefficient:

$$f(R) = \frac{\alpha}{S} = \frac{(1 - R)^2}{2R} \quad (18)$$

where $f(R)$ is the Kubelka-Munk function and S is the scattering coefficient. Prior to Tauc plot construction $f(R)$ is used in place of α. It is made on the assumption that S is not wavelength dependent.

The registered wavelengths λ were calculated to photon energy accordingly:

$$h\nu(eV) = \frac{hc}{\lambda} = \frac{1239.8(eV \cdot nm)}{\lambda \,(nm)} \quad (19)$$

where h is the Planck constant and c is the speed of light.

3.4. Method for Tauc coefficient n estimation

The first step is the recording of UV–vis spectra. Then, depending on

3

the instrument ordinate mode (transmittance or reflectance) the data is calculated to absorption coefficient or a value proportional to absorption coefficient using the Kubelka-Munk model; wavelength is calculated to photon energy. Subsequently, $\log(\alpha h\nu)$ is plotted vs. $h\nu$. Depending on the run of the curve, particular range or ranges are fitted with linear or quadratic functions. Finally, the n value is estimated for each directional derivative and finally can be used for construction of the Tauc plot and further estimation of band gap or band gaps. The detailed procedure is visualized in Fig. 1.
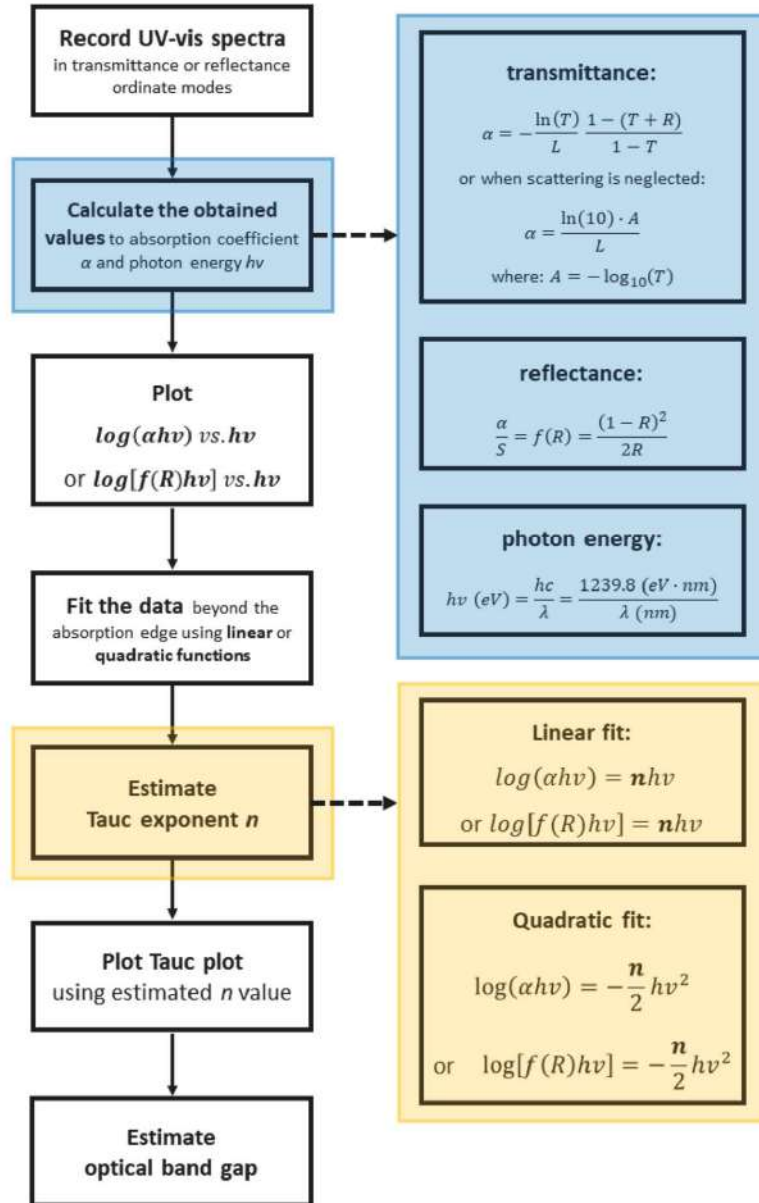
Fig. 1. The procedure allowing to estimate Tauc exponent n and optical band gap value from UV–vis spectroscopy data.

4

3.5. DFT + U calculations

DFT + U calculations were performed for bulk equilibrium crystalline anatase and rutile using Quantum ATK Synopsys R-2020 with all functions as implemented. LDA + U approach was used for band structure calculations with Perdew-Zunger (PZ) functional. Hubbard U parameter was set to 7.5 eV according to Patrick et al. [3] and Orhan et al. [28]. Fritz-Haber Institute (FHI) potentials were chosen with double zeta polarized functions as a basis set. $6 \times 6 \times 9$ k-point mesh with Monkhorst-Pack grid was selected as sampling. Zero energy was assumed as the middle of a band gap.

4. Results and discussion

First, the transition types from the measured UV–vis data in transmission mode are studied. The $\log(f(R)h\nu)$ vs. $h\nu$ plot for the thin 15 nm film of TiO_2 on FTO is displayed in Fig. 2 a. Two linear ranges are identified. The first located at photon energy from about 3.50 to 3.60 eV, is assigned indirect (allowed) transition as the n directly corresponds to the originally derived value of 2. The second one located in the range of 3.80–3.90 eV does not correspond to any original n of 1/2, 2, 3/2 nor 3. Therefore, it is speculated that more than one transition is probable. Assuming that the $n = 1.2$ results from the overlapping of two (or more) other n values, the unquestionable transition is direct (allowed) because the n is higher than 1/2 and lower than 3/2. However, the remaining transitions could be any of the others including direct (forbidden), indirect (allowed) or indirect (forbidden).

Tauc plots corresponding to estimated transitions for the TiO_2 thin 15 nm film on FTO are presented in Fig. 2 b and c. The optical band gaps were estimated from the intersection of the fitted straight line with the abscissa axis. They are 3.10 and 3.40 eV for the first and second linear ranges, respectively. The estimated n values along with the listed probable transitions and the optical band gaps are given in Table 1.

The $\log(f(R)h\nu)$ vs. $h\nu$ plots for the TiO_2 nanotubes (TNT) and the

Table 1
Estimated Tauc coefficients and corresponding probable transitions for the TiO_2 thin film, TiO_2 nanotubes and the composites.

Ordinate mode	Sample	Estimated Tauc coefficient n	R-Square	Transition	Band Gap/ eV
transmittance	TiO_2| FTO	2.0	0.998	indirect (allowed),	3.10
		1.2	0.999	direct (allowed) and others	3.40
reflectance	TNT	1.9	0.993	indirect (allowed)	2.91
		1.1	0.981	direct (allowed) and others	3.23
	Cr_2O_3| TNT	1.0	0.984	direct (allowed) and others	3.33
	MoO_3| TNT	1.5	0,993	direct (forbidden)	3.07
	WO_3| TNT	1.5	0.996	direct (forbidden)	2.99

composites - TNT with sputtered thin 15 nm films of Cr_2O_3, MoO_3 and WO_3 are displayed in Fig. 3. In the case of pristine TiO_2 nanotubes, two linear ranges are found. The first is located right outside the absorption edge at about 3.35–3.50 eV whereas the second one is at about 3.55–3.75 eV. The estimated n values are 1.9 and 1.1, respectively. Note that the values are similar to those obtained from the measurements performed in transmission for a thin film of TiO_2 on FTO. Similarly, the $n = 1.9$ is assigned to indirect (allowed) transition whereas $n = 1.1$ to direct (allowed) and one or more of the others. Therefore, we speculate that there are two band gaps. Photons with lower energy can be absorbed *via* indirect (allowed) transition whereas in the case of higher energy photons there are two or more permitted transitions.
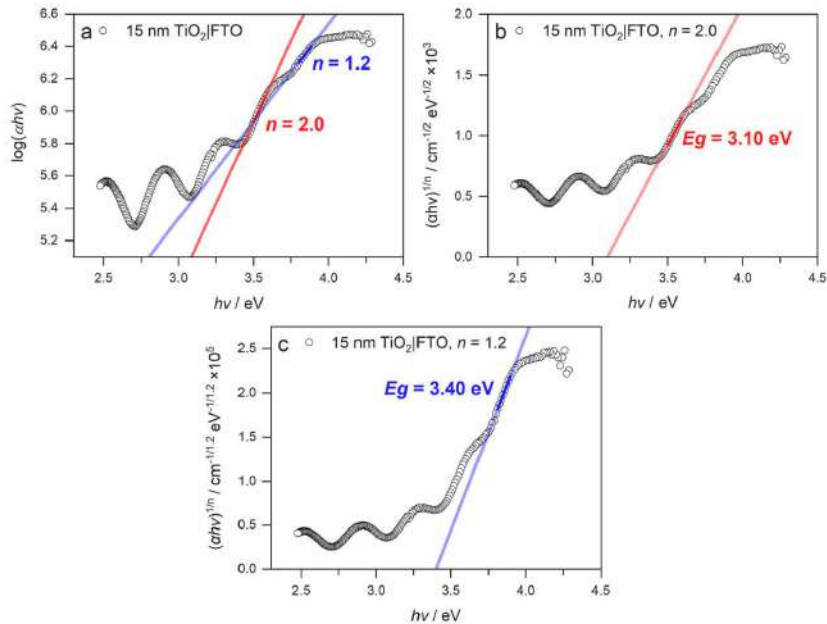
Fig. 2. The absorption data for the thin 15 nm film of TiO_2 on FTO: (a) $\log[f(R)h\nu]$ vs. $h\nu$ plot, (b) and (c) Tauc plots.
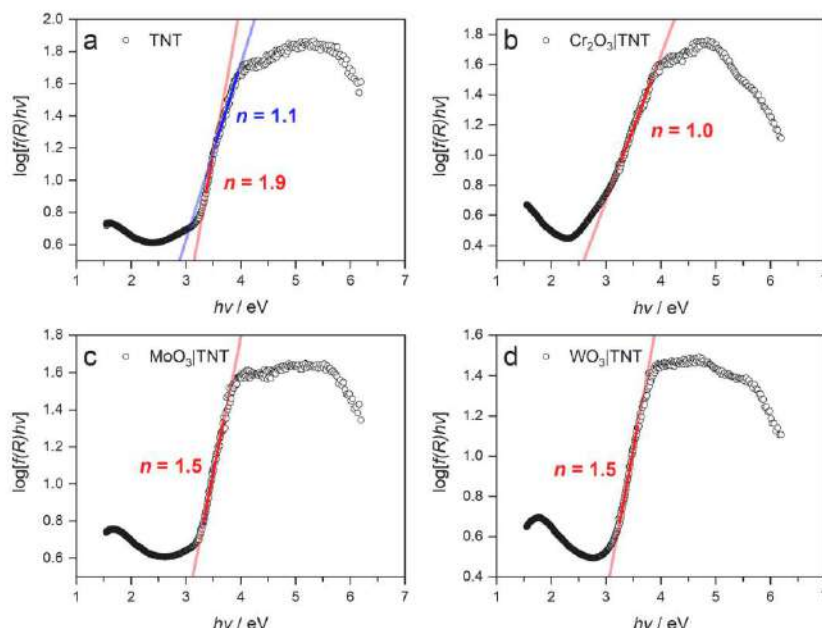
5

Fig. 3. $\log[f(R)h\nu]$ vs. $h\nu$ plots for the (a) TiO$_2$ nanotubes (TNT) and the composites - TNT with sputtered thin 15 nm films of (b) Cr$_2$O$_3$ (Cr$_2$O$_3$|TNT), (c) MoO$_3$ (MoO$_3$|TNT) and (d) WO$_3$ (WO$_3$|TNT).

The Cr$_2$O$_3$|TNT (Fig. 3 b) exhibits $n = 1.0$. It is assigned to direct (allowed) and one or more other probable transitions. The MoO$_3$|TNT (Fig. 3 c) and WO$_3$|TNT (Fig. 3 d) exhibit $n = 1.5$ corresponding to the originally derived value, and thus, they are assigned direct (forbidden) transition. This is contradictory to the experimentalists who tend to choose $n = 1/2$ or $n = 2$ for Cr$_2$O$_3$ [19,20], MoO$_3$ [29,30] and WO$_3$ [31, 32] thin films for Tauc plot construction.

For comparison purposes, the Tauc exponents were also estimated *via* fitting the data with quadratic functions (see Fig. S1 in Supplementary Information file) for the TNT and the composites. It is worth noting that, the n values are similar to those estimated from linear functions.

It is also worth comparing the results obtained from our method to those from the method previously reported by Sangiorgi et al. [25]. At first, the cited method requires knowledge of the material's band gap. Then, the experimental data is plotted as $\log[f(R)h\nu]$ vs. $\log(h\nu\text{-}Eg)$. Finally, the Tauc coefficient n is estimated from the slope of the linear fit. We applied Sangiorgi et al. [25] method for our data from the TiO$_2$ nanotubes, assuming different E_g values equal to 2.8, 2.9, 3.0, 3.1, 3.2 and 3.3 eV. The results are displayed in Fig. S2 in the Supplementary Information file. The estimated Tauc coefficients n are: 2.16, 1.84, 1.61, 1.35, 1.19, and 1.0 eV, respectively. Therefore, the Tauc coefficient estimated from the method proposed by Sangiorgi et al. [25] highly depends on the assumed value of band gap. Such a problem does not concern the method described in the present work. Herein, Tauc coefficient n is estimated directly from the measured UV–vis spectra simply by plotting $\log[(f(R)h\nu]$ vs. $h\nu$ and there is no need to assume band gap value. An alternative approach for n estimation involving an inverse logarithmic derivative of Tauc or Cody expressions was developed by Jarosiński et al. [33]. Resulting n values for TiO$_2$ layers were also equal to 1 with a corresponding band gap equal to 3.24 eV. This method is particularly focused on studying multilayers.

Tauc plots for the TiO$_2$ nanotubes and the composites are presented in Fig. 4. The Tauc coefficients n taken for the construction of the Tauc

plot correspond to those estimated from the $\log[f(R)h\nu]$ vs. $h\nu$ plots and not to the quantized ones ($n = 3$, 2, 3/2 and 1/2). Band gaps were estimated from the intersection of the fitted straight line with the abscissa axis. The range for linear fit was chosen outside the exponential tail corresponding to the absorption edge. The results indicate that the TiO$_2$ nanotubes (TNT) exhibit 2.91 eV of indirect band gap and 3.23 eV of a direct one. In the case of indirect transition, the estimated band gap is very close to the value for TiO$_2$ nanotubes fabricated in ethylene glycol, equal to 2.84 eV [34]. The composite materials exhibit band gap of 3.33, 3.07 and 2.99 eV for the Cr$_2$O$_3$|TNT, MoO$_3$|TNT and WO$_3$|TNT, respectively. The literature values for Cr$_2$O$_3$, MoO$_3$ and WO$_3$ thin films are about 2.90–3.20 eV and depend on the annealing temperature [20, 29,31]. Also, in this work different n values were chosen. Therefore, the estimated values cannot be directly compared.

The presence of two ranges in the $\log[f(R)h\nu]$ vs. $h\nu$ plots and correspondingly two calculated band gap values can be justified by the fact that TiO$_2$ nanotubes are composed of both anatase and rutile phases. The first range with n = 1.9 corresponds to E_g = 2.91 eV which resembles experimentally (3.03 eV) [35] and computationally (2.99 eV) estimated band gap value for rutile (see DFT + U simulations section). Per analogy, the second range with n = 1.1 corresponds to E_g = 3.23 eV, which most probably comes from anatase phase. Moreover, there is only one linear range in case of TNT composites. This is expectable, because the transition metals are sputtered on the surface of TNT, where only the anatase is present. Therefore, the linear range corresponding to the rutile phase is diminished.

Band structures calculated using density functional theory with Hubbard correction and density of states of rutile and anatase TiO$_2$ are presented in Figs. 5 and 6, respectively. Rutile has a tetragonal crystal structure with P4$_2$/mm point group symmetry. It exhibits both direct and indirect band gap calculated as 2.99 eV, which is very close to the experimental value of 3.03 eV obtained with a high resolution absorption spectroscopy [35] and other more accurate simulations involving
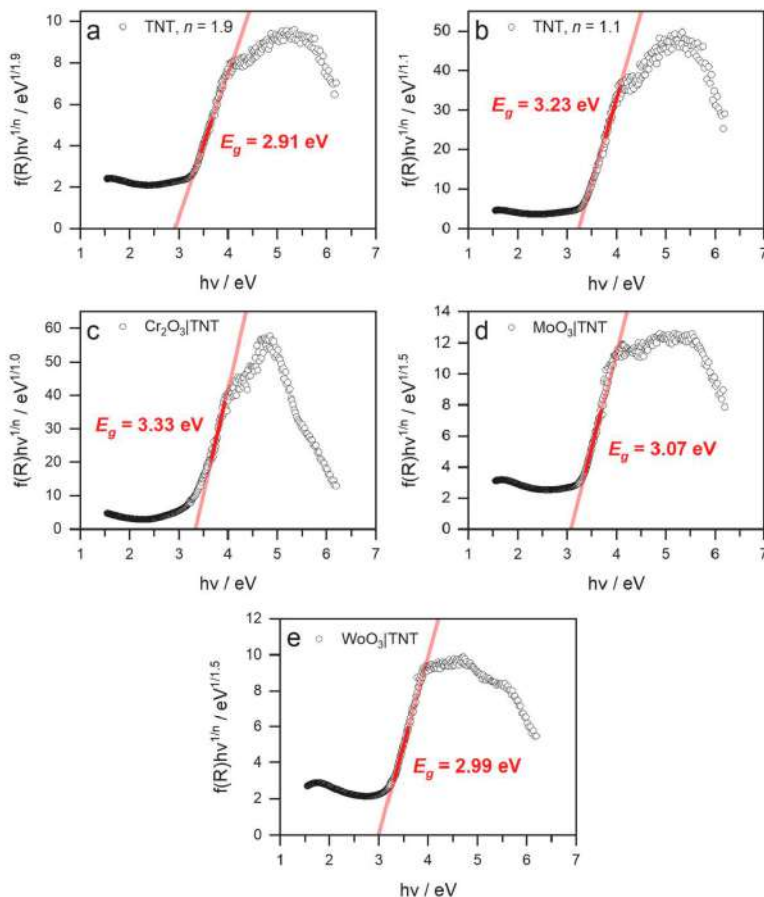
6

Fig. 4. Tauc plots for the (a) TiO_2 nanotubes (TNT) and the composites - TNT with sputtered thin 15 nm films of (b) Cr_2O_3 (Cr_2O_3|TNT), (c) MoO_3 (MoO_3|TNT) and (d) WO_3 (WO_3|TNT).

DFT + U + J approach: 3.04 eV [28]. Anatase also has a tetragonal structure with $I4_1/amd$ point group symmetry. It exhibits a typical indirect band gap of 3.42 eV which is also close to the experimental value of 3.47 eV obtained from Angle Resolved Photoemission Spectroscopy (ARPES) [36] or 3.50 eV from DFT + U + J [28]. Moreover, in the case of anatase also a direct band gap can be distinguished and in the gamma point is equal to 3.93 eV.

It is worth noting that, these band structures are calculated for non-defected materials, and therefore, sub-band levels are not identified. Generally, during the absorption experiment, more than one transition occurs [8]. Comparison of theoretical and experimental band gap values leads to several observations. First, the calculated values are higher compared to experimental ones, because the optical band gap is lower regarding the electronic band gap and the difference is in the exciton binding energy [37]. Then according to Tauc plots, there are two transitions for pristine TiO_2 regardless of its morphology (film or nano-tubes). The first linear range with n = 2.0 was ascribed to indirect allowed and the second range with n = 1.2 to the direct mixed with indirect transitions. Nonetheless, the first range corresponds to a lower bandgap than the second one. This statement is in agreement with a

straightforward theoretical prediction that the direct transition is possible for higher photon energies (see Fig. 6).

Moreover, according to the considerations based on the Fermi golden rule, the probability of a direct transition is higher compared to the indirect one. Therefore, the direct transition should dominate the spectrum of rutile. In the case of anatase, the indirect transition should dominate for lower photon energies. However, for higher photon energies both transitions are probable, and therefore, the direct transition is more probable, which is reflected as the second linear range both in the experimental logarithmic plots and in theoretical band structures. Such phenomenon is known in the model indirect semiconductor – intrinsic silicon, for photon energies exceeding 3 eV [38].

The results presented in Figs. 2 and 3 obtained via transmission and diffuse reflectance spectroscopy show that two transitions are indeed present for both TiO_2 thin film and nanotubes. The band structure analysis supports our approach that more than one optical transition should be taken into account when interpreting experimentally determined Tauc coefficient n, and therefore, calculated bandgap. This issue is an important topic in the field of designing photoactive semi-conductors, in particular, in the case of maximizing efficiencies of

7
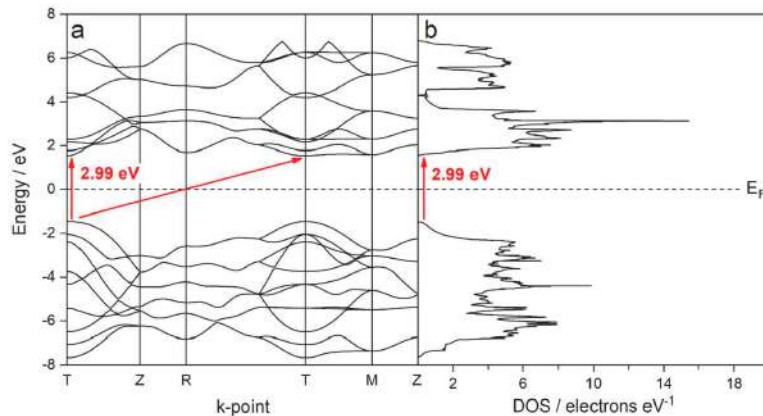
Fig. 5. (a) Band structure and (b) DOS for rutile TiO$_2$ calculated using DFT + U approach.
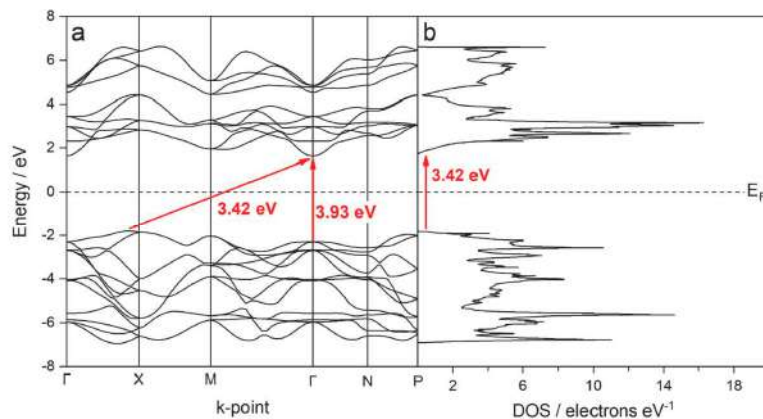
Fig. 6. (a) Band structure and (b) DOS for anatase TiO$_2$ calculated using DFT + U approach.

energy conversion in real devices. This might be especially important in the cases, where the band gap depends on the design and construction details [10]. It is also believed that the information gathered from the estimated Tauc coefficients can be beneficial to explain the differences in the photoresponse of nanomaterials and composites.

5. Conclusions

In this work, a facile method allowing for direct estimation of the Tauc coefficient n and the transition type from the obtained UV–vis spectroscopy data is presented. The method involves plotting $\log(\alpha h\nu)$ vs. $h\nu$ and fitting the data with linear or quadratic functions. The n value can be calculated from the slope factor. It was applied to transparent TiO$_2$ thin nm film on FTO (TiO$_2$|FTO), non-transparent bare TiO$_2$ nanotubes (TNT) and those with deposited thin 15 nm films of Cr$_2$O$_3$ (Cr$_2$O$_3$|TNT), MoO$_3$ (MoO$_3$|TNT), and WO$_3$ (WO$_3$|TNT). The obtained n values were used for further construction of Tauc plots.

For the TiO$_2$|FTO, two linear ranges were found. They correspond to $n = 2.0$ (E$_g$ = 3.10 eV) and 1.2 (E$_g$ = 3.40 eV). The first was assigned to indirect (allowed) transition whereas the second to more than one probable transition. Similar n values of 1.9 (E$_g$ = 2.91 eV) and 1.1 (E$_g$ =

3.23 eV) were found for the TNT. For the Cr$_2$O$_3$|TNT single transition with $n = 1.0$ (E$_g$ = 3.33 eV) was found. Since the value does not correspond to any original n directly, it is speculated that besides direct (allowed), any of the other transitions could be probable. For the MoO$_3$| TNT and WO$_3$|TNT, $n = 1.5$ was estimated. It was assigned to direct (forbidden) transition and the estimated band gaps are 3.07 and 2.99 eV, respectively.

In addition to that, band structures and density of states were calculated for rutile and anatase TiO$_2$ using density functional theory with Hubbard correction. The obtained results indicate that rutile exhibits both direct and indirect transition corresponding to 2.99 eV, whereas anatase indirect with 3.42 eV. The theoretical study supports our approach that more than one transition should be taken into account when interpreting experimentally measured absorption data.

CRediT authorship contribution statement

Łukasz Haryński: Conceptualization, Methodology, Validation, Investigation, Data curation, Writing – original draft, Writing – review & editing, Visualization, Project administration. **Adrian Olejnik:** Conceptualization, Methodology, Formal analysis, Writing – original

draft, Writing – review & editing, Visualization, Project administration. **Katarzyna Grochowska:** Writing – review & editing, Supervision. **Katarzyna Siuzdak:** Resources, Writing – review & editing, Supervision, Funding acquisition.

Declaration of competing interest

The authors declare that they have no known competing financial interests or personal relationships that could have appeared to influence the work reported in this paper.

Acknowledgements

Appendix A. Supplementary data

Supplementary data to this article can be found online at https://doi.org/10.1016/j.optmat.2022.112205.

References

[1] M.D. Scafetta, A.M. Cordi, J.M. Rondinelli, S.J. May, Band structure and optical transitions in LaFeO₃: theory and experiment, J. Phys. Condens. Matter 26 (2014) 505502, https://doi.org/10.1088/0953-8984/26/50/505502.

[2] A. Stan, N.E. Dahlen, R. van Leeuwen, Levels of self-consistency in the GW approximation, J. Chem. Phys. 130 (2009) 114105, https://doi.org/10.1063/1.3089567.

[3] C.E. Patrick, F. Giustino, GW quasiparticle bandgaps of anatase TiO₂ starting from DFT+U, J. Phys. Condens. Matter 24 (2012) 202201, https://doi.org/10.1088/0953-8984/24/20/202201.

[4] D.A. Papaconstantopoulos, M.J. Mehl, The Slater–Koster tight-binding method: a computationally efficient and accurate approach, J. Phys. Condens. Matter 15 (2003) R413, https://doi.org/10.1088/0953-8984/15/10/201.

[5] A. Damascelli, Probing the electronic structure of complex systems by ARPES, Phys. Scripta T109 (2004) 61–74, https://doi.org/10.1238/Physica.Topical.109a00061.

[6] A. Dolgonos, T.O. Mason, K.R. Poeppelmeier, Direct optical band gap measurement in polycrystalline semiconductors: a critical look at the Tauc method, J. Solid State Chem. 240 (2014) 43–48, https://doi.org/10.1016/j.jssc.2016.05.010.

[7] W.P. Dumke, Optical transitions involving impurities in semiconductors, Phys. Rev. 132 (1963) 1998–2002, https://doi.org/10.1103/PhysRev.132.1998.

[8] J.B. Coulter, D.P. Birnie, Assessing Tauc plot slope quantification: ZnO thin films as a model system, Phys. Status Solidi B 255 (2018) 1700393.

[9] Y. Feng, S. Lin, S. Huang, G. Conibeer, Can Tauc plot extrapolation be used for direct-band-gap semiconductor nanocrystals? J. Appl. Phys. 117 (2015) 125701, https://doi.org/10.1063/1.4916090.

[10] S.K. Suram, P.F. Newhouse, J.M. Gregoire, High throughput light absorber discovery, Part 1: an algorithm for automated Tauc analysis, ACS Comb. Sci. 18 (2016) 673–681, https://doi.org/10.1021/acscombsci.6b00053.

[11] A. Dolgonos, T.O. Mason, K.R. Poeppelmeier, Direct optical band gap measurement in polycrystalline semiconductors: a critical look at the Tauc method, J. Solid State Chem. 240 (2016) 43–48, https://doi.org/10.1016/j.jssc.2016.05.010.

[12] E.A. Davis, N.F. Mott, Original Articles Conduction in non-crystalline systems V. Conductivity, optical absorption and photoconductivity in amorphous semiconductors, Philos. Mag. A J. Theor. Exp. Appl. Phys. 22 (1970) 903–922, https://doi.org/10.1080/14786437008221061.

[13] C. Kittel, Introduction to Solid State Physics, eighth ed., Wiley, 2004.

[14] N.S. Peighambardoust, S. Khameneh Asl, R. Mohammadpour, S.K. Asl, Band-gap narrowing and electrochemical properties in N-doped and reduced anodic TiO₂ nanotube arrays, Electrochim. Acta 270 (2018) 245–255, https://doi.org/10.1016/j.electacta.2018.03.091.

[15] Y. Cao, T. Wu, W. Dai, H. Dong, X. Zhang, TiO₂ nanosheets with the Au nanocrystal-decorated edge for mitochondria-targeting enhanced sonodynamic therapy, Chem. Mater. 31 (2019) 9105–9114, https://doi.org/10.1021/acs.chemmater.9b03430.

[16] H. Kaur, S. Kaur, J. Singh, M. Rawat, S. Kumar, Expanding horizon: green synthesis of TiO₂ nanoparticles using Carica papaya leaves for photocatalysis application, Mater. Res. Express 6 (2019), 095034.

[17] P. Parthasarathy, Synthesis and UV detection characteristics of TiO₂ thin film prepared through sol gel route, IOP Conf. Ser. Mater. Sci. Eng. 360 (2018), 012056.

[18] R. Kaur Jyoti, J. Sharma, S.K. Tripathi, Synthesis and characterization of TiO₂ nanoparticles for memory device application, AIP Conf. Proc. 2220 (2020), 020056, https://doi.org/10.1063/5.0001842.

[19] Z. Hu, M. Xu, Z. Shen, J.C. Yu, A nanostructured chromium(iii) oxide/tungsten(vi) oxide p–n junction photoanode toward enhanced efficiency for water oxidation, J. Mater. Chem. A. 3 (2015) 14046–14053.

[20] C.-S. Cheng, H. Gomi, H. Sakata, Electrical and optical properties of Cr₂O₃ films prepared by chemical vapour deposition, Phys. Status Solidi 155 (1996) 417–425, https://doi.org/10.1002/pssa.2211550215.

[21] P. Makuła, M. Pacia, W. Macyk, How to correctly determine the band gap energy of modified semiconductor photocatalysts based on UV–vis spectra, J. Phys. Chem. Lett. 9 (2018) 6814–6817, https://doi.org/10.1021/acs.jpclett.8b02892.

[22] S.R. White, L.J. Sham, Electronic properties of flat-band semiconductor heterostructures, Phys. Rev. Lett. 47 (1987) 879–882, https://doi.org/10.1103/PhysRevLett.47.879.

[23] S. Licht, Multiple band gap semiconductor/electrolyte solar energy conversion, J. Phys. Chem. B 105 (2001) 6281–6294, https://doi.org/10.1021/jp010552j.

[24] W.B. Jackson, S.M. Kelso, C.C. Tsai, S.-J. Oh, Energy dependence of the optical matrix element in hydrogenated amorphous and crystalline silicon, Phys. Rev. B 31 (1985) 5187–5198, https://doi.org/10.1103/PhysRevB.31.5187.

[25] N. Sangiorgi, L. Aversa, R. Tatti, R. Verucchi, A. Sanson, Spectrophotometric method for optical band gap and electronic transitions determination of semiconductor materials, Opt. Mater. 64 (2017) 18–25, https://doi.org/10.1016/j.optmat.2016.11.014.

[26] P. Kupracz, K. Grochowska, J. Wawrzyniak, K. Siuzdak, The interaction of the pulsed laser irradiation with titania nanotubes - theoretical studies on the thermal effect, Int. J. Therm. Sci. 162 (2021) 106800, https://doi.org/10.1016/j.ijthermalsci.2020.106800.

[27] Ł. Haryński, K. Grochowska, J. Karczewski, J. Ryl, K. Siuzdak, Scalable route towards superior photoresponse of UV-Laser-Treated TiO₂ nanotubes, ACS Appl. Mater. Interfaces 12 (2020) 3225–3235, https://doi.org/10.1021/acsami.9b19206.

[28] O.K. Orhan, D.D. O'Regan, First-principles Hubbard U and Hund's J corrected approximate density functional theory predicts an accurate fundamental gap in rutile and anatase TiO₂, Phys. Rev. B 101 (2020) 245137, https://doi.org/10.1103/PhysRevB.101.245137.

[29] K.M. Shafeeq, E. Rizwana, C.H.R. Kishor, P.M. Aneesh, Growth and characterization of α-MoO₃ thin films grown by spray pyrolysis technique, AIP Conf. Proc. (2019) 1–5, https://doi.org/10.1063/1.5093870, 2082.

[30] M. Szkoda, K. Trzciński, M. Łapiński, A. Lisowska-Oleksiak, Photoinduced K⁺ intercalation into MoO₃/FTO photoanode—the impact on the photoelectrochemical performance, Electrocatalysis 11 (2020) 111–120, https://doi.org/10.1007/s12678-019-00561-2.

[31] S.K. Gullapalli, R.S. Vemuri, C.V. Ramana, Structural transformation induced changes in the optical properties of nanocrystalline tungsten oxide thin films, Appl. Phys. Lett. 96 (2010), https://doi.org/10.1063/1.3421540.

[32] L. Mohan, A.V. Avani, P. Kathirvel, R. Marnadu, J.R. Joshua, M. Shkir, S. Saravanakumar, Investigation on structural, morphological and electrochemical properties of Mn doped WO₃ nanoparticles synthesized by co-precipitation method for supercapacitor applications, J. Alloys Compd. 882 (2021) 160670.

[33] Ł. Jarosiński, J. Pawlak, S.K.J. Al-Ani, Inverse logarithmic derivative method for determining the energy gap and the type of electron transitions as an alternative to the Tauc method, Opt. Mater. 88 (2019) 667–673, https://doi.org/10.1016/j.optmat.2018.12.041.

[34] P. Roy, S. Berger, P. Schmuki, TiO₂ nanotubes: synthesis and applications, Angew. Chem. Int. J. 50 (2011) 2904–2939, https://doi.org/10.1002/anie.201001374.

[35] J. Pascual, J. Camassel, H. Mathieu, Fine structure in the intrinsic absorption edge of TiO₂, Phys. Rev. B 18 (1978) 5606–5614, https://doi.org/10.1103/PhysRevB.18.5606.

[36] E. Baldini, L. Chiodo, A. Dominguez, M. Palummo, S. Moser, M. Yazdi-Rizi, G. Auböck, B.P.P. Mallett, H. Berger, A. Magrez, C. Bernhard, M. Grioni, A. Rubio, M. Chergui, Strongly bound excitons in anatase TiO₂ single crystals and nanoparticles, Nat. Commun. 8 (2017) 1–11, https://doi.org/10.1038/s41467-017-00016-6.

[37] A. Chaves, J.G. Azadani, H. Alsalman, D.R. da Costa, R. Frisenda, A.J. Chaves, S. H. Song, Y.D. Kim, D. He, J. Zhou, A. Castellanos-Gomes, F.M. Peeters, Z. Liu, C. L. Hinkle, S.-H. Oh, P.D. Ye, S.J. Koester, Y.H. Lee, P. Avouris, X. Wang, T. Low, Bandgap engineering of two-dimensional semiconductor materials, Npj 2D, Mater. Appl. 4 (2020) 29, https://doi.org/10.1038/s41699-020-00162-4.

[38] D.E. Aspnes, A.A. Studna, Dielectric functions and optical parameters of Si, Ge, GaP, GaAs, GaSb, InP, InAs, and InSb from 1.5 to 6.0 eV, Phys. Rev. B 27 (1983) 985–1009, https://doi.org/10.1103/PhysRevB.27.985.

Supporting Information

A Precise Method for Tauc Exponent and Corresponding Electronic Transitions Determination in Semiconductors from UV-Vis Spectroscopy Data

Łukasz Haryński[a,1,*], Adrian Olejnik[a,b,1], Katarzyna Grochowska[a], and Katarzyna Siuzdak[a]
[1]These authors contributed equally to this work

[a]*Centre for Plasma and Laser Engineering, The Szewalski Institute of Fluid−Flow Machinery, Polish Academy of Sciences, Fiszera 14 Street, 80-231 Gdańsk, Poland*
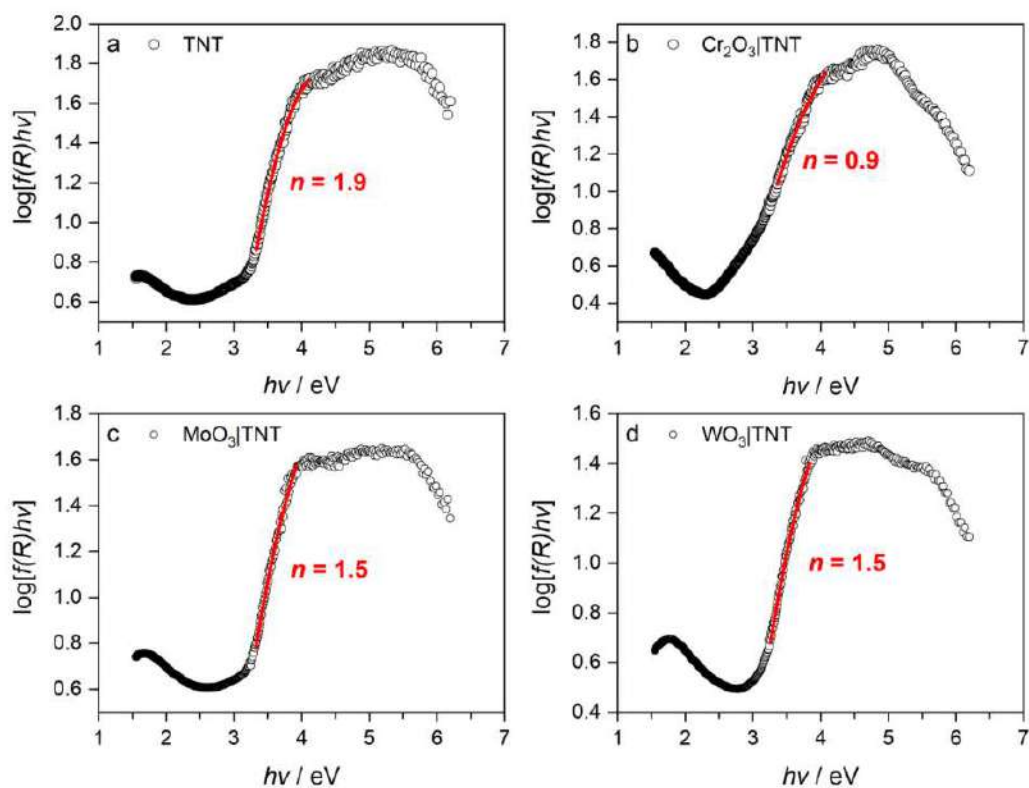[b]*Faculty of Electronics, Telecommunications And Informatics, Gdańsk University of Technology, Narutowicza 11/12 Street, 80-233 Gdańsk, Poland*

[*]Corresponding author: Łukasz Haryński (email address: lharynski@imp.gda.pl)

[1]These authors contributed equally to this work.

Section S1: Log($f(R)hv$) *vs.* hv plots fitted with square function for the TiO_2 nanotubes and the composites.

Figure S1. Log($f(R)hv$) *vs.* hv plots for the (a) TiO_2 nanotubes (TNT) and the composites - TNT with sputtered thin 15 nm films of (b) Cr_2O_3 (Cr_2O_3|TNT), (c) MoO_3 (MoO_3|TNT) and (d) WO_3 (WO_3|TNT).

Section S2: Tauc coefficients n from the TiO$_2$ nanotubes estimated *via* Sangiorgi et al.[1] method
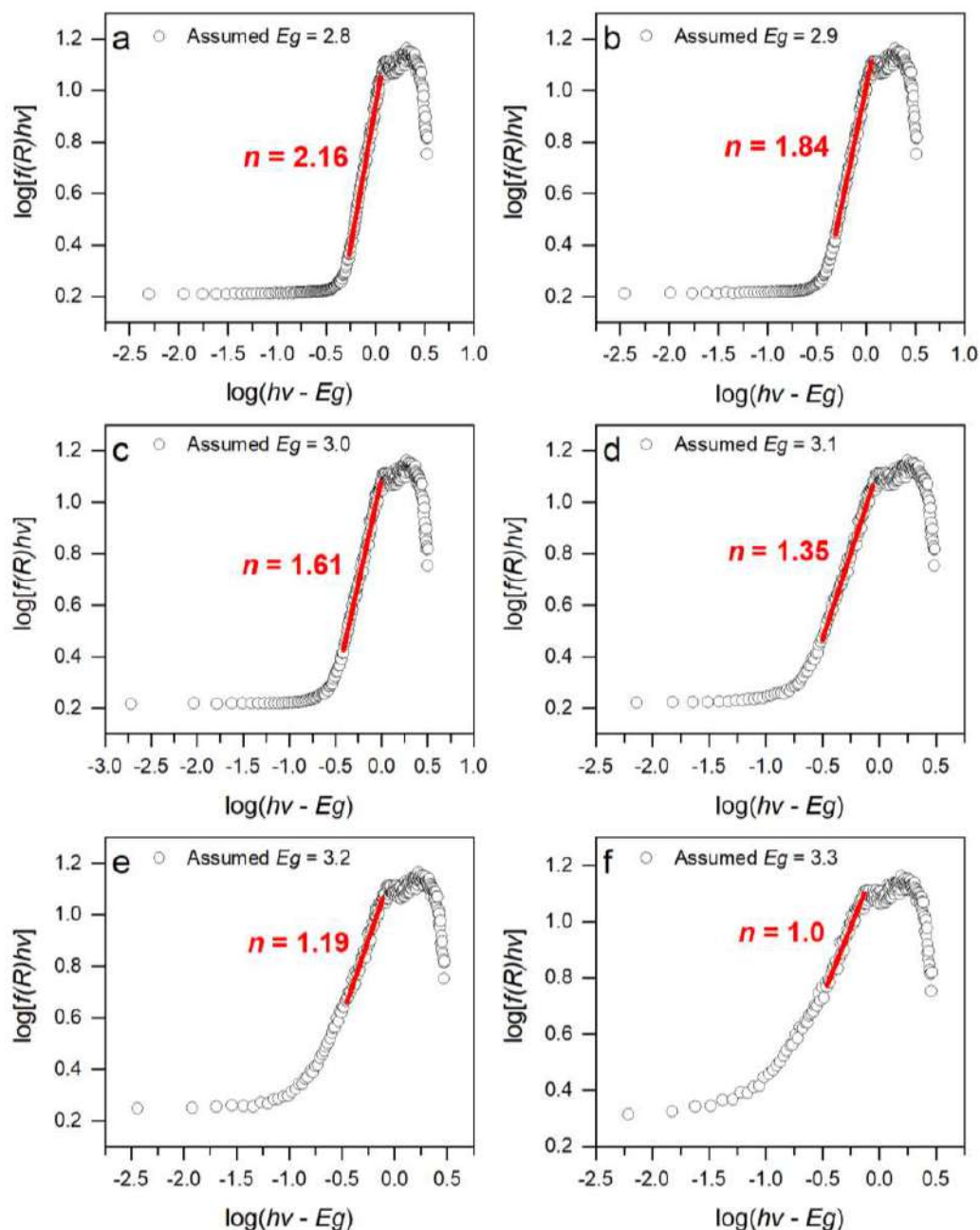
Figure S2. $\log[f(R)hv)$ vs. $\log(hv\text{-}Eg)$ from the TiO$_2$ nanotubes (TNT) assuming a different band gap Eg values of: (a) 2.8 eV, (b) 2.9 eV, (c) 3.0 eV, (d) 3.1 eV, (e) 3.2 eV), and (f) 3.3 eV.

Section S3: References

[1] N. Sangiorgi, L. Aversa, R. Tatti, R. Verucchi, A. Sanson, Spectrophotometric method for optical band gap and electronic transitions determination of semiconductor materials, Opt. Mater. (Amst). 64 (2017) 18–25. https://doi.org/https://doi.org/10.1016/j.optmat.2016.11.014.

5.4. Paper 4: Linking Optical and Electronic Properties to Photoresponse of Heterojunctions Based on Titania Nanotubes and Chromium, Molybdenum, and Tungsten Oxides.

In the previous work (paper 3) a precise method for the determination of Tauc exponent for the TiO_2 nanotubes combined with Cr, Mo, and W oxides, deposited using magnetron sputtering technology was presented. On the basis of the obtained values, each sample was assigned with an electronic transition type: TNT to indirect (allowed), Cr_2O_3|TNT to direct (allowed) and others, while MoO_3|TNT and WO_3|TNT to direct (forbidden). This work focuses on the investigation of the optical properties and band structure of the investigated samples. In particular, the correlation between the estimated transition types and the photocurrent generation is considered.

SEM images (see Fig. S2 in the supporting information) revealed that after magnetron sputtering of metals, the deposited species are located around the top of the nanotubes while the subsequent thermal treatment results in the formation of aggregates of nanoparticles (see Fig. 1 in the paper). The deconvolution of the high-resolution XPS spectra revealed that TiO_2 is in the +4 oxidation state, however, a weak signal from the +3 oxidation state suggesting the presence of oxygen vacancy was also found. Spectra registered from the TiO_2 nanotubes after magnetron sputtering of metals followed by the calcination showed that chromium forms different oxides Cr_2O_3, CrO_2, CrO_3, and CrOOH, molybdenum non-stoichiometric MoO_3 whereas tungsten is solely in the WO_3 state. The linear sweep voltammograms registered under AM 1.5 G, 100 mW cm^{-2} illumination (see Fig. 7 a in the paper) demonstrated that the Cr_2O_3|TNT exhibits 1.65-fold superior photoresponse compared to the bare TiO_2 nanotubes. UV-vis and photocurrent spectra (see Fig. 3 and Fig. 4 in the paper, respectively) revealed an Urbach tail which indicates sub-band gap absorption. LSV tests registered with an installed UV filter (see Fig. 7 b in the paper 4) revealed over 17-fold increased photoresponse of Cr_2O_3|TNT compared to bare TiO_2 nanotubes and confirmed enabled visible light absorption. The analysis of Mott-Schottky plots (see Figure S6 in supporting information), in turn, showed a positive shift of flat band potential. Therefore, the obtained results clearly indicate that magnetron sputtering of Cr followed by calcination results in the formation of additional states deep within the band gap which contribute to the absorption of visible light. The opposite tendency namely deteriorated photoresponse (see Fig. 7 a in the paper), was, however, found for the MoO_3|TNT and WO_3|TNT. No distinct difference between the absorption spectra, optical band gaps, and flat-band potentials compared to the bare TiO_2 nanotubes has been found. Nevertheless, the estimated Tauc exponents for

these materials ($n = 1.4$) suggest the forbidden nature of the transitions (see Fig. 5 in the paper) which was found to be responsible for deteriorated photoresponse. The above-described considerations were supported by theoretical study. The projected local density of states for the heterojunctions demonstrated that mid-gap states at the $TiO_2|Cr_2O_3$ are the most densely populated which correlates with the experimental data.

Summarizing, chromium, molybdenum, and tungsten oxides were applied to TiO_2 nanotubes using magnetron sputtering technology. It was demonstrated that the deposition of chromium oxides can significantly enhance the visible photoresponse of the TiO_2 nanotubes which is crucial for further applications in photoelectrochemical devices. Moreover, based on the obtained results for all the considered heterojunctions, it is anticipated that the estimation of the transition type based on the Tauc exponent is a crucial diagnostic parameter for sample photoresponse, even better than the optical band gap.

Research Article

Linking optical and electronic properties to photoresponse of heterojunctions based on titania nanotubes and chromium, molybdenum, and tungsten oxides

Łukasz Haryński [a,*], Adrian Olejnik [b], Jakub Karczewski [c], Jacek Ryl [c], Katarzyna Grochowska [a], Katarzyna Siuzdak [a]

[a] Centre for Plasma and Laser Engineering, The Szewalski Institute of Fluid–Flow Machinery, Polish Academy of Sciences, Fiszera 14 Street, 80-231, Gdańsk, Poland
[b] Department of Metrology and Optoelectronics, Faculty of Electronics, Telecommunications and Informatics, Gdańsk University of Technology, Narutowicza 11/12 St., 80-233, Gdańsk, Poland
[c] Faculty of Applied Physics and Mathematics, Institute of Nanotechnology and Materials Engineering, Gdańsk University of Technology, Narutowicza 11/12 Street, 80-233, Gdańsk, Poland

ABSTRACT

The development of photosensitization strategies for titanium dioxide is necessary for the enhancement of its optical and electronic properties towards its application potential in solar photoelectrochemistry. In this work, significant differences in the photosensitizing capability of the 6th group transition metal oxides applied on the surface of titania nanotubes are reported. For the first time, correlations between the experimentally determined Tauc coefficients, sample photoresponse, and ab-initio simulated properties of the heterojunctions are established. Experimental results show undoubtedly that the decoration of TiO_2 nanotubes with chromium oxides leads to the enhanced photoresponse, which originates from the interplay of mid-gap states and both direct and indirect nature of the transitions contributing to the optical absorption. The opposite tendency and decrease of photocurrent were found for molybdenum and tungsten oxides which exhibited forbidden nature of dominating transition. Although computations report intraband states in all interfaces, experimentally only chromium oxides contribute to the photocurrent. The uniqueness of this interface lies in the highest density of states in the vicinity of the conduction band and the low energy difference between the direct and indirect transitions of the innate chromium oxide. The obtained results demonstrate that the determination of the Tauc exponent and the nature of optical transition are more reliable experimental predictors of the photoactivity enhancement in the heterojunctions than the value of the band gap.

1. Introduction

TiO2 nanotubes are an n-type semiconductor with a vast spectrum of applications in solar cells [1] or photocatalysis [2]. They have gained particular interest not only due to the unique geometry but also to the inexpensiveness and chemical stability [3]. They can be fabricated via electrochemical oxidation of a titanium substrate – anodization [4]. The method is to apply an anodic bias voltage to the titanium substrate immersed in an electrolyte and maintain it for a certain period of time [4]. Depending on the processing parameters, including electrolyte composition, time, voltage, or temperature, the TiO2 nanotubes could form different geometries [4], and hence, be tailored for a particular application. The as-obtained nanotubes are amorphous, and they are usually annealed at elevated temperature to reach crystal structure [5]. TiO2 nanotubes exhibit a large 3.1 eV band gap and their absorption is mainly limited to the UV part of the solar spectrum, and due to that, pristine TiO2 nanotubes do not convert solar-to-current energy efficiently [4]. The combination of the TiO2 nanotubes with other metal oxides is a prominent strategy for alleviating this issue. Their incorporation in titania can narrow the band gap through the formation of mid-gap states and contribute to better performances. Also, at the interface between TiO2 nanotubes and other metal oxides, there is a space region with an electric potential gradient which can facilitate electron-hole separation and transport of charge [6,7]. Nevertheless, not

only the band gap width and the potential at the junction influence the photoresponse of solids. From time-dependent perturbation theory, it is known that the probability of an indirect transition is lower compared to a direct transition due to the momentum conservation considerations [8]. Also, each of these transitions can be allowed or forbidden by the selection rules [9]. Such transitions cannot be triggered by the electric dipole interaction and must follow complicated mechanisms such as multiphoton absorption [9], hence they are very unlikely to occur. Therefore, the nature of the transition is another crucial factor.

Experimentally, optical band gap can be estimated from the UV–vis spectroscopy data *via* Tauc equation:

$$(\alpha h\nu)^{1/n} = A(h\nu - E_g) \qquad (1)$$

where h is Planck constant, ν is frequency, A is Tauc slope, E_g is band gap and n is Tauc exponent which is typically chosen as one of four numbers corresponding to dominating transition in studied semiconductor: 1/2 for direct (allowed) transitions, 3/2 for direct (forbidden) transitions, 2 for indirect (allowed) transitions and 3 for indirect (forbidden) transitions [10]. The optical band gap value is then determined from the intersection of the fitted straight line with the abscissa axis. However, to do so, one must know the transition type to substitute the correct Tauc exponent. For widely studied semiconductors, such as TiO$_2$, the literature is consistent in this matter both by theoretical [11] and experimental studies [12], and an indirect (allowed) transition is suggested. Nevertheless, the problem arises for new, nano-sized, or multi-component materials. In the previous work [8], principles of a method allowing for experimental estimation of the Tauc exponent based on the UV–vis spectroscopy have been demonstrated. Essentially, the Tauc exponent can be calculated from the slope of the log($\alpha h\nu$) vs. $h\nu$ plot. The method is particularly important because an information about the transition type is provided without any assumptions regarding the investigated material.

In this work, the experimental results obtained by UV–vis spectroscopy and photoelectrochemical measurements with ab-initio density functional theory (DFT) coupled with non-equilibrium Green's functions (NEGF) simulations of the TiO$_2$ decorated with chromium, molybdenum, and tungsten oxides are parallelized. The DFT coupled with NEGF is a simulation approach suitable for studying the electrical and optical properties of heterojunctions [13]. In general, the Kohn-Sham orbitals obtained by DFT are utilized for transport calculations performed in e.g. the Landauer-Buttkier regime [14]. For this paper, projected local density of states (PLDOS) analysis [15] is used to elucidate the creation and properties of the electronic states formed at the interface of junctions [13]. Herein, it is reported that the determination of the transition types from the Tauc exponent is a prominent experimental predictor for photoresponse of heterojunctions, even better than the band gap and band structure.

2. Methods

TiO$_2$ nanotubes were fabricated via 1 step electrochemical oxidation of Ti foil (Strem 99.7%, 0.127 mm). First, the foil has been cut into (2 × 3) cm^2 pieces. Subsequently, it has been cleaned in turn in acetone (Chempur, p.a.), ethanol (Chempur, 96%, p.a.), and deionized water (HYDROLAB, 0.05 μS) for 10 min in each one in an ultrasonic bath. Afterward, they were dried in a steam of cold air (Air Liquide, ALPHAGAZ™ 1 Air). Each anodization was realized in a two-electrode system where Ti foil served as an anode and Pt mesh as a cathode. Each electrochemical cell was filled with a 50 ml electrolyte containing: 0.5 g NH$_4$F (Chempur, p.a.), 7.5 ml deionized H$_2$O, and 42.5 ml glycol ethylene (Chempur, p.a.). A fixed distance of 2 cm was kept between the electrodes. The temperature was set to 23 °C and controlled by a thermostat (Julabo F-12) working in a flow mode. During the process, 40 V was maintained for 15 min with a voltage ramp-up and ramp-down times of 6.66 min. After the process, the samples were rinsed with

ethanol and allowed to dry in the air freely. The as-obtained TiO$_2$ nanotubes were thermally annealed in a tubular furnace (Nabertherm, P330) at 450 °C in the air for 2 h using a heating ramp-up of 2 °C min^{-1}. After that time, the samples were allowed to cool down freely to an ambient temperature.

Transition metals were deposited using a magnetron sputtering machine (Quorum, Q150T S) and metallic disc targets of chromium (TK8845, Quorum Technologies), molybdenum (Micro to nano, 99.95% Mo), and tungsten (Micro to nano, 99.95% W). During the process, the thickness of the deposited material was set to 15 nm and it was *in-situ* controlled by quartz crystal microbalance. After the deposition, the samples were thermally annealed in a tubular furnace (Nabertherm, P330) both to crystallize and oxidize the deposited metals. The samples with chromium and molybdenum were calcined at 450 °C while those with tungsten at 400 °C.

Scanning electron microscope (SEM) images in top view and cross-section were captured using Schottky field emission SEM (FEI Quanta FEG 250) with an ET secondary electron detector. The acceleration voltage was kept at 10 kV.

X-ray diffraction (XRD) measurements were carried out using an X-ray diffractometer (Bruker D2 Phaser 2nd generation) using CuKα radiation and LynxEye XE-T detector at room temperature.

High-resolution X-ray photoelectron spectroscopy (XPS) analyses were carried out in the core-level binding energy of Ti *2p*, Cr *2p*, Mo *3d*, W *4f*, and C *1s* to evaluate the surface chemical states of the studied samples. Escalab 250 Xi multispectroscope was used, operating with Al Kα X-ray source, 250 μm spot diameter. The pass energy was 20 eV. Low-energy electron and Ar$^+$ ions flow was used for charge compensation, with final x-axis calibration at C *1s* (284.8 eV) adventitious carbon.

UV–vis spectroscopy measurements were performed using Lambda 35 UV–vis Spectrometer. The data was collected in reflectance mode using a slit width of 2 nm and a scan speed of 120 nm min^{-1}. Wavelengths (λ) were calculated to photon energy accordingly:

$$h\nu \; (eV) = \frac{hc}{\lambda} = \frac{1239.8 \; (eV \times nm)}{\lambda \; (nm)} \qquad (2)$$

where h is the Planck constant and c is the speed of light. For Tauc plot construction, the Kubelka-Munk radiative transfer model $f(R)$ was used to extract a value proportional to absorption coefficient α, since R is not directly proportional to the absorption coefficient:

$$f(R) = \frac{K}{S} = \frac{(1-R)^2}{2R} \qquad (3)$$

where, K and S stay for Kubelka-Munk coefficients, which are in turn proportional to the absorption and scattering coefficients (s):

$$\frac{\alpha}{s} \propto \frac{K}{S} \qquad (4)$$

3D maps of photocurrent as a function of incident light wavelength and potential were measured using a photoelectric spectrometer (Instytut Fotonowy) equipped with a potentiostat. The measurements were performed in a three-electrode system with Ag/AgCl/3 M KCl reference electrode and Pt wire counter electrode. The photocurrent was calculated as a difference between current registered under the illumination and in the dark. The illumination and dark periods were 5 and 10 s, respectively. For the calculations of each current (under illumination and in dark) an average of the last 50% of each period was taken to minimize the contribution of the current from recombination. The data was collected with a 10 nm step of wavelength and 0.1 V of potential. After each polarization, the potential was held for 60 s before current measurements to reach a steady-state.

Sample photoresponse was investigated by a linear sweep voltammetry using potentiostat/galvanostat (Autolab PGSTAT302 N) in a three-electrode system with Ag/AgCl/3 M KCl reference electrode (MINERAL) and Pt mesh counter electrode under chopped light

illumination. As a light source, solar light simulator (LOT Quantum Design, Series LS0500) equipped with an automatic light shutter was used. The shutter was programmed for 5 s. For the measurements carried out in the visible range, an additional UV filter (OPTEL, GG420) was installed. It allows for sample irradiation with wavelengths above 420 nm. The electrochemical cell was equipped with a quartz window (Continental Trade, Ø50 × 1.0 mm) allowing for sample illumination. Before the measurements, the light intensity was calibrated to 1000 W m^{-2} using Silicon Reference Cell (Rera Solutions, Model: Open RR-1002). The samples with chromium oxides were examined in 0.5 M Na_2SO_4 (pH = 6.86) whereas those with molybdenum and tungsten oxides in 0.5 M Na_2SO_4 acidified with H_2SO_4 (CHEMPUR, 95% p.a.) to pH = 2.89. The pH values were chosen based on the Atlas of Electrochemical Equilibria in Aqueous Solutions by Marcel Pourbaix [16]. Before the measurements, each electrolyte was deaerated with argon 5.0 (Air Liquide, ALPHAGAZ™ 1 Ar), and during the testing, a continuous flow of Ar above the solution was kept.

For the construction of Mott-Schottky plots, electrochemical impedance spectra were recorded for a single frequency of 1 kHz with a 10 mV amplitude of the AC signal. Before each spectrum registration, the potential was held for 30 s to reach steady-state conditions. The capacitance of the space charge layer was then calculated using the following equation:

$$C_{SC} = \frac{1}{2\pi f Z_{im}} \quad (5)$$

where f is the frequency of the AC signal, and Z_{im} is the imaginary part of the impedance.

Atomic structures of heterojunctions were designed using a builder tool provided by Atomistic ToolKit Quantumwise (ATK, Synopsys, USA) as reported in Ref. [17]. Density functional theory (DFT) on the generalized gradient approximation (GGA) level of theory with the Perdew-Burke-Ernzerhof (PBE) functional was applied as implemented in the package. The Linear Combination of Atomic Orbitals (LCAO) method [18] with medium ATK basis set and Pseudo-Dojo norm-conserving pseudopotentials were applied [19]. For the facilitation of several geometry optimizations, a pre-optimization was used using a Dreading force field [19]. Before the calculation of band structures, a DFT -1/2 band gap correction procedure was implemented [19]. 12 eV energy window was taken with zero at the Fermi level. Optical spectra of bulk anatase, MoO_3, and WO_3 were computed based on the susceptibility tensor calculated from DFT orbitals using Kubo-Greenwood formula [19].

3D periodic cells used for band structure and optical spectra calculations were single cells taken from Materials Project database. Precisely, TiO_2 was a body centered tetragonal cell containing 2 Ti atoms with 3.7842 × 3.7842 × 9.5146 Å³ dimensions; Cr_2O_3 was a trigonal cell containing 12 Cr atoms with 5.070 × 5.070 × 13.8716 Å³ dimensions [20]; MoO_3 was an orthorhombic cell containing 4 Mo atoms with 3.7610 × 3.9693 × 14.4254 Å³ dimensions [21]; WO_3 was a cubic cell containing 1 W atom with 3.8627 × 3.8627 × 3.8627 Å³ [22] dimensions.

Semiconductor heterojunctions were built and optimized according to the procedure provided in the ATK documentation [17]. Briefly, two electrodes consisting of a series of unit cells are built and connected through the scattering region in between. While atomic positions in the electrode zones are fixed, in the scattering region they can change during geometry optimization procedure, according to the chemical interactions between surface atoms. The system is periodic in X and Y directions, but Dirichlet boundary conditions are applied in the Z direction, which is the direction of the junction [23]. Electrodes and scattering region are relaxed separately and then relaxed again after assembly. Projected local density of states (PLDOS) analysis [15] is performed using non-equilibrium Green's function (NEGF) methodology [24] in the Landauer-Buttiker regime [14], with PBE-GGA, calculated

orbitals as an input. All crystal orientations for heterojunction calculations were taken (001). Systems were built by multiplying the number of single cells used for band structure calculations in all three spatial directions maintaining balance between the system size and atomic stresses on the interface. Precisely, deformations due to the surface stress did not exceed 7% of strain. Detailed information on the construction of heterojunction systems is given in Table 1.

Projected local density of states (PLDOS) analysis [15] is performed using non-equilibrium Green's function (NEGF) methodology [24] in the Landauer-Buttiker regime [14], with PBE-GGA, calculated orbitals as an input. DFT orbitals are calculated with 4 × 4 × 150 Å³ density k-point mesh and 125 Ha density mesh cutoff. Then, Green's functions are calculated for each k-point and each of 501 sampling energies using contour integrals with real axis contour and 0.001 Ha point density. Therefore, the number of contour points is equal to the number of k-points multiplied by the number of energies for each structure [23]. Then, density matrix is obtained from the Green's function as a sum over all contour points. In the case of PLDOS calculations, 12 eV energy window is taken with zero at the Fermi level (matching to the window in band structure calculations) with 501 sampling energies, 125 Ha density mesh energy cutoff, and 7 × 7 × 1 Å³ density k-point mesh.

3. Results and discussion

In the present work, four samples: bare TiO_2 nanotubes, denoted as the TNT, and the nanocomposites based on the TiO_2 nanotubes with magnetron-sputtered 15 nm of Cr, Mo, and W after calcination are investigated. According to their chemical composition, described later, they are labeled as Cr_2O_3|TNT, MoO_3|TNT, and WO_3|TNT, respectively.

SEM images of the TNT are displayed in Fig. S1. They reveal the TNT sample is composed of the 1.44 ± 0.05 μm long nanotubes with an internal diameter and wall thickness of 90 ± 8 and 13 ± 3 nm, respectively. SEM images of the TiO_2 nanotubes after magnetron sputtering of metals are shown in Fig. S2. One can observe that the deposited species are located around the top of the nanotubes. Finally, SEM images after magnetron sputtering followed by the calcination are displayed in Fig. 1. They demonstrate that after thermal treatment, the deposited species are in form of aggregates of nanoparticles on the top of the nanotubes. The mean size of the nanoparticles is given in Table 2. SEM images in a cross-section view are displayed in Fig. S3.

In addition to the SEM analysis, X-ray diffraction measurements were performed to reveal the crystal structure of the investigated materials (see Fig. S4). The XRD pattern of the TNT sample contains peaks corresponding to the titanium (from the substrate) [ICDD PDF-4+ Card No. 01-089-5009], and anatase [ICDD PDF-4+ Card No. 00-001-0562] along with a weak peak of the rutile face (110) [ICDD PDF-4+ Card No. 01-073-2224]. The patterns of the Cr_2O_3|TNT and MoO_3|TNT samples contain no peaks corresponding to the crystal structures of these metal oxides, whereas the WO_3|TNT shows two peaks from the WO_3 (002) and (110) faces [ICDD PDF-4+ Card No. 01-088-0545].

Since XRD patterns of the Cr_2O_3|TNT and MoO_3|TNT samples revealed no peaks corresponding to the crystallographic structures of the deposited species, Fig. 2 reports surface analysis with the XPS. Fig. 2 a displays the Ti 2p region of the TNT sample. It was deconvoluted into two doublets. The first at 458.7 and 464.5 eV is assigned to the +4

Table 1
Structural details of the atomistic heterojunction structures.

Structure	Left electrode	Scattering region	Right electrode
TiO_2|Cr_2O_3	4 anatase cells (8 Ti atoms)	4 anatase cells (8 Ti atoms) and 1 Cr_2O_3 cell (12 Cr atoms)	1 Cr_2O_3 cell (12 Cr atoms)
TiO_2|MoO_3	5 anatase cells (10 Ti atoms)	1 anatase cell (2 Ti atoms) and 1 MoO_3 cell (4 Mo atoms)	2 MoO_3 cells (8 Mo atoms)
TiO_2|WO_3	6 anatase cells (12 Ti atoms)	2 anatase cells 4 Ti atoms and (4 WO_3 cells 4 W atoms)	8 WO_3 cells (8 W atoms)
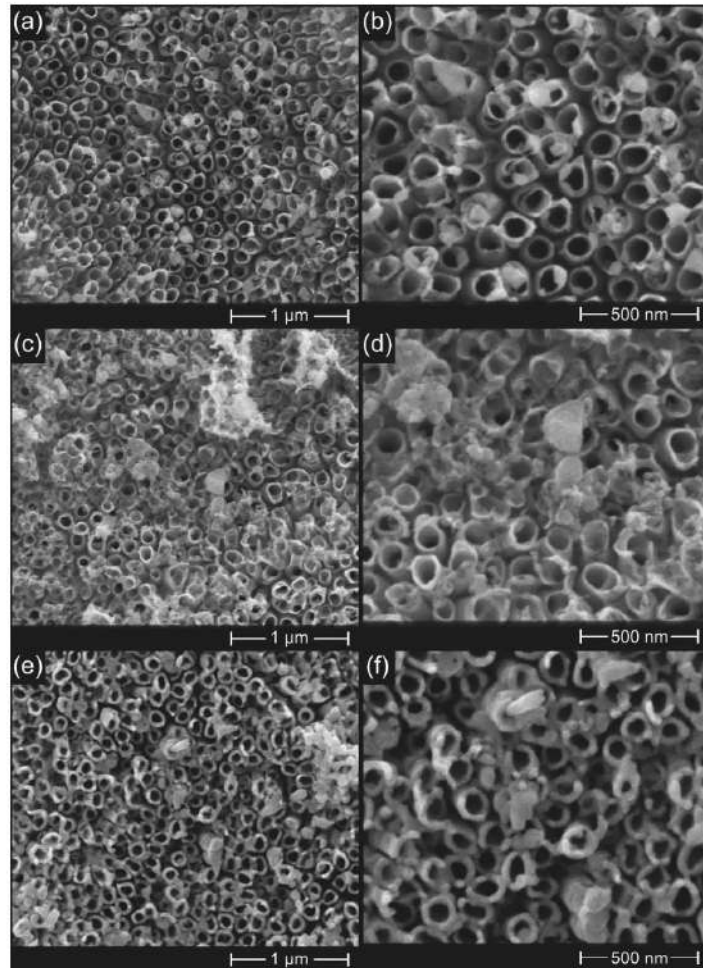
Fig. 1. SEM images in a top view of the (a–b) Cr_2O_3|TNT, (c–d) MoO_3|TNT, (e–f) WO_3|TNT.

Table 2
Mean size of the nanoparticles of the chromium, molybdenum, and tungsten oxides.

Sample	Mean size of the nanoparticles [nm]
Cr_2O_3|TNT	67 ± 23
MoO_3|TNT	133 ± 41
WO_3|TNT	129 ± 34

oxidation state [25] whereas the second at 457.2 and 462.8 eV suggests the presence of oxygen vacancies [26]. The remaining signals are recognized as satellites based on their intensities and positions with respect to the energy separation from the main Ti^{4+} peaks [27]. Fig. 2 b shows the Cr $2p$ 3/2 region of the Cr_2O_3|TNT sample. It was deconvoluted into four signals: 575.0, 576.1, 577.0, 578.0 eV assigned to the CrO_2, Cr_2O_3, CrOOH, and CrO_3, respectively [28]. Fig. 2 c shows the Mo $2p$ region of the MoO_3|TNT sample. It was deconvoluted into three

doubles: 233.1 (236.3), 232.1 (235.2), and 235.3 (238.3) eV. The first two doublets are assigned to +6 and +5 oxidation states, respectively, indicating the presence of oxygen vacancies in MoO_3 [29]. The last one is recognized as a satellite [30]. Fig. 2 d presents the W $4f$ region of the WO_3|TNT sample. It was deconvoluted into one doublet at the 35.7 and 37.8 eV. The registered data suggests that tungsten is solely in the WO_3 state [31] which is in line with the registered XRD pattern.

Fig. 3 a displays UV–vis spectra of the investigated samples. The TNT exhibits an absorption edge at about 395 nm (3.14 eV). In the range from 400 to 900 nm, a broad absorption band extends. Nearly the same runs were registered for the MoO_3|TNT, and WO_3|TNT for which the absorption edges are also at about 395 nm (3.14 eV). However, the spectrum registered for the Cr_2O_3|TNT reveals an Urbach tail [32] within 400–510 nm (see an arrow) which suggests additional mid-gap states which may contribute to the significant activity under the illumination with a visible part of the solar spectrum [32].

The shape of the obtained optical spectra can be justified by
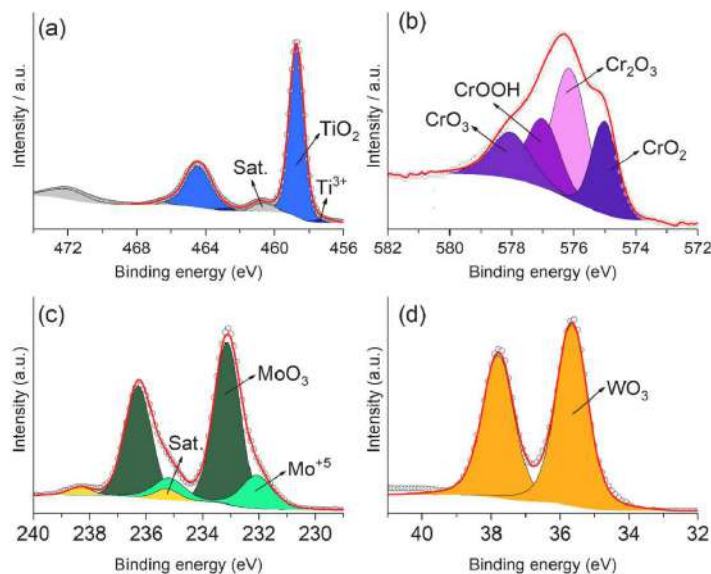
Fig. 2. XPS spectra displaying (a) Ti $2p$ region of the TNT, (b) Cr $2p$ 3/2 region of the $Cr_2O_3|TNT$, (c) Mo $3d$ region of the $MoO_3|TNT$, and (d) W $4f$ of the $WO_3|TNT$.
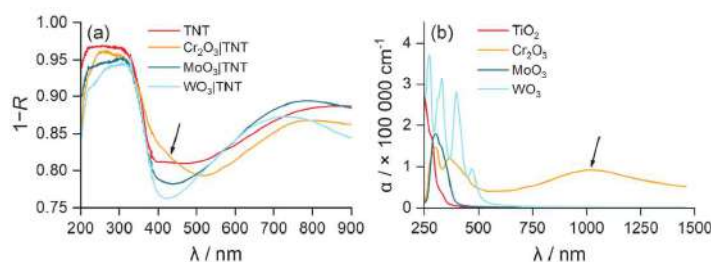
Fig. 3. Absorption data (a) experimentally measured UV–vis spectra for the TNT, $Cr_2O_3|TNT$, $MoO_3|TNT$, and $WO_3|TNT$; (b) calculated data for the TiO_2, $TiO_2|Cr_2O_3$, $TiO_2|MoO_3$, and $TiO_2|WO_3$.

comparison with DFT calculated absorption coefficients for TiO_2, Cr_2O_3, WO_3, and MoO_3. All oxides except Cr_2O_3 exhibit an absorption edge beginning at 355 nm for TiO_2, 388 nm for MoO_3, and 540 nm for WO_3. The value for TiO_2 is in good correspondence with the experimentally observed decrease in reflectance beginning at 380 nm. However, in the computed absorption spectrum of chromium oxide, a significant absorption band is present at 1020 nm (see an arrow), which presumably is responsible for the presence of the Urbach tail in Fig. 3 a. It stems from the intraband transitions because the DFT-computed Fermi level of Cr_2O_3 lies at the bottom of the conduction band (see Fig. 9). Surprisingly, despite the theoretical absorption edge of MoO_3 and WO_3 is lower than that of TiO_2, it is not manifested in the spectra of the experimentally assembled junctions and is not reflected in absorption enhancement. This issue will be thoroughly exploited in the following sections.

To verify the absorption data, 3D maps of the photocurrent spectra were measured and are displayed in Fig. 4. The TNT (Fig. 4 a) exhibits photocurrent onset at about 395 nm which is in line with the absorption edge observed on the UV–vis spectrum. Beyond that range (400–900 nm) nearly no photocurrent is registered. The spectrum of the $Cr_2O_3|$ TNT (Fig. 4 b) reveals an Urbach tail [32] in the range from 400 to 510

nm. Considering spectra registered from the $MoO_3|TNT$ and $WO_3|TNT$ (Fig. 4 c-d), one can observe that the photocurrent onset remains unchanged compared to the TNT sample. Therefore, the absorption and photocurrent spectra unanimously indicate that the deposition of chromium oxides contributes to additional mid-gap states, whereas the deposition of molybdenum and tungsten oxides nearly does not change the optical properties of TiO_2 nanotubes.

Before optical band gap determination, Tauc exponents along with corresponding transition types were determined from the UV–vis spectroscopy data using the recently developed method [8]. The $\log(f(R)h\nu)$ vs $h\nu$ data is presented in Fig. 5. For the TNT (Fig. 5 a), the absorption edge was fitted with a quadratic function due to the parabolic run of the absorption edge. The estimated Tauc exponent is equal to 2.0 which corresponds to the well-established indirect (allowed) transition of TiO_2. For the $Cr_2O_3|TNT$ two transitions are identified. One at 2.5–3.1 eV exhibiting $n = 0.4$ is assigned to direct (allowed) transition. However, the second at 3.3–3.8 eV exhibits $n = 1.0$ which does not correspond to any of the commonly used values. Because of that, it is speculated that within that range (3.3–3.8 eV) there is more than one optical transition. It is assigned to direct (allowed) and one or more of the remaining
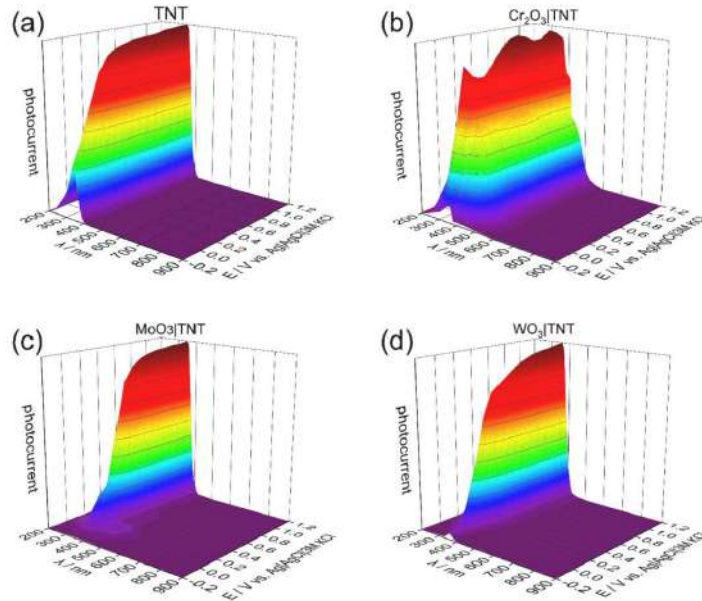
5

Fig. 4. 3D maps of the normalized photocurrent spectra of the (a) TNT, (b) Cr_2O_3|TNT, (c) MoO_3|TNT, and (d) WO_3|TNT.
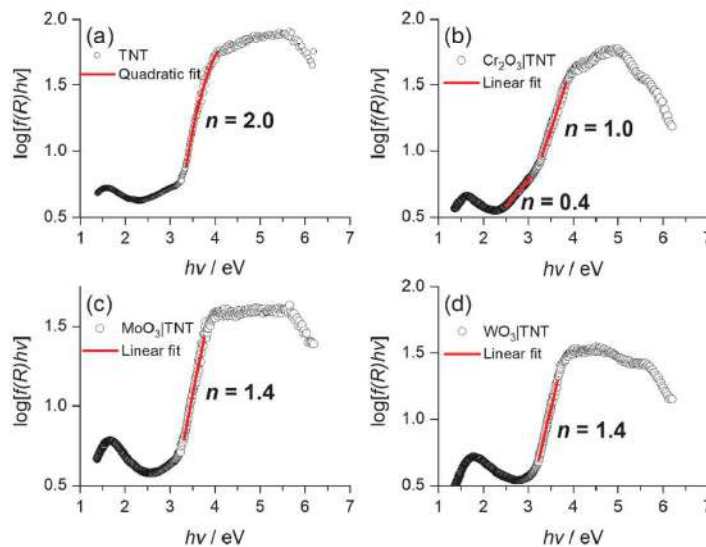
Fig. 5. $\log(f(R)h\nu)$ vs $h\nu$ plots for the (a) TNT, (b) Cr_2O_3|TNT, (c) MoO_3|TNT, and (d) WO_3|TNT.

transitions. The MoO_3|TNT and WO_3|TNT samples exhibit $n = 1.4$ and they are assigned to direct (forbidden) transition. Note that the estimated transition types are in agreement with our previous work [8].

Tauc plots of the investigated samples are displayed in Fig. 6. They were calculated using n values from the $\log(f(R)h\nu)$ vs $h\nu$ plots. The TNT exhibits a 2.99 eV band gap (Fig. 6 a) which is close to the value for the

anodic TiO_2 nanotubes estimated from the photocurrent onset method (2.84 eV) [33]. The Cr_2O_3|TNT sample exhibits a 3.62 eV band gap (Fig. 6 b) with a 1.80 eV intraband transition (Fig. 6 c). In turn, the MoO_3|TNT and WO_3|TNT samples exhibit a 3.22 and 3.18 eV wide band gaps, respectively. The estimated Tauc exponents along with the assigned optical transitions and band gaps are listed in Table 3.

6
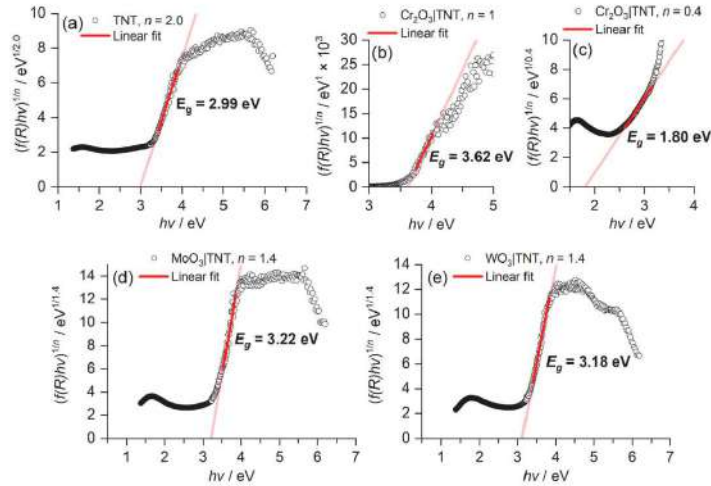
Fig. 6. Tauc plots of the (a) TNT, (b–c) Cr$_2$O$_3$|TNT, (d) MoO$_3$|TNT, (e) WO$_3$|TNT.

Table 3
Estimated Tauc exponents, transition types, and optical band gaps of the TNT, Cr$_2$O$_3$|TNT, MoO$_3$|TNT, and WO$_3$|TNT.

Sample	Tauc exponent	Transition type	Optical band gap [eV]
TNT	2.0	indirect (allowed)	2.99
Cr$_2$O$_3$|	0.4	direct (allowed)	1.80
TNT	1.0	direct (allowed) + others	3.62
MoO$_3$|TNT	1.4	direct (forbidden)	3.22
WO$_3$|TNT	1.4	direct (forbidden)	3.18

The linear voltammograms registered under the light-chopped illumination with AM 1.5 G, 1000 W m^{-2} are displayed in Fig. 7. In general, all the samples exhibit positive photocurrent along with anodic polarization indicating n-type semiconducting properties [34]. At low bias potential (from −0.2 to +0.2 V), sharp decay of current density peaks are observed. According to Taffala [35] et al., it is related to electron-hole surface recombination and/or a decrease in band bending. Compared to the TNT exhibiting photocurrent of 33 µA cm^{-2} at +0.65 V, the Cr$_2$O$_3$|TNT shows enhanced photoresponse of 52 µA cm^{-2} whereas a decrease is found for the MoO$_3$|TNT and WO$_3$|TNT, exhibiting 18 and 25 µA cm^{-2}, respectively. Both dark current and photocurrent of the MoO$_3$|TNT, and WO$_3$|TNT follow oxidation current peak during anodic

polarization (from −0.25 V to about +0.50 V). To investigate the origin of this peak, cyclic voltammograms in dark were registered (see Fig. S5). The cyclic voltammograms of the MoO$_3$|TNT, and WO$_3$|TNT exhibit reduction and oxidation peaks in the cathodic range which based on their shape and position, and taking into account the pH of the electrolyte, are assigned to the proton adsorption and desorption, respectively [36].

The linear voltammograms registered under the illumination with the visible light (with installed UV filter) are displayed in Fig. 7 b. Similarly to the voltammograms registered under UV–vis illumination, current spikes at low bias potential and the oxidation peaks for the MoO$_3$|TNT and WO$_3$|TNT are observed. The TNT shows a photocurrent of about 1.5 µA cm^{-2} at +0.65 V. Such poor photoresponse is related to the wide band gap of TiO$_2$. Significant photoresponse of about 23 µA cm^{-2} was found for the Cr$_2$O$_3$|TNT. The origin of such visible activity is likely related to the additional mid-gap states provided by Cr oxides suggested both by the UV–vis and photoresponse spectra. In turn, the MoO$_3$|TNT and WO$_3$|TNT exhibit similarly poor photoresponse as the TNT.

To summarize the optical and electronic properties of the investigated samples, band-energy-level diagrams were constructed. Flat band potentials (E$_F$) were determined from the Mott-Schottky plots (see Fig. S6). The conduction bands (E$_{CB}$, grey solid lines) were placed 0.2 V above the particular flat band potentials. Indeed, based on the literature
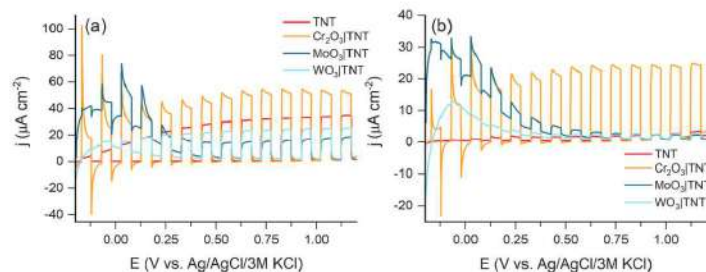

Fig. 7. Linear voltammograms of the TNT, Cr$_2$O$_3$|TNT, MoO$_3$|TNT, and WO$_3$|TNT registered under light-chopped illumination with (a) AM 1.5 G, 100 mW cm^{-2} and (b) visible part of the spectrum.

7

[37], the difference between E_{CB} and E_F is from 0.1 to 0.4 V depending on the semiconductor conductivity. Matsumoto et al. [37] suggest that 0.2 V should be assumed if the conductivity is unknown. Finally, the valence bands (E_{VB}, black solid lines) were shifted from E_{CB} by the value of calculated optical band gaps (see Fig. 6). The whole procedure was based on the work reported by Pinaud et al. [38]. Fig. 8 displays the band-energy-level diagram prepared based on the experimentally determined values. The presented results allow to establish the following key finding: the value of the optical band gap and relative positions of E_F, E_{CB}, and E_{VB} are not sufficient enough to explain the origin of sample photoresponse. The $MoO_3|TNT$ and $WO_3|TNT$ samples with nearly the same band gaps and band alignment compared to the TNT exhibit significantly deteriorated photoresponse. Indeed, change in the position of the E_F and mid-gap states could be responsible for the superior photoresponse of the $Cr_2O_3|TNT$, however, the $MoO_3|TNT$ and $WO_3|TNT$ with nearly the same optical and electronic properties as the TNT exhibits significantly deteriorated photoresponse which can be essentially explained by the forbidden nature of dominating transition. Therefore, based on the obtained results it is anticipated that the determination of a transition type is a crucial experimental predictor for sample photoresponse.

The abovementioned considerations are supported by DFT study on several levels of complexity. Fig. 9 (b–d) shows PLDOS analysis performed on the DFT optimized structure of heterojunctions $TiO_2|Cr_2O_3$, $TiO_2|MoO_3$, and $TiO_2|WO_3$. Chromium oxide (III) was chosen for the simulations due to its highest abundance on the XPS spectra (Fig. 2). Innate bands structures of the bulk oxides are given for reference on the left and right sides of the PLDOS plots.

Pristine anatase exhibits a typical indirect band gap of 3.18 eV and 3.59 eV directly calculated on the DFT -1/2 level of theory (Fig. 9 a). Deviations from the experimentally estimated 2.99 eV originate from the fact that the non-defected anatase is simulated and the optical band gap is typically lower than the electronic one [39,40]. In general, after assembly of the anatase with other oxides in the junction the energy gap stays intact ranging from 3.1 to 3.4 eV. Anatase conduction and valence bands bend along the length of the simulation box due to the long-range interactions with other electrode until the contact with different crystals is reached [41]. In the case of chromium oxide, close distances between chromium and titanium atoms at the interface are reported, suggesting strong $TiO_2|Cr_2O_3$ intermolecular interactions (inset on Fig. 9 b). This is accompanied by the creation of a set of densely packed mid-gap states

over the length of the chromium part of the box forming a shallow quantum well of 1.5 nm length for the creation of excitons. Moreover, the energy distance between the valence band of the Cr_2O_3 and the onset of the newly introduced states is equal to 1.28 eV. Those mid-gap states are not reported in the band structures of pristine crystals of either anatase or chromium oxide, which suggests that their origin is purely due to the interactions between surfaces. It is anticipated that they lead to the emergence of the Urbach tail on the UV–vis and photocurrent spectra and the manifestation of the direct transition in the first linear range of the Tauc plot. Differences in values (1.28 eV and 1.80 eV, Table 3) might come from the fact that not all the mid-gap states participate in the Urbach tail. Considering their close connection with Cr_2O_3 conduction band, they are also responsible for the enhancement of photocurrents in the visible range.

Mid-gap states are also introduced in the $TiO_2|MoO_3$ junction on the whole energy range, reducing the apparent band gap to 0.8 eV compared to the 2.5 eV of the pristine MoO_3. However, in contrast to the chromium oxide case, they are less populated and mainly separated from the E_V and E_C. Therefore, they cannot participate in the conduction of photocurrent and due to the very small effective band gap, they would generate excitons mainly in the NIR range of the spectrum. It is also reflected with a high experimentally obtained band gap equal to 3.1 eV originating mostly from pristine TiO_2. These observations might explain the lack of changes reported on the UV–vis spectra compared to the pristine TiO_2, and the smallest observed photocurrents (Fig. 3 a and b). This result is similar to the theoretically predicted shape of n-n semiconductor heterojunctions by Oldham in 1963 [42].

Completely different behavior is observed in the case of $TiO_2|WO_3$ assemblies. In this setup, bands of the two semiconductors bend in such a way that a staggered configuration is formed [43] at the intersection of unit cells (inset in Fig. 9 d). Similar correlations between the shape of PLDOS and intermolecular interactions were observed in the case of graphene MoS_2 heterojunctions [44] and at the Si–Ge interfaces [44]. Considering that the band gap of the pristine anatase is similar to the energy gap in the deep well, no significant differences in photocurrents and experimental band gaps after modification of nanotubes are noted (Fig. 4 d). In general, even though band gaps of pristine WO_3 and MoO_3 are smaller than TiO_2, unfavorable alignments of energy levels on interfaces prohibit enhancement of the photocurrents, which was confirmed experimentally.

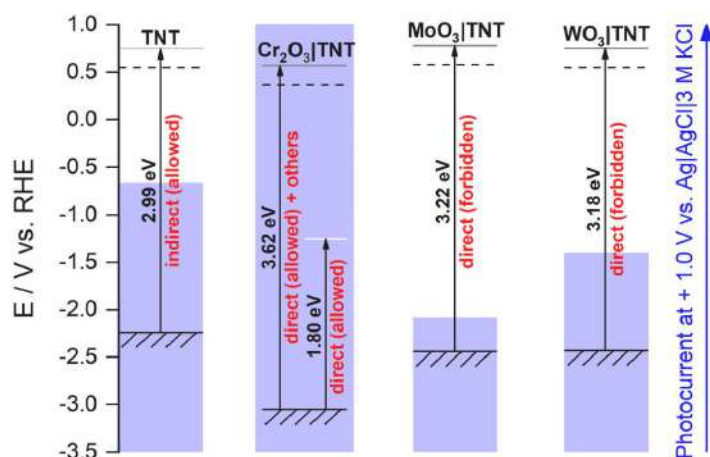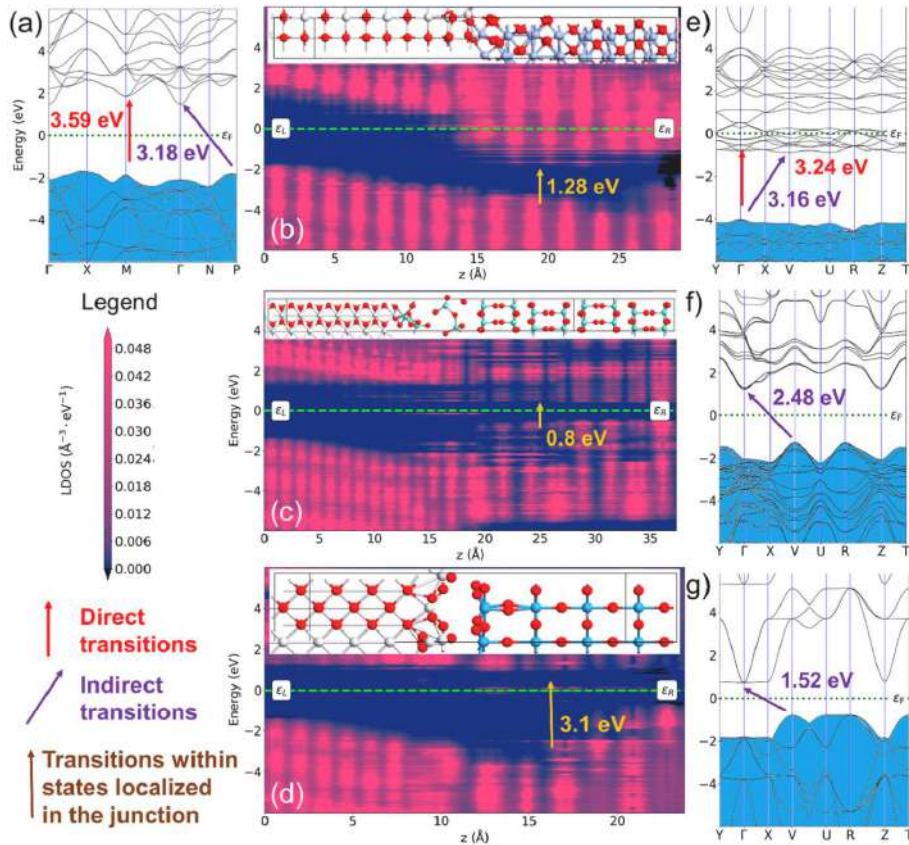Another link with experimental observables involves the Tauc

Fig. 8. Experimentally measured band-energy-level diagrams for the TNT, $Cr_2O_3|TNT$, $MoO_3|TNT$, and $WO_3|TNT$. Black solid lines correspond to valence bands, dashed lines to flat-band potentials, and grey solid lines to conduction band positions; arrows indicate band gaps width.

Fig. 9. DFT simulations of metal oxide heterojunctions (a) band structure of pure TiO_2 anatase; (b–d) projected local density of states plots for $TiO_2|Cr_2O_3$, $TiO_2|MoO_3$, and $TiO_2|WO_3$ junctions, atomic configurations of the unit cells are given in insets; (e–g) band structures of pure Cr_2O_3 (trigonal), MoO_3 and WO_3.

coefficients estimated for $TiO_2|Cr_2O_3$ junction and the type of the simulated transitions in pristine metal oxide crystals. While all other oxides exhibit indirect transitions, only Cr_2O_3 has a direct transition (3.24 eV) almost equal to the indirect one (3.16 eV). Experimentally determined band gap for the $TiO_2|Cr_2O_3$ junction is higher (3.62 eV - Table 3) mainly because the film consists of many chromium oxides in different oxidation states. The small energy difference between direct and indirect transitions makes that direct type would dominate, which was reflected in the lowest value of the Tauc exponent among all studied junctions. Therefore, the Tauc exponent is a prominent experimental tool for predicting the photoresponse of materials, rather than the pure optical value of the band gap itself. This idea was already schematically depicted in Fig. 8.

4. Conclusions

In this work, completely different optical and photoelectrochemical properties of the TiO_2 nanotubes decorated with different metal oxides of the 6th group have been shown. Although PLDOS theoretical analysis detected mid-gap states in all junctions, only the decoration with chromium oxides resulted in the presence of Urbach tail on the UV–vis and photocurrent spectra as well as a significant activity under

illumination with the visible part of the solar spectrum. This is because the mid-gap states at the $TiO_2|Cr_2O_3$ junction are the most densely populated and are lying just below the conduction band of the innate chromium oxide. It correlates with the lowest value of the Tauc exponent $n = 1.0$ and the predicted presence of both direct and indirect transitions for the $Cr_2O_3|TNT$ sample. Moreover, despite the small PLDOS estimated band gap of the $TiO_2|MoO_3$ at the junction and the small band gap of the innate WO_3, no photocurrent enhancement is experimentally observed for the $MoO_3|TNT$ and $WO_3|TNT$ samples compared to the pristine TiO_2 nanotubes. Nevertheless, the estimated Tauc exponent ($n = 1.4$) for these two junctions suggests the forbidden nature of dominating transitions. Therefore, it is concluded that the Tauc exponent and corresponding transition types are more accurate experimental predictors of photosensitization than the value of the optical band gap itself.

CRediT authorship contribution statement

Łukasz Haryński: Conceptualization, Methodology, Validation, Investigation, Data curation, Writing – original draft, Writing – review & editing, Visualization. **Adrian Olejnik:** Conceptualization, Methodology, Formal analysis, Writing – original draft, Writing – review &

9

editing, Visualization. **Jakub Karczewski:** Investigation. **Jacek Ryl:** Investigation. **Katarzyna Grochowska:** Writing – review & editing. **Katarzyna Siuzdak:** Resources, Writing – review & editing, Supervision, Funding acquisition.

Declaration of competing interest

The authors declare the following financial interests/personal relationships which may be considered as potential competing interests: Katarzyna Siuzdak reports financial support was provided by Polish National Science Centre Poland.

Data availability

Data will be made available on request.

Acknowledgment

Appendix A. Supplementary data

Supplementary data to this article can be found online at https://doi.org/10.1016/j.optmat.2022.113183.

References

[1] P. Roy, S.P. Albu, P. Schmuki, TiO₂ nanotubes in dye-sensitized solar cells: higher efficiencies by well-defined tube tops, Electrochem. Commun. 12 (2010) 949–951, https://doi.org/10.1016/j.elecom.2010.04.029.

[2] X. Zhou, N. Liu, P. Schmuki, Photocatalysis with TiO₂ nanotubes: "colorful" reactivity and designing site-specific photocatalytic centers into TiO₂ nanotubes, ACS Catal. 7 (2017) 3210–3235, https://doi.org/10.1021/acscatal.6b03709.

[3] V.K. Mahajan, S.K. Mohapatra, M. Misra, Stability of TiO₂ nanotubes arrays in photoelectrochemical studies, Int. J. Hydrogen Energy 33 (2008) 5369–5374, https://doi.org/10.1016/j.ijhydene.2008.06.074.

[4] J.M. Macak, H. Tsuchiya, A. Ghicov, K. Yasuda, R. Hahn, S. Bauer, P. Schmuki, TiO₂ nanotubes: self-organized electrochemical formation, properties and applications, Curr. Opin. Solid State Mater. Sci. 11 (2007) 3–18, https://doi.org/10.1016/j.cossms.2007.08.004.

[5] A. Ghicov, H. Tsuchiya, J.M. Macak, P. Schmuki, Annealing effects on the photoresponse of TiO₂ nanotubes, Phys. Status Solidi A 203 (2006) R28–R30, https://doi.org/10.1002/pssa.200622041.

[6] W.G. Oldham, A.G. Milnes, n-n Semiconductor heterojunctions, Solid State Electron. 6 (1963) 121–132, https://doi.org/10.1016/0038-1101(63)90005-4.

[7] M. Umeno, Y. Sugito, H. Hattori, Y. Amemiya, Hot photo-carrier and hot electron effects in p-n junctions, Solid State Electron. 21 (1978) 191–195, https://doi.org/10.1016/0038-1101(78)90137-5.

[8] Ł. Haryński, A. Olejnik, K. Grochowska, K. Siuzdak, A facile method for Tauc exponent and corresponding electronic transitions determination in semiconductors directly from UV–Vis spectroscopy data, Opt. Mater. (Amst.) 127 (2022), 112205, https://doi.org/10.1016/j.optmat.2022.112205.

[9] D.J. Griffiths, Introduction to Quantum Mechanics, Pretince Hall, 1995.

[10] C. Malerba, F. Biccari, C.L.A. Ricardo, M. D'Incau, P. Scardi, A. Mittiga, Absorption coefficient of bulk and thin film Cu₂O, Sol. Energy Mater. Sol. Cells 95 (2011) 2848–2854, https://doi.org/10.1016/j.solmat.2011.05.047.

[11] Y. Wang, R. Zhang, J. Li, L. Li, S. Lin, First-principles study on transition metal-doped anatase TiO₂, Nanoscale Res. Lett. 9 (2014) 1–8, https://doi.org/10.1186/1556-276X-9-46.

[12] P. Makuła, M. Pacia, W. Macyk, How to correctly determine the band gap energy of modified semiconductor photocatalysts based on UV-vis spectra, J. Phys. Chem. Lett. 9 (2018) 6814–6817. http://10.1021/acs.jpclett.8b02892.

[13] P. Damle, A.W. Ghosh, S. Datta, First-principles analysis of molecular conduction using quantum chemistry software, Chem. Phys. 281 (2002) 171–187, https://doi.org/10.1016/S0301-0104(02)00496-2.

[14] S. Datta, Exclusion principle and the Landauer-Buttiker formalism, Phys. Rev. B 45 (1992) 1347–1362, https://doi.org/10.1103/PhysRevB.45.1347.

[15] J. Gao, D. Nandi, M. Gupta, Density functional theory - projected local density of states - based estimation of Schottky barrier for monolayer MoS₂, J. Appl. Phys. 124 (2018), 014502 https://doi.org/10.1063/1.5030538.

[16] M. Pourbaix, Atlas of Electrochemical Equilibria in Aqueous Solutions, National Association of Corrosion Engineers, Houston, 1966.

[17] Atomistix Toolkit Version 2019.03, Synopsys QuantumWise A/S, (n.d.).

[18] J.M. Soler, E. Artacho, J.D. Gale, A. García, J. Junquera, P. Ordejón, D. Sánchez-Portal, The SIESTA method for ab initio order-N materials simulation, J. Phys.

Condens. Matter 14 (2002) 2745–2779, https://doi.org/10.1088/0953-8984/14/11/302.

[19] M.J. van Setten, M. Giantomassi, E. Bousquet, M.J. Verstraete, D.R. Hamann, X. Gonze, G.M. Rignanese, The PSEUDODOJO: training and grading a 85 element optimized norm-conserving pseudopotential table, Comput. Phys. Commun. 226 (2018) 39–54, https://doi.org/10.1016/j.cpc.2018.01.012.

[20] The materials Project, n.d. https://materialsproject.org/materials/mp-19399/. (Accessed 27 September 2022).

[21] The materials Project, n.d. https://materialsproject.org/materials/mp-20589/. (Accessed 27 September 2022).

[22] The materials Project, n.d. https://materialsproject.org/materials/mp-19390. (Accessed 27 September 2022).

[23] D. Stradi, U. Martinez, A. Blom, M. Brandbyge, K. Stokbro, General atomistic approach for modeling metal-semiconductor interfaces using density functional theory and nonequilibrium Green's function, Phys. Rev. B 93 (2016) 28–38, https://doi.org/10.1103/PhysRevB.93.155302.

[24] M. Brandbyge, J.L. Mozos, P. Ordejón, J. Taylor, K. Stokbro, Density-functional method for nonequilibrium electron transport, Phys. Rev. B Condens. Matter 65 (2002) 1654011–16540117, https://doi.org/10.1103/PhysRevB.65.165401.

[25] B. Siemensmeyer, J.W. Schultze, XPS and UPS studies of gas-phase oxidation, electrochemistry and corrosion behaviour of Ti and Ti5Ta, Surf. Interface Anal. 16 (1990) 309–314, https://doi.org/10.1002/sia.740160164.

[26] L.-Q. Wang, D.R. Baer, M.H. Engelhard, A.N. Shultz, The adsorption of liquid and vapor water on TiO₂(110) surfaces: the role of defects, Surf. Sci. 344 (1995) 237–250, https://doi.org/10.1016/0039-6028(95)00859-4.

[27] M. Oku, H. Matsuta, K. Wagatsuma, Y. Waseda, S. Kohiki, Removal of inelastic scattering part from Ti2p XPS spectrum of TiO₂ by deconvolution method using O1s as response function, J. Electron. Spectrosc. Relat. Phenom. 105 (1999) 211–218, https://doi.org/10.1016/S0368-2048(99)00067-5.

[28] G.P. Halada, C.R. Clayton, Photoreduction of hexavalent chromium during X-ray photoelectron spectroscopy analysis of electrochemical and thermal films, J. Electrochem. Soc. 138 (1991) 2921–2927, https://doi.org/10.1149/1.2085340.

[29] M.A. Bica de Moraes, B.C. Trasferetti, F.P. Rouxinol, R. Landers, Molybdenum oxide thin films obtained by the hot-filament metal oxide deposition technique, Chem. Mater. 16 (2004) 513–520, https://doi.org/10.1021/cm034551a.

[30] Y. Pan, J. Wei, D. Han, Q. Xu, D. Gao, Y. Yang, Y. Wei, Hetero-nanostructures constructed by 2D porous metal oxide/hydroxide nanosheets supported on 1D hollow Co₉S₈ nanowires for hybrid supercapacitors with high areal capacity, Inorg. Chem. Front. 8 (2021) 4676–4684, https://doi.org/10.1039/D1QI00814E.

[31] F.Y. Xie, L. Gong, X. Liu, Y.T. Tao, W.H. Zhang, S.H. Chen, H. Meng, J. Chen, XPS studies on surface reduction of tungsten oxide nanowire film by Ar+ bombardment, J. Electron. Spectrosc. Relat. Phenom. 185 (2012) 112–118, https://doi.org/10.1016/j.elspec.2012.01.004.

[32] H. Yaghoubi, Z. Li, Y. Chen, T.H. Ngo, V.R. Bhethanabotla, B. Joseph, S. Ma, R. Schlaf, A. Takshi, Toward a visible light-driven photocatalyst: the effect of midgap-states-induced energy gap of undoped TiO₂ nanoparticles, ACS Catal. 5 (2015) 327–335, https://doi.org/10.1021/cs501539q.

[33] P. Roy, S. Berger, P. Schmuki, TiO₂ nanotubes: synthesis and applications, Angew. Chemie - Int. J. 50 (2011) 2904–2939, https://doi.org/10.1002/anie.201001374.

[34] K.L. Hardee, A.J. Bard, Semiconductor electrodes X. Photoelectrochemical behavior of several polycrystalline metal oxide electrodes in aqueous solutions, J. Electrochem. Soc. 124 (1977) 215–224, https://doi.org/10.1149/1.2133269.

[35] D. Tafalla, P. Salvador, Kinetic approach to the photocurrent transients in water photoelectrolysis at n-TiO₂ electrodes, J. Electrochem. Soc. 137 (1990) 1810–1815.

[36] S. Prass, J. St-Pierre, M. Klingele, K.A. Friedrich, N. Zamel, Hydrogen oxidation artifact during platinum oxide reduction in cyclic voltammetry analysis of low-loaded PEMFC electrodes, Electrocatalysis 12 (2021) 45–55, https://doi.org/10.1007/s12678-020-00627-6.

[37] Y. Matsumoto, Energy positions of oxide semiconductors and photocatalysis with iron complex oxides, J. Solid State Chem. 126 (1996) 227–234.

[38] B.A. Pinaud, Z. Chen, D.N. Abram, T.F. Jaramillo, Thin films of sodium birnessite-type MnO₂: optical properties, electronic band structure, and solar photoelectrochemistry, J. Phys. Chem. C 115 (2011) 1932–7447.

[39] Á. Morales-García, S. Rhatigan, M. Nolan, F. Illas, On the use of DFT+U to describe the electronic structure of TiO₂ nanoparticles: (TiO₂)₃₅ as a case study, J. Chem. Phys. 152 (2020), https://doi.org/10.1063/5.0012271.

[40] O.K. Orhan, D.D. O'Regan, First-principles Hubbard U and Hund`s J corrected approximate density functional theory predicts an accurate fundamental gap in rutile and anatase TiO₂, Phys. Rev. B 101 (2020), 245137, https://doi.org/10.1103/PhysRevB.101.245137.

[41] M. Ramesh, M.K. Niranjan, First principle study of bias voltage dependent Schottky barrier height of Pt/MgO interface, 3Rd Int. Conf. Condens. Matter Appl. Phys. 2220 (2020), 090017, https://doi.org/10.1063/5.0001437.

[42] W.G. Oldham, A.G. Milnes, n-n Semiconductor heterojunctions, Solid State Electron. 6 (1963) 121–132, https://doi.org/10.1016/0038-1101(63)90005-4.

[43] Y. Kim, E. Coy, H. Kim, R. Mrówczyński, P. Torruella, D.W. Jeong, K.S. Choi, J. H. Jang, M.Y. Song, D.J. Jang, F. Peiro, S. Jurga, H.J. Kim, Efficient photocatalytic production of hydrogen by exploiting the polydopamine-semiconductor interface, Appl. Catal. B Environ. 280 (2021), 119423, https://doi.org/10.1016/j.apcatb.2020.119423.

[44] Y. Zhou, Y. Yang, Y. Guo, Q. Wang, X. Yan, Influence of length and interface structure on electron transport properties of graphene-MoS₂ in-plane heterojunction, Appl. Surf. Sci. 497 (2019), 143764, https://doi.org/10.1016/j.apsusc.2019.143764.

Linking Optical and Electronic Properties to Photoresponse of Heterojunctions Based on Titania Nanotubes and Chromium, Molybdenum, and Tungsten Oxides.

Łukasz Haryński, Adrian Olejnik, Jakub Karczewski, Jacek Ryl, Katarzyna Grochowska and Katarzyna Siuzdak
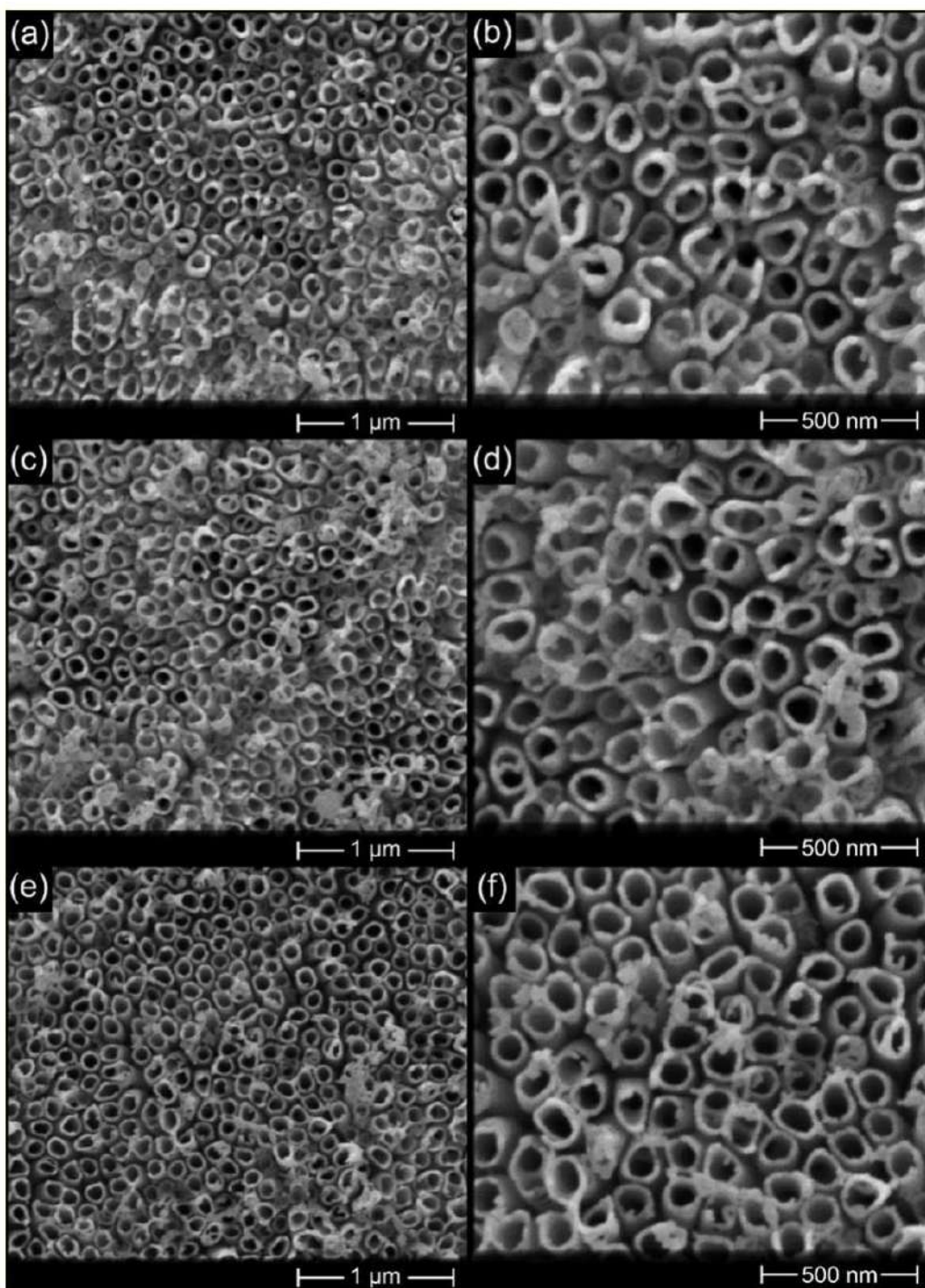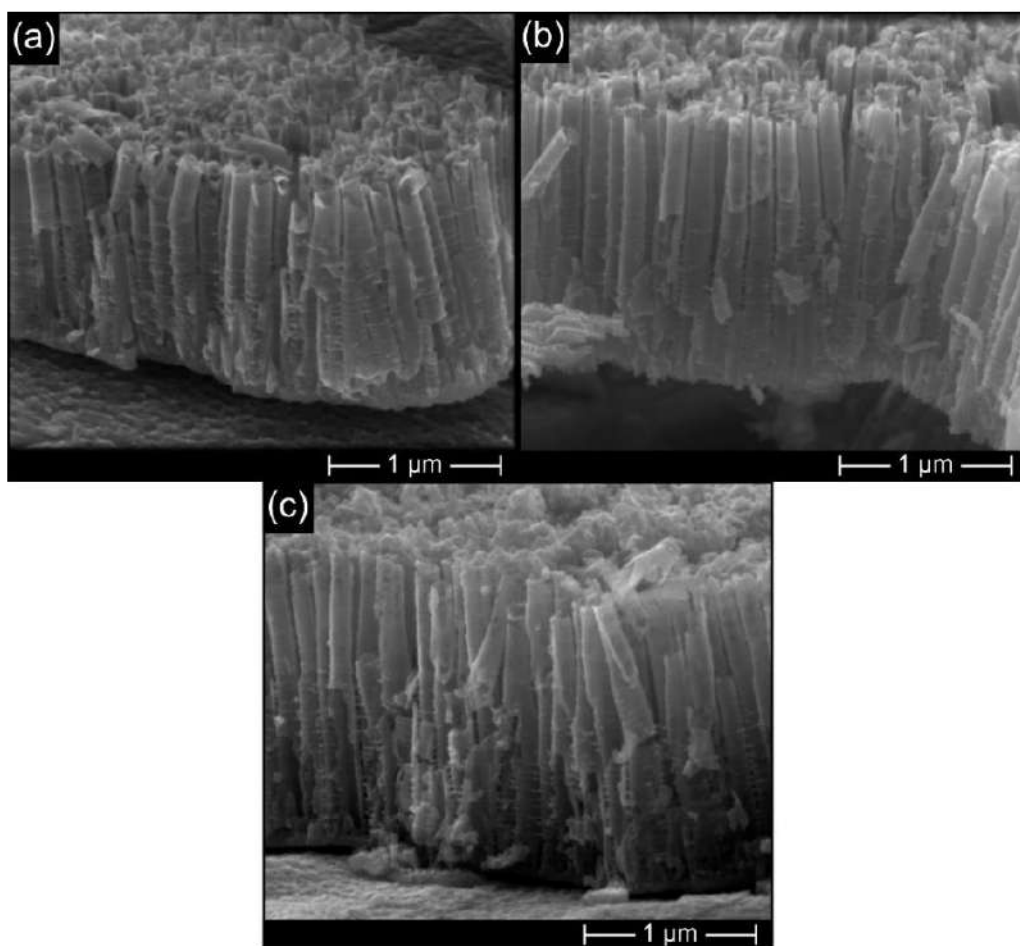
S1

Section 1: SEM images

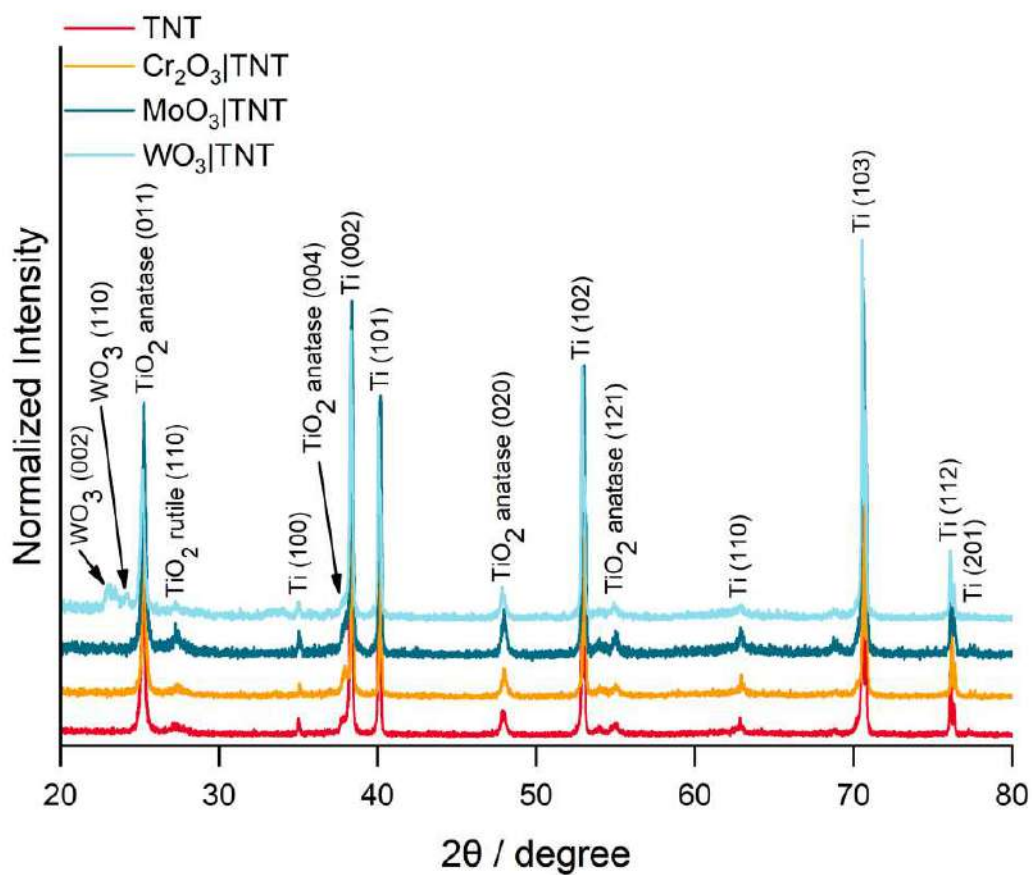**Figure S1.** SEM images in (a) a top view and (b) a cross-section view of the TNT sample.

Figure S2. SEM images in a top view of the TiO$_2$ nanotubes after magnetron sputtering of 15 nm of (a-b) chromium, (c-d) molybdenum, and (e-f) tungsten.
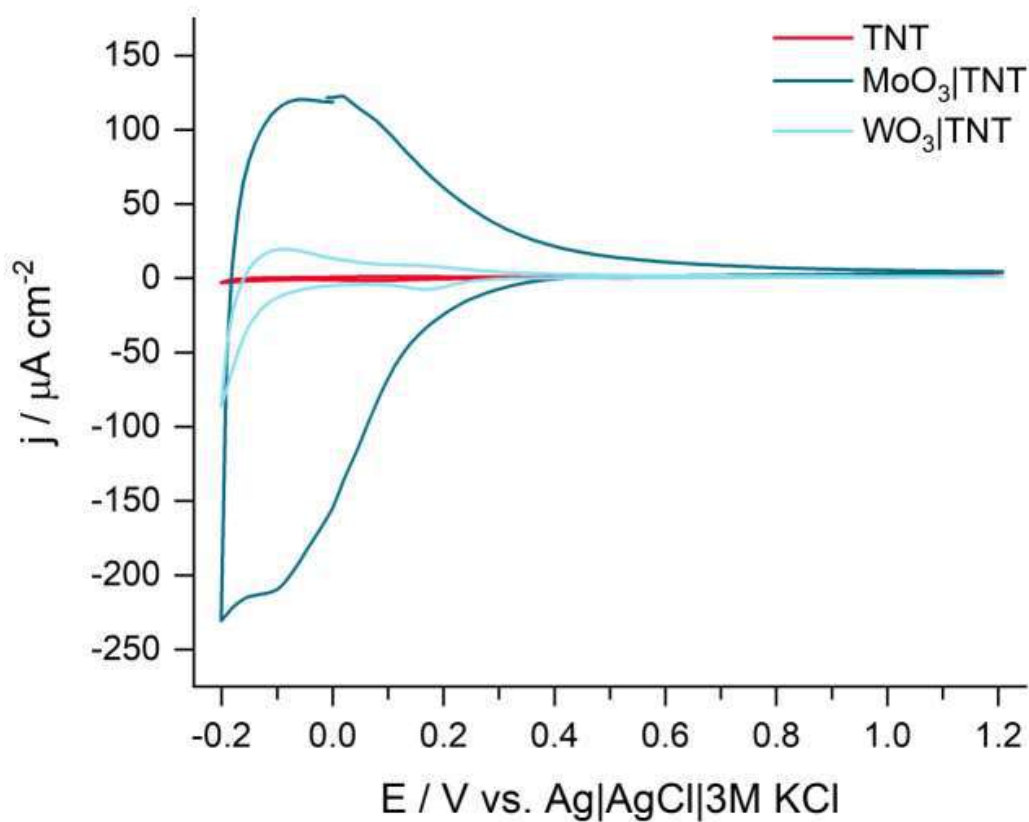
Figure S3. SEM images in a cross-section view of the (a) Cr_2O_3|TNT, (b) MoO_3|TNT, and (c) WO_3|TNT.
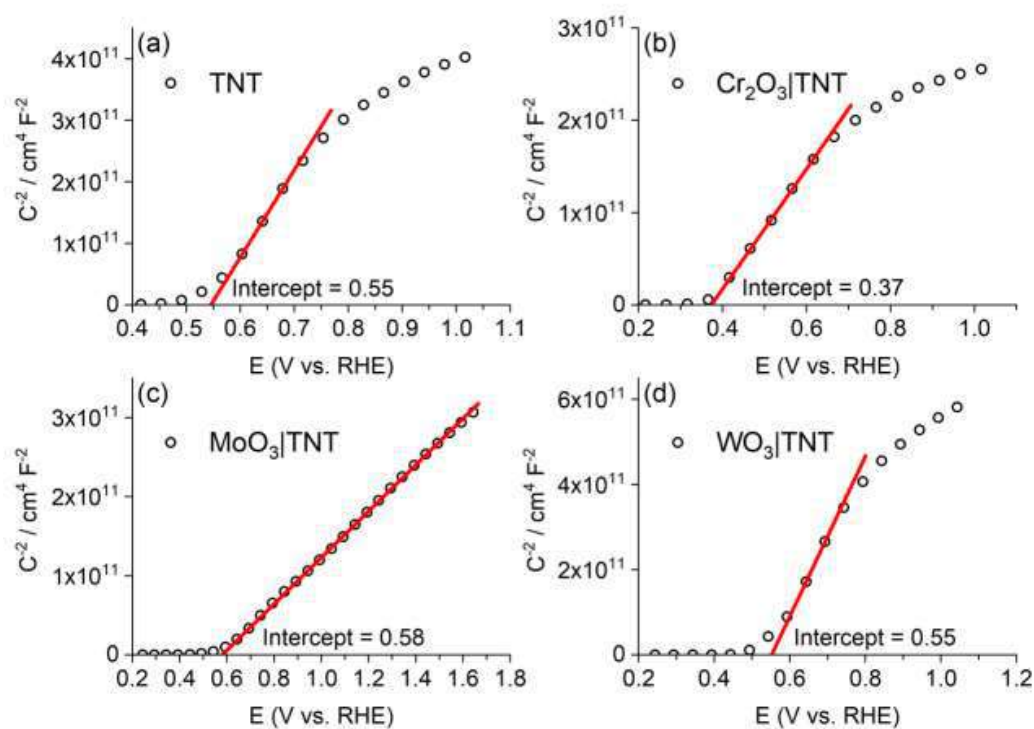
Section 2: XRD Patterns

Figure S4. XRD patterns of the TNT, Cr_2O_3|TNT, MoO_3|TNT, and WO_3|TNT.

Section 3: Cyclic voltammograms

Figure S5. Cyclic voltammograms registered in dark for the TNT, MoO$_3$|TNT, and WO$_3$|TNT.

Section 4: Mott-Schottky plots

Figure S6. Mott-Schottky plots of the (a) TNT, (b) Cr_2O_3|TNT, (c) MoO_3|TNT, and (d) WO_3|TNT.

Chapter 6. Summary and conclusions

The presented dissertation shows a new scalable method for structure modulation of TiO_2 nanotubes towards superior photoresponse using pulsed UV laser treatment as well as a study of the optical and electronic properties of the TiO_2 nanotubes combined with Cr, Mo, and W oxides using magnetron sputtering technology.

The first part of the thesis (Papers 1-2), presents a study on the laser treatment of TiO_2 nanotubes. The literature revision revealed that pulsed UV laser treatment of TiO_2 nanotubes can improve their electronic properties towards superior photoresponse by defect introduction resulting in an increase in donor density. However, typically it was realized in a static mode. To take advantage of the industrial potential of anodic TiO_2 nanotubes, any further modifications should account large-scale production. Therefore, a new scalable method for laser modification of TiO_2 nanotubes was developed and elaborated. In particular, the optical system was equipped with a beam homogenizer ensuring a square beam profile and a sample holding system with a motorized table. In such a system both precisely selected as well as any large area can be modified. Moreover, processing parameters such as frequency and speed of the motorized table can be easily scaled up, as they scale proportionally. Raman spectra of the laser-treated samples showed controlled modulation of a crystal structure along with the beam energy fluence. Optimum conditions regarding superior photocurrent up to 1.45-fold for 40 mJ cm^{-2} compared to the bare TiO_2 nanotubes have been captured. The analysis of Mott-Schottky plots showed a significant shift of flat band potential of the laser-treated TiO_2 nanotubes which suggests an increase in the number of occupied states. Taking into account no distinct photocurrent under the illumination with visible light, the additional states are located rather shallow than deep within the band gap. These advances will hopefully bring laser technology to wider commercialization for modifications of functional materials.

The second part of the thesis (Papers 3-4), studies the optical and electronic properties of TiO_2 nanotubes combined with metal oxides of the 6th group of the periodic table. The metals were deposited using magnetron sputtering followed by calcination. In the preliminary tests, it has been observed that the combination with chromium oxides results in superior photoresponse both under the illumination with AM 1.5 G, 100 mW cm^{-2} as well as the visible part of the spectrum. The opposite tendency was found for molybdenum and tungsten oxides. To explain this, an attempt was made to determine optical band gaps through the Tauc equation. However, to do so, information regarding the transition type to substitute a correct exponent is required. Studying the literature it has been observed that different authors assume different transitions and, in

general, it is done without any justification. Therefore, in the present dissertation, a new systematized method allowing the determination of the transition type based on the measured absorption data was elaborated and validated. Taylor series expansion of the logarithmic version of the Tauc equation allowed for independent absorption data on the optical band gap. Because of that, the Tauc exponent can be obtained directly from the experimentally measured absorption data without any assumptions regarding the investigated material. The estimated Tauc exponents for the TiO_2 in the form of thin film and nanotubes were equal to 2.0 and 1.9, respectively, which corresponds to the widely estimated indirect (allowed) transition occurring in titania and validates the method. The obtained Tauc exponents for the TiO_2 nanotubes combined with the investigated metal oxides allowed for the determination of optical band gap values, and then, band structures. The obtained results for the TiO_2 nanotubes with chromium oxides showed sub-band gap absorption which is responsible for an increase in photoresponse. However, band gap values and band structures were not sufficient enough to explain the deteriorated photoresponse after the deposition of molybdenum and tungsten oxides, as they remain unchanged compared to the bare TiO_2 nanotubes. Nevertheless, the obtained Tauc exponents for the TiO_2 nanotubes with molybdenum and tungsten oxides correspond to direct (forbidden) transition, which based on the transition probability, is very unlikely to occur. Therefore, the elaborated method is crucial not only for more precise determination of optical band gap but also can be used for the estimation of optical transition which can be used as a predictor for sample photoresponse. The above-described findings provide a solid base to implement laser and magnetron sputtering technologies for large-scale modifications of anodic titania nanotubes.

The conducted research and obtained results allowed to draw the following general conclusions:

1. Controlled degradation of the crystal structure of the TiO$_2$ nanotubes resulting in the superior photoresponse by pulsed UV laser treatment can be achieved in the scalable system with a beam homogenizer and motorized table without any liquid media,

2. Tauc exponent can be estimated from the experimental data, in particular, from the $\log(\alpha h v)$ vs. $h v$ dependence without any assumptions regarding the investigated material such as band gap width,

3. Transition types anticipated based on the experimentally estimated Tauc exponent can be crucial predictor for sample photoresponse, even better than optical band gap.

The main scientific achievements of the present dissertation include:

➢ Selection of optimum laser beam parameters in the scalable system equipped with a beam homogenizer and motorized table towards superior photoresponse of TiO$_2$ nanotubes **(Paper 1)**,

➢ Expansion of the absorption range of the TiO$_2$ nanotubes by the visible light after combination with Cr oxides **(Papers 3-4)**,

➢ Elaboration of a systematic method for determination of Tauc exponent and corresponding transition types based on the experimental data **(Paper 3)**.

➢ Design and 3D printing of a container for cleaning titanium substrates **(Papers 1, 3, and 4)**,

➢ Design and assembly of an experimental setup for photoelectrochemical tests **(Papers 1 and 4)**.

Personal data and list of scientific achievements

Personal data

Name	mgr inż. Łukasz Haryński
Affiliation	Institute of Fluid-Flow Machinery Polish Academy of Sciences
Scopus ID	57213676423
Orcid ID	0000-0001-9615-9996

List of scientific achievements (by Scopus)

h-index	4
Citations	44 (by 33 documents)
Number of articles (from the JCR list)	9
Number of articles (outside the JCR list)	1
Number of book chapters	1
Number of utility models	1
Participation in international conferences	3 (oral presentations)
Participation in research projects	1

Detailed list of scientific achievements

Articles from the JCR list:

1) <u>Łukasz Haryński</u>, Katarzyna Grochowska, Jakub Karczewski, Jacek Ryl, Katarzyna Siuzdak, Scalable route toward superior photoresponse of UV-laser-treated TiO_2 nanotubes, ACS *Applied Materials & Interfaces* 2020, 12, 3225-3235, doi:10.1021/acsami.9b19206. **(Paper 1)**
(IF$_{2020}$ = 9.229; MEiN = 200 pts)

2) <u>Łukasz Haryński</u>, Katarzyna Grochowska, Piotr Kupracz, Jakub Karczewski, Emerson Coy, Katarzyna Siuzdak, The in-depth studies of pulsed UV laser-modified TiO_2 nanotubes: The influence of geometry, crystallinity, and processing parameters, *Nanomaterials* 2020, 10, 430, doi:10.3390/nano10030430.
(IF$_{2020}$ = 5.076, MEiN = 100 pts)

3) Katarzyna Grochowska, Nikolay Nedyalkov, Jakub Karczewski, <u>Łukasz Haryński</u>, Gerard Śliwiński, Katarzyna Siuzdak, Anodic titania nanotubes decorated with gold nanoparticles produced by laser-induced dewetting of thin metallic films, *Scientific Reports* 2020, 10, 20506, doi:10.1038/s41598-020-77710-x.
(IF$_{2020}$ = 4.379, MEiN = 140 pts)

4) <u>Łukasz Haryński</u>, Katarzyna Grochowska, Jakub Karczewski, Jacek Ryl, Jakub Rysz, Katarzyna Siuzdak, Free-standing TiO_2 nanotubes decorated with spherical nickel nanoparticles as a cost-efficient electrocatalyst for oxygen evolution reaction, *RSC Advances* 2021, 11, 219-228, doi:10.1039/D0RA07563A.
(IF$_{2021}$ = 4.036, MEiN = 100 pts)

5) Katarzyna Siuzdak, <u>Łukasz Haryński</u>, Jakub Wawrzyniak, Katarzyna Grochowska, Review on robust laser light interaction with titania – Patterning, crystallization and ablation processes, *Progress in Solid State Chemistry* 2021, 62, 100297, doi:10.1016/j.progsolidstchem.2020.100297.
(IF$_{2021}$ = 8.389, MEiN = 200 pts) **(Paper 2)**

6) <u>Łukasz Haryński</u>, Jakub Karczewski, Jacek Ryl, Katarzyna Grochowska, Katarzyna Siuzdak, Rapid development of the photoresponse and oxygen evolution of TiO_2 nanotubes sputtered with Cr thin films realized via laser annealing, *Journal of Alloys and Compounds* 2021, 877, 160316, doi:10.1016/j.jallcom.2021.160316.
(IF$_{2021}$ = 6.371, MEiN = 100 pts)

7) <u>Łukasz Haryński</u>, Adrian Olejnik, Katarzyna Grochowska, Katarzyna Siuzdak, A facile method for Tauc exponent and corresponding electronic transitions determination in semiconductors directly from UV–vis spectroscopy data, *Optical Materials* 2022, 127, 112205, doi:10.1016/j.optmat.2022.112205.

   (IF$_{2021}$ = 3.754, MEiN = 70 pts) **(Paper 3)**

8) <u>Łukasz Haryński</u>, Adrian Olejnik, Jakub Karczewski, Jacek Ryl, Katarzyna Grochowska, Katarzyna Siuzdak, Linking optical and electronic properties to photoresponse of heterojunctions based on titania nanotubes and chromium, molybdenum, and tungsten oxides, *Optical Materials* 2022, 134, 113183, doi:10.1016/j.optmat.2022.113183

   (IF$_{2021}$ = 3.754, MEiN = 70 pts) **(Paper 4)**

Articles outside the JCR list:

1) <u>Łukasz Haryński</u>, Katarzyna Grochowska, Oświeć mnie, czyli jak oddziałuje światło z materią, *Fizyka w Szkole z Astronomią* 2019, 4, 19-23

Book chapters:

1) Katarzyna Siuzdak, <u>Łukasz Haryński</u>, Jakub Wawrzyniak, Piotr Kupracz, Katarzyna Grochowska, Self-standing Nanoarchitectures in Inamuddin, Rajender Boddula, Abdullah M. Asiri (eds) Self-standing Substrates. Engineering Materials. Springer 2020, Chapter 1, 1-56, doi: 10.1007/978-3-030-29522-6_1

Utility models:

1) <u>Łukasz Haryński</u>, Katarzyna Grochowska, Katarzyna Siuzdak, Kuweta Do Czyszczenia Podłóż Metalicznych, Korzystnie Folii Tytanowych, No. W.128308.

Participation in international conferences (oral presentations):

1) <u>Łukasz Haryński</u>, Piotr Kupracz, Katarzyna Grochowska, Katarzyna Siuzdak, *UV laser-induced phase conversion of free-standing TiO$_2$NTs*, EUROMAT 2019, 1-5 September, Stockholm, Sweden

2) <u>Łukasz Haryński</u>, Jakub Karczewski, Jacek Ryl, Katarzyna Grochowska, Katarzyna Siuzdak, *Optical Properties and Photoresponse of TiO$_2$ Nanotubes Decorated with Metal Oxides of the 6th Main Group of the Periodic Table*, NanoTech 2022, 1-3 June, Poznań, Poland

3) <u>Łukasz Haryński</u>, Adrian Olejnik, Katarzyna Grochowska, Katarzyna Siuzdak, *Experimental Method for the Tauc Exponent and Corresponding Transition Types Determination*, IWASOM'2022, 10-15 July, Gdańsk, Poland

Participation in research projects:

1) *Towards superior photoactivity of TiO$_2$ nanotubes modified by pulsed laser nanostructuring*, National Science Centre, SONATA BIS 7, 2017/26/E/ST5/00416

University scholarships:

1) The Szewalski Institute of Fluid-Flow Machinery Polish Academy of Sciences for the best PhD students in the academic years 2020/2021 and 2021/2022.
2) Gdańsk University of Technology Rector's scholarship for the best PhD students in the academic years 2020/2021 and 2021/2022.
3) Gdańsk University of Technology pro-quality scholarship in the academic years 2020/2021 and 2021/2022.

Appendix: authors contribution statement

Paper 1: <u>Łukasz Haryński</u>, Katarzyna Grochowska, Jakub Karczewski, Jacek Ryl, Katarzyna Siuzdak, Scalable route toward superior photoresponse of UV-laser-treated TiO_2 nanotubes, *ACS Applied Materials & Interfaces* 2020, 12, 3225-3235, doi:10.1021/acsami.9b19206.

<u>**Łukasz Haryński:**</u> planning of the experiments; synthesis of titania nanotubes; carrying out the UV-vis and Raman spectroscopy, cyclic and linear voltammetry, chronoamperometry, and electrochemical impedance spectroscopy tests; analysis of the obtained results; maintaining research data; writing an original draft, cover letter, and response on reviewers' comments; data visualization; preparation of graphical abstract.
<u>My contribution is estimated at 60 %.</u>

Signature

Katarzyna Grochowska: taking part in the planning of experiments and discussion of the results regarding the morphology, and structural and optical properties of the investigated materials, revision of the manuscript and response on reviewers' comments.
<u>My contribution is estimated at 5 %.</u>

Signature

Jakub Karczewski: obtaining SEM images.
<u>My contribution is estimated at 5 %.</u>
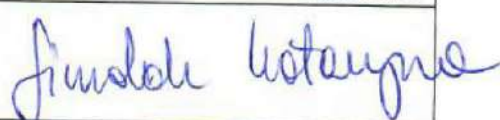
Signature

Jacek Ryl: carrying out the XPS, fitting and analysis of the XPS spectra.
<u>My contribution is estimated at 10 %.</u>

Signature

Katarzyna Siuzdak: development and design of the methodology; acquisition of the financial support for the project leading to this publication; provision of study materials, reagents, and other analysis tools; taking part in planning of the experiment and analysis of the results; supervision; revision of the manuscript and response on reviewers' comments.
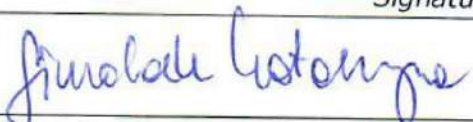My contribution is estimated at 20 %.

	Signature

Paper 2: Katarzyna Siuzdak, <u>Łukasz Haryński</u>, Jakub Wawrzyniak, Katarzyna Grochowska, Review on robust laser light interaction with titania – Patterning, crystallization and ablation processes, *Progress in Solid State Chemistry* 2021, 62, 100297, doi:10.1016/j.progsolidstchem.2020.100297.

Katarzyna Siuzdak: writing an abstract, introduction, and conclusions of the original draft, cover letter and response on reviewers' comments; responsibility for the activity planning and execution.
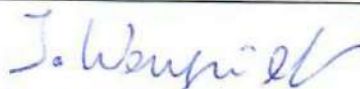<u>My contribution is estimated at 25 %.</u>

Signature

<u>Łukasz Haryński:</u> writing a Section 5 entitled *Laser induced phase transformation* of the original draft and response on reviewers' comments.
<u>My contribution is estimated at 25 %.</u>

Signature

Jakub Wawrzyniak: writing Sections 3 and 4 entitled *Surface modification and patterning via laser irradiation* and *Ablation-induced TiO$_2$ deposition* of the original draft, respectively and response on reviewers' comments.
<u>My contribution is estimated at 25 %.</u>

Signature

Katarzyna Grochowska: writing Section 2 entitled *Laser-material interaction* of the original draft and response on reviewers' comments; consulting the content of the whole manuscript.
<u>My contribution is estimated at 25 %.</u>

Signature

Paper 3: Łukasz Haryński, Adrian Olejnik, Katarzyna Grochowska, Katarzyna Siuzdak, A facile method for Tauc exponent and corresponding electronic transitions determination in semiconductors directly from UV–vis spectroscopy data, *Optical Materials* 2022, 127, 112205, doi:10.1016/j.optmat.2022.112205

Łukasz Haryński: development and design of the methodology; planning of the experiments; synthesis of titania nanotubes; magnetron sputtering of metals, carrying out the UV-vis spectroscopy tests; analysis of the obtained results; maintaining research data; writing an original draft, cover letter, and response on reviewers' comments; data visualization; preparation of graphical abstract.

My contribution is estimated at 40 %.

Signature
Łukasz Haryński (signature)

Adrian Olejnik: development and design of the methodology; performing the DFT calculations; analysis of the obtained results; writing an original draft, and response on reviewers' comments.

My contribution is estimated at 40 %.

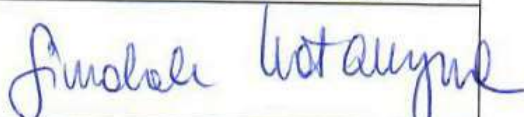| Signature |
|---|
| *Adrian Olejnik (signature)* |

Katarzyna Grochowska: taking part in the discussion of the results, revision of the manuscript and response on reviewers' comments.

My contribution is estimated at 5 %.

Signature
K. Grochowska (signature)

Katarzyna Siuzdak: acquisition of the financial support for the project leading to this publication; provision of study materials, reagents, and other analysis tools; taking part in planning of the experiment and analysis of the results; supervision; revision of the manuscript and response on reviewers' comments.

My contribution is estimated at 15 %.

Signature
Siuzdak Katarzyna (signature)

Paper 4: <u>Łukasz Haryński</u>, Adrian Olejnik, Jakub Karczewski, Jacek Ryl, Katarzyna Grochowska, Katarzyna Siuzdak, Linking optical and electronic properties to photoresponse of heterojunctions based on titania nanotubes and chromium, molybdenum, and tungsten oxides, *Optical* Materials 2022, 134, 113183, doi: 10.1016/j.optmat.2022.113183.
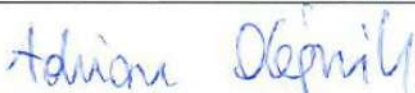
Łukasz Haryński: development and design of the methodology; planning of the experiments; synthesis of titania nanotubes; magnetron sputtering of metals, carrying out the UV-vis, photocurrent, and Raman spectroscopy, cyclic and linear voltammetry, and electrochemical impedance spectroscopy tests; analysis of the obtained results; maintaining research data; writing an original draft, cover letter, and response on reviewers' comments; data visualization; preparation of graphical abstract.

<u>My contribution is estimated at 50 %.</u>

Signature

Adrian Olejnik: performing the DFT calculations; analysis of the obtained results; writing an original draft, and response on reviewers' comments.

<u>My contribution is estimated at 10 %.</u>

Signature

Jakub Karczewski: obtaining SEM images and carrying out the XRD.

<u>My contribution is estimated at 10 %.</u>

Signature

Jacek Ryl: carrying out the XPS, fitting and analysis of the XPS spectra.

<u>My contribution is estimated at 10 %.</u>
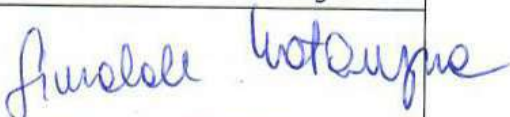
Signature

Katarzyna Grochowska: taking part in the discussion of the results, revision of the manuscript and response on reviewers' comments.

<u>My contribution is estimated at 5 %.</u>

Signature

Katarzyna Siuzdak: acquisition of the financial support for the project leading to this publication; provision of study materials, reagents, and other analysis tools; taking part in planning of the experiment and analysis of the results; supervision; revision of the manuscript and response on reviewers' comments. My contribution is estimated at 15 %.

Signature

References

1. Renewable Energy Resources: Bioenergy, Geothermal, Hydropower, Ocean, Solar, Wind Available online: https://www.irena.org/ (accessed on 22 April 2022).

2. Pu, P.; Cachet, H.; Ngaboyamahina, E.; Sutter, E.M.M. Relation between Morphology and Conductivity in TiO_2 Nanotube Arrays: An Electrochemical Impedance Spectrometric Investigation. *J. Solid State Electrochem.* **2013**, *17*, 817–828, doi:10.1007/s10008-012-1931-0.

3. Lee, K.; Mazare, A.; Schmuki, P. One-Dimensional Titanium Dioxide Nanomaterials: Nanotubes. *Chem. Rev.* **2014**, *114*, 9385–9454, doi:10.1021/cr500061m.

4. Durdu, S.; Cihan, G.; Yalcin, E.; Altinkok, A. Characterization and Mechanical Properties of TiO_2 Nanotubes Formed on Titanium by Anodic Oxidation. *Ceram. Int.* **2021**, *47*, 10972–10979, doi:10.1016/j.ceramint.2020.12.218.

5. Kasuga, T.; Hiramatsu, M.; Hoson, A.; Sekino, T.; Niihara, K. Formation of Titanium Oxide Nanotube. *Langmuir* **1998**, *14*, 3160–3163, doi:10.1021/la9713816.

6. Kasuga, T.; Hiramatsu, M.; Hoson, A.; Sekino, T.; Niihara, K. Titania Nanotubes Prepared by Chemical Processing. *Adv. Mater.* **1999**, *11*, 1307–1311, doi:10.1002/(SICI)1521-4095(199910)11:15<1307::AID-ADMA1307>3.0.CO;2-H.

7. Shin, H.; Jeong, D.-K.; Lee, J.; Sung, M.M.; Kim, J. Formation of TiO_2 and ZrO_2 Nanotubes Using Atomic Layer Deposition with Ultraprecise Control of the Wall Thickness. *Adv. Mater.* **2004**, *16*, 1197–1200, doi:10.1002/adma.200306296.

8. Roy, P.; Berger, S.; Schmuki, P. TiO_2 Nanotubes: Synthesis and Applications. **2011**, *50*, 2904–2939, doi:10.1002/anie.201001374.

9. Xiang, C.; Sun, L.; Wang, Y.; Wang, G.; Zhao, X.; Zhang, S. Large-Scale, Uniform, and Superhydrophobic Titania Nanotubes at the Inner Surface of 1000 Mm Long Titanium Tubes. *J. Phys. Chem. C* **2017**, *121*, 15448–15455, doi:10.1021/acs.jpcc.7b03124.

10. Ghicov, A.; Tsuchiya, H.; Macak, J.M.; Schmuki, P. Annealing Effects on the Photoresponse of TiO_2 Nanotubes. *Phys. Status Solidi A* **2006**, *203*, R28–R30, doi:10.1002/pssa.200622041.

11. Zwiebach, B. MIT OpenCourseWare, 8.06 Quantum Physics III, Spring 2018, Available online: https://ocw.mit.edu/courses/8-06-quantum-physics-iii-spring-2018/ (accessed on 27 April 2022).

12. Sopha, H.; Mirza, I.; Turčičova, H.; Pavlinak, D.; Michalicka, J.; Krbal, M.; Rodriguez-Pereira, J.; Hromadko, L.; Novák, O.; Mužík, J.; et al. Laser-Induced Crystallization of Anodic TiO_2 Nanotube Layers. *RSC Adv.* **2020**, *10*, 22137–22145, doi:10.1039/D0RA02929G.

13. Xu, Y.; Melia, M.A.; Tsui, L.; Fitz-Gerald, J.M.; Zangari, G. Laser-Induced Surface Modification at Anatase TiO_2 Nanotube Array Photoanodes for Photoelectrochemical Water Oxidation. *J. Phys. Chem. C* **2017**, *121*, 17121–17128, doi:10.1021/acs.jpcc.7b05368.

14. Chen, Z.; Jaramillo, T.F. The Use of UV-Visible Spectroscopy to Measure the Band Gap of a Semiconductor Available online: https://mmrc.caltech.edu/Cary%20UV-Vis%20Int.Sphere/Literature/Spectroscopy%20Jaramillo.pdf (accessed on 27 April 2022).

15. Macak, J.M.; Tsuchiya, H.; Ghicov, A.; Yasuda, K.; Hahn, R.; Bauer, S.; Schmuki, P. TiO_2 Nanotubes: Self-Organized Electrochemical Formation, Properties and Applications. *Curr. Opin. Solid State Mater. Sci.* **2007**, *11*, 3–18, doi:10.1016/j.cossms.2007.08.004.

16. Wang, Y.; Zhang, R.; Li, J.; Li, L.; Lin, S. First-Principles Study on Transition Metal-Doped Anatase TiO_2. *Nanoscale Res. Lett.* **2014**, *9*, 46, doi:10.1186/1556-276X-9-46.

17. Murphy, A. Band-Gap Determination from Diffuse Reflectance Measurements of Semiconductor Films, and Application to Photoelectrochemical Water-Splitting. *Sol. Energy Mater. Sol. Cells* **2007**, *91*, 1326–1337, doi:10.1016/j.solmat.2007.05.005.

18. Honsberg, C.B.; Bowden, S.G. Photovoltaics Education Website, Available online: https://www.pveducation.org/ (accessed on 27 April 2022).

19. Hall, L.H.; Bardeen, J.; Blatt, F.J. Infrared Absorption Spectrum of Germanium. *Phys. Rev.* **1954**, *95*, 559–560, doi:10.1103/PhysRev.95.559.

20. Griffiths, D.J. *Introduction to Quantum Mechanics*; Prentice Hall: Englewood Cliffs, N.J, 1995; ISBN 978-0-13-124405-4.

21. Makuła, P.; Pacia, M.; Macyk, W. How To Correctly Determine the Band Gap Energy of Modified Semiconductor Photocatalysts Based on UV–Vis Spectra. *J. Phys. Chem. Lett.* **2018**, *9*, 6814–6817, doi:10.1021/acs.jpclett.8b02892.

22. Roy, P.; Kim, D.; Lee, K.; Spiecker, E.; Schmuki, P. TiO_2 Nanotubes and Their Application in Dye-Sensitized Solar Cells. *Nanoscale* **2010**, *2*, 45–59, doi:10.1039/B9NR00131J.

23. O'Regan, B.; Grätzel, M. A Low-Cost, High-Efficiency Solar Cell Based on Dye-Sensitized Colloidal TiO_2 Films. *Lett. Nat.* **1991**, *353*, 737–740, doi:10.1038/353737a0.

24. Roy, P.; Albu, S.P.; Schmuki, P. TiO_2 Nanotubes in Dye-Sensitized Solar Cells: Higher Efficiencies by Well-Defined Tube Tops. *Electrochem. Commun.* **2010**, *12*, 949–951, doi:10.1016/j.elecom.2010.04.029.

25. Haryński, Ł.; Olejnik, A.; Grochowska, K.; Siuzdak, K. A Facile Method for Tauc Exponent and Corresponding Electronic Transitions Determination in Semiconductors Directly from UV–Vis Spectroscopy Data. *Opt. Mater.* **2022**, *127*, 112205, doi:10.1016/j.optmat.2022.112205.

26. Chen, X.; Liu, L.; Yu, P.Y.; Mao, S.S. Increasing Solar Absorption for Photocatalysis with Black Hydrogenated Titanium Dioxide Nanocrystals. *Science* **2011**, *331*, 746–750, doi:10.1126/science.1200448.

27. Rajaraman, T.S.; Parikh, S.P.; Gandhi, V.G. Black TiO_2: A Review of Its Properties and Conflicting Trends. *Chem. Eng. J.* **2020**, *389*, 123918, doi:10.1016/j.cej.2019.123918.

28. Nakajima, T.; Nakamura, T.; Shinoda, K.; Tsuchiya, T. Rapid Formation of Black Titania Photoanodes: Pulsed Laser-Induced Oxygen Release and Enhanced Solar Water Splitting Efficiency. *J Mater Chem A* **2014**, *2*, 6762–6771, doi:10.1039/C4TA00557K.

29. Zuñiga-Ibarra, V.A.; Shaji, S.; Krishnan, B.; Johny, J.; Sharma Kanakkillam, S.; Avellaneda, D.A.; Martinez, J.A.A.; Roy, T.K.D.; Ramos-Delgado, N.A. Synthesis and Characterization of Black TiO_2 Nanoparticles by Pulsed Laser Irradiation in Liquid. *Appl. Surf. Sci.* **2019**, *483*, 156–164, doi:10.1016/j.apsusc.2019.03.302.

30. Yaghoubi, H.; Li, Z.; Chen, Y.; Ngo, H.T.; Bhethanabotla, V.R.; Joseph, B.; Ma, S.; Schlaf, R.; Takshi, A. Toward a Visible Light-Driven Photocatalyst: The Effect of Midgap-States-Induced Energy Gap of Undoped TiO_2 Nanoparticles. *ACS Catal.* **2015**, *5*, 327–335, doi:10.1021/cs501539q.

31. Oldham, W.H.; Milnes, A.G. N-n Semiconductor Heterojunctions. *Solid-State Electron.* **1963**, *6*, 121–132, doi:10.1016/0038-1101(63)90005-4.

32. Anderson, R.L. Germanium-Gallium Arsenide Heterojunctions [Letter to the Editor]. *IBM J. Res. Dev.* **1960**, *4*, 283–287, doi:10.1147/rd.43.0283.

33. Yamauchi, T.; Tabuchi, M.; Nakamura, A. Size Dependence of the Work Function in InAs Quantum Dots on GaAs(001) as Studied by Kelvin Force Probe Microscopy. *Appl. Phys. Lett.* **2004**, *84*, 3834–3836, doi:10.1063/1.1745110.

34. Carcia, P.F.; McCarron III, E.M. Synthesis and Properties of Thin Film Polymorphs of Molybdenum Trioxide. *Synth. Prop. Thin Film Polymorphs Molybdenum Trioxide* **1987**, *155*, 53–63, doi:10.1016/0040-6090(87)90452-4.

35. Zheng, H.; Ou, J.Z.; Strano, M.S.; Kaner, R.B.; Mitchell, A.; Kalantar-zadeh, K. Nanostructured Tungsten Oxide - Properties, Synthesis, and Applications. *Adv. Funct. Mater.* **2011**, *21*, 2175–2196, doi:10.1002/adfm.201002477.

36. Hu, Z.; Xu, M.; Shen, Z.; Yu, J.C. A Nanostructured Chromium(III) Oxide/Tungsten(VI) Oxide p–n Junction Photoanode toward Enhanced Efficiency for

Water Oxidation. *J. Mater. Chem. A* **2015**, *3*, 14046–14053, doi:10.1039/C5TA02528A.

37. Kröger, M.; Hamwi, S.; Meyer, J.; Riedl, T.; Kowalsky, W.; Kahn, A. Role of the Deep-Lying Electronic States of MoO_3 in the Enhancement of Hole-Injection in Organic Thin Films. *Appl. Phys. Lett.* **2009**, *95*, 123301, doi:10.1063/1.3231928.

38. Metikoš-Huković, M.; Ceraj-Cerić, M. P-Type and N-Type Behavior of Chromium Oxide as a Function of the Applied Potential. *J. Electrochem. Soc.* **1987**, *134*, 2193–2197.

39. Abdullah, M.M.; Rajab, F.M.; Al-Abbas, S.M. Structural and Optical Characterization of Cr_2O_3 Nanostructures: Evaluation of Its Dielectric Properties. *AIP Adv.* **2014**, *4*, 027121, doi:10.1063/1.4867012.

40. Cheng, C.-S.; Gomi, H.; Sakata, H. Electrical and Optical Properties of Cr_2O_3 Films Prepared by Chemical Vapour Deposition. *Phys. Status Solidi A* **1996**, *155*, 417–425, doi:10.1002/pssa.2211550215.

41. Wang, Y.; Fu, H.; Yang, X.; An, X.; Zou, Q.; Xiong, S.; Han, D. Pt Nanoparticles-Modified WO_3@TiO_2 Core–Shell Ternary Nanocomposites as Stable and Efficient Photocatalysts in Tetracycline Degradation. *J. Mater. Sci.* **2020**, *55*, 14415–14430, doi:10.1007/s10853-020-05014-6.

42. Xiao, T.; Tang, Z.; Yang, Y.; Tang, L.; Zhou, Y.; Zou, Z. In Situ Construction of Hierarchical WO_3/g-C_3N_4 Composite Hollow Microspheres as a Z-Scheme Photocatalyst for the Degradation of Antibiotics. *Appl. Catal. B Environ.* **2018**, *220*, 417–428, doi:10.1016/j.apcatb.2017.08.070.

43. Sangiorgi, N.; Aversa, L.; Tatti, R.; Verucchi, R.; Sanson, A. Spectrophotometric Method for Optical Band Gap and Electronic Transitions Determination of Semiconductor Materials. *Opt. Mater.* **2017**, *64*, 18–25, doi:10.1016/j.optmat.2016.11.014.

44. Ding, J.; Ming, J.; Lu, D.; Wu, W.; Liu, M.; Zhao, X.; Li, C.; Yang, M.; Fang, P. Study of the Enhanced Visible-Light-Sensitive Photocatalytic Activity of Cr_2O_3-Loaded Titanate Nanosheets for Cr(VI) Degradation and H_2 Generation. *Catal. Sci. Technol.* **2017**, *7*, 2283–2297, doi:10.1039/C7CY00644F.

45. Reyes-Gil, K.R.; Robinson, D.B. WO_3 -Enhanced TiO_2 Nanotube Photoanodes for Solar Water Splitting with Simultaneous Wastewater Treatment. *ACS Appl. Mater. Interfaces* **2013**, *5*, 12400–12410, doi:10.1021/am403369p.

46. Liu, H.; Lv, T.; Zhu, C.; Zhu, Z. Direct Bandgap Narrowing of TiO_2/MoO_3 Heterostructure Composites for Enhanced Solar-Driven Photocatalytic Activity. *Sol. Energy Mater. Sol. Cells* **2016**, *153*, 1–8, doi:10.1016/j.solmat.2016.04.013.

47. Haryński, Ł.; Grochowska, K.; Siuzdak, K. Kuweta Do Czyszczenia Podłóż Metalicznych, Korzystnie Folii Tytanowych, No. W.128308.

48. Xu, Y.; Melia, M.A.; Tsui, L.; Fitz-Gerald, J.M.; Zangari, G. Laser-Induced Surface Modification at Anatase TiO_2 Nanotube Array Photoanodes for Photoelectrochemical Water Oxidation. *J. Phys. Chem. C* **2017**, *121*, 17121–17128, doi:10.1021/acs.jpcc.7b05368.

49. Swann, S. Magnetron Sputtering. *Phys. Technol.* **1988**, *19*, 67–75, doi:http://iopscience.iop.org/0305-4624/19/2/304.

50. Dvorak, F.; Zazpe, R.; Krbal, M.; Sopha, H.; Prikryl, J.; Ng, S.; Hromadko, L.; Bures, F.; Macak, J.M. One-Dimensional Anodic TiO_2 Nanotubes Coated by Atomic Layer Deposition: Towards Advanced Applications. *Appl. Mater. Today* **2019**, *14*, 1–20, doi:10.1016/j.apmt.2018.11.005.

51. Yoo, J.E.; Lee, K.; Altomare, M.; Selli, E.; Schmuki, P. Self-Organized Arrays of Single-Metal Catalyst Particles in TiO_2 Cavities: A Highly Efficient Photocatalytic System. *Angew. Chem. Int. Ed.* **2013**, *52*, 7514–7517, doi:10.1002/anie.201302525.

52. Grochowska, K.; Ryl, J.; Karczewski, J.; Śliwiński, G.; Cenian, A.; Siuzdak, K. Non-Enzymatic Flexible Glucose Sensing Platform Based on Nanostructured TiO_2 – Au Composite. *J. Electroanal. Chem.* **2019**, *837*, 230–239, doi:10.1016/j.jelechem.2019.02.040.

53. Boentoro, T.W.; Szyszka, B.; Martinu, L. Protective Coatings for Durability Enhancement of Optical Surfaces. In *Optical Thin Films and Coatings*; Elsevier, 2018; pp. 539–564 ISBN 978-0-08-102073-9.

54. Haryński, Ł.; Karczewski, J.; Ryl, J.; Grochowska, K.; Siuzdak, K. Rapid Development of the Photoresponse and Oxygen Evolution of TiO_2 Nanotubes Sputtered with Cr Thin Films Realized via Laser Annealing. *J. Alloys Compd.* **2021**, *877*, 160316, doi:10.1016/j.jallcom.2021.160316.

55. *Surface Analysis by Auger and X-Ray Photoelectron Spectroscopy*; Briggs, D., Grant, J.T., Eds.; IM Publications: Chichester, West Sussex, U.K, 2003; ISBN 978-1-901019-04-9.

56. Parsons, R. Atlas of Electrochemical Equilibria in Aqueous Solutions. *J. Electroanal. Chem. Interfacial Electrochem.* **1967**, *13*, 471, doi:10.1016/0022-0728(67)80059-7.

57. Cardon, F.; Gomes, W.P. On the Determination of the Flat-Band Potential of a Semiconductor in Contact with a Metal or an Electrolyte from the Mott-Schottky Plot. *J. Phys. Appl. Phys.* **1978**, *11*, L63–L67, doi:10.1088/0022-3727/11/4/003.

58. Park, B.H.; Li, L.S.; Gibbons, B.J.; Huang, J.Y.; Jia, Q.X. Photovoltaic Response and Dielectric Properties of Epitaxial Anatase-TiO_2 Films Grown on Conductive

La$_{0.5}$Sr$_{0.5}$CoO$_3$ Electrodes. *Appl. Phys. Lett.* **2001**, *79*, 2797–2799, doi:10.1063/1.1412822.

59. Haryński, Ł.; Grochowska, K.; Kupracz, P.; Karczewski, J.; Coy, E.; Siuzdak, K. The In-Depth Studies of Pulsed UV Laser-Modified TiO$_2$ Nanotubes: The Influence of Geometry, Crystallinity, and Processing Parameters. *Nanomaterials* **2020**, *10*, 430, doi:10.3390/nano10030430.

60. Bott, A.W. Electrochemistry of Semiconductors. *Curr. Sep.* **1998**, *17*, 87–91.

61. Li, A.; Wang, Z.; Yin, H.; Wang, S.; Yan, P.; Huang, B.; Wang, X.; Li, R.; Zong, X.; Han, H.; et al. Understanding the Anatase–Rutile Phase Junction in Charge Separation and Transfer in a TiO$_2$ Electrode for Photoelectrochemical Water Splitting. *Chem. Sci.* **2016**, *7*, 6076–6082, doi:10.1039/C6SC01611A.